Dynamic Analysis of Gearwheels with Viscoelastic Damping Treatments

João Filipe Seabra da Costa

Dissertation submitted to
Faculdade de Engenharia da Universidade do Porto
for the degree of:

Master in Mechanical Engineering

Advisor:
Professor Doutor José Dias Rodrigues
(Associate Professor)

Co-Advisor:
Professor João Pereira Amorim

Laboratório de Vibrações de Sistemas Mecânicos
Departamento de Engenharia Mecânica
Faculdade de Engenharia da Universidade do Porto

Porto, 2018

The work presented in this dissertation was performed at
Laboratory of Vibrations of Mechanical Systems
Department of Mechanical Engineering
Faculty of Engineering
University of Porto
Porto, Portugal.

João Filipe Seabra da Costa
E-mail: up201304647@fe.up.pt

Faculdade de Engenharia da Universidade do Porto
Departamento de Engenharia Mecânica
Laboratório de Vibrações de Sistemas Mecânicos
Rua Dr. Roberto Frias s/n, Sala M206
4200-465 Porto
Portugal

Abstract

Rotating circular structures occur in many technical applications, such as computer hard drives, turbines, saws, clutches, disk brakes and gears, just to mention a few. These experience vibrations that if not contained can cause instabilities, leading to serious damages and, ultimately, to their failure. Thus, it is important to determine the dynamic behavior of these spinning components while in the design stage, where the influence of the global spinning movement is taken into account, and to develop convenient vibration energy dissipation methods. Marsaudon and Cutuli [2014] proposed a damping device to be applied in gearwheels of turbine engines' speed-reducing gearboxes, based on constrained viscoelastic material circumferential patches applied in the wheel's web, obtaining promising results.

The present work addresses the study of the dynamic behavior and vibration control of spinning circular structures, namely plane and sloped (with axial extension, in addition to the radial extension) gearwheels, through viscoelastic damping treatments, using the finite element method. Four node facet shell elements based on a layerwise plate theory are considered, in order to correctly represent the shear strains induced in the dissipative layer and to easily geometrically model the studied components, and the rotational effects implemented. The validation tests for the developed numerical tool are conducted with numerical examples obtained from the literature and with results obtained using a commercial finite element method software. The damping efficiency of circumferential and radial damping devices' configurations is analyzed and discussed. In the circumferential group were considered the completely covered surface, an outer annular shape and inner annular shape, these last two both complete and split into two, four and six sections. In the radial group were considered two, four and six patches, also both complete and split. The web's inclination angle effect is studied and a comparison between the treatments' setups is made.

Keywords: gearwheel, rotating disk, viscoelastic damping treatment, finite element method, layerwise plate theory, rotating facet shell element.

Resumo

Estruturas circulares em rotação pode sem encontradas numa vasta gama de aplicações técnicas, como discos rígidos de computadores, turbinas, serras, embraiagens, discos de travões e engrenagens, apenas para mencionar algumas. Estas experienciam vibrações mecânicas que, quando não controladas, causam instabilidades no seu funcionamento, podendo levar à ocorrência de danos graves e, em último caso, à falha do sistema. Assim, torna-se importante determinar o comportamento dinâmico dos componentes em rotação ainda na fase do projeto e dimensionamento, tendo sempre em consideração a influência do movimento global de rotação, e desenvolver métodos convenientes de dissipação da energia de vibração. Marsaudon and Cutuli [2014] propuseram um dispositivo de amortecimento a ser aplicado em rodas dentadas de redutores de motores de turbina baseado em trechos circunferenciais de material viscoelástico com camada de restrição aplicados na alma da roda, tendo verificado resultados bastante promissores.

O presente trabalho aborda o estudo do comportamento dinâmico e do controlo de vibrações de estruturas circulares em rotação, nomeadamente rodas dentadas planas e inclinadas (com extensão axial, para além da radial), através de tratamentos de amortecimento com materail viscoelástico, usando o método dos elementos finitos. Elementos casca de faceta com quatro nós baseados numa teoria de placa *layerwise* são considerados, com o objetivo de representar corretamente as tensões de corte induzidas na camada dissipativa e de facilmente modelar geometricamente os componentes estudados, e os efeitos resultantes da rotação implementados. Os testes de validação da presente ferramenta numérica desenrolam-se recorrendo a exemplos apresentados na literatura e a resultados obtidos através de *software* comercial de aplicação do método dos elementos finitos. A eficiência do amortecimento desenvolvido por dispositivos com configurações circunferenciais e radiais é analisada e discutida. No grupo das configurações circunferenciais foram consideradas a cobertura completa de toda a superfície tratável, um anel exterior e um anel interior, estes dois últimos tanto completos como interrompidos em duas, quatro e seis secções. No grupo das configurações radiais foram considerados dois, quatro e seis setores circulares, também completos e interrompidos. O efeito do ângulo de inclinação da alma da roda dentada é estudado, e é feita a comparação entre a disposição dos tratamentos.

Palavras-chave: roda dentada, disco em rotação, tratamento de amortecimento com material viscoelástico, método dos elementos finitos, teoria de placa *layerwise*, elemento casca de faceta em rotação.

To *Tico*, who inspires me constantly
but would never read this.

"Agir, eis a inteligência verdadeira. Serei o que quiser. Mas tenho que querer o que for. O êxito está em ter êxito, e não em ter condições de êxito. Condições de palácio tem qualquer terra larga, mas onde estará o palácio se não o fizerem ali?"

Bernardo Soares, in *Livro do Desassossego*

Acknowledgements

The present work is the result of a personal knowledge and experience build-up over many years, but only achieved with the help and presence of many people, to whom I would like to express my gratitude.

First of all, I would like to express my acknowledgment to Faculdade de Engenharia da Universidade do Porto for challenge me continuously over the last five years, forcing me to improve both technically and personally and for making me a very capable future engineer. For all the professors and staff, I am thankful for the continuous efforts made in order to give me the opportunity to study in a prestigious and respected institution.

To Professor Doutor José Dias Rodrigues, my advisor, I would like to thank his supervision, support, extremely valuable transmitted knowledge and for awakening my curiosity for dynamics and vibration mechanics. I am also extremely grateful to Professor João Amorim, my co-advisor, for all the support, patience, confidence and friendship during this long semester, and without whom the present work would not be possible.

To my long time friends José Silvares, João Marcelo and Miguel Costa I would like to thank the past twenty years of companionship, fun and support. Without you, I would never be half the person I became. To the ones that welcomed me in this city five years ago and since then were my second family, specially Rafael Quinta, Rafael Vieira, Daniel Silva, João Varela, Rui Costa, Pedro Silva and Francisca Silva, I would like to express my gratitude for all the help, unforgettable moments, support and the friendship. You turned all the waves into a lot smoother sea to sail.

To Ana, my girlfriend, I am extremely thankful for all the unconditional care, companionship and love over the last seven years. A simple smile, a simple word, even your simple presence, can enlighten the darkest of moments. I love you.

Last, but not least, I am deeply grateful to my father, Vítor, my mother, Dina, and my brother, Pedro, for the unconditional support, affection and comprehension. I owe you the person I am today and all the sacrifices that you continuously made so that I could take this and other opportunities. You gave me the wings to fly, so I would like you to know that all my victories will forever be yours too.

Contents

Abstract **i**

Acknowledgements **ix**

Contents **xi**

List of Figures **xv**

List of Tables **xix**

1 Introduction **1**
1.1 Motivation 2
1.2 Objectives 4
1.3 Layout 5

2 Spinning Disk Mechanical Model **7**
2.1 Introduction 8
2.2 Analytical Models of a Spinning Disk 9
2.3 Finite Element Models of a Spinning Disk 13
2.3.1 Coriolis Effect 16
2.3.2 Centrifugal Softening Effect 16
2.3.3 Centrifugal Stiffening Effect 18

3 Viscoelastic Damping Treatments **21**
3.1 Introduction 22
3.2 Viscoelastic Damping Treatments 22
3.2.1 Configuration of Viscoelastic Damping Treatments 23
3.2.1.1 Free Layer Damping Treatments 23
3.2.1.2 Constrained Layer Damping 23
3.2.1.3 Integrated Layer Damping Treatments 24
3.2.2 Optimization of Viscoelastic Damping Treatments 25
3.2.2.1 Partial Local Treatments 25
3.2.2.2 Multi-Layer and Multi-Material Treatments 26
3.2.2.3 Treatments with Amplification Mechanisms 26
3.2.2.4 Oriented Treatments 26
3.3 Characterization of Viscoelastic Materials 27
3.3.1 The Complex Modulus 28
3.3.2 The Effects of Temperature and Frequency of Loading 28

3.3.2.1 The Effect of Temperature 29
3.3.2.2 The Effect of Frequency 30
3.3.2.3 Viscoelastic Material Selection 30
3.4 Numerical Simulation of Viscoelastic Damping Treatments 31
3.4.1 Viscoelastic Material Constitutive Modelling 32
3.4.1.1 Complex Modulus Model 32
3.4.1.2 ADF Model 33
3.4.2 Viscoelastic Damping Treatment Spatial Modelling 34
3.4.2.1 Combined Models 34
3.4.2.2 Discrete Layer Models 36
3.4.3 Viscoelastic Damping Treatments Analysis Methods 37
3.4.3.1 Direct Frequency Analysis 37
3.4.3.2 Numerical Integration in the Time Domain 38
3.4.3.3 Complex Eigensolution Analysis 39
3.4.3.4 Modal Strain Energy Method 40

4 Layerwise Finite Element Formulation 43
4.1 Introduction 44
4.2 Reissner-Mindlin Plate Theory 46
4.2.1 Strain and Stress Fields 46
4.2.2 Stress-Strain Relation 47
4.3 Layerwise Theory 48
4.3.1 Displacement Field 49
4.3.2 Strain Field 49
4.3.3 Stress Field 52
4.3.4 Elastic Strain Energy 53
4.3.5 Kinetic Energy 54
4.3.6 Variational Formulation - Hamilton's Principle 56
4.3.7 Layerwise Plate Finite Element Formulation 56
4.3.7.1 Geometric and Displacement Field Interpolation 56
4.3.7.2 Weak Form Finite Element Discretization 58
4.3.7.3 Numerical Integration - Gauss Quadrature 60
4.3.7.4 Shear Locking Protection Through Selective Integration . . 63
4.3.8 Centrifugal Stiffness Matrix 63

5 Numerical Simulation Methods 67
5.1 Geometrical Modeling 68
5.1.1 Gearwheel 68
5.1.2 Viscoelastic Damping Device 70
5.1.3 Mesh Parameters 72
5.2 Finite Element Method Software 74
5.2.1 Basic Procedure 74
5.3 Implemented Finite Element and Numerical Method Validation 79
5.3.1 Plane Disk 79
5.3.1.1 Stationary Case 79
5.3.1.2 Spinning Case 84
5.3.2 Sloped Disk 86
5.3.3 Numerical Simplifications 88

6 Analysis of the Non-Treated Gearwheels **93**
6.1 Introduction . . . 94
6.2 Non-Treated Gearwheel . . . 94
6.3 Individual Evaluation of the Spinning Effects . . . 106
6.3.1 Centrifugal Softening Effect . . . 106
6.3.2 Centrifugal Stiffening Effect . . . 107
6.3.3 Combined Centrifugal Softening and Stiffening Effects . . . 109
6.3.4 Coriolis Effect . . . 109

7 Analysis of Circumferentially Configured Viscoelastic Damping Devices **113**
7.1 Introduction . . . 114
7.2 Plane Damped Gearwheel . . . 114
7.2.1 Segmented Configurations . . . 123
7.3 Sloped Damped Gearwheel . . . 139
7.3.1 Segmented Configurations . . . 149
7.4 Inclination Effect . . . 155
7.5 Conclusion . . . 156

8 Analysis of Radially Configured Viscoelastic Damping Devices **161**
8.1 Introduction . . . 162
8.2 Plane Damped Gearwheel . . . 163
8.2.1 Segmented Configurations . . . 173
8.3 Sloped Damped Gearwheel . . . 180
8.3.1 Segmented Configurations . . . 187
8.4 Inclination Effect . . . 193
8.5 Conclusion . . . 193

9 Conclusion **197**
9.1 Future Work . . . 200

References **201**

List of Figures

1.1 Schematic representation of a gearwheel vibration viscoelastic damper device proposed by Didier [1992]. 2
1.2 Schematic representation of the *Arriel 1*® turbine engine [Marsaudon and Cutuli, 2014]. 3
1.3 Schematic representation of the treated gearwheel [Marsaudon and Cutuli, 2014]. 3

2.1 Schematic representation to demonstrate the centrifugal softening effect. . . 17
2.2 Schematic representation of the geometric stiffness matrix, $[K_g]$, determination process. 19

3.1 Free layer damping treatment. 23
3.2 Constrained layer damping treatment. 24
3.3 Integrated layer damping treatment. 24
3.4 Total deformation energy density distribution in the viscoelastic layer [Moreira, 2004]. 25
3.5 Stress and strain induced by a harmonic loading in a viscoelastic material: *(a)* Representation of the lag, *(b)* Representation of the hysteretic behavior. Moreira [2004] 27
3.6 Storage modulus, G', and loss factor, η, of a viscoelastic material dependence with the temperature and the frequency of strain [Moreira, 2004]. . . 29
3.7 Variation of storage modulus and loss factor of a viscoelastic material with temperature [Rao, 2003]. 30
3.8 Schematic representation of the beam-plate model. 35
3.9 Schematic representation of the brick-plate model with rigid links. 35
3.10 Schematic representation of the brick-plate model with offset. 36
3.11 Schematic representation of the layered brick model. 36
3.12 Schematic representation of a layerwise discrete layer model. 37
3.13 Representation of the cyclic process of DFA analysis of viscoelastic treatments [Moreira, 2004]. 39
3.14 Iterative modal strain energy method (IMSE) algorithm [Vasques et al., 2010b]. 42

4.1 Schematic representation of a straight normal line deformation according to the Kirchhoff-Love plate theory [Oñate, 2013]. 45
4.2 Schematic representation of a straight normal line deformation according to the Reissner-Mindlin plate theory and of the sign convention used [Oñate, 2013]. 45

4.3 Layerwise theory - kinematic model [Moreira, 2004]. 48
4.4 Four-node finite element for a facet shell configuration - local and natural coordinate systems. 57

5.1 Representation of the *Arriel 1*® turbine engine with the studied gearwheel marked with a red box [Safran Helicopter Engines, 2012]. 68
5.2 Schematic representation of the gear designed with the KISSsoft® software. 69
5.3 Schematic representation of the frustoconical designed gear. 70
5.4 3M^{TM} ISD112 shear storage modulus and loss factor temperature and frequency dependence [3M, 2017]. 71
5.5 3M^{TM} ISD112 storage modulus and loss factor at 27 °C obtained trough the three term series ADF model. 72
5.6 Structured circular mesh used. 73
5.7 Structured three-dimensional circular mesh used. 74
5.8 Local elemental coordinate system. 75
5.9 Simplified modal analysis algorithm. 77
5.10 Simplified modal analysis algorithm. 78
5.11 Modes 1 to 3 natural frequencies convergence representation. 82
5.12 Modes 4 to 6 natural frequencies convergence representation. 83
5.13 Modes 6 to 10 natural frequencies convergence representation. 83
5.14 Sloped rotating disk's Campbell diagram. 88
5.15 Plane disk's receptance Bode diagram - No treatment, exact approach and simplified approach. 91
5.16 Zoom of the plane disk's receptance Bode diagram - No treatment, exact approach and simplified approach. 92

6.1 Non-treated plane gearwheel 1st mode shapes' displacement along each direction. 95
6.2 Non-treated plane gearwheel 2nd mode shape's displacement along each direction. 96
6.3 Non-treated plane gearwheel 3rd mode shapes' displacement along each direction. 97
6.4 Non-treated plane gearwheel 4th mode shape's displacement along each direction. 98
6.5 Non-treated plane gearwheel 5th mode shapes' displacement along each direction. 99
6.6 Non-treated sloped gearwheel 1st mode shapes' displacement along each direction. 100
6.7 Non-treated sloped gearwheel 2nd mode shapes' displacement along each direction. 101
6.8 Non-treated sloped gearwheel 3rd and 4th mode shapes' displacement along each direction. 102
6.9 Non-treated sloped gearwheel 5th mode shapes' displacement along each direction. 103
6.10 Inclination angle influence on the non-treated gearwheel's natural frequencies. 104
6.11 Non-treated plane and sloped gearwheel receptance FRF. 106
6.12 Centrifugal softening effect between 0 and 6000 rpm. 107
6.13 Centrifugal softening effect between 0 and 100 000 rpm. 107
6.14 Centrifugal stiffening effect between 0 and 6000 rpm. 108
6.15 Centrifugal stiffening effect between 0 and 100 000 rpm. 108

6.16 Combined centrifugal softening and stiffening effects between 0 and 100 000 rpm. . . . 109
6.17 Campbell diagrams for the plane and sloped cases, between 0 and 6000 rpm. 110
6.18 Campbell diagrams for the plane and sloped cases, between 0 and 100 000 rpm. . . . 111

7.1 Complete circumferential damping devices' configurations. . . . 114
7.2 Mode shapes for the plane gearwheel with treatable surface completely covered. . . . 116
7.3 Plane gearwheel with complete outer ring damping device mode shapes. . . 117
7.4 Plane gearwheel with complete inner ring damping device mode shapes. . . 119
7.5 Receptance's Bode plot for the complete circumferential damping device configurations applied on the plane gearwheel. . . . 121
7.6 External ring configuration mode 1 mode shape's directional displacements. 123
7.7 Split circumferential damping devices' configurations. . . . 124
7.8 Plane gearwheel with outer ring configuration split into two sections mode shapes. . . . 126
7.9 Plane gearwheel with outer ring configuration split into four sections mode shapes. . . . 127
7.10 Plane gearwheel with outer ring configuration split into six sections mode shapes. . . . 129
7.11 Receptance Bode plot for the split outer ring damping device configurations on the plane gearwheel. . . . 131
7.12 Plane gearwheel with inner ring configuration split into two sections mode shapes. . . . 133
7.13 Plane gearwheel with inner ring configuration split into four sections mode shapes. . . . 134
7.14 Plane gearwheel with inner ring configuration split into six sections mode shapes. . . . 136
7.15 Receptance Bode plot for the split inner ring damping device configurations on the plane gearwheel. . . . 138
7.16 Sloped gearwheel treated area completely covered mode shapes. . . . 141
7.17 Sloped gearwheel with complete outer ring damping device mode shapes. . 142
7.18 Sloped gearwheel with complete inner ring damping device mode shapes. . . 143
7.19 Receptance's Bode plot for the complete circumferential damping device configurations applied on the sloped gearwheel. . . . 145
7.20 Mode (1,0) deformed mesh for the outer ring device configuration on the plane gearwheel. . . . 146
7.22 Mode (2,0) deformed mesh for the exterior ring device configuration on the plane gearwheel. . . . 147
7.23 Mode (2,0) deformed mesh for the exterior ring device configuration on the sloped gearwheel. . . . 148
7.24 Outer ring configuration split into two sections mode shapes for the sloped gearwheel. . . . 151
7.25 Outer ring configuration split into four sections mode shapes for the sloped gearwheel. . . . 152
7.26 Outer ring configuration split into six sections mode shapes for the sloped gearwheel. . . . 153
7.27 Receptance Bode plot for the split outer ring damping device configurations on the sloped gearwheel. . . . 155

7.28 Inclination angle effect on the damping behavior of the completely covered area configuration. 156
7.29 Inclination angle effect on the damping behavior of the outer ring configuration. 157
7.30 Inclination angle effect on the damping behavior of the inner ring configuration. 157
7.31 Loss factor-added mass weighting parameter, H, values for the circumferential damping treatments applied on the plane gearwheel. 158
7.32 Loss factor-added mass weighting parameter, H, values for the circumferential damping treatments applied on the sloped gearwheel. 159

8.1 Complete radial damping devices' configurations. 162
8.2 Split radial damping devices' configurations. 163
8.3 Plane gearwheel with two sections radial damping device mode shapes. . . . 165
8.4 Plane gearwheel with four sections radial damping device mode shapes. . . 166
8.5 Plane gearwheel with six sections radial damping device mode shapes. . . . 168
8.6 Receptance's Bode plot for the complete radial damping device configurations applied on the plane gearwheel. 170
8.7 Plane gearwheel with split two sections radial damping device mode shapes. 175
8.8 Plane gearwheel with split four sections radial damping device mode shapes. 176
8.9 Plane gearwheel with split six sections radial damping device mode shapes. 178
8.10 Sloped gearwheel with two sections radial damping device mode shapes. . . 181
8.11 Sloped gearwheel with four sections radial damping device mode shapes. . . 182
8.12 Sloped gearwheel with six sections radial damping device mode shapes. . . 183
8.13 Receptance's Bode plot for the complete radial damping device configurations applied on the sloped gearwheel. 185
8.14 Sloped gearwheel with split two sections radial damping device mode shapes. 188
8.15 Sloped gearwheel with split four sections radial damping device mode shapes. 189
8.16 Sloped gearwheel with split six sections radial damping device mode shapes. 191
8.17 Inclination angle effect on the damping behavior of the two sections radial configuration. 194
8.18 Loss factor-added mass weighting parameter, H, values for the radial damping treatments applied on the plane gearwheel. 195
8.19 Loss factor-added mass weighting parameter, H, values for the radial damping treatments applied on the sloped gearwheel. 196

List of Tables

4.1 Nodal parameters for the shape functions 58
4.2 Location and weight coefficients of the integration points, according to the Gauss quadrature [Moreira, 2004] 61

5.1 Considered gearwheel dimensions 70
5.2 3M^{TM} ISD112 ADF parameters using three series ($n = 3$) [Vasques et al., 2010a] 71
5.3 Viscoelastic and constraining layers' thicknesses, Poisson's ratios and densities considered 72
5.4 Dimensions and constitutive properties of the disk analyzed by D'Angelo and Mote [1993] 79
5.5 Stationary plane disk, 5×20 Mesh (100 Elements) 80
5.6 Stationary plane disk, 10×20 Mesh (200 Elements) 80
5.7 Stationary plane disk, 10×30 Mesh (300 Elements) 81
5.8 Stationary plane disk, 10×40 Mesh (400 Elements) 81
5.9 Stationary plane disk, 20×50 Mesh (1000 Elements) 82
5.10 Stationary plane disk with multiple layers 84
5.11 Dimensions and constitutive properties of the annular plate studied by Hsieh and Abel [1995] 85
5.12 Hsieh and Abel [1995] rotating annular plate's natural frequencies 85
5.13 Dimensions and constitutive properties of the analyzed sloped disk 86
5.14 Rotating sloped disk modal analysis 86
5.15 Treated plane disk characteristics 89
5.16 Modal analysis simplification validation 89

6.1 Non-treated plane gearwheel modal analysis results 94
6.2 Outer rim influence for the plane case, $\Omega = 6000$ rpm 105
6.3 Outer rim influence for the sloped case, $\Omega = 6000$ rpm and Coriolis effect considered 105

7.1 Circumferential damping devices' dimensions 115
7.2 Complete circumferential damping devices' configurations modal analysis results for the plane gearwheel 115
7.3 Loss factor and added mass weighting, H, for the complete circumferential configurations in the plane gearwheel 122
7.4 Outer split ring damping devices' configurations loss factor results for the plane gearwheel. 125

7.5 Loss factor and added mass weighting, H, for the complete and split outer ring configurations in the plane gearwheel 125
7.6 Inner split ring damping devices' configurations loss factor results for the plane gearwheel. 132
7.7 Loss factor and added mass weighting, H, for the complete and split inner ring configurations in the plane gearwheel 132
7.8 Comparison between the loss factors of each split circumferential configuration for the plane gearwheel 139
7.9 Complete circumferential damping devices configurations' modal analysis results for the sloped gearwheel 140
7.10 Loss factor and added mass weighting, H, for the complete circumferential configurations in the sloped gearwheel 140
7.11 Outer split ring damping devices' configurations loss factor results for the sloped gearwheel. 150
7.12 Loss factor and added mass weighting, H, for the complete and split outer ring configurations in the sloped gearwheel 150

8.1 Radial damping devices' dimensions 163
8.2 Complete radial damping devices configurations' modal analysis results for the plane gearwheel 164
8.3 Loss factor and added mass weighting, H, for the complete radial configurations in the plane gearwheel 164
8.4 Comparison between the damping capacities of the radial and inner split circumferential configurations for the plane gearwheel 171
8.5 Comparison between the loss factor-added mass weighting parameter of the radial and inner split circumferential configurations for the plane gearwheel 172
8.6 Comparison between the damping capacities of the radial and outer split circumferential configurations for the plane gearwheel 172
8.7 Comparison between the loss factor-added mass weighting parameter of the radial and outer split circumferential configurations for the plane gearwheel 173
8.8 Interrupted radial configurations' loss factor results for the plane gearwheel 174
8.9 Interrupted radial configurations' loss factor-added mass weighting parameter results for the plane gearwheel 174
8.10 Complete radial damping devices configurations' modal analysis results for the sloped gearwheel 180
8.11 Loss factor and added mass weighting, H, for the complete radial configurations in the sloped gearwheel 180
8.12 Comparison between the damping capacities of the radial and outer split circumferential configurations for the sloped gearwheel 186
8.13 Comparison between the loss factor-added mass weighting parameter of the radial and outer split circumferential configurations for the sloped gearwheel 186
8.14 Interrupted radial configurations' loss factor results for the sloped gearwheel 187
8.15 Interrupted radial configurations' loss factor-added mass weighting parameter results for the sloped gearwheel 187

Chapter 1

Introduction

In this work, the finite element method is used to study the dynamic behavior of rotating gearwheels with viscoelastic damping treatments.

Power transmission is a fundamental aspect of any mechanical system. Gear transmissions are a widely used solution in different equipments due to their efficiency, simplicity and readiness to market. However, as any moving mechanism, the occurrence of mechanical vibrations in the gearwheels can harm their correct functioning and lead to the premature components' failure. Thus, it is important to fully understand and, by any means, predict their dynamic behavior while at the design stage and to reduce these vibrations.

The dynamic study of rotating disks started with a linear analytic approach by Lamb and Southwell [1921], where a thin membrane model was considered and the flexural rigidity artificially added. Baddour and Zu [2001b] presented a linear and a non-linear mathematical models that gather all the previously studies concerning this subject. However, the increase of the computers' processing capacity together with the need to study more complex geometries and phenomena, led to the growth of interest in numerical approaches, where the finite element method plays a major role in the field of structural mechanics. This method is based in the domain's discretization into smaller and simpler parts (the finite elements) and the solving of equations obtained through variational methods over these sub-domains, yielding approximate values of the variables at a discrete number of points, the nodes.

Mechanical vibrations can be damped and controlled by active or passive damping mechanisms. Active damping relies on the real-time response of piezoelectric patches, electro-rheologic and magneto-rheologic fluids or shape-memory alloys and polymers against the vibratory motion to mitigate it. Passive damping mechanisms rely on the addition of tailored mechanisms based on materials, fluids or electrical systems, able to dissipate a significant amount of the deformation energy that is absorbed by the damping treatment when the host structure vibrates. In this last group, one must emphasize the use of viscoelastic materials, which has grown in the automotive, railway and aircraft industries, mostly because of the excellent weight/benefit and cost/benefit ratios when used in optimal designs and configurations. Note that with the increasing use of this damping method grows the need of models which correctly represent the physical phenomena involved in these applications but, at the same time, properly and easily model the involved geometries, such as the layerwise plate theory.

1.1 Motivation

It is known that the vibrations that appear in high-speed rotating gears can damage them along with other components involved in the power transmission and speed-reducing systems. Previous methods to damp this effect consisted of the opening of an annular groove in the inner peripheral surface of the teeth rim, where a split annular metal ring was received. Although that solution enabled vibrations to be significantly reduced, it presented the drawbacks of shape discontinuities, with the consequent zones of stress concentration, and of giving rise to the teeth ring wearing, with consequent undesirable wear and appearance of metal fillings in the lubrication system. Another used solution was to adapt the shape of the gearwheel to the vibratory behaviour, which led to the drawback of increasing its weight.

Yet another solution was very similar to the first one, but the metal ring housed in the annular groove placed in the teeth outer rim was used as a support member for a damper device, formed by a viscoelastic material layer and a backing one. This method was presented in a patent proposed by Didier [1992], whose schematic representation can be seen in Figure 1.1. Note that number **7** represents the steel support member, that conduces the vibrations to the damping device, number **8** represents a viscoelastic layer and number **9** represents the backing layer. Furthermore, it is possible to identify that all the set is not continuous, presenting a discontinuity that allows its assemble in the gearwheel, also resulting in the appearance of radial stresses in the support layer. However, this method does not overcome the geometry discontinuities and wearing problems.

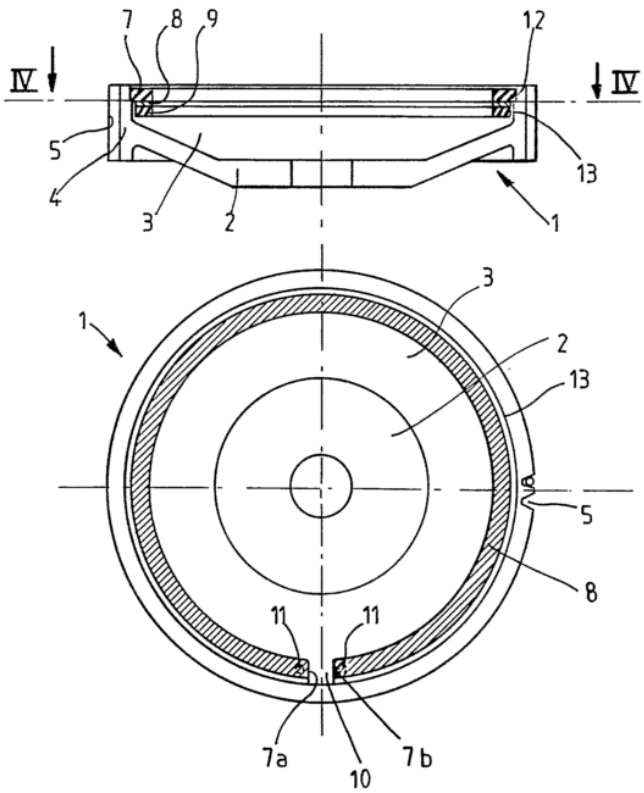

Figure 1.1: Schematic representation of a gearwheel vibration viscoelastic damper device proposed by Didier [1992].

The case studied here was presented in a patent submitted by Marsaudon and Cutuli

[2014], that report the application of viscoelastic damping treatments, following the constrained layer damping (CLD) configuration, in the web of a gearwheel used in high-speed reducing gearboxes. After some research, this invention was developed for turbine engines of helicopters, namely the *Arriel 1*® model (Figure 1.2) of the company Safran Helicopter Engines (previously known as Turbomeca), which belongs to the Safran S.A. group.

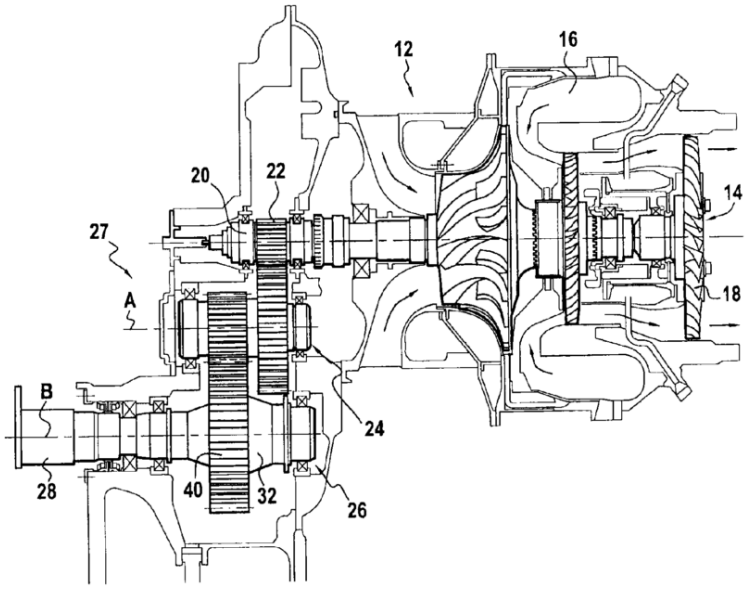

Figure 1.2: Schematic representation of the *Arriel 1*® turbine engine [Marsaudon and Cutuli, 2014].

According to what is presented in the patent, the concerned gearwheel is the outlet one identified by the number **26** (Figure 1.3), connected to the output shaft (**B**). Furthermore, it is also possible to identify that the gear extends in the axial direction, that is, presents a frustoconically shaped web because of the slant angle α, that must preferably lie between 65° and 90°, according to the authors. Note that numbers **30** and **34** represent the gear's web and teeth rim, respectively, number **42** the damping device and numbers **44** and **46** the viscoelastic material and backing layers.

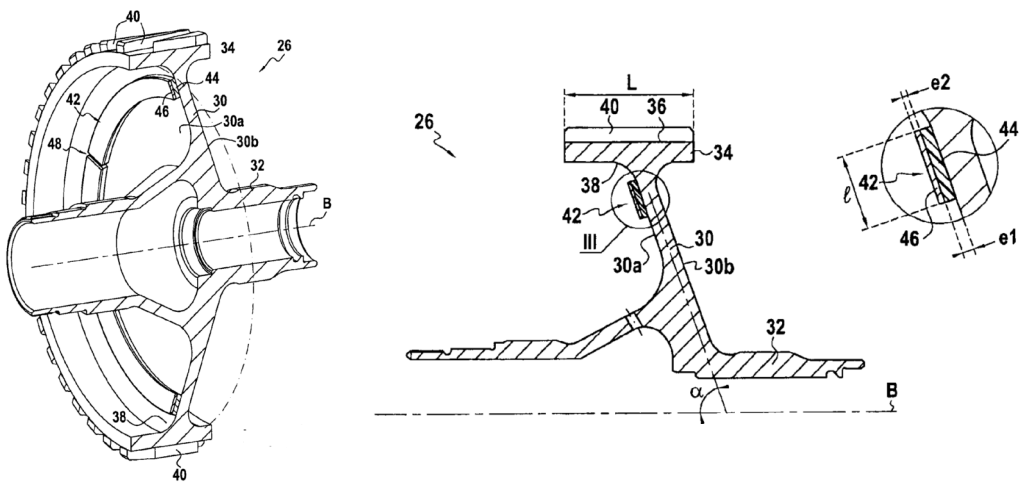

Figure 1.3: Schematic representation of the treated gearwheel [Marsaudon and Cutuli, 2014].

This vibration damper method differs from the previous, namely the one proposed by Didier [1992], mainly in its positioning and assembling method. In fact, the damper device is fixed directly on the web of the gearwheel, and not in the teeth outer rim. One could easily question this decision, arguing that a decrease in efficiency should be expected because the further from the rotation axis, the greater the displacements of the viscoelastic layer and, consequently, the associated loss factors. However, Marsaudon and Cutuli [2014] observed, with surprise, that the positioning of the damper device on the web can lead to satisfactory damping levels, that are at least equivalent to the ones obtained in the prior art. The inventors also refer that the viscoelastic and backing layers should be arranged closer to the annular rim than to the hub to achieve greater damping efficiency, as expected. On the other hand, the anchorage of the damping device on the web is secured through vulcanization or adhesive bounding of the viscoelastic layer, which makes it possible to avoid generating sudden geometry changes, the metal-metal contact associated with wearing problems and the distortion of the vibration's characteristics caused by the support member.

Furthermore, Marsaudon and Cutuli [2014] state that the present invention makes it possible to obtain vibration damping by compression, whereas the previous methods only worked by shear. According to what is presented in the patent, the vibration modes of the gearwheel are substantially flexural, which means that the displacement will mainly occur in the transverse (axial) direction. Thus, since the damping device is arranged in succession and perpendicular to the web (parallel to the displacement direction), the backing layer, by means of its inertia, will exert traction/compression forces on the viscoelastic layer, that oppose the mode shape movement, attenuating and counterbalancing the vibratory deflections. In fact, the inventors claim to have observed, with surprise, that the compression damping obtained by means of the present damping device is just as effective as the shear damping of the prior art.

In what concerns the damping device characteristics, the inventors claim that it should be annular in shape, continuous or split, as presented in Figure 1.3, in which the backing layer preferably presents a radial length that is not less than the radial length of the viscoelastic material, enabling the first to completely cover the second, thereby protecting it. As for dimensions, it is said that the radial length of the vibration damper device may lie in the range of 5 to 15 mm, for a web with 35 mm of radial length. Furthermore, the layer of viscoelastic material is preferably an elastomer with a thickness of $0.1 - 3$ mm, being adapted to the selected modes to damp, and the backing layer must be made of a more rigid material (e.g. steel) with a thickness of $0.5 - 2$ mm. One can easily see that, for some cases, Marsaudon and Cutuli [2014] consider a viscoelastic layer that is thicker than the backing one, which is not very common in this type of damping treatments. Moreover, the inventors state that the damper device must be placed inside the truncated cone shape formed by the web, allowing the rise of the centrifugal force effects and thus improving the damping capabilities.

1.2 Objectives

The main goal of the present work is to study the efficiency of local viscoelastic damping treatments in gearwheels using the finite element method. However, there were some intermediate tasks that needed to be achieved in order to correctly simulate all the associated phenomena. Thus, the objectives aimed in the present work are the following:

- Study the phenomena involved in the rotational movement of disks and circular plates, and their influence on the dynamic behavior of the structures;

- Understand the working principles of the viscoelastic damping treatments and analyze their dependencies, in order to be able to implement them in a mechanical model;
- Implement and validate a rotating facet shell finite element based on a layerwise plate theory and develop the necessary tools to geometrically model gearwheels with viscoelastic damping treatments;
- Analyze the dynamic behavior of the undamped systems in order to better understand the influences of the inclination angle and spinning velocity;
- Study the damping efficiency of circumferentially configured devices, like the ones proposed by Marsaudon and Cutuli [2014], as well as suggest and assay different partial configurations.

1.3 Layout

This dissertation is structured in nine chapters, being the first one the present Introduction, where the main motivations and objectives for the execution of the work are presented. The next chapters are the following:

- **Chapter 2, Spinning Disk Mechanical Model** - In this chapter, both analytical and finite element approaches for the dynamic study of spinning disks are presented and the effects resulting from the rotational movement studied;
- **Chapter 3, Viscoelastic Damping Treatments** - The main subjects regarding the viscoelastic damping treatments are presented in this chapter. Beyond the principles on which the damping effects are based, the common configurations and some optimization techniques are also referred. The viscoelastic materials' characterization through the complex modulus and their dependence on the temperature and frequency are also studied. Finally, the aspects related to their numerical simulation through the finite element method are analyzed, namely the constitutive modelling of viscoelastic materials, the spatial modelling of the treatments and the common analysis methods;
- **Chapter 4, Layerwise Finite Element Formulation** - In this chapter, the basis for the formulation of a spinning facet shell finite element based on a layerwise plate theory are presented. First, the Reissner-Mindlin plate theory is briefly addressed. Then, the layerwise theory is properly studied, always including the rotational effects, leading to the presentation of the involved matrices' calculation process in order to easily implement the developed element;
- **Chapter 5, Numerical Simulation Methods** - Some aspects regarding the numerical simulation of the damped gearwheels and the validation of the implemented finite element are presented in this chapter. Firstly, the studied gearwheels' dimensions and the treatments' characteristics are considered, as well as the used mesh parameters. Then, the developed finite element method software is presented from a user point of view and some adopted simplifications explained. Finally, the implemented finite element and the used numerical procedures are validated, comparing results with information presented in the literature or values obtained using commercial software;

- **Chapter 6, Analysis of the Non-Treated Gearwheels** - In this chapter, the dynamic behavior of the analyzed gearwheels without the damping devices is studied in detail. Initially, the inclination angle influence on the modal analysis results is approached. Then, the thicker outer rim effects are presented and interpreted. Finally, the influence of each rotational effect in the natural frequencies, for both plane and sloped gearwheels, is analyzed;

- **Chapter 7, Analysis of Circumferentially Configured Viscoelastic Damping Devices** - In this chapter, the damping efficiency of circumferential complete and split devices is studied for both plane and sloped gearwheels. All the area covered with the viscoelastic treatment, an exterior ring and an inner ring were considered and their performance was analyzed and compared;

- **Chapter 8, Analysis of Radially Configured Viscoelastic Damping Devices** - A new damping device configuration was proposed and assayed in this chapter, the radially shaped treatments. Two, four and six radial patches were considered, their performance analyzed and compared between them and with the circumferential configurations previously studied;

- **Chapter 9, Conclusion** - In this final chapter, the conclusions drawn from the damping efficiency results obtained throughout the work are summarized. The advantages and disadvantages of the tested damping devices are highlighted. This chapter ends with some suggestions for future works regarding the subject of viscoelastic damping of rotating elements, namely disks and gearwheels.

Chapter 2

Spinning Disk Mechanical Model

The present chapter addresses issues regarding the mechanical and mathematical modelling of spinning disks. Initially, some analytical approaches to the problem will be presented. Next, models of spinning finite elements are studied, from where the finite element formulation of the present problem will be based. For further information regarding these subjects, one can consult the references used throughout this chapter, specifically Lamb and Southwell [1921], Hsieh and Abel [1995], Baddour and Zu [2001a,b], Nayfeh et al. [2001], Yoo and Kim [2002] and Kirchgäßner [2016].

2.1 Introduction

Spinning disks can be found in many engineering applications, such as circular saw blades, turbine rotors, brake systems, fans, gears and computer storage devices, that may experience severe vibration issues, leading to the failure of those systems. Thus, the dynamics of spinning disks must be researched, and the first step to achieve it is to develop a suitable mathematical model that captures the essential physics of the problem [Baddour and Zu, 2001a,b]. The special difficulty of this problem arises from the fact that centrifugal force and flexural rigidity are both operative and that the normal modes of vibration depend on their relative importance [Lamb and Southwell, 1921]. Furthermore, the Coriolis effects produce vibration couplings between different vibration modes, generating complex vibration mode shapes [Hashemi et al., 2009].

The centrifugal stress-system will depend upon many factors, such as the inner and outer diameters, the possible existence of attached components (e.g. blades) and their size, leading to an impossible previous assumption regarding the distribution of these forces of all cases.

Rotating flexible structures were initially idealized as rotating beams, since such idealization usually enabled to obtain accurate modal characteristics with a simpler calculation process. Southwell and Gough [1921] introduced a simple and reliable algebraic equation, referred to as Southwell equation, to calculate the natural frequencies of rotating beams. Even though many rotating structures can be successfully idealized as beams, some of them, such as blades with low aspect ratios, behave like plates rather than beams, which means that plate models are required to accurately predict their modal characteristics [Yoo and Kim, 2002]. One other example of a structure that can not be idealized as a beam is the case of the rotating disk.

The first linear analysis of rotating disks was performed analytically by Lamb and Southwell [1921], who investigated the natural frequencies of a complete circular disk clamped at its center and free at its periphery. They determined the exact natural frequencies for a rotating membrane using power series techniques, which were then combined with previously published results for non-rotating geometries to provide lowest natural frequency bounds for a rotating disk with both flexural and membrane effects present, and, additionally, used the Rayleigh's method to provide upper bounds for the natural frequencies. In a subsequent publication by Southwell [1922], the previous results were extended to include the case of an annulus centrally partially-clamped (the disk is constrained in the transverse but not in the radial direction at its interior radius) and free in its periphery.

As a result of the fast computer processing, the analytical models and methods were substituted by numerical methods, such as the finite element method. Dokainish and Rawtani [1971] used the finite element technique to determine the natural frequencies and the mode shapes of a cantilever plate assembled on a rotating hub and studied the effect of the aspect ratio, speed of rotation, disc radius and setting angle on the natural frequencies, not considering the Coriolis and gyroscopic effects. Hsieh and Abel [1995] published two possible approaches for the analysis of rotating bladed-disk assemblies and their comparison, in which the motion equations attainment process as resulting matrices are presented. Yoo and Kim [2002] derived a set of linear equations of motion for the modal analysis of rotating cantilever thin plates by applying the hybrid variables in the Rayleigh-Ritz method. Kirchgäßner [2016] also developed the equation of motion of a disk, referring to a co-rotating reference system. Most of the previous studies for rotating plates are based on the Kirchhoff thin plate theory, which ignores the effects of transverse shear strain and rotary inertia, leading to the overvalue of natural frequencies, with the inaccuracy

increasing as the thickness of the plate increases. The studies of rotating Mindlin plates are quite limited. Hashemi et al. [2009] published what was, by the author's knowledge, the first and, until recently, the only analysis of in-plane and out-of-plane coupling vibration and buckling behavior of rotating Mindlin plates. Fang and Zhou [2016] developed the modal analysis of rotating cantilever rectangular Mindlin plates with variable thickness, presenting the influence of various geometric parameters.

In the next sections, the more determinant analytical and finite element method models for the spinning disk are presented, as a way to develop the mathematical formulation for the problem being studied.

2.2 Analytical Models of a Spinning Disk

Starting with the model proposed by Lamb and Southwell [1921], the analysis made was about the transverse vibrations with a circular disk of uniform thickness rotating about its axis with constant angular velocity. The assumptions that the disk was so thin and the rotational speed so high that the flexural forces were negligible were also considered, leading to the consideration of a linear-membrane structure. Baddour and Zu [2001b] reviewed this and other analytical models, through simple yet very complete analysis and comparisons.

When an elastic disk rotates about its axis, the induced tensions act along and perpendicular to the radius. For small transverse deflections, it is assumed that these are not affected, but that they have a component in the vertical direction that provides the restoring force to the equilibrium position. In this analysis, since an equilibrium configuration is assumed, the in-plane inertia of the disk is ignored [Baddour and Zu, 2001b]. Simmonds [1962] presented the equation of motion governing the transverse vibratory displacement, w, of a flat spinning membrane, in a polar coordinate system, (r, θ, z), as:

$$\rho \frac{\partial^2 w}{\partial t} = \frac{1}{r}\frac{\partial}{\partial r}\left(r\sigma_{rr}\frac{\partial w}{\partial r} + \sigma_{r\theta}\frac{\partial w}{\partial \theta}\right) + \frac{1}{r}\frac{\partial}{\partial \theta}\left(\sigma_{r\theta}\frac{\partial w}{\partial r} + \frac{\sigma_{\theta\theta}}{r}\frac{\partial w}{\partial \theta}\right) \tag{2.1}$$

where ρ represents the density of the disk's material, σ_{rr}, $\sigma_{\theta\theta}$ and $\sigma_{r\theta}$ represent the normal and shear in-plane stresses resulting from the membrane's spinning, and r, θ and t represent the usual radial, angular and temporal variables. The resulting partial differential equation is of second order, which means that a separation of variables leads to a hypergeometric equation in the radial variable, where the series solution is known to be logarithmically infinite at the outer edge unless the series terminates. Forcing it to terminate leads to the natural frequencies of vibration and correspondent natural modes of vibration, that are characterized by nodal circles and diameters [Baddour, 2001].

It must be noted that, inherent to this derivation, the in-plane vibrations are neglected, since an equilibrium situation is assumed for the in-plane stresses. However, the transverse vibration problem is inevitably linked to the solution of the in-plane problem, since the first requires the previous determination of the in-plane stresses.

Thus far, by reason of considering a circular thin membrane, the disk's bending stiffness has not been considered. For this purpose, Lamb and Southwell [1921] proposed an artificial term, proportional to $\nabla^4 w$, added to the right-hand side of Equation 2.1, which becomes:

$$\rho \frac{\partial^2 w}{\partial t} = \frac{1}{r}\frac{\partial}{\partial r}\left(r\sigma_{rr}\frac{\partial w}{\partial r} + \sigma_{r\theta}\frac{\partial w}{\partial \theta}\right) + \frac{1}{r}\frac{\partial}{\partial \theta}\left(\sigma_{r\theta}\frac{\partial w}{\partial r} + \frac{\sigma_{\theta\theta}}{r}\frac{\partial w}{\partial \theta}\right) - \frac{Eh^2}{3\left(1-\nu^2\right)}\nabla^4 w \tag{2.2}$$

where E, ν and h represent the Young's modulus and Poisson's ration of the material and the disk's half-thickness, respectively. Note the left-hand side term and the first two terms from the right-hand side of the equation account for the membrane effects created by the rotation and the last term is associated with the bending stiffness, where $\Delta^4 w$ is given by:

$$\nabla^4 w = \left[\frac{\partial^2}{\partial r^2} + \frac{1}{r}\frac{\partial}{\partial r} + \frac{1}{r^2}\frac{\partial^2}{\partial \theta^2}\right]^2 w \tag{2.3}$$

This results in a fourth-order partial differential equation that has historically been difficult to solve exactly. In theory, it can be solved with a series; however, this approach quickly becomes unwieldy and deduction of general results become difficult, if not impossible at all. The authors worked around these problems by applying the Rayleigh's energetic method to the problem and by proposing an approximation to calculate the eigenvalues of a spinning disk using the membrane eigenvalues (Equation 2.1) and the stationary disk eigenvalues (widely known and published in the literature). The subsequent publication by Southwell [1922] continued the investigation of the particular case of a circular disk clamped at the inner radius and free in the outer edge [Baddour, 2001].

However, it should be noted that this model does not consider the effects of in-plane inertia, thus neglecting the centrifugal and Coriolis forces acting in the plane of the disk. When modelling stationary plates using linear theories (such as Kirchhoff), the in-plane inertia is included and the in-plane and transverse free vibration problems decouple, which means that they can be solved independently. Thus, there seems to be no theoretical justification to neglect these effects in the spinning case, leading to the expectation of, when considering a linear theory, the appearance of in-plane inertia terms and the decoupling of the equations [Baddour and Zu, 2001b].

Both models previously presented are linear models. The non-linear spinning disk equations were first derived by Nowinski [1964], using the von Kármán plate equations as a starting point. These equations are as follows:

$$\begin{aligned}&\frac{Eh^2}{12\left(1-\nu^2\right)}\nabla^4 w + \rho\frac{\partial^2 w}{\partial t^2} + \frac{1}{2}\rho\Omega^2 r^2 \nabla^2 w + \rho\Omega^2 r\frac{\partial w}{\partial r} = \\ &= \frac{\partial^2 w}{\partial r^2}\left(\frac{1}{r}\frac{\partial \phi}{\partial r} + \frac{1}{r^2}\frac{\partial^2 \phi}{\partial \theta^2}\right) + \frac{\partial^2 \phi}{\partial r^2}\left(\frac{1}{r}\frac{\partial w}{\partial r} + \frac{1}{r^2}\frac{\partial^2 w}{\partial \theta^2}\right) - 2\frac{\partial}{\partial r}\left(\frac{1}{r}\frac{\partial w}{\partial \theta}\right)\frac{\partial}{\partial r}\left(\frac{1}{r}\frac{\partial \phi}{\partial \theta}\right)\end{aligned} \tag{2.4a}$$

$$\begin{aligned}&\frac{1}{E}\left[\nabla^4 \phi - 2(1-\nu)\Omega^2 \rho\right] = \\ &= -\frac{1}{r}\left(\frac{\partial w}{\partial r} + \frac{1}{r}\frac{\partial^2 w}{\partial \theta^2}\right)\frac{\partial^2 w}{\partial r^2} - \frac{2}{r^3}\frac{\partial^2 w}{\partial r \partial \theta}\frac{\partial w}{\partial \theta} + \frac{1}{r^2}\left(\frac{\partial^2 w}{\partial r \partial \theta}\right)^2 + \frac{1}{r^4}\left(\frac{\partial w}{\partial \theta}\right)^2\end{aligned} \tag{2.4b}$$

where Ω represents the angular velocity of the disk, ϕ is a stress function and, again, $\nabla^4 = \nabla^2\nabla^2$, with $\nabla^2 = \left(\frac{\partial^2}{\partial r^2} + \frac{1}{r}\frac{\partial}{\partial r} + \frac{1}{r^2}\frac{\partial^2}{\partial \theta^2}\right)$, in the cylindrical coordinate system.

The non-linear modelling of the spinning disk using the von Kármán theory still ignores the in-plane inertia, which is justified by the author with the fact that it is usually ignored when modelling a stationary problem. It was shown in other publications, namely by Chu and Herrmann [1956], that ignoring the in-plane inertia of a stationary deforming plate is the first-order perturbation approximation to the full problem, and the resulting advantage is the fact that a stress function may be used, reducing the number of non-linear coupled differential equations from three to two. However, the same authors that presented the previous results also studied the spinning disk problem and concluded that

the in-plane inertia can not be ignored as for the stationary problem [Baddour and Zu, 2001b]. However, they all neglect both rotary and in-plane inertias of the disk, which do not represent the reality of the situations.

Baddour and Zu [2001b] proposed a new linear and non-linear mathematical model for the spinning disk problem using the following assumptions:

- The disk is modelled purely as a classical Kirchhoff or von Kármán plate, leading to the bending stiffness as the only restoring force and to the absence of transverse shear;
- Only thin disks are considered;
- The in-plane inertia of the plane is not neglected, as no theoretical justification of this can be found;
- Hamilton's principle is used to obtain the motion equations, so that the correct boundary conditions are automatically obtained;
- The effect of the rotary inertia is automatically included.

Note that the effects of shear are not included in this model, because of the Kirchhoff and von Kármán theories' assumptions. Considering that $u(r,\theta)$ and $v(r,\theta)$ represent the radial and tangential displacements of the middle surface of the disk, that are themselves functions of the in-plane coordinates and of time, t, the displacement of an arbitrary point (r,θ) can be expressed as:

$$u_r = u(r,\theta) - z\frac{\partial w}{\partial r} \quad ; \quad u_\theta = v(r,\theta) - \frac{z}{r}\frac{\partial w}{\partial \theta} \quad ; \quad u_z = w(r,\theta) \tag{2.5}$$

Considering a plane stress condition, $\sigma_{zz} = \sigma_{rz} = \sigma_{\theta z} = 0$, the strain-displacement expressions for both linear and non-linear theories are given by:

- *Von Kármán plate theory:*

$$\varepsilon_{rr} = \frac{\partial u_r}{\partial r} + \frac{1}{2}\left(\frac{\partial u_z}{\partial r}\right)^2 \tag{2.6a}$$

$$\varepsilon_{\theta\theta} = \frac{u_r}{r} + \frac{1}{r}\frac{\partial u_\theta}{\partial \theta} + \frac{1}{2r^2}\left(\frac{\partial u_z}{\partial \theta}\right)^2 \tag{2.6b}$$

$$\varepsilon_{r\theta} = \frac{1}{2r}\left[\frac{\partial u_r}{\partial \theta} - u_\theta + r\frac{\partial u_\theta}{\partial r} + \frac{\partial u_z}{\partial r}\frac{\partial u_z}{\partial \theta}\right] \tag{2.6c}$$

- *Kirchhoff plate theory:*

$$\varepsilon_{rr} = \frac{\partial u_r}{\partial r} \tag{2.7a}$$

$$\varepsilon_{\theta\theta} = \frac{u_r}{r} + \frac{1}{r}\frac{\partial u_\theta}{\partial \theta} \tag{2.7b}$$

$$\varepsilon_{r\theta} = \frac{1}{2r}\left[\frac{\partial u_r}{\partial \theta} - u_\theta + r\frac{\partial u_\theta}{\partial r}\right] \tag{2.7c}$$

Then, after determining the potential and kinetic energies expressions, Baddour and Zu [2001b] used the Hamilton's principle to derive the fully linear and non-linear motion equations, as follows:

- *Non-linear equations*, derived from the von Kármán theory

$$\frac{\rho\left(1-\nu^2\right)}{E}\left[\frac{\partial^2 u}{\partial t^2}-\Omega^2(r+u)-2\Omega\frac{\partial v}{\partial t}\right]=\frac{(1-\nu)}{2r^2}\frac{\partial^2 u}{\partial\theta^2}+\frac{(1+\nu)}{2r}\frac{\partial^2 v}{\partial r\partial\theta}+\frac{\partial^2 u}{\partial r^2}+$$
$$+\frac{1}{r}\left[\frac{(1-\nu)}{2}\left(\frac{\partial w}{\partial r}\right)^2-\frac{(3-\nu)}{2r}\frac{\partial v}{\partial\theta}-\frac{(1+\nu)}{2r^2}\left(\frac{\partial w}{\partial\theta}\right)^2-\frac{u}{r}+\frac{\partial u}{\partial r}\right]+$$
$$+\frac{(1+\nu)}{2r^2}\frac{\partial w}{\partial r}\frac{\partial^2 w}{\partial\theta^2}+\frac{\partial w}{\partial r^2}+\frac{(1+\nu)}{2r^2}\frac{\partial w}{\partial\theta}\frac{\partial^2 w}{\partial r\partial\theta} \tag{2.8a}$$

$$\frac{\rho\left(1-\nu^2\right)}{E}\left[\frac{\partial^2 v}{\partial t^2}-\Omega^2 v+2\Omega\frac{\partial u}{\partial t}\right]=\frac{(1+\nu)}{2r}\frac{\partial w}{\partial r}\frac{\partial^2 w}{\partial r\partial\theta}+\frac{(1+\nu)}{2}\frac{\partial^2 v}{\partial r}+$$
$$+\frac{1}{r}\left[\frac{(1-\nu)}{2r}\frac{\partial w}{\partial r}\frac{\partial w}{\partial\theta}+\frac{(3-\nu)}{2r}\frac{\partial u}{\partial\theta}+\frac{(1-\nu)}{2}\frac{\partial v}{\partial r}-\frac{v}{r}\frac{(1-\nu)}{2}\right]+ \tag{2.8b}$$
$$+\frac{(1+\nu)}{2r}\frac{\partial^2 u}{\partial r\partial\theta}+\frac{1}{r^2}\frac{\partial^2 v}{\partial\theta^2}+\frac{1}{r^3}\frac{\partial w}{\partial\theta}\frac{\partial^2 w}{\partial\theta^2}+\frac{(1-\nu)}{2r}\frac{\partial w}{\partial\theta}\frac{\partial^2 w}{\partial r^2}$$

$$\frac{\rho\left(1-\nu^2\right)}{E}\left[\frac{\partial^2 w}{\partial t^2}+\frac{h^2\Omega^2}{12}\nabla^2 w-\frac{h^2}{12}\frac{\partial^2}{\partial t^2}\nabla^2 w\right]+\frac{h^2}{12}\nabla^4 w=$$
$$=\frac{1}{r^4}\frac{\partial w}{\partial\theta}\left[\frac{3}{2}\frac{\partial w}{\partial\theta}\frac{\partial^2 w}{\partial\theta^2}-\frac{r}{2}\frac{\partial w}{\partial\theta}\frac{\partial w}{\partial r}+\frac{r^2}{2}\frac{\partial w}{\partial\theta}\frac{\partial^2 w}{\partial r^2}+r^2\frac{\partial^2 w}{\partial r\partial\theta}\frac{\partial w}{\partial r}+\frac{r(1+\nu)}{2}\frac{\partial u}{\partial\theta}+\right.$$
$$\left.+\frac{r^2(1+\nu)}{2}\frac{\partial^2 u}{\partial r\partial\theta}+\frac{rv(1-\nu)}{2}+r\frac{\partial^2 v}{\partial\theta^2}+\frac{r^3(1-\nu)}{2}\frac{\partial^2 v}{\partial r^2}-\frac{r^2(1-\nu)}{2}\frac{\partial v}{\partial r}\right]+$$
$$+\frac{1}{r^4}\frac{\partial w}{\partial r}\left[r^2\frac{\partial^2 w}{\partial r\partial\theta}\frac{\partial w}{\partial\theta}+\frac{r^3}{2}\left(\frac{\partial w}{\partial r}\right)^2+\frac{r^2}{2}\frac{\partial w}{\partial r}\frac{\partial^2 w}{\partial\theta^2}+\frac{3r^4}{2}\frac{\partial w}{\partial r}\frac{\partial^2 w}{\partial r^2}+r^3(1+\nu)\frac{\partial u}{\partial r}+\right.$$
$$\left.+\frac{r^2(1-\nu)}{2}\frac{\partial^2 u}{\partial\theta^2}+r^4\frac{\partial^2 u}{\partial r^2}+\frac{r^3(1+\nu)}{2}\frac{\partial^2 v}{\partial r\partial\theta}-\frac{r^2(1-\nu)}{2}\frac{\partial v}{\partial\theta}\right]+$$
$$+\frac{1}{r^4}\frac{\partial^2 w}{\partial\theta^2}\left[vr^2\frac{\partial u}{\partial r}+r\left(u+\frac{\partial v}{\partial\theta}\right)\right]+\frac{\partial^2 w}{\partial r^2}\left[\frac{\partial u}{\partial r}+\frac{v}{r}\left(u+\frac{\partial v}{\partial\theta}\right)\right]+$$
$$+\frac{(1-\nu)}{r^2}\frac{\partial^2 w}{\partial r\partial\theta}\left[\frac{\partial u}{\partial\theta}-v+r\frac{\partial v}{\partial r}\right] \tag{2.8c}$$

- *Linear equations*, derived from the linear Kirchhoff theory

$$\frac{\rho(1-\nu^2)}{E}\left[\frac{\partial^2 u}{\partial t^2}-\Omega^2(r+u)-2\Omega\frac{\partial v}{\partial t}\right]=\frac{(1-\nu)}{2r^2}\frac{\partial^2 u}{\partial\theta^2}+\frac{(1+\nu)}{2r}\frac{\partial^2 v}{\partial r\partial\theta}+\frac{\partial^2 u}{\partial r^2}+$$
$$+\frac{1}{r}\left[\frac{\partial u}{\partial r}-\frac{(3-\nu)}{2r}\frac{\partial v}{\partial\theta}-\frac{u}{r}\right] \tag{2.9a}$$

$$\frac{\rho(1-\nu^2)}{E}\left[\frac{\partial^2 v}{\partial t^2}-\Omega^2 v-2\Omega\frac{\partial u}{\partial t}\right]=\frac{1}{r^2}\frac{\partial^2 v}{\partial\theta^2}+\frac{(1+\nu)}{2r}\frac{\partial^2 u}{\partial r\partial\theta}+\frac{(1-\nu)}{2}\frac{\partial^2 v}{\partial r^2}+$$
$$+\frac{1}{r}\left[\frac{(1-\nu)}{2}\frac{\partial v}{\partial r}-\frac{(3-\nu)}{2r}\frac{\partial u}{\partial\theta}-\frac{(1-\nu)}{2}\frac{v}{r}\right] \tag{2.9b}$$

$$\frac{\rho(1-\nu^2)}{E}\left[\frac{\partial^2 w}{\partial t^2}+\frac{h^2\Omega^2}{3}\nabla^2 w-\frac{h^2}{3}\frac{\partial^2}{\partial t^2}\nabla^2 w\right]=-\frac{h^2}{3}\nabla^4 w \tag{2.9c}$$

- *Linear equations, derived from non-linear strain considerations*, considering small displacements in the equilibrium state

$$\frac{\rho(1-\nu^2)}{E}\left[\frac{\partial^2 u}{\partial t^2}-\Omega^2(r+u)-2\Omega\frac{\partial v}{\partial t}\right]=\frac{(1-\nu)}{2r^2}\frac{\partial^2 u}{\partial\theta^2}+\frac{(1+\nu)}{2r}\frac{\partial^2 v}{\partial r\partial\theta}+\frac{\partial^2 u}{\partial r^2}+ +\frac{1}{r}\left[\frac{\partial u}{\partial r}-\frac{(3-\nu)}{2r}\frac{\partial v}{\partial\theta}-\frac{u}{r}\right] \tag{2.10a}$$

$$\frac{\rho(1-\nu^2)}{E}\left[\frac{\partial^2 v}{\partial t^2}-\Omega^2 v-2\Omega\frac{\partial u}{\partial t}\right]=\frac{1}{r^2}\frac{\partial^2 v}{\partial\theta^2}+\frac{(1+\nu)}{2r}\frac{\partial^2 u}{\partial r\partial\theta}+\frac{(1-\nu)}{2}\frac{\partial^2 v}{\partial r^2}+ +\frac{1}{r}\left[\frac{(1-\nu)}{2}\frac{\partial v}{\partial r}-\frac{(3-\nu)}{2r}\frac{\partial u}{\partial\theta}-\frac{(1-\nu)}{2}\frac{v}{r}\right] \tag{2.10b}$$

$$\frac{\rho(1-\nu^2)}{E}\left[\frac{\partial^2 w}{\partial t^2}+\frac{h^2\Omega^2}{3}\nabla^2 w-\frac{h^2}{3}\frac{\partial^2}{\partial t^2}\nabla^2 w\right]=-\frac{Eh^2}{3(1-\nu^2)}\nabla^4 w+ +\frac{1}{r}\frac{\partial}{\partial r}\left(r\sigma_{rr}\frac{\partial w}{\partial r}\right)+\frac{\sigma_{\theta\theta}}{r^2}\frac{\partial^2 w}{\partial\theta^2} \tag{2.10c}$$

Note that the full non-linear representation of the spinning disk problem requires the solution of three non-linearly coupled partial differential equations. Furthermore, the linear transverse vibration expression (Equation 2.9c) resembles the equation of the linear transverse vibration of a stationary disk. On the other hand, the equation resulting from the linearization of the non-linear model (Equation 2.10c) is the same equation obtained by Lamb and Southwell [1921] for the transverse vibration of a spinning disk, with the exception of the terms $\nabla^2 w$ and $\frac{\partial^2}{\partial t^2}\nabla^2 w = \nabla^2\ddot{w}$, that arise from the effects of in-plane deformation and rotary inertia. Baddour and Zu [2001a] proceeded to the comparison between the proposed and existing models, demonstrating that these two terms affect the dynamic characteristics of the rotating disk in a significant way. Chen [2011] examined this model and discussed a consistent approach which is capable of reducing the fully non-linear transverse motion equations (Equation 2.8c) to the classical linear equation proposed by Lamb and Southwell [1921] (Equation 2.2), but also to the non-linear equation derived by Nowinski [1964] (Equation 2.4a), based on the analysis of the orders of magnitude of each term.

2.3 Finite Element Models of a Spinning Disk

As an inherent characteristic of the finite element method, it requires the subdivision of the domain into smaller, simpler parts, the finite elements. For the case being studied, the spinning disk will be discretized in plate elements. So, the finite element model will be based on the mathematical formulation of rotating plates.

In general, the system of equations of motion for a rotating system based on a fixed reference frame is highly non-linear because of the significant displacements resulting from the full-body spinning motion. On the other hand, a formulation referring to a co-rotating reference system yields equations which may be easily linearized if the displacements are small and the rotational speed remains constant [Kirchgäßner, 2016]. So, the presented finite element method models will be formulated in a frame common with the spinning movement, so that linear motion equations are obtained and the modal analysis easily achieved.

Hsieh and Abel [1995] presented and compared two approaches for the analysis of rotating plates, where only one is of interest for the present dissertation, the *distributed*

mass (DM) approach, that treats the structure as a continuum, with mass uniformly distributed in the structure, and thus being the general consideration for all types of finite elements. The author starts by defining the element geometry, $\{r\}$, and the displacement field, $\{u\}$, as:

$$\{r\} = \left[\mathcal{N}'\right]\{c\} \tag{2.11}$$

$$\{u\} = [\mathcal{N}]\{q\} \tag{2.12}$$

where $\{c\}$ represent the nodal coordinates of the element, $\{q\}$ the nodal generalized displacement vector, $[\mathcal{N}']$ the coordinates shape function matrix and $[\mathcal{N}]$ the displacement shape function matrix. Note that $[\mathcal{N}']$ and $[\mathcal{N}]$ are identical for an isoparametric formulation.

The strain-displacement and the stress-strain relations are defined as usual, as:

$$\{\varepsilon\} = [\mathcal{B}]\{q\} \tag{2.13}$$

$$\{\sigma\} = [\mathcal{D}]\{\varepsilon\} \tag{2.14}$$

where $[\mathcal{B}]$ and $[\mathcal{D}]$ represent the strain and constitutive matrices, respectively.

Considering a co-rotating referential system, the instantaneous position vector of a material point in the element, $\{P\}$, is given as:

$$\{P\} = \{r\} + \{u\} \tag{2.15}$$

The corresponding absolute velocity, $\{v\}$, is given by:

$$\{v\} = \{\dot{P}\} = \{\dot{u}\} + \{\omega\} \times \{P\} = [\mathcal{N}]\{\dot{q}\} + [\Omega]\left(\left[\mathcal{N}'\right]\{c\} + [\mathcal{N}]\{q\}\right) \tag{2.16}$$

where $\{\omega\}$ and $[\Omega]$ represent the rotational speed vector and matrix, respectively, given by:

$$\{\omega\} = \begin{Bmatrix} \omega_x \\ \omega_y \\ \omega_z \end{Bmatrix} \tag{2.17a}$$

$$[\Omega] = \begin{bmatrix} 0 & -\omega_z & \omega_y \\ \omega_z & 0 & -\omega_x \\ -\omega_y & \omega_x & 0 \end{bmatrix} \tag{2.17b}$$

Having the velocity field defined, it is possible to determine the kinetic energy of the element. Thus, it is given by:

$$\Pi^K = \frac{1}{2}\int_V \rho\{v\}^{\mathrm{T}}\{v\}\,\mathrm{d}V \tag{2.18}$$

in which V and ρ represent the element's volume and the density of the material, respectively. Substituting Equation 2.16, after manipulation, results in:

$$\begin{aligned}\Pi^K = &\frac{1}{2}\int_V \rho\{\dot{q}\}^{\mathrm{T}}[\mathcal{N}]^{\mathrm{T}}[\mathcal{N}]\{\dot{q}\}\,\mathrm{d}V + \frac{1}{2}\int_V \rho\{r\}^{\mathrm{T}}\left[\Omega^2\right]\{r\}\,\mathrm{d}V + \\ &+\frac{1}{2}\int_V \rho\{q\}^{T}[\mathcal{N}]^{\mathrm{T}}\left[\Omega^2\right][\mathcal{N}]\{q\}\,\mathrm{d}V + \int_V \rho\{\dot{q}\}^{T}[\mathcal{N}]^{\mathrm{T}}[\Omega]\{r\}\,\mathrm{d}V + \\ &+\int_V \rho\{r\}^{\mathrm{T}}\left[\Omega^2\right][\mathcal{N}]\{q\}\,\mathrm{d}V + \int_V \rho\{\dot{q}\}^{\mathrm{T}}[\mathcal{N}]^{\mathrm{T}}[\Omega][\mathcal{N}]\{q\}\,\mathrm{d}V\end{aligned} \tag{2.19}$$

where $[\Omega^2] = [\Omega]^{\mathrm{T}}[\Omega]$.

For the (geometrically linear) potential energy, recalling Equations 2.13 and 2.14, it is given by:

$$\Pi^P = \frac{1}{2}\int_V \{\varepsilon\}^{\mathrm{T}}\{\sigma\}\,\mathrm{d}V = \frac{1}{2}\int_V \{q\}^{\mathrm{T}}[\mathcal{B}]^T[\mathcal{D}][\mathcal{B}]\{q\}\,\mathrm{d}V \tag{2.20}$$

Hsieh and Abel [1995] then applied the Lagrange equation:

$$\frac{\mathrm{d}}{\mathrm{d}t}\left(\frac{\partial \Pi^K}{\partial \dot{q}}\right) - \frac{\partial \Pi^K}{\partial q} + \frac{\partial \Pi^P}{\partial q} = \left\{F^{\mathrm{ext}}\right\} \tag{2.21}$$

and obtained the following matrix form of the motion equations:

$$[m]\{\ddot{q}\} + [c_c(\Omega)]\{\dot{q}\} + ([k_e] + [k_a(\Omega)] - [k_r(\Omega)])\,\{q\} + \{f_c'(\Omega)\} = \{f^{\mathrm{ext}}\} \tag{2.22}$$

in which $[m]$ represents the element mass matrix, $[c_c]$ the element Coriolis effects matrix, $[k_e]$ the element elastic stiffness matrix, $[k_a]$ the element centripetal stiffness matrix, $[k_r]$ the element centrifugal softening matrix, $\{f_c'\}$ the element rotational centrifugal force vector and $\{f^{\mathrm{ext}}\}$ the element external load vector. In the aforementioned publication, the authors also present the expressions to determine the previous matrices and vectors, as follows:

$$[m] = \int_V \rho[\mathcal{N}]^{\mathrm{T}}[\mathcal{N}]\,\mathrm{d}V \tag{2.23a}$$

$$[c_c] = 2\int_V \rho[\mathcal{N}]^{\mathrm{T}}[\Omega][\mathcal{N}]\,\mathrm{d}V \tag{2.23b}$$

$$[k_e] = \int_V [\mathcal{B}]^{\mathrm{T}}[\mathcal{D}][\mathcal{B}]\,\mathrm{d}V \tag{2.23c}$$

$$[k_a] = \int_V \rho[\mathcal{N}]^{\mathrm{T}}[A][\mathcal{N}]\,\mathrm{d}V \tag{2.23d}$$

$$[k_r] = \int_V \rho[\mathcal{N}]^{\mathrm{T}}\left[\Omega^2\right][\mathcal{N}]\,\mathrm{d}V \tag{2.23e}$$

$$\{f_c'\} = \int_V \rho[\mathcal{N}]^{\mathrm{T}}[A][\mathcal{N}']\{c\}\,\mathrm{d}V - \int_V \rho[\mathcal{N}]^{\mathrm{T}}[\Omega^2][\mathcal{N}']\{c\}\,\mathrm{d}V \tag{2.23f}$$

where $[A] = [\dot{\Omega}]$ represents the rotational acceleration matrix.

After assembly, the final global motion equations result in:

$$[M]\{\ddot{Q}\} + [C_c]\{\dot{Q}\} + ([K_e] + [K_a] - [K_r])\,\{Q\} + \{F_c'\} = \{F^{\mathrm{ext}}\} \tag{2.24}$$

Applying the presented approach to the case being studied, with constant spinning speed, it can be easily concluded that the rotational acceleration matrix and, consequently, the centripetal stiffness matrix and the first integral of the rotational centrifugal force

vector are null. That is, $[k_a] = [0]$ and $\{f_c\} = -\int_V \rho[\mathcal{N}]^T[\Omega^2][\mathcal{N}']\{c\}\,\mathrm{d}V$, resulting in the following global motion equations:

$$[M]\{\ddot{Q}\} + [C_c(\Omega)]\{\dot{Q}\} + ([K_e] - [K_r(\Omega)])\,\{Q\} + \{F_c(\Omega)\} = \{F^{\text{ext}}\} \tag{2.25}$$

Analyzing the final equations of motion, it is possible to identify three new terms that contemplate the rigid-body rotational movement phenomena, namely the *Coriolis effect*, the *centrifugal softening effect* and the *centrifugal stiffening effect*.

2.3.1 Coriolis Effect

The Coriolis effect is included in the skew-symmetric matrix $[C_c]$ ($[c_c]$ for the element case), which expression (Equation 2.23b) is very similar to the one of the mass matrix, with the inclusion of the spinning velocity matrix, previously presented. This matrix appears multiplying by the general velocity vector, leading to the frequent designation as "Coriolis damping matrix", despite not being a source of damping [Hsieh and Abel, 1995; Kirchgäßner, 2016].

Considering the stationary disk case, as a result of the geometric symmetry, the bending natural vibration modes appear in pairs, that is, there are two modes with the same natural frequency and the same shape, but rotated by 90° in the plane. However, when considering a rotating structure, these pairs of natural vibration modes split into forward and backward travelling waves, when considering a stationary observer, because of the Coriolis effect. The splitting phenomenon leads to these natural modes no longer present the same natural frequency values, since the disk rotation increases the speed of the forward whirl relatively to a stationary frame, thereby increasing its frequency and decreasing the frequency of the opposing natural movement [Ahn and Mote, 1998]. This fact may lead to the appearance of critical working speeds, that correspond to the point when the natural frequency and the rotating speed coincide, leading to elastic instabilities. When a disk is thin and analyzed in a rotating frame, the Coriolis effects are not significant and the splitting in the frequency values may not be easily identified [Kirchgäßner, 2016].

According to Kirchgäßner [2016], there is a relation between the frequencies calculated in a rotational coordinate system, $\omega_{n_{\text{rot}}}$, and the ones obtained in an inertial frame, $\omega_{n_{\text{fix}}}$, given by:

$$\omega_{n_{\text{fix}}} = \omega_{n_{\text{rot}}} \pm \frac{2\pi}{60}\Omega \;\; [\text{rad/s}] \tag{2.26}$$

where Ω represents the disk rotating speed, expressed in rotations per minute (rpm), and the plus and minus signs correspond to the forward and backward movements, respectively.

2.3.2 Centrifugal Softening Effect

One other effect presented in the aforementioned approach to analyze rotating structures, namely disks, is the softening effect, considered in the model by the centrifugal softening matrix, $[K_r]$ ($[k_r]$ for the element case), which expression (Equation 2.23e) is very similar to the one of the mass matrix, with the inclusion of the squared spinning velocity matrix. Note that, despite being positive semi-definite and, consequently, its terms being positive or null according to the used formulation, the softening effect is materialized by the minus sign in the matrix motion equations.

This phenomenon, known as spin or centrifugal softening effect, results from the consideration of large deflections in the structure due to circumferential relative motions, and thus geometric non-linearity. To clarify, consider a very simple example of a rotating

spring, with linear stiffness k, with an attached mass m in one end and with the rotation axis in the other (Figure 2.1).

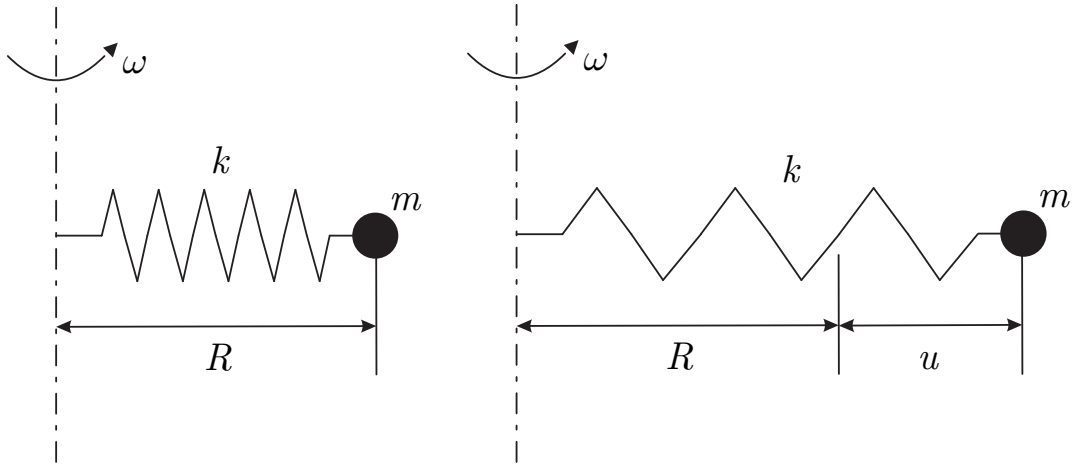

(a) Initial configuration. **(b)** Deformed configuration.

Figure 2.1: Schematic representation to demonstrate the centrifugal softening effect.

Considering that the displacement resulting from centrifugal effects, u, is small when compared to the initial position, R, of the mass, the static force equilibrium results in:

$$\begin{aligned} F_k &= F_c \\ ku &= mR\omega^2 \end{aligned} \tag{2.27}$$

where F_k and F_c represent the spring and centrifugal forces, respectively, acting on the mass element.

However, when the displacement presents an order of magnitude that can not be neglected when formulating the centrifugal force, the previous equilibrium results in:

$$\begin{aligned} F_k &= F_c \\ ku &= m(R+u)\omega^2 \\ (k - m\omega^2)u &= mR\omega^2 \end{aligned} \tag{2.28}$$

Comparing Equations 2.27 and 2.28, it is easily concluded that the equivalent stiffness of the second case is lower than the one in the first case, because of the $m\omega^2$ therm that subtracts the spring stiffness coefficient, and thus verifying a softening phenomenon when not considering small and negligible displacements. In this simple yet considerably illustrative example, the centrifugal softening effect is strong, and the natural frequency of the system tends to zero when the rotating speed tends to $\sqrt{\frac{k}{m}}$ [Genta and Silvagni, 2014].

Considering the case of the rotating disk, the visualization of the effects may be more difficult, but the principles are the same. Furthermore, it is possible to conclude that the influence of the centrifugal softening in the plane geometry disk will only occur in the in-plane normal modes, since only in these the in-plane displacements change the distance to the rotational axis. This follows the conclusions presented in Genta and Silvagni [2014] for rotational beams, where the authors concluded that the centrifugal softening effects were only found when considering an extensional theory (axial displacements were considered), and that its influence becomes significant only at very high rotational speeds.

2.3.3 Centrifugal Stiffening Effect

Finally, the centrifugal stiffening effect is considered in the model by the centrifugal force vector, $\{F_c\}$ ($\{f_c\}$ for the element case, determined by the second therm of Equation 2.23f for constant rotational speed). Note that, even considering a natural regime, that is, with no external loads applied ($\{F^{\text{ext}}\} = \{0\}$), the rotational movement will generate a body force, the centrifugal force, acting in the radial direction and that depends on the mass, on the square of the rotational speed and on the position of the considered point. The fact that the centrifugal force acts away from the rotation axis induces traction stresses for the centrally clamped rotating disk, therefore leading to an increase in the structure's stiffness.

However, when a modal or frequency response analysis is wanted, the centrifugal force vector can not be present in the matrix motion equations. Thus, the centrifugal stiffening effects must be accounted for with a matrix, usually named "geometric stiffness matrix" [Hsieh and Abel, 1995; Kirchgäßner, 2016]. Its determination results from the consideration of the non-linear strain components, namely second order strain-displacement terms, which means that more geometric non-linearities are present in the aforementioned finite element approach. Hsieh and Abel [1995] present the necessary procedure to achieve this, following the updated Lagrangian approach, presented by Bathe [1982], that makes use of the second Piola-Kirchhoff stress tensor and the Green-Lagrange strain tensor. This is, basically, the consideration of the centrifugal force as a pre-stress applied in the structure and the linearisation around the system's stationary state [Hashemi et al., 2009].

First, the global static problem is solved trough the determination of the generalized displacement field, $\{Q_c\}$, caused by the centrifugal force, that is, considering the centrifugal force vector, $\{F_c\}$, as the imposed load and the stiffness matrix as the combination of the elastic, $[K_e]$, and softening, $[K_r]$, matrices, as follows:

$$([K_e] - [K_r])\{Q_c\} = \{F_c\} \tag{2.29}$$

Next, using the strain-displacement and stress-strain relations, the correspondent stress field is calculated, given by Equations 2.13 and 2.14. Finally, the centrifugal stiffness matrix is determined, in the element formulation, as:

$$[k_g] = \int_V [G]^T [\tau] [G] \, \mathrm{d}V \tag{2.30}$$

where $[G]$ represents the non-linear strain-displacement relation matrix and $[\tau]$ is a matrix with the stress field components.

After assembling, results the global centrifugal, or geometric, stiffness matrix, $[K_g]$ (Figure 2.2). Note that the existence of any other pre-stress applied in the structure can be considered through the present process, only adding the external force vector in the right-hand side of Equation 2.29.

The resulting motion equations for the rotating structure will be:

$$[M]\{\ddot{Q}\} + [C_c(\Omega)]\{\dot{Q}\} + ([K_e] - [K_r(\Omega)] + [K_g(\Omega)])\{Q\} = \{0\} \tag{2.31}$$

Note that, despite being considered non-linearities throughout the presented approach, the final system of equations allows its linear solving.

Finally, it is important to notice that, for the same structure, the variation of the spinning velocity will lead to a totally new centrifugal system (different Coriolis and softening effects and new centrifugal force distribution), which requires a new determination of the aforementioned matrices and vector.

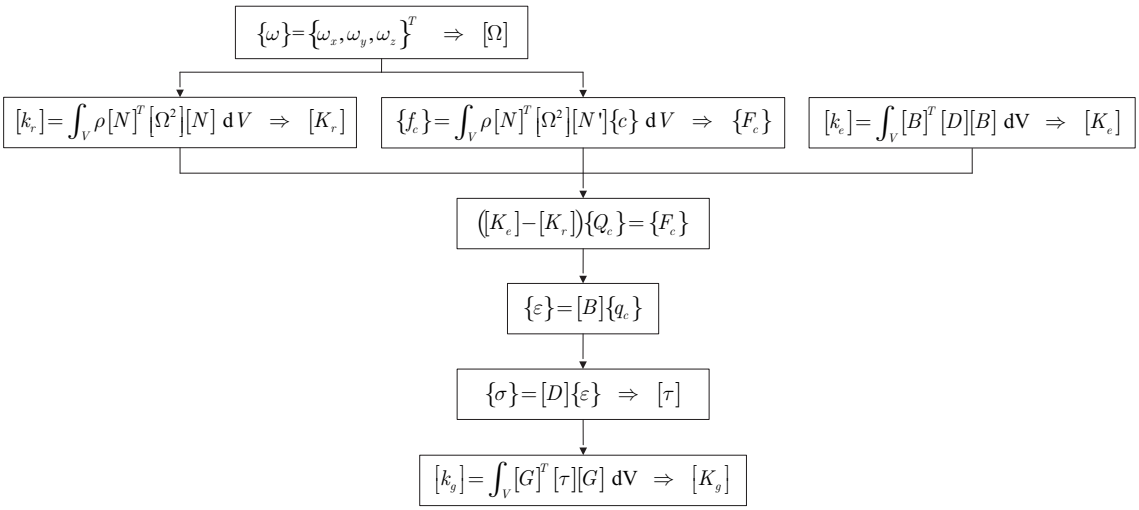

Figure 2.2: Schematic representation of the geometric stiffness matrix, $[K_g]$, determination process.

Chapter 3

Viscoelastic Damping Treatments

The present chapter addresses some issues regarding viscoelastic materials and viscoelastic damping treatments. Initially, the differences between active and passive damping treatments will be discussed. Next, viscoelastic damping treatments will be studied, namely their configurations and characteristics. Finally, the properties and characterization of viscoelastic materials will be addressed, as well as the problematic regarding their numerical simulation in a finite element method software. For further information regarding these subjects, one can consult the references used throughout this chapter, specifically Jones [2001], Moreira [2004], Vasques et al. [2010b] and Moreira [2014].

3.1 Introduction

The developments of Structural Engineering over the past decades have been aiming the structural efficiency of constructions, using new, lighter and stiffer materials and implementing more versatile production and assembly processes. Despite the progresses, these modifications can be associated with the gradual removal of the inherent dissipative mechanisms of structures when compared, for example, with the heavy cast iron structures or with the screwed or revited connections. One can readily conclude that the reduction of structures' and components' damping capacity leads to more frequent incidents related with irreversible fatigue damages raised by the continued action of mechanical excitations. In fact, damping has been, and often still is, an invisible requirement for good mechanical design, and if the damping capacity of a structure is not able to dissipate the energy of vibrations induced by dynamic loads it is necessary to implement additional damping mechanisms, which can be divided in *active* or *passive* dissipative elements.

Active damping mechanisms classifies a set of devices that actively react against a vibration motion to mitigate it. In fact, they are based on the real-time response of a device or component, such as piezoelectric patches, electro-rheologic and magneto-rheologic fluids, and shape-memory alloys and polymers, to the structure's vibration, based on a closed-loop control relying on sensors, actuators and power electronics, revealing higher efficiency within low frequency range [Moreira, 2014].

Passive damping mechanisms rely on the addition of tailored mechanisms based on materials, fluids or electrical systems able to dissipate a significant amount of the deformation energy that is absorbed by the damping treatment when the host structure vibrates. Shunted-piezoelectric ceramics, shape-memory alloys and viscoelastic materials represent interesting forms of passive damping implementations. These mechanisms are effective within medium-high frequency range and can operate in an autonomous way, not relying on external power sources or control circuits [Moreira, 2014].

This dissertation will only consider passive damping mechanisms, namely viscoelastic treatments.

3.2 Viscoelastic Damping Treatments

Viscoelastic damping treatments assume a prominent position in the passive damping mechanisms mostly because of their high dissipative capacity combined with simplicity, low price and small induced structural changes.

The great damping capacity of viscoelastic materials is due to their particular molecular structure. In fact, these materials dissipate the deformation energy to the exterior in the form of heat due to the interaction of their long and reticulated molecular chains when deformed. However, viscoelastic materials are not structural efficient since they reveal significant weight combined with low stiffness. Therefore, the correct use of these materials' damping capabilities results of its integration into a structural efficient component or structure, made of aluminium alloys or steel, or carbon composites, thus enabling the symbiosis of the properties of both materials when used in superficial or integrated viscoelastic damping treatments.

These passive damping mechanisms are mostly applied nowadays in the aeronautic and automotive industries, where their use as superficial treatments allow the reduction of vibrations in structural panels.

3.2.1 Configuration of Viscoelastic Damping Treatments

The application of viscoelastic materials for the damping treatment of structural vibrations is essentially achieved using three configurations: *free layer damping* (FLD), *constrained layer damping* (CLD) and *integrated layer damping* (ILD). Each one of these dispositions presents a set of distinctive features, and therefore guides the selection of the best setting for each application.

3.2.1.1 Free Layer Damping Treatments

Free layer damping treatments (Figure 3.1) are obtained by the deposition of a layer of viscoelastic material on the surface of the structure that is being treated. The principal advantages of this method are the low cost of application and the simple analytic or numerical representation and simulation. However, this type of viscoelastic damping treatment requires a noticeable thick layer of material because it will mostly be subjected to internal traction-compression loads, which are pretty inefficient in terms of energy dissipation.

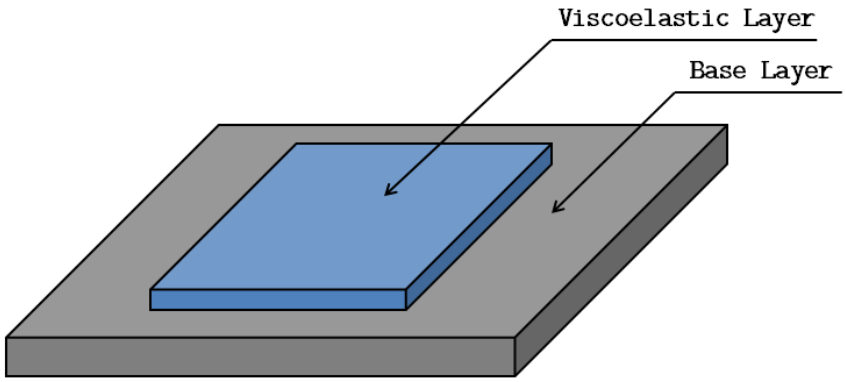

Figure 3.1: Free layer damping treatment.

In fact, the efficiency of this type of treatments increases with the thickness of the viscoelastic layer up to approximately the double of the thickness of the base panel or plate, from which it remains approximately constant. In addition to the effects of the thickness ratio, the efficiency of the free layer damping treatment varies directly with the ratio between the storage modulus of the viscoelastic material and the elastic modulus of the structure's material. This is the reason why high storage modulus materials are preferably used in this method, namely plasticized PVC.

In general, despite being inexpensive and easy to apply, these treatments are poorly efficient and induce significant changes in the mass and rigidity of the final assembled structure.

3.2.1.2 Constrained Layer Damping

The constrained layer configuration (Figure 3.2) is very similar to the one presented previously, since it is also obtained by deposition of a layer of viscoelastic material on the surface of the structure, but it now has a restriction layer on top, made of an elastic material with reasonably high elastic modulus. This top layer will act as a constraint to the bending of first layer, which will induce significant shear strains in the viscoelastic material, thus enabling greater efficiency of the treatment with thinner layers.

Along with the thinner layers, the storage modulus of the viscoelastic material is relatively low to promote the shear strain, which combined will induce minor changes in

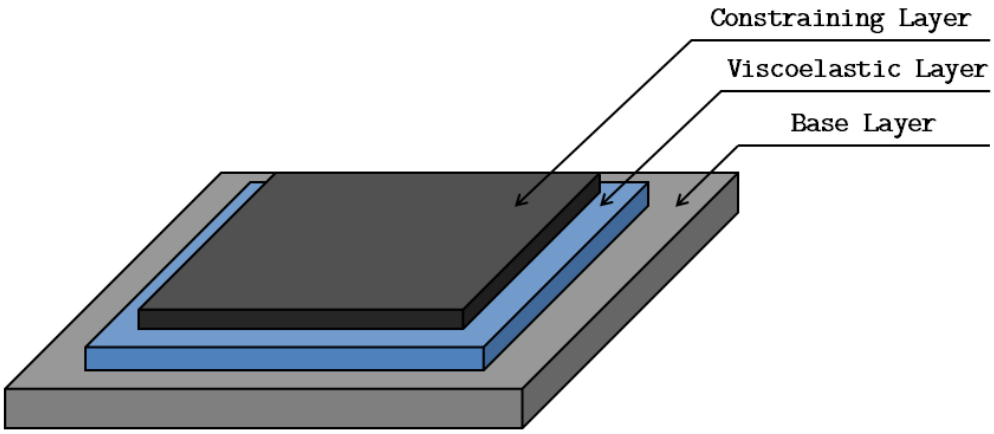

Figure 3.2: Constrained layer damping treatment.

the mass and rigidity of the final component or structure. In fact, these changes that occur are mostly due to the restriction layer and not to the dissipative one. However, the analytic and numerical modelling and simulation of this configuration is not simple and requires special care with the shear strains that occur in the dissipative layer.

The constrained layer damping treatments are also easy to apply and low cost.

3.2.1.3 Integrated Layer Damping Treatments

The integrated layer configuration (Figure 3.3) consists of applying the viscoelastic material between two layers of the base material, which can be related with the core of a sandwich structure. This is the configuration that allows the maximum efficiency of the viscoelastic damping treatment because the induced shear strains are higher as a result of the positioning of the viscoelastic layer over the neutral plane of the assembled structure.

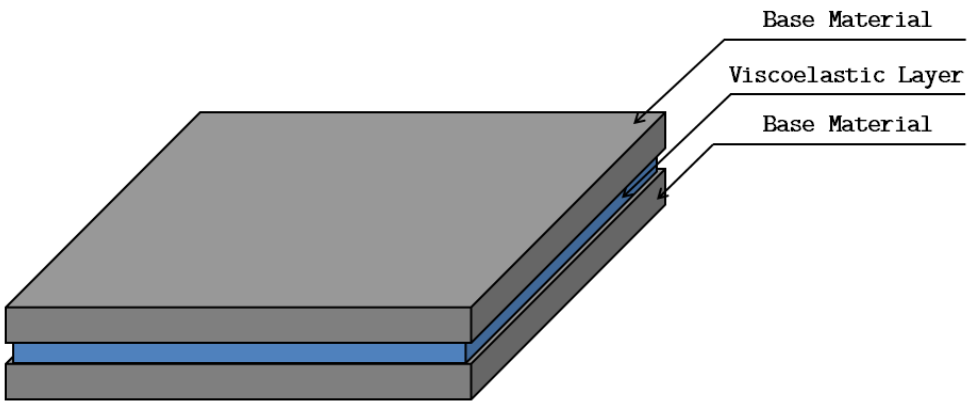

Figure 3.3: Integrated layer damping treatment.

While the previous configurations are applied as corrective treatments, that is, after the production of the structure or component, this configuration requires special stages and processes during its production, such as adapting/changing the process and the raw material.

As one can easily conclude, the shear strains field of the viscoelastic layer is strongly influenced by the configuration of the treatment. Figure 3.4 represents the distribution of

the total deformation energy density in the viscoelastic layer for the first natural vibration mode for the same beam but subjected to the three different damping treatments.

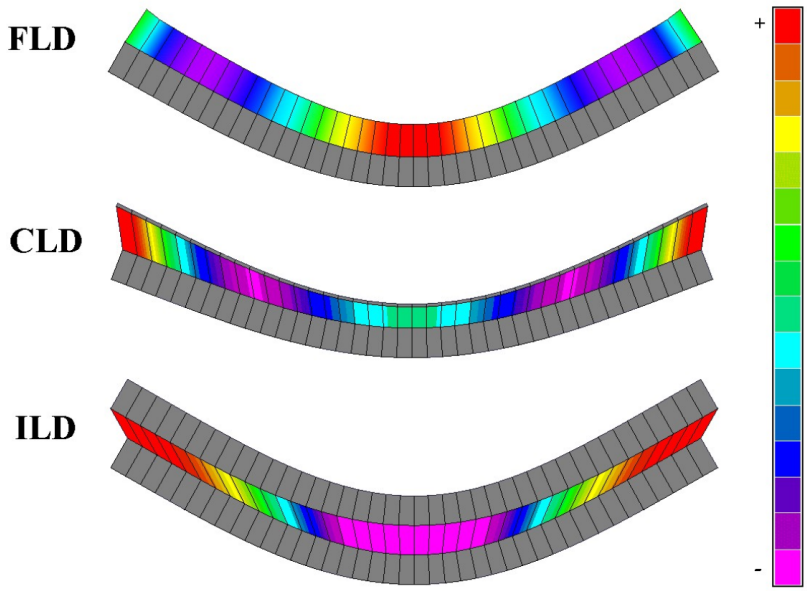

Figure 3.4: Total deformation energy density distribution in the viscoelastic layer [Moreira, 2004].

3.2.2 Optimization of Viscoelastic Damping Treatments

In addition to their reduced cost, high efficiency (specially in the constrained and integrated layer configuration) and self-sufficiency, there are a group of optimization techniques for the passive viscoelastic damping treatments that allow the reduction of structural changes, the increase of the treatment's efficiency, the reduction of their total cost, the capability of selective modal damping and the increase of the efficient range. In the present dissertation will be presented some of these techniques that may be interesting at a later stage of the work, namely *partial local treatments*, *multi-layer and multi-material treatments*, *treatments with amplification mechanisms* and *oriented treatments*.

3.2.2.1 Partial Local Treatments

This technique consists in reducing the treated area of the structure without drastically reduce it's damping efficiency. In fact, the application of partial treatments in specific segments can result in high efficient passive damping solutions that are much cheaper inducing less structural changes, specially in the mass distribution. This optimization technique is applied in the FLD and CLD configurations, and can be obtained by strategically and regularly placing the treatment onto some segments of the structure's surface or by applying the viscoelastic damping treatment on the entire surface and then drilling some holes in them, that must represent 40 to 60% of its area, significantly reducing the set's mass [Moreira, 2004].

Regarding the CLD configuration, the best location of the damping patches is a controversial issue. While some authors state that the best location for the partial local damping treatment is near to the antinodes of the vibrating structure, which correspond to the locations with higher out-of-plane displacements, others indicate the nodes as the

location where shear strain reaches its maximum and thus correspond to the best treatment spot. The best location will depend on the relative thickness of the constraining layer in respect to the host structure. In fact, for thick constraining layers, leading to a CLD configuration similar to the ILD configuration, the best treatment spots are located near to the structure vibration nodes, while for thinner constraining layers these locations move towards the antinodes' regions [Moreira, 2014].

While addressing the configuration's thickness, one can also present the influence of the viscoelastic material's thickness on the treatment's efficiency. One can easily identify that the damping efficiency of a viscoelastic damping treatment is proportional to the shear strain energy stored in the viscoelastic material, which depends on the volume of the material contributing to this energy storage and on the imposed shear strain levels. While the relation between the viscoelastic material layer's thickness and the shear strain level is opposite (for the same strain of the host structure, thinner layers are subjected to higher shear strain), the volume contributing for the total strain energy is directly proportional to its thickness. Thus, contrary to the FLD configuration, where a direct relation between the viscoelastic layer's thickness and the damping efficiency is observed, the CLD configuration does not present such a direct relation, leading to the exploration of this aspect for optimization purposes [Moreira, 2014].

3.2.2.2 Multi-Layer and Multi-Material Treatments

The multi-layer optimization technique is obtained by the superposition of layers of different viscoelastic materials, with different transition temperatures, and seeks to obtain an efficient treatment with a wider temperature range. In fact, the efficiency of a single layer treatment is limited by the transition temperature of the viscoelastic material while the efficiency of a multi-layer treatment is given by the combination of the relative efficiency of each material of each layer [Moreira, 2004].

Furthermore, the application of viscoelastic layers intercalated with constraining layers (the multi-material optimization technique) allows the maximization of the shear strain in each viscoelastic layer [Moreira, 2014].

3.2.2.3 Treatments with Amplification Mechanisms

This technique consists in the application of amplification mechanisms between the host structure and the viscoelastic layer. They can be materialized as a spacing layer with a high shear modulus and low weight, which leads to a greater strain in the lower surface of the viscoelastic material and to higher energy dissipation. These spacing layers can be honeycomb sandwich plates or plates made of rigid polymeric foams [Moreira, 2004].

3.2.2.4 Oriented Treatments

Most of the viscoelastic materials are isotropic. However, some applications would benefit from the directional dependence of stiffness and loss factor of the viscoelastic layer, giving rise to a selective treatment, showing different damping for different vibration modes of the structure. One way to materialize this optimization technique consists in the introduction of oriented fibres into a viscoelastic layer, which leads to an oriented shear strain field and, consequently, to different efficiencies depending on the direction [Moreira, 2004].

3.3 Characterization of Viscoelastic Materials

It can be experimentally observed that when a viscoelastic material is subjected to a harmonic loading, the resulting strain is also harmonic and with the same frequency as the load. However, and contrary to what happens with elastic materials, there is a certain lag, δ, between the verified strain, $\varepsilon(t)$, and the stress, $\sigma(t)$, imposed by the load, as can be seen in Figure 3.5 *(a)*. Figure 3.5 *(b)* shows a representation of the measured stress and the measured strain, where one can easily identify an elliptical shape, which is called the hysteretic cycle. The angle between the ellipse's major axes and the abscissa's axis is proportional to the material's stiffness or elastic behavior, while the ratio between the ellipse's minor and major axis indicates its damping capacity. One can easily comprehend that if the material is elastic, without any damping properties, the hysteretic cycle shapes itself as a well known straight line, where its slope represents the material's stiffness.

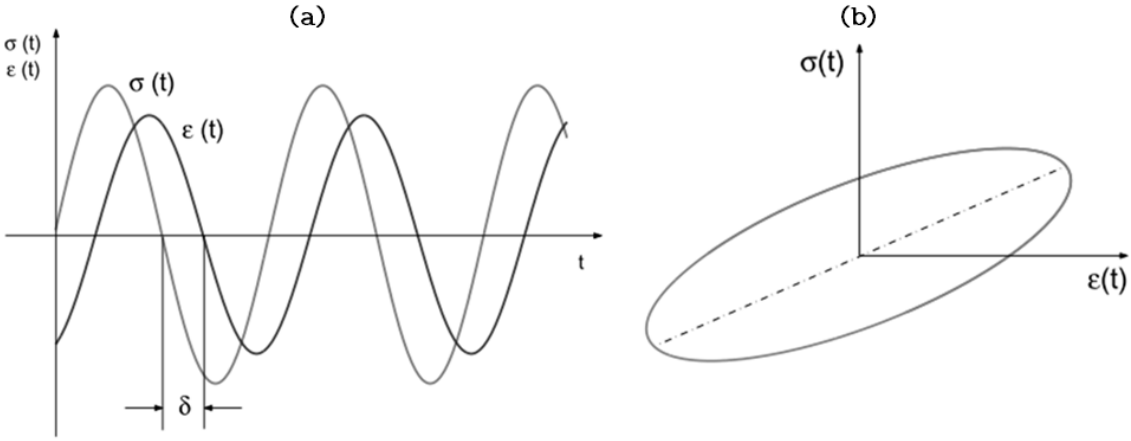

Figure 3.5: Stress and strain induced by a harmonic loading in a viscoelastic material: *(a)* Representation of the lag, *(b)* Representation of the hysteretic behavior. Moreira [2004]

As said before and shown in Figure 3.5 *(a)*, a harmonic loading will also induce a harmonic stress field given by:

$$\sigma(t) = \sigma_0 \sin(\omega t) \tag{3.1}$$

A viscoelastic material will respond with an harmonic strain, given by:

$$\varepsilon(t) = \varepsilon_0 \sin(\omega t - \delta) \tag{3.2}$$

where δ represents the lag between the stress and the strain, being an indicator of the material's damping capacity.

Equation 3.2 can be rewritten as:

$$\sigma(t) = \sigma_0 \sin(\omega t - \delta + \delta) = \sigma_0 \sin(\omega t - \delta)\cos(\delta) + \sigma_0 \cos(\omega t - \delta)\sin(\delta) \tag{3.3}$$

Substituting the terms $\sin(\omega t - \delta)$ and $\cos(\omega t - \delta)$ in Equation 3.3 with the terms in Equation 3.2 and their derivatives and assuming that the frequency ω is always positive, one can easily obtain the following:

$$\sigma(t) = \frac{\sigma_0}{\varepsilon_0}\varepsilon(t)\cos(\delta) + \frac{\sigma_0}{\omega\varepsilon_0}\frac{d\varepsilon(t)}{dt}\sin(\delta) \tag{3.4}$$

Naming the therm $\frac{\sigma_0}{\varepsilon_0}\cos(\delta)$ as the *extensional storage modulus*, E', one can obtain the constitutive relation of a viscoelastic material as:

$$\sigma(t) = E'\varepsilon(t) + \frac{E'}{\omega}\frac{d\varepsilon(t)}{dt}\tan(\delta) \tag{3.5}$$

For a shear strain $\gamma(t)$, Equation 3.5 is written as:

$$\tau(t) = G'\gamma(t) + \frac{G'}{\omega}\frac{d\gamma(t)}{dt}\tan(\delta) \tag{3.6}$$

where $\tau(t)$ represents the shear stress and G' represents the *shear storage modulus*. The term $\tan(\delta)$, present in both forms of the constitutive relation, is equivalent to the material's *loss factor*, currently represented by the Greek letter η.

3.3.1 The Complex Modulus

Generalizing the function representing the harmonic strain with a complex exponential $\varepsilon(t) = \varepsilon_0 e^{\jmath\omega t}$, Equation 3.5 can be written in the frequency domain as:

$$\sigma(\omega) = E'(\omega)\varepsilon(\omega) + \jmath E'(\omega)\eta(\omega)\varepsilon(\omega) = \bar{E}(\omega)\varepsilon(\omega) \tag{3.7}$$

where $\bar{E}(\omega)$ represents the *complex extensional modulus* of the material, which allows the simple representation of a material's viscoelastic effect in stationary harmonic regime.

The real component of the complex modulus, $E'(\omega)$, is called the storage modulus and represents the capability that the material has to storage elastic strain energy, while the imaginary component, given by the product between the storage modulus and the loss factor, $E''(\omega) = E'(\omega)\eta(\omega)$, is called the loss modulus and it is representative of the material's damping capacity [Moreira, 2004].

3.3.2 The Effects of Temperature and Frequency of Loading

The viscoelastic materials used for damping purposes may vary from high-stiffness plastics, used mainly in the FLD configuration, to low-storage modulus adhesives, used in the CLD and ILD configurations. Despite being homogeneous and isotropic, and presenting a linear behavior between certain levels of strain, their properties heavily depend on the temperature and on the frequency of the loading they are subjected. This dependence can be seen in Figure 3.6 for a viscoelastic material. In fact, the mechanical behavior of viscoelastic materials depends primarily on the behavior of their long reticulated molecular chains, which interact with each other according to the material's temperature and frequency at which the initial equilibrium configuration is changed.

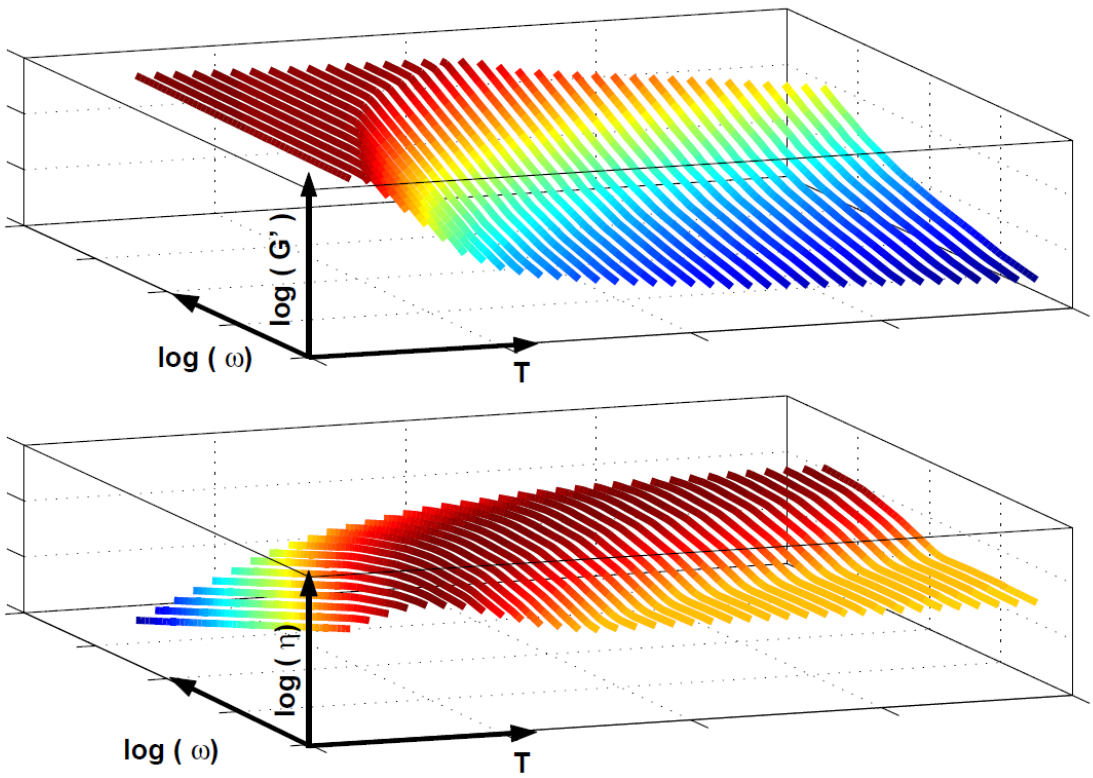

Figure 3.6: Storage modulus, G', and loss factor, η, of a viscoelastic material dependence with the temperature and the frequency of strain [Moreira, 2004].

3.3.2.1 The Effect of Temperature

The damping capacity and the stiffness of a viscoelastic material are directly related with its transition temperature, at which the material changes from its vitreous state, associated to high levels of stiffness, to a amorphous state, associated to low levels of stiffness and the lower damping capacity. Thus, the efficiency of the treatment strongly depends on the relation between the operating and transition temperatures.

According to Rao [2003], for a typical polymeric viscoelastic material, four regions can be identified, as presented in Figure 3.7. The first region corresponds to the glassy state, where the material has very large storage modulus, which changes slowly with the temperature increase, but very low damping capacity, which, on the other hand, presents significant increase with the temperature. The second region is the transition region, where the material changes from glassy state to a rubbery one, presenting a strong decrease of the storage modulus and an increase on the loss factor, and usually corresponds to the temperature range where the damping capacity peaks. In the rubbery state, both modulus and loss factor present low values and remain mostly constant with the increase of temperature. Finally, the flow region is typical for a few damping materials such as thermoplastics, where the material continues to soften (decrease of the storage modulus) and the loss factor increases, reaching very high values.

The working temperature of passive damping mechanisms based on viscoelastic materials can vary between -40 and $150°C$, depending on the application [Moreira, 2004]. When the application requires damping efficiency over a large temperature range (high temperature gradient), optimization techniques based on multi-layer and multi-material must be used, according to what was presented in Section 3.2.2.

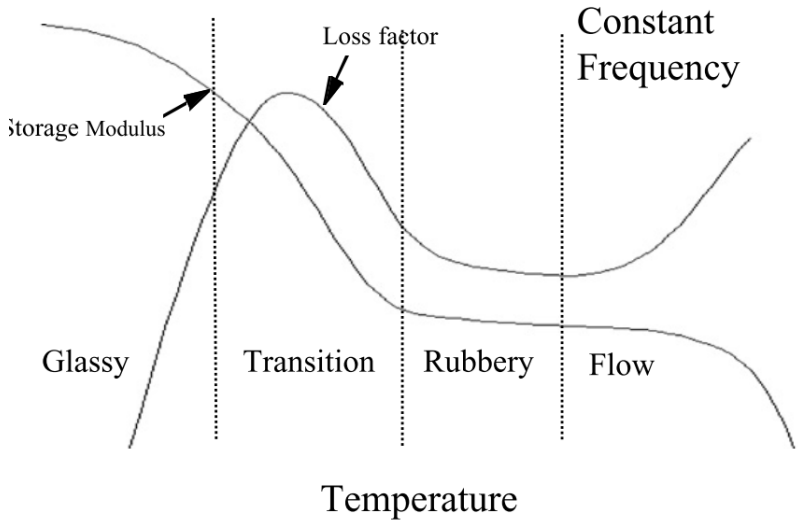

Figure 3.7: Variation of storage modulus and loss factor of a viscoelastic material with temperature [Rao, 2003].

3.3.2.2 The Effect of Frequency

When a viscoelastic material is deformed, its long and reticulated molecular chains suffer a perturbation relatively to their initial equilibrium position, inducing their interaction as a way to counteract the imposed strain field. This is achieved by rearranging of the molecular chains, leading to a new equilibrium position.

One can easily comprehend that for a cyclic harmonic strain the molecular chains tend to achieve a dynamic equilibrium, in line with the stimulus. Thus, when a viscoelastic material is cyclically loaded with a high frequency, it will present high stiffness, because the interaction between the molecular chains will be more important, while for a lower frequency the molecules will be allowed to move slower, leading to lower stiffness values.

3.3.2.3 Viscoelastic Material Selection

Knowing that the behavior of viscoelastic materials varies with temperature and loading frequency is a primary step at the design stage of a viscoelastic material for a given application. In fact, the loss factor peak should ideally correspond to the working temperature or extend itself along a wide range of temperatures, to ensure that the damping capacity is at their maximum. On the other hand, the frequency dependence must also be studied, so that the loss factor presents high values in the application range, therefore showing great damping capacity. Finally, the storage modulus must be high enough according to the needs of the application, so that the mechanical behavior of the whole structure does not present significant changes.

As can be easily concluded, the temperature and frequency dependences induce serious problems in the selection of the best viscoelastic material for a given application, so in the vast majority of cases, a balanced solution must be achieved.

3.4 Numerical Simulation of Viscoelastic Damping Treatments

The analysis of viscoelastic damping treatments started with an analytical approach of said damping mechanisms, namely when applied in beams. One of the first cases were the Oberst equations, presented by Oberst and Frankenfeld [1952], based on the hypothesis that the straight sections of a treated beam remain straight after deformation, that are still today a good tool to help on the characterization of viscoelastic materials using the FLD configuration in beams. Kerwin [1959] later presented an analytical model to determine the efficiency of viscoelastic damping treatments using the CLD configuration, restricted to the cases when the backing layer's thickness is much smaller than the host beam's thickness. The most important analytical model regarding the CLD configuration applied to beams are the *RKU equations*. These fourth order equations of motion were proposed by Ross et al. [1959] and were based on a set of simplification hypothesis, namely the imposition of sinusoidal mode shapes and the neglect of extensional shear of the viscoelastic layer. Bhimaraddi [1995] showed that the RKU model underestimates the loss factor value when the viscoelastic material presents high storage modulus [Moreira, 2004].

There are also some publications regarding the analytical modelling of viscoelastic treatments in plates, but in a much more reduced number. Yan and Dowell [1972] presented a fourth order differential equation to describe the dynamic behavior of sandwich plates and shells, assuming a constant distribution of the shear strain along the layers. Sadasiva Rao and Nakra [1974] developed a similar analytical model, but considering asymmetric geometries and the effects of rotational and translatory inertia. Given the interest in optimizing the viscoelastic damping mechanisms namely by applying partial treatments, due to the advantages presented in Section 3.2.2, some authors developed approximated analytical models based on the analysis of the deformation energy and on the consideration of the model shapes of the untreated geometry [Moreira, 2004].

The application field of viscoelastic damping treatments usually consists in three-dimensional complex structures. However, the analytical models previously presented only allow the analysis of plates and shells with simple geometries and well defined boundary conditions. Thus, analysis techniques based on numerical methods have been developed, which allow the determination of the treatments dynamic effects and efficiency for essentially any geometry and configuration. The most preponderant numerical method is the finite element method, mostly because of its important and great applicability in the structural engineering field, whereby there has been a strong development in such numerical methods that can efficiently simulate the behavior of viscoelastic damping treatments [Moreira, 2004].

Despite the simplicity associated with these damping mechanisms and applications, their correct design and simulation with the finite element method requires specially developed tools. The first main issue is the need to consider the frequency and temperature dependence of viscoelastic materials' constitutive properties. Secondly, since the damping treatments in continuous structures is materialized and simulated through discrete and distributed viscoelastic elements in the form of discrete layers, the correct and careful spacial discretization is required. Lastly, the selection of a convenient analysis method is also necessary, this being mainly influenced by the objectives of the simulation and the constitutive modelling used throughout the algorithm. It is common to find the first and last problems previously presented being associated or treated as one, not always presenting a clear distinction [Moreira, 2004].

However, that distinction will be made in the next subsections, where these three

questions will be addressed.

3.4.1 Viscoelastic Material Constitutive Modelling

There are some difficulties associated with the characterization of a viscoelastic material's damping capacity and with the consideration of its properties when using numerical simulation. In fact, in addition to their considerable loss factor, viscoelastic materials present different behaviors according to the working temperature and the frequency of the stimulus, as previously presented. Thus, the modelling of these materials must follow procedures that allow the right characterization of their viscoelastic damping and the consideration of the temperature and frequency dependencies.

For simplification reasons, the temperature dependence may be removed from the characterization and simulation process by considering isothermal conditions. Thus, although the working temperature vary in a large scale, leading to different behaviors, the consideration of discrete constant temperature levels simplifies significantly the modelling procedure. However, one must be aware of the errors committed when considering constant temperature regimes, because the damping mechanism associated with viscoelastic materials is more than a dynamic process, it is a thermodynamic process. In fact, one can easily comprehend that, because the damping capacity of these materials results from the dissipation of mechanical energy in the form of heat, the cyclic deformation process will result in the increase of the material's temperature if the energy is not properly dissipated to the exterior.

Even when considering the isothermal condition hypothesis, the definition of a reliable, accurate and cost-efficient constitutive model for viscoelastic materials is an open challenge for both experimental and numerical fields of research. While the experimental characterization procedure requires a simple yet representative constitutive model able to describe the material properties with a limited set of data parameters, a numerical simulation calls for a simple model able to be used in a standard manner inside a numerical algorithm [Moreira, 2014].

In this dissertation will only be presented the constitutive modelling approaches relevant to the finite element method implementation of said materials, namely the *complex modulus model* and the *ADF model*.

3.4.1.1 Complex Modulus Model

The complex modulus approach is a simple and accurate model, but requires the storage and direct use of long tabular data comprising the storage and loss modulus values defined or measured for a long set of frequencies. If there is information about the storage and loss modulus for frequency-temperature pairs, the superposition principles may be used to extrapolate and interpolate data.

Considering a generalized dynamic system with n degrees of freedom constituted by elastic and viscoelastic elements, its equation of motion in the time domain can be written as:

$$[M]\{\ddot{x}(t)\} + [C]\{\dot{x}(t)\} + \left[\bar{K}\right]\{x(t)\} = \{f(t)\} \tag{3.8}$$

where matrices $[M]$, $[C]$ and $\left[\bar{K}\right]$ represent, respectively, the mass, viscous damping and complex stiffness matrices of the dynamic system.

Complex stiffness matrix $\left[\bar{K}\right]$ can be subdivided into a real matrix, $[K_e]$, characterizing the elastic components, and a complex matrix, $\left[\bar{K}_v(\omega)\right]$, representing the viscoelastic components of the global stiffness. That is:

$$\left[\bar{K}\right] = [K_e] + \left[\bar{K}_v\right] \tag{3.9}$$

While the elastic stiffness matrix $[K_e]$ represents the stiffness of the purely elastic elements, is real and constant, the viscoelastic stiffness matrix $\left[\bar{K}_v(\omega)\right]$ is complex, dependent of the loading frequency and the temperature, if one does not consider isothermal conditions. Generalizing, the complex stiffness matrix presents terms associated with the extensional stiffness, that are related to the complex extensional modulus, $\bar{E}(\omega)$, and terms associated with the shear stiffness, related to the complex shear modulus, $\bar{G}(\omega)$, of said viscoelastic material.

Despite these two modulus not being exactly linearly proportional, due to the Poisson's coefficient, ν, is also frequency dependent and because the extensional and shear loss factors are not exactly identical, it is assumed that there is a proportional relation between their storage components, given by:

$$G'(\omega) = \frac{E'(\omega)}{2\,(1+\nu)} \tag{3.10}$$

which makes it possible to decompose the complex viscoelastic stiffness matrix on:

$$\left[\bar{K}_v\right] = \bar{G}\,(\omega)\,[K_v] \tag{3.11}$$

where $\bar{G}\,(\omega)$ represents the complex shear modulus, a frequency dependent parameter, and $[K_v]$ represents the factorized viscoelastic stiffness matrix, composed only by real and constant terms and obtained for a unitary shear modulus.

Considering a stationary harmonic motion, where both the excitation and the response are also harmonic functions, $\{f(t)\} = \{F(\omega)\}\,e^{\jmath\omega t}$ and $\{x(t)\} = \left\{\bar{X}(\omega)\right\}e^{\jmath\omega t}$, respectively, one can easily rewrite Equation 3.8 in the frequency domain as:

$$\left(-\omega^2\,[M] + \jmath\omega\,[C] + \left([K_e] + \bar{G}(\omega)\,[K_v]\right)\right)\left\{\bar{X}(\omega)\right\} = \{F(\omega)\} \tag{3.12}$$

The complex modulus model is often associated with the direct frequency analysis, in which the system presented by Equation 3.12 is solved for discrete values of frequency, or with the iterative process of complex modal analysis, obtaining the complex eigenvalues and eigenvectors and updating the values of the viscoelastic material properties for each natural frequency.

3.4.1.2 ADF Model

The anelastic displacement field (ADF) model represents the complex module of a viscoelastic material as a series of terms such as:

$$G(\omega) = G_0\left(1 + \sum_{i=1}^{n_{ADF}} \Delta_i \frac{\omega^2 + \jmath\omega\Omega_i}{\omega^2 + \Omega_i^2}\right) = G_0\left(1 + \sum_{i=1}^{n_{ADF}} \Delta_i \frac{\omega^2}{\omega - \jmath\Omega_i}\right) \tag{3.13}$$

where G^0 represents the low frequency shear storage modulus, as in the GHM model, and Δ_i and Ω_i are model parameters named, respectively, the relaxation resistance and the inverse of the characteristic relaxation time for a constant deformation regime. These model parameters represent the viscoelastic material's behavior with the frequency variation and are also obtained by a curve-fitting process with the experimental values.

The hypothesis behind the ADF model is that the displacement field can be divided in two components: the elastic component, $\{x(t)\}^E$, instantly proportional to the imposed

loads, and the anelastic component, $\{x(t)\}^A$, non-instantly proportional to the stress field, that is:

$$\{x(t)\} = \{x(t)\}^E + \{x(t)\}^A \tag{3.14}$$

3.4.2 Viscoelastic Damping Treatment Spatial Modelling

As one should know, the structure's domain spatial discretization in regular and uniform sub-domains, called the finite elements, is the base of the finite element method. When simulating viscoelastic damping treatments, the approach of this discretization problem will vary with the configuration of said treatments.

The spacial modelling of FLD configurations is relatively simple because the concerned damping mechanism is based on the storage and dissipation of extensional deformation energy by the viscoelastic layer, as a result of its extensional and flexural strain. In this case, the use of beam or plate elements based on the classic theory of laminates allows the correct representation of the induced strain field [Moreira, 2004].

However, the spacial modelling of CLD and ILD configurations requires a correct representation of the high shear strains induced in the viscoelastic layer developed by the restrictive action of the elastic backing layer, which is the most preponderant effect behind their high efficiency damping capacity. The classic theory of laminates is not adequate to represent the shear strain, therefore the use of a different spatial modelling technique is required, namely the *combined models* and the *discrete layer models* [Moreira, 2014].

Regardless the model used in the spatial modelling of viscoelastic damping treatments, the mesh must be sufficiently refined to be able to correctly represent the natural vibration modes of the structure, within the studied frequency range [Moreira, 2004].

3.4.2.1 Combined Models

Combined (or layered) models are commonly applied in commercial finite element method software and use a spatial model obtained as a stratified scheme of standard finite elements, such as beams, plates or hexahedral elements, therefore modelling each layer individually and allowing good results because of the correct description of the shear strains developed in the viscoelastic layer.

There can be identified four different modelling approaches using a layered combination of standard finite elements, namely the *beam-plate model*, the *brick-plate model with rigid link*, the *brick-plate model with offset* and the *layered brick model*.

The first one, the beam-plate model presented in Figure 3.8 and proposed by Killian and Lu [1984], is the simpler combined model and it uses a combination of two plate elements, representative of the two exterior elastic layers, and four beam elements representative of the damping layer, which flexural stiffness must be related to the viscoelastic material's stiffness and which degrees of freedom correspond to the ones of the adjacent plates. This model is not commonly used mostly because of its difficult and time-consuming modelling process, and the required definition of equivalent beams' properties in such way that they correctly simulate the viscoelastic material's extensional and shear stiffness.

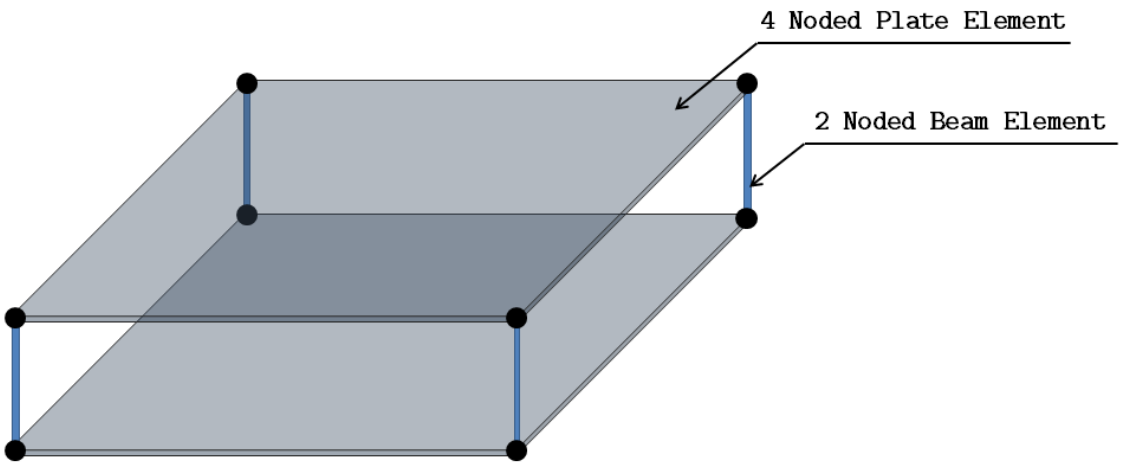

Figure 3.8: Schematic representation of the beam-plate model.

The brick-plate model with rigid link, presented in Figure 3.9, uses two plate elements, representative of the two exterior elastic layers, and one hexahedral/brick finite element with eight nodes, representative of the viscoelastic layer. Despite correctly representing the spatial distribution of the layers, this model requires the modelling of three different layers of elements and, consequently, four layers of nodes. Additionally, the establishment and implementation of rigid link connections (RBEs) to interconnect the degrees of freedom of the adjacent nodes. Furthermore, this model allows the correct representation of curved structures and is the only one that can simulate the detachment of layers by simply manipulating the RBEs.

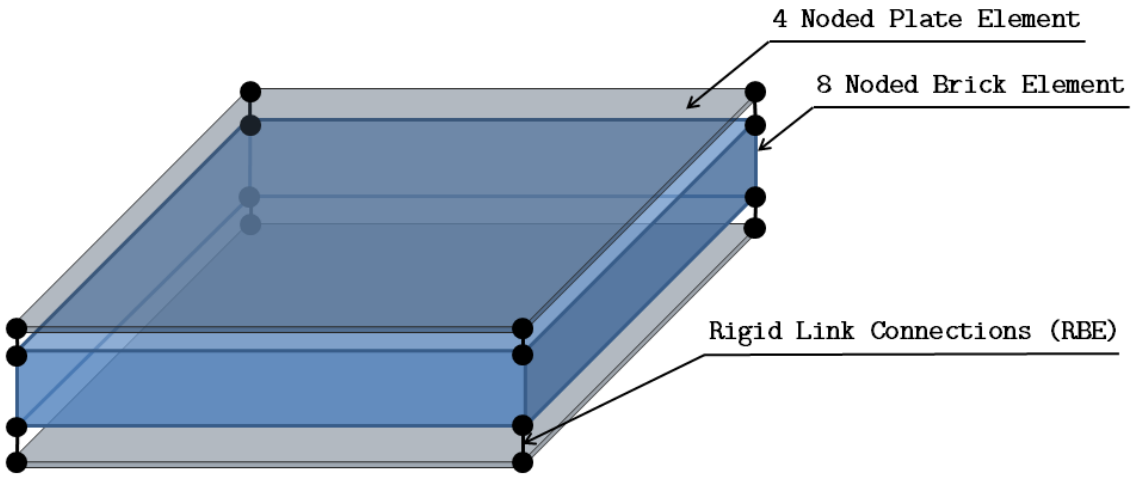

Figure 3.9: Schematic representation of the brick-plate model with rigid links.

The brick-plate model with offset, presented in Figure 3.10 and proposed by Johnson and Kienholz [1982], is very similar to the model presented previously, the main difference being that the plate finite elements share the nodal positions of the solid heaxahedral element, representing the viscoelastic layer, thus avoiding the generation of the rigid link connections. In return, in order to coincide all the nodal positions, it is necessary to introduce an offset in the nodal positions of the plate elements, corresponding to one-half of their thickness. Despite not being recommended the use of this model with curved structures, it requires less modelling work and leads to less sparse matrices.

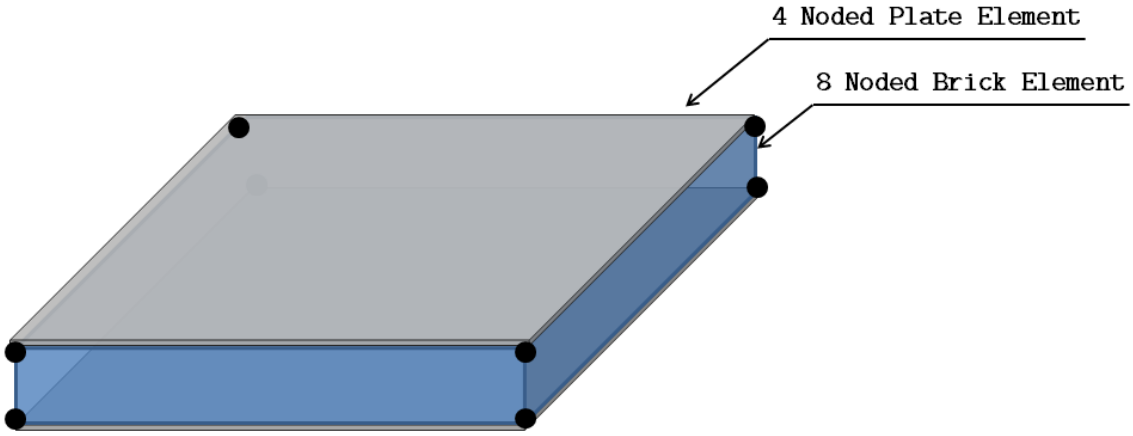

Figure 3.10: Schematic representation of the brick-plate model with offset.

The last combined model, the layered brick model presented in Figure 3.11, uses three overlapping hexahedral finite elements, one for each layer. Despite this model's spatial modelling simplicity and readiness, its use requires special attention in the finite element formulation to avoid numerical issues, as shear locking, due to the aspect ratio (ratio between the major and minor dimensions of the element) of the elastic outer layers [Moreira, 2014]. In fact, the shear locking problem in the elastic layers occurs for aspect ratios higher than 5:1 when using full, or uniform, integration, while this limit rises up to 100:1 when dealing with reduced integration. For the brick elements representing the viscoelastic layers, this limit rises up to 5000:1, which means that even for very thick layers the shear locking effects do not affect significantly the structure's global stiffness matrix [Moreira, 2004].

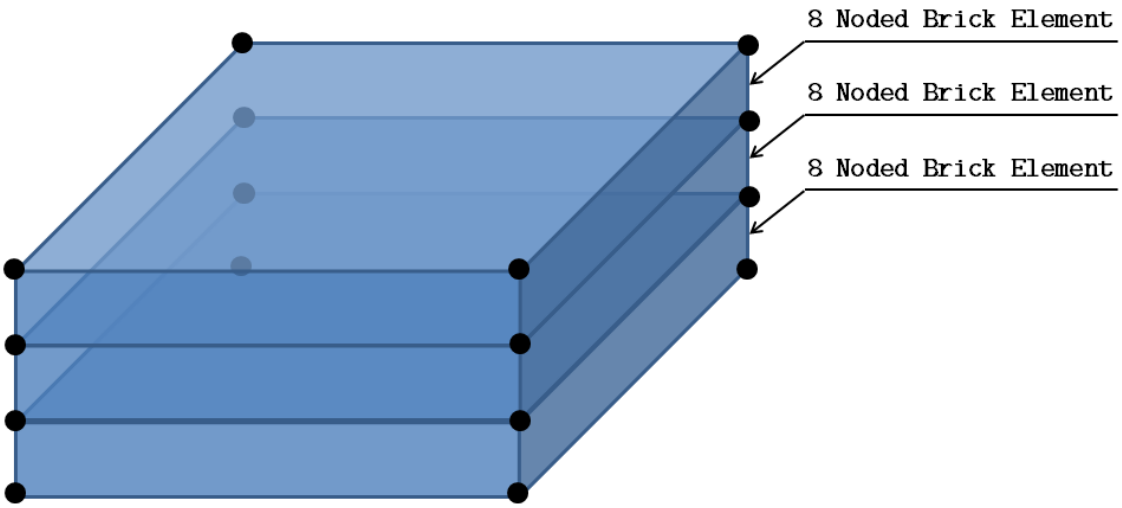

Figure 3.11: Schematic representation of the layered brick model.

3.4.2.2 Discrete Layer Models

The discrete layer models (Figure 3.12) rely on a layerwise plate finite element theory, allowing a much more easier spatial modelling of the mesh, since it becomes possible to use a bi-dimensional mesh generator, and an easier optimization procedure, since the

redefinition of the structure's geometric and constitutive parameters is faster. In this modelling technique, each layer is individually defined by a Mindlin or other first-order shear plate formulation, and the kinematic interdependency between layers is imposed in the definition of each displacement field. Mixed formulations ca also be employed to additionally impose the continuity of stresses at the layers' interfaces [Moreira, 2004, 2014].

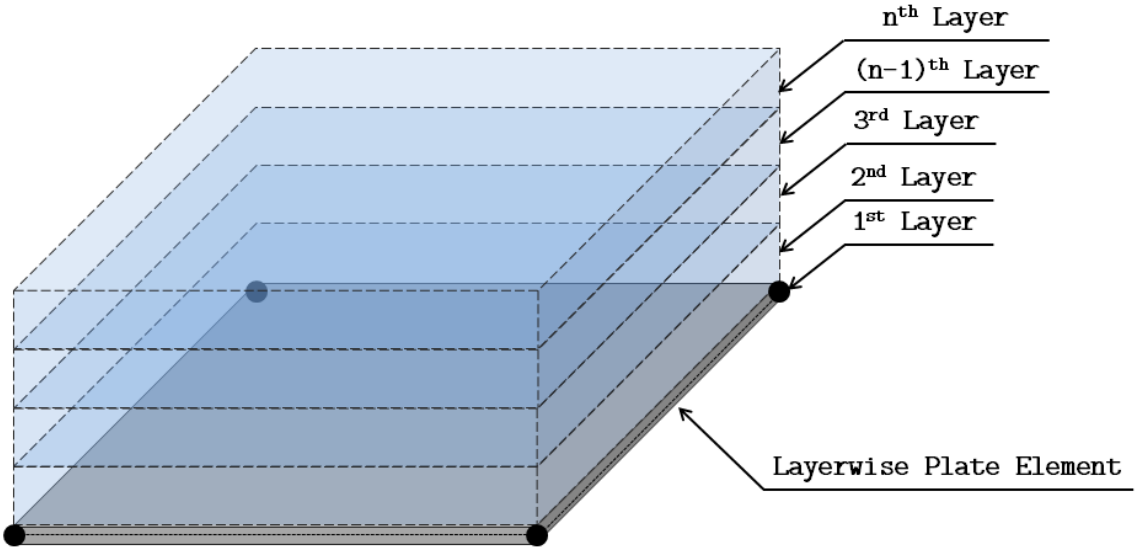

Figure 3.12: Schematic representation of a layerwise discrete layer model.

The layerwise plate finite element formulation will be addressed better later in this dissertation, in Chapter 4.

3.4.3 Viscoelastic Damping Treatments Analysis Methods

As said before, the analysis methods of viscoelastic damping treatments not only depend on the desired solution domain but also on the selected constitutive model, in such a way that in the majority of publications regarding this subject are not dissociated. Although, their differentiation is patent in this dissertation.

Hereinafter, the analysis methods relevant for this dissertation will be presented, namely the *direct frequency analysis*, the *numerical integration in the time domain*, the *complex modes analysis* and the *modal strain energy method*.

3.4.3.1 Direct Frequency Analysis

Considering a harmonic stationary vibration, the complex modulus constitutive modelling of the viscoelastic material can be directly used to develop a direct frequency analysis (DFA), by updating the material's properties for each considered frequency value. Considering isothermal conditions, the characteristic equation of motion of a system with only viscoelastic damping can be written as:

$$[M]\{\ddot{x}(t)\} + \left[\bar{K}(\omega)\right]\{x(t)\} = \{f(t)\} \tag{3.15}$$

where $[M]$ and $\left[\bar{K}(\omega)\right]$ represent the mass and complex stiffness matrices, respectively.

Assuming the following expression as the harmonic excitation applied to the system:

$$\{f(t)\} = \{F(\omega)\}\, e^{\jmath\omega t} \tag{3.16}$$

the stationary response will also be a harmonic function, with the same frequency but with a relative lag δ, that is:

$$\{x(t)\} = \{X(\omega)\}\, e^{\jmath\omega-\delta} = \left\{\bar{X}(\omega)\right\} e^{\jmath\omega t} \tag{3.17}$$

Substituting Equation 3.17 and its derivative in Equation 3.15, it is possible to define an algebraic equations system as:

$$\left(\left[\bar{K}(\omega)\right] - \omega^2\,[M]\right)\left\{\bar{X}(\omega)\right\} = [\mathcal{Z}(\omega)]\left\{\bar{X}(\omega)\right\} = \{F(\omega)\} \tag{3.18}$$

where $[\mathcal{Z}(\omega)]$ represents the dynamic stiffness matrix. Solving said equation system, it is possible to determine the complex vector $\left\{\bar{X}(\omega)\right\}$, which is dependent on the frequency ω and the system's parameters.

The frequency response functions (FRF) are arranged in the receptance matrix $[\alpha(\omega)]$, which corresponds to the inverse matrix of the dynamic stiffness matrix, and where a column l represents the complex response vector for an excitation applied only in the l degree of freedom, and can be obtained through the expression:

$$\alpha_{jl}(\omega) = \left(\frac{\bar{X}_j(\omega)}{F_l}\right)_{F_i=\begin{cases}0,\ i=1,...,n\\ 1,\ i\neq l\end{cases}} \tag{3.19}$$

where $\bar{X}_j(\omega)$ represents the response's amplitude and lag for the degree of freedom j resulting for the excitation F_l applied in the degree of freedom l. This FRF vector can be directly obtained through the resolution of the following equations system:

$$[\mathcal{Z}(\omega)]\left\{\bar{X}(\omega)\right\}_l = \{F_l(\omega)\} \tag{3.20}$$

where, according to what was presented before, $\{F_l(\omega)\}$ is a vector with only one non-null component, corresponding to the degree of freedom l.

The direct frequency analysis of a system with viscoelastic damping treatment can be obtained by means of a cyclic process presented on Figure 3.13 over the desired frequency range. As said before, the viscoelastic constitutive properties are introduced in this analysis method by means of the material's complex modulus, which allows the update of its properties for each frequency evaluated, thus representing that dependence.

The main disadvantage of this analysis method is its high computational cost and time consumption, once it needs to solve a complex linear equation system, with the dimension of the global problem for each frequency value evaluated. Furthermore, one can not obtain directly the system's modal parameters, namely its natural frequencies and modal loss factors, using the DFA. In fact, it is necessary to obtain the modal model of the system, that can be generated by modal identification techniques.

3.4.3.2 Numerical Integration in the Time Domain

Parametric constitutive models described in the time domain, like the GHM and ADF, can be introduced in the equation of motion written in the time domain, like Equation 3.15 for a system with only viscoelastic damping, an then reorganize it to allow a straightforward resolution by using a numerical integration method, like the Newmark and Wilson-θ algorithms. These direct numerical integration methods are based on the following assumptions:

1. The equation of motion is only verified for discrete time instants separated by regular intervals Δt;

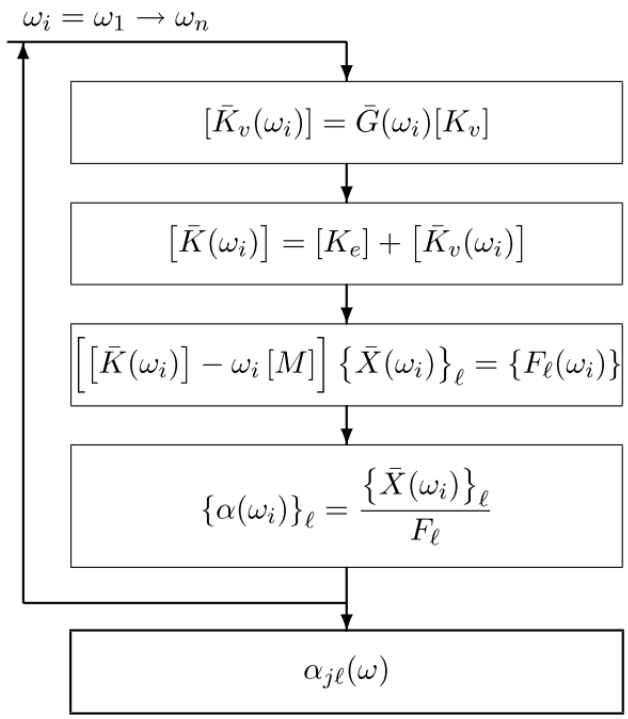

Figure 3.13: Representation of the cyclic process of DFA analysis of viscoelastic treatments [Moreira, 2004].

2. A variation law for the acceleration, velocity or displacement for the intervals Δt is allowed.

It is also necessary to consider some initial conditions of velocity and displacement, $\{\dot{x}(0)\}$ and $\{x(0)\}$ respectively. Then, the solution is obtained for each time instant.

3.4.3.3 Complex Eigensolution Analysis

Assuming a free response model of a dynamic system with viscoelastic damping, its complex eigenvalue problem is described by:

$$\left[\bar{K}(\omega)\right]\left\{\bar{\phi}\right\}_r = \bar{\lambda}^2\,[M]\left\{\bar{\phi}\right\}_r \tag{3.21}$$

where $\left[\bar{K}(\omega)\right]$ and $[M]$ represent, respectively, the complex stiffness and mass matrices of the system.

If constant properties of the viscoelastic material are assumed within the evaluated frequency range, then the solution of Equation 3.21 can be described by a complex eigenvector matrix, $\left[\bar{\Phi}\right]$, and a complex diagonal eigenvalue matrix, $\left[\bar{\Lambda}\right]$:

$$\left[\bar{\Phi}\right] = \left[\left\{\bar{\phi}\right\}_1 |...| \left\{\bar{\phi}\right\}_n\right] \tag{3.22a}$$

$$\left[\bar{\Lambda}\right] = \begin{bmatrix} \bar{\lambda}_1^2 & & \\ & \ddots & \\ & & \bar{\lambda}_n^2 \end{bmatrix} \tag{3.22b}$$

Each eigenvector, $\left\{\bar{\phi}\right\}_r$, is defined by a real component, $\{\phi_R\}_r$ and an imaginary component, $\{\phi_I\}_r$. For instance, the eigenvalues, $\bar{\lambda}_r^2$, are also defined by a real component,

which represents the square of the damped system's natural frequency, ω_r^2, and by an imaginary component, which represents the modal loss factor, η_r, as:

$$\bar{\lambda}_r^2 = \omega_r^2 \left(1 + \jmath \eta_r\right) \tag{3.23}$$

After some mathematical manipulation of Equation 3.21, one can obtain the following relation:

$$\bar{\lambda}_r = \frac{\left\{\bar{\phi}\right\}_r^T \left[\bar{K}\right] \left\{\bar{\phi}\right\}_r}{\left\{\bar{\phi}\right\}_r^T \left[M\right] \left\{\bar{\phi}\right\}_r} \tag{3.24}$$

which can be formally identical to the Rayleigh's quotient of a non-damped system.

Considering a symmetric complex stiffness matrix, the modal loss factor, η_r, can be obtained through:

$$\eta_r = \frac{\left\{\bar{\phi}\right\}_r^T \left[K_{\Im}\right] \left\{\bar{\phi}\right\}_r}{\left\{\bar{\phi}\right\}_r^T \left[K_{\Re}\right] \left\{\bar{\phi}\right\}_r} \tag{3.25}$$

where $[K_I]$ and $[K_R]$ represent the imaginary and the real components of the global stiffness matrix, respectively, that is, $[K_I] = \Im\left(\left[\bar{K}\right]\right)$ and $[K_R] = \Re\left(\left[\bar{K}\right]\right)$.

One can easily identify from Equation 3.25 that the loss factor physically represents the ratio between the dissipated energy, which is proportional to the imaginary component of the complex stiffness matrix, and the stored deformation energy, which is proportional to the real component of the complex stiffness matrix.

Note that, as said initially, this method assumes that both storage modulus and loss factor remain constant within the frequency range evaluated, which does not meet the real behavior of a viscoelastic material. To overcome this problem, one can consider that the viscoelastic material's properties remain constant not within all the range but only in the neighborhood of each natural vibration frequency, which leads to an iterative procedure of resolution of the eigenvalue problem for each evaluated mode, updating the complex stiffness matrix with the constitutive characteristics for the correspondent frequency. This allows obtaining more realistic loss factor values, but becomes a more time-consuming process.

3.4.3.4 Modal Strain Energy Method

The modal strain energy (MSE) method, proposed by Johnson and Kienholz [1982], is based in the hypothesis that the eigenvalues and eigenvectors of the undamped system are representative of the damped system. That is, the solutions of the real eigenproblem:

$$\left[K_R\left(\omega_r\right)\right] \left\{\phi\right\}_r = \omega_r^2 \left[M\right] \left\{\phi\right\}_r \tag{3.26}$$

can be used as the solutions of the complex problem, which means that, using the physical definition of loss factor as the ratio between the dissipated and stored energies (Equation 3.25), it is possible to determine an approximate value for each modal loss factor, $\tilde{\eta}_r$, as:

$$\tilde{\eta}_r = \frac{\left\{\bar{\phi}\right\}_r^T \left[K_{\Im}\right] \left\{\bar{\phi}\right\}_r}{\left\{\bar{\phi}\right\}_r^T \left[K_{\Re}\right] \left\{\bar{\phi}\right\}_r} \tag{3.27}$$

Equation 3.27 can be rewritten directly in an energy formulation, through the expression:

$$\tilde{\eta}_r = \frac{\sum_{k=1}^{n} \eta_{k_r} \Pi_{k_r}}{\sum_{k=1}^{n} \Pi_{k_r}} \tag{3.28}$$

where η_{k_r} and Π_{k_r} represent, respectively, the modal loss factor of each layer k and the correspondent deformation energy for the rth natural vibration mode. It is in this way that the MSE method is used with the finite element method, where the sum of the energy fractions is performed for each element.

Despite only determine approximated values, this is a very simple, prompt and low time-consuming method to evaluate the damping levels reached with different configurations of the viscoelastic treatments, and to study the influence of the different system's parameters.

However, it must be noticed that the MSE method is only valid for systems where the damping levels are low, since for strongly damped systems, associated with very close natural frequency values and, consequently, coupled natural vibration modes, the error between the approximated loss factor and its real value is significant. In fact, small superficial viscoelastic damping treatments do not modify significantly the host structure's natural frequencies, but the introduction of meaningly thicker and bigger layers may induce important stiffness and mass distribution modifications, which lead to a necessary previous evaluation of these changes before the application of the MSE method.

Hu et al. [1995] proposed a modified MSE method that introduces the stiffness imaginary component contribution in the eigenproblem as:

$$\left([K_r] + \Psi\,[I]\right) \left\{\tilde{\phi}\right\}_r = \tilde{\omega}_r^2 \left(1 + \Psi \tilde{\eta}_r\right) [M] \left\{\tilde{\phi}\right\}_r \tag{3.29}$$

where Ψ parameter is a real constant defined as the ratio between the sum of the global stiffness matrix imaginary component's eigenvalues, λ_{I_r}, and the sum of the real component's eigenvalues, λ_{R_r}:

$$\Psi = \frac{\sum_{r=1}^{n} \lambda_{I_r}}{\sum_{r=1}^{n} \lambda_{R_r}} \tag{3.30}$$

The approximated loss factor is obtained through:

$$\tilde{\eta}_r = \frac{\left\{\tilde{\phi}\right\}_r^T [K_{\Im}] \left\{\tilde{\phi}\right\}_r}{\left\{\tilde{\phi}\right\}_r^T [K_{\Re}] \left\{\tilde{\phi}\right\}_r} \tag{3.31}$$

This modification of the MSE method results on an iterative process that allows a better approximation to the loss factor for systems with higher levels of damping.

Iterative Modal Strain Energy Method

The original MSE method can, however, be also applied under an iterative approach where the stiffness matrix is updated with the new corrected complex stiffness of the calculated mode, originating the *Iterative Modal Strain Energy Method (IMSE)*. In general, this procedure allows to obtain more realistic values of the modal loss factors and natural frequencies with the drawback of requiring more processing time [Vasques et al., 2010b].

Following this line of thought, a modification to the original MSE algorithm is proposed in order to introduce the stiffness changes of the structural damped system through an iterative procedure which more appropriately considers the effects of the variation of the storage and loss moduli with the frequency. An iterative calculation of the real (undamped) eigensolution is performed using the continuously iteratively updated real part of the stiffness matrix, which is done according to the viscoelastic material properties at the value of frequency of the current iteration within the vicinity of the natural mode being considered. Once the convergence of the undamped natural frequency of the natural mode under analysis is verified, the correspondent modal loss factor is determined by means of the same methodology used in the original MSE method, present in Equation 3.27, but using the correspondent imaginary part of the stiffness matrix defined at the converged value of frequency. This iterative process is presented in Figure 3.14 [Vasques et al., 2010b].

IMSE algorithm

Step 1. Eigensolution with $\omega = \omega^0$

$$\mathrm{Re}[\mathbf{K}(\mathrm{j}\omega^0)]\boldsymbol{\phi}_r = (\omega_r^0)^2\mathbf{M}\boldsymbol{\phi}_r$$

Step 2. Loop for each eigenpair $\left(\omega_r^0, \boldsymbol{\phi}_r\right)$ with $r = 1, \ldots, p$

i. Initial value

$$\omega_r^i = \omega_r^0$$

ii. Iterative loop for each natural frequency and mode shape

- Eigensolution $\left(\omega_s^0, \phi_s\right)$ with $s = 1, \ldots, r$

$$\mathrm{Re}[\mathbf{K}(\mathrm{j}\omega_r^i)]\boldsymbol{\phi}_s = (\omega_s^{i+1})^2\mathbf{M}\boldsymbol{\phi}_s$$

- Iterated natural frequency

$$\begin{cases} \omega_s^{i+1} : \text{rejected}, & \text{for } s < r \\ \omega_r^{i+1} = \sqrt{(\omega_s^{i+1})^2}, & \text{for } s = r \end{cases}$$

- Convergence condition test

$$\Delta_\omega = \frac{\left|\omega_r^{i+1} - \omega_r^i\right|}{\omega_r^{i+1}} \leq \Delta_{\max}$$

iii. Modal loss factor

$$\eta_r = \frac{\boldsymbol{\phi}_r^{\mathrm{T}}\,\mathrm{Im}[\mathbf{K}(\mathrm{j}\omega_r^{i+1})]\boldsymbol{\phi}_r}{\boldsymbol{\phi}_r^{\mathrm{T}}\,\mathrm{Re}[\mathbf{K}(\mathrm{j}\omega_r^{i+1})]\boldsymbol{\phi}_r}$$

Figure 3.14: Iterative modal strain energy method (IMSE) algorithm [Vasques et al., 2010b].

Chapter 4

Layerwise Finite Element Formulation

The present chapter addresses some issues regarding the theoretical foundations of the layerwise model. Initially, it will be presented the thick plate deformation theory (the Reissner-Mindlin theory), on which the layerwise theory is based. Next, the theory of deformation by layers, one of the bases of the layerwise model, is studied, namely the resultant definition of the displacement, strain and stress fields, as well as the potential and kinetic energies. Then, the formulation of a layerwise plate finite element is addressed. Finally, some improvement mechanisms to the basic formulation are presented to avoid the shear locking effects. For further information regarding these subjects, one can consult the references used throughout this chapter, specifically Moreira [2004], Moreira et al. [2006], Oñate [2013] and Arab et al. [2017].

4.1 Introduction

Viscoelastic damping treatments' efficiency is mostly related to the high shear strain imposed in the viscoelastic layer, from what one can conclude that the correct numerical simulation of their dynamic behavior is dependent of a correct representation of said shear strains and of the resulting strain energy.

As was presented in Section 3.4.2, the spatial modelling of viscoelastic damping treatments can be made through combined (or layered) models or discrete layer models, which rely on a layerwise plate finite element theory. These last models overcome the first ones for situations where the thickness of the viscoelastic material is relatively small, which generally correspond to the passive damping dynamic control of light structures, since its application to complex geometries is easier and the spatial modelling requires less processing time. However, most of the proposed layerwise models are developed according to a set of simplifying assumptions that restrict their applicability to cases that differ from the ones that they were formulated for. Thus, it is important to formulate and validate a finite element based on the layerwise theory that respects the following requirements:

1. Do not consider any simplifying assumptions regarding the structure or the laminate material distribution;
2. Consider all kinds of strains in each layer, except the normal strain along the thickness;
3. Consider protection mechanisms in finite element against numerical locking, namely shear locking;
4. Allow the usage of the element in a flat facet shell system configuration.

Plates and shells are particular forms of three-dimensional solids in which the thickness, h, is much smaller than the other two dimensions. The application of three-dimensional models to simulate these solids usually leads to time-consuming algorithms and not so efficient programs. So, bi-dimensional finite elements were developed to be used with plates, namely the *Kirchhoff-Love plate theory* and the *Reissner-Mindlin plate theory*.

The plate theory proposed by Kirchhoff-Love (Figure 4.1) allows the appropriate kinematic characterization of thin plates subjected to flexural solicitations, using interpolative functions with $\mathbf{C^1}$ continuity and is based on the following assumptions: [Oñate, 2013]

- The points in the middle plane of the plate ($z = 0$) only move vertically ($u(z = 0) = v(z = 0) = 0$);
- The points along a normal to the middle plane have the same vertical displacement, which means that the plate's thickness does not change;
- The normal stress, σ_z, is negligible, which corresponds to plane stress assumptions;
- A straight line normal to the undeformed middle plane remains straight and normal to the deformed middle plane, which corresponds to a normal orthogonality condition.

On the other hand, the plate theory proposed by Reissner-Mindlin (Figure 4.2), in which the thick plate theory is based on, only requires interpolation functions with $\mathbf{C^0}$ continuity, which means that is only necessary to guarantee the continuity of the variables that define the kinematic behavior between elements and not their derivatives, and is based in the following assumptions: [Oñate, 2013]

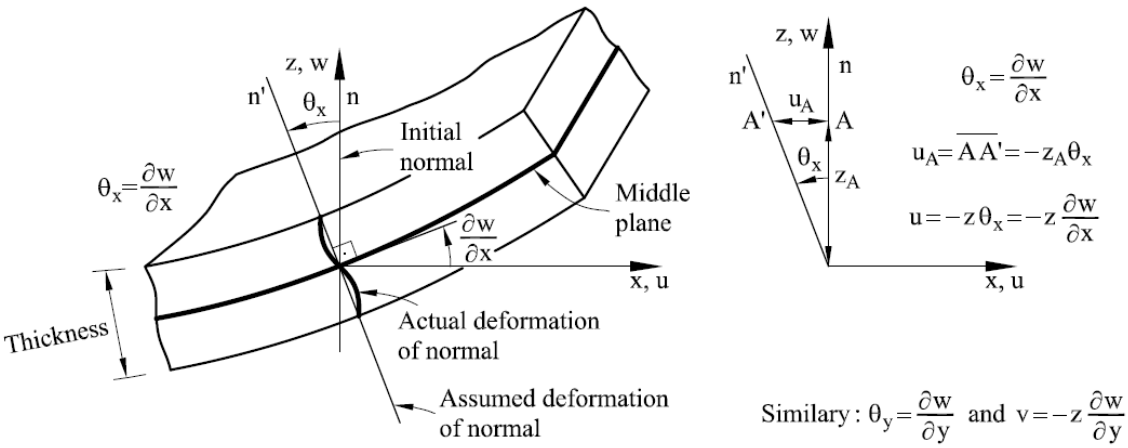

Figure 4.1: Schematic representation of a straight normal line deformation according to the Kirchhoff-Love plate theory [Oñate, 2013].

- The points in the middle plane of the plate ($z = 0$) only move vertically ($u(z = 0) = v(z = 0) = 0$);
- The points along a normal to the middle plane have the same vertical displacement, which means that the plate's thickness does not change;
- The normal stress, σ_z, is negligible, which corresponds to plane stress assumptions;
- A straight line normal to the undeformed middle plane remains straight but not necessarily orthogonal to the deformed middle plane.

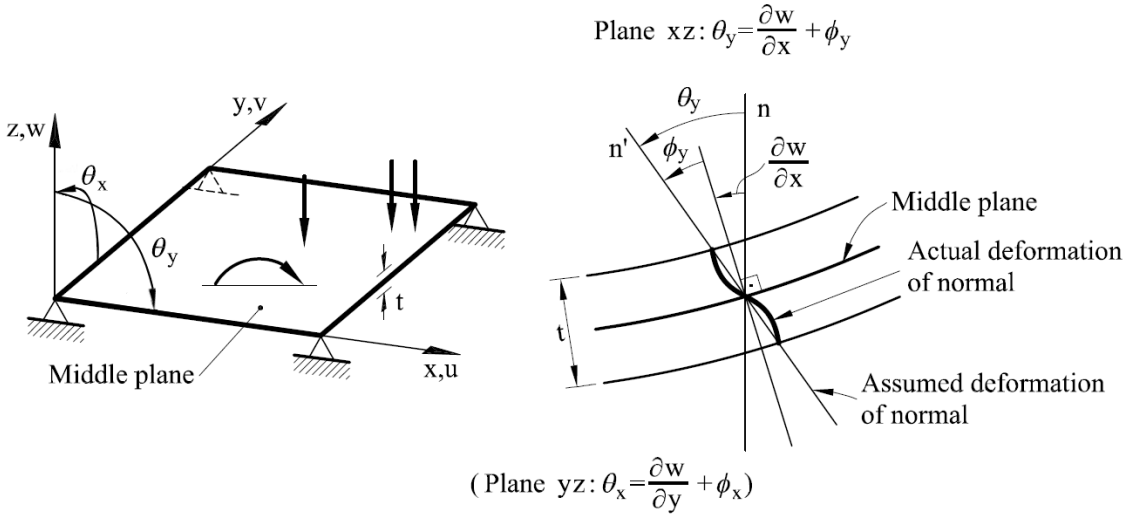

Figure 4.2: Schematic representation of a straight normal line deformation according to the Reissner-Mindlin plate theory and of the sign convention used [Oñate, 2013].

Regarding its interest to this dissertation, only the Reissner-Minldin plate theory will be studied and presented in the next Section.

4.2 Reissner-Mindlin Plate Theory

One can easily comprehend, from Figure 4.2, that the three-dimensional displacement field, according to the thick plate theory, is defined using three variables, namely the vertical displacement, w, and the two orthogonal rotations, θ_x and θ_y, as:

$$\begin{aligned} u(x,y,z) &= z\theta_y(x,y) \\ v(x,y,z) &= -z\theta_x(x,y) \\ w(x,y,z) &= w(x,y) \end{aligned} \tag{4.1}$$

where θ_x and θ_y represent the rotations according to the x and y direction, respectively, as presented in Figure 4.2, which can be interpreted as the rotations of the straight line representing the "average" deformation of the normal, and not the real deformed one, because it gets distorted.

4.2.1 Strain and Stress Fields

From substituting the previously presented displacement field into the expressions for the strains in a three-dimensional solid, and considering the assumptions of the Reissner-Mindlin plate theory, one simply gets the strain field as:

$$\begin{aligned} \varepsilon_{xx} &= \frac{\partial u}{\partial x} = z\frac{\partial \theta_y}{\partial x} \\ \varepsilon_{yy} &= \frac{\partial v}{\partial y} = -z\frac{\partial \theta_x}{\partial y} \\ \varepsilon_{zz} &= \frac{\partial w}{\partial z} = 0 \\ \gamma_{xy} &= \frac{\partial u}{\partial y} + \frac{\partial v}{\partial x} = z\left(\frac{\partial \theta_y}{\partial y} - \frac{\partial \theta_x}{\partial x}\right) \\ \gamma_{xz} &= \frac{\partial u}{\partial z} + \frac{\partial w}{\partial x} = \theta_y + \frac{\partial w}{\partial x} \\ \gamma_{yz} &= \frac{\partial v}{\partial z} + \frac{\partial w}{\partial y} = -\theta_x + \frac{\partial w}{\partial y} \end{aligned} \tag{4.2}$$

The strain vector containing the significant strains is, therefore:

$$\{\varepsilon\} = \left\{ \begin{array}{c} \varepsilon_{xx} \\ \varepsilon_{yy} \\ \gamma_{xy} \\ \cdots\cdots \\ \gamma_{xz} \\ \gamma_{yz} \end{array} \right\} = \left\{ \begin{array}{c} z\dfrac{\partial \theta_y}{\partial x} \\ -z\dfrac{\partial \theta_x}{\partial y} \\ z\left(\dfrac{\partial \theta_y}{\partial y} - \dfrac{\partial \theta_x}{\partial x}\right) \\ \cdots\cdots \\ \theta_y + \dfrac{\partial w}{\partial x} \\ -\theta_x + \dfrac{\partial w}{\partial y} \end{array} \right\} = \left\{ \begin{array}{c} \{\varepsilon_b\} \\ \cdots\cdots \\ \{\varepsilon_s\} \end{array} \right\} \tag{4.3}$$

where $\{\varepsilon_b\}$ and $\{\varepsilon_s\}$ contain the bending and the shear strains, respectively. For instance, this strain vector can be expressed as:

$$\{\varepsilon\} = \begin{bmatrix} z & 0 & 0 & 0 & 0 \\ 0 & -z & 0 & 0 & 0 \\ 0 & 0 & z & 0 & 0 \\ 0 & 0 & 0 & 1 & 0 \\ 0 & 0 & 0 & 0 & 1 \end{bmatrix} \left\{ \begin{array}{c} \dfrac{\partial \theta_y}{\partial x} \\ \dfrac{\partial \theta_x}{\partial y} \\ \left(\dfrac{\partial \theta_y}{\partial y} - \dfrac{\partial \theta_x}{\partial x} \right) \\ \cdots\cdots \\ \theta_y + \dfrac{\partial w}{\partial x} \\ -\theta_x + \dfrac{\partial w}{\partial y} \end{array} \right\} = [S] \left\{ \begin{array}{c} \{\hat{\varepsilon}_b\} \\ \cdots\cdots \\ \{\hat{\varepsilon}_s\} \end{array} \right\} = [S] \{\hat{\varepsilon}\} \tag{4.4}$$

where $\{\hat{\varepsilon}\}$ is the generalized strain vector, composed by the generalized bending, $\{\hat{\varepsilon}_b\}$, and transverse shear, $\{\hat{\varepsilon}_s\}$, strain vectors, and $[S]$ is the strain transformation matrix.

Considering the assumptions behind the Reissner-Mindlin plate theory, namely the plane stress consideration ($\sigma_z = 0$), the stress vector can be written as:

$$\{\sigma\} = \left\{ \begin{array}{c} \sigma_{xx} \\ \sigma_{yy} \\ \tau_{xy} \\ \cdots\cdots \\ \tau_{xz} \\ \tau_{yz} \end{array} \right\} = \left\{ \begin{array}{c} \{\sigma_b\} \\ \cdots\cdots \\ \{\sigma_s\} \end{array} \right\} \tag{4.5}$$

4.2.2 Stress-Strain Relation

The relation between stress and strain is given by the constitutive equations of three-dimensional elasticity. Considering a homogeneous and isotropic material these can also be divided into the bending and transverse shear components and are given by:

- *Bending components relation*:

$$\begin{aligned} &\{\sigma_b\} = [D_b] \{\varepsilon_b\} \\ &\left\{ \begin{array}{c} \sigma_{xx} \\ \sigma_{yy} \\ \tau_{xy} \end{array} \right\} = \frac{E}{1-\nu^2} \begin{bmatrix} 1 & \nu & 0 \\ \nu & 1 & 0 \\ 0 & 0 & \frac{1-\nu}{2} \end{bmatrix} \left\{ \begin{array}{c} \varepsilon_{xx} \\ \varepsilon_{yy} \\ \gamma_{xy} \end{array} \right\} \end{aligned} \tag{4.6}$$

- *Transverse shear components relation*

$$\begin{aligned} &\{\sigma_s\} = [D_s] \{\varepsilon_s\} \\ &\left\{ \begin{array}{c} \tau_{xz} \\ \tau_{yz} \end{array} \right\} = G \begin{bmatrix} 1 & 0 \\ 0 & 1 \end{bmatrix} \left\{ \begin{array}{c} \gamma_{xz} \\ \gamma_{yz} \end{array} \right\} \end{aligned} \tag{4.7}$$

where E, ν and G represent the Young's modulus, the Poisson's ratio and the shear modulus of the homogeneous and isotropic material, respectively.

It is based on the thick plate theory that the layer deformation theory, associated to the layerwise model and presented next, is developed.

4.3 Layerwise Theory

As said in Section 3.4.2, the layerwise theory allows the condensation of the information relative to the layers of a three-dimensional laminated solid in a bi-dimensional finite element. Plus, it is particularly appealing in situations involving significant shear strain energy, which is the viscoelastic damping treatment's case.

The layerwise theory divides the structure into diverse layers, being each one's kinematic behavior studied according to the Reissner-Mindlin thick plate theory, resulting in a model that: [Moreira et al., 2006]

- Accounts for membrane extensional and shear strains in each layer;
- Considers the thickness strain negligible;
- Incorporates the rotary and translational inertias of each layer;
- Considers linear elastic and viscoelastic theories;
- Considers homogeneous and isotropic/orthotropic materials in each layer

The displacement field's continuity at the interface between layers is imposed and assured in its description. This multi-layer deformation theory associates an independent rotational field to each individual layer. Thus, considering a laminated plate constituted by n layers, presented in Figure 4.3, one can consider that the layer k presents the rotations β_{k_x} and β_{k_y}[1], in each orthogonal direction, that are particular and independent of the other layers' displacements. This allows the thorough description of the behavior of each layer in a multiple layer laminate constituted by different materials, as the viscoelastic damping treatments [Moreira, 2004].

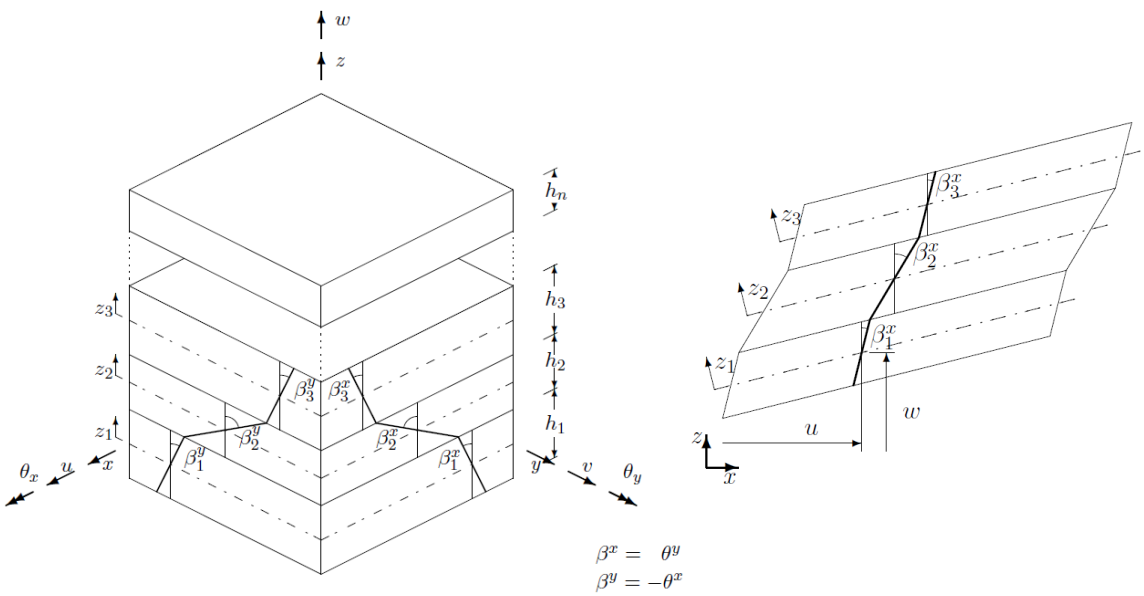

Figure 4.3: Layerwise theory - kinematic model [Moreira, 2004].

[1]Throughout this dissertation, β_{k_x} will represent the rotation angle between a line initially normal to the undeformed middle plane after deformation and the yy axis and β_{k_y} will represent the rotation angle between the same line and the xx axis, resulting in the relations present in Figure 4.3.

4.3.1 Displacement Field

Considering a generic layer k of a multiple layer laminate plate, presenting a thickness h_k, the normal position of a point can be determined by its distance to the plate's middle plane, z_k, according to what is presented in Figure 4.3. Furthermore, considering that it presents a plane area A, the volume of said layer, Ω_k, can be written as:

$$\Omega_k = \left\{ (x, y, z_k) \in \mathbb{R}^3 | z_k \in \left[-\frac{h_k}{2}, \frac{h_k}{2} \right], (x, y) \in A \subset \mathbb{R}^2 \right\} \tag{4.8}$$

The displacement field for said layer, $\{u\}_k$, will be defined by three components, one in each orthogonal direction, as:

$$\{u\}_k = \left\{ \begin{array}{c} u_k(x, y, z) \\ v_k(x, y, z) \\ w_k(x, y) \end{array} \right\} = \left\{ \begin{array}{c} u_0 + \frac{h_1}{2}\beta_{1_x} + \sum_{j=2}^{k-1} h_j \beta_{j_x} + \frac{h_k}{2}\beta_{k_x} + z_k \beta_{k_x} \\ v_0 + \frac{h_1}{2}\beta_{1_y} + \sum_{j=2}^{k-1} h_j \beta_{j_y} + \frac{h_k}{2}\beta_{k_y} + z_k \beta_{k_y} \\ w_0 \end{array} \right\} \tag{4.9}$$

where u_0, v_0 and w_0 represent the translations of the reference layer, $k = 1$. The displacement field of a layer k is, thus, determined by the translations of the reference layer (note that the transverse displacement, $w(x, y) = w_0(x, y)$, is the same for all layers, representing the non-crushing condition) and the rotations β_{k_x} and β_{k_y}. Furthermore, its continuity is guaranteed through a set of coupling terms relating the displacement of a layer with the one in the interface with the previous layer, $k - 1$.

The displacement of a single point can be obtained through a set of generalized variables, namely the generalized displacement field, $\{d\}$, whose vector can be represented as:

$$\{d\} = \left\{ u_0, v_0, w_0, \beta_{1_x}, \beta_{1_y}, \cdots, \beta_{k_x}, \beta_{k_y}, \cdots, \beta_{n_x}, \beta_{n_y} \right\} \tag{4.10}$$

considering a multiple layer laminate with n layers. Thus, the displacement field, u_k, can be determined as:

$$\{u\}_k = [\mathcal{N}]_k \{d\} \tag{4.11}$$

where the matrix $[\mathcal{N}]$ is defined as:

$$\left[\begin{array}{ccccccccccc:ccc} 1 & 0 & 0 & \frac{h_1}{2} & 0 & \cdots & h_j & 0 & \cdots & \frac{h_k}{2} + z_k & 0 & 0 & \cdots & 0 \\ 0 & 1 & 0 & 0 & \frac{h_1}{2} & \cdots & 0 & h_j & \cdots & 0 & \frac{h_k}{2} + z_k & 0 & \cdots & 0 \\ 0 & 0 & 1 & 0 & 0 & \cdots & 0 & 0 & \cdots & 0 & 0 & 0 & \cdots & 0 \end{array} \right] \tag{4.12}$$

4.3.2 Strain Field

Based on the displacement field of a layer k (Equation 4.9), and considering the assumptions considered in the Reissner-Mindlin plate theory, one can define its strain field, $\{\varepsilon\}_k$, as:

$$\{\varepsilon\}_k = \begin{Bmatrix} \varepsilon_{k_{xx}} \\ \varepsilon_{k_{yy}} \\ \gamma_{k_{xy}} \\ \gamma_{k_{xz}} \\ \gamma_{k_{yz}} \end{Bmatrix} = \begin{Bmatrix} \dfrac{\partial u_k}{\partial x} \\ \dfrac{\partial v_k}{\partial y} \\ \dfrac{\partial u_k}{\partial y} + \dfrac{\partial v_k}{\partial x} \\ \dfrac{\partial u_k}{\partial z} + \dfrac{\partial w_k}{\partial x} \\ \dfrac{\partial v_k}{\partial z} + \dfrac{\partial w_k}{\partial y} \end{Bmatrix} \tag{4.13}$$

It is possible to distinguish four contributions to the components of the strain field, namely the *membrane*, *bending*, *coupling* and *shear terms*. This distinction can be made as follows:

$$\begin{aligned} \varepsilon_{k_{xx}} = & \frac{\partial u_0}{\partial x} + && \text{(membrane term, } \varepsilon_{xx}^M) \\ & + \frac{h_1}{2}\frac{\partial \beta_{1_x}}{\partial x} + \sum_{j=2}^{k-1} h_j \frac{\partial \beta_{j_x}}{\partial x} + \frac{h_k}{2}\frac{\partial \beta_{k_x}}{\partial x} + && \text{(coupling term, } \varepsilon_{xx}^C) \\ & + z_k \frac{\partial \beta_{k_x}}{\partial x} && \text{(bending term, } \varepsilon_{xx}^B) \end{aligned} \tag{4.14a}$$

$$\begin{aligned} \varepsilon_{k_{yy}} = & \frac{\partial v_0}{\partial y} + && \text{(membrane term, } \varepsilon_{yy}^M) \\ & + \frac{h_1}{2}\frac{\partial \beta_{1_y}}{\partial y} + \sum_{j=2}^{k-1} h_j \frac{\partial \beta_{j_y}}{\partial y} + \frac{h_k}{2}\frac{\partial \beta_{k_y}}{\partial y} + && \text{(coupling term, } \varepsilon_{yy}^C) \\ & + z_k \frac{\partial \beta_{k_y}}{\partial y} && \text{(bending term, } \varepsilon_{yy}^B) \end{aligned} \tag{4.14b}$$

$$\begin{aligned} \gamma_{k_{xy}} = & \frac{\partial u_0}{\partial y} + \frac{\partial v_0}{\partial x} + && \text{(membrane term, } \gamma_{xy}^M) \\ & + \frac{h_1}{2}\frac{\partial \beta_{1_x}}{\partial y} + \sum_{j=2}^{k-1} h_j \frac{\partial \beta_{j_x}}{\partial y} + \frac{h_k}{2}\frac{\partial \beta_{k_x}}{\partial y} + && \\ & + \frac{h_1}{2}\frac{\partial \beta_{1_y}}{\partial x} + \sum_{j=2}^{k-1} h_j \frac{\partial \beta_{j_y}}{\partial x} + \frac{h_k}{2}\frac{\partial \beta_{k_y}}{\partial x} + && \text{(coupling term, } \gamma_{xy}^C) \\ & + z_k \frac{\partial \beta_{k_x}}{\partial y} + z_k \frac{\partial \beta_{k_y}}{\partial x} && \text{(bending term, } \gamma_{xy}^B) \end{aligned} \tag{4.14c}$$

$$\gamma_{k_{xz}} = \beta_{k_x} + \frac{\partial w_0}{\partial x} \quad \text{(transverse shear term, } \gamma_{xz}^S) \tag{4.14d}$$

$$\gamma_{k_{yz}} = \beta_{k_y} + \frac{\partial w_0}{\partial y} \quad \text{(transverse shear term, } \gamma_{yz}^S) \tag{4.14e}$$

From the Solid Mechanic's principles, the differential operator matrix, $[\mathcal{L}]$, can be applied to obtain the strain field from the displacement field as:

$$\{\varepsilon\}_k = [\mathcal{L}]\,\{u\}_k$$

$$\begin{Bmatrix} \varepsilon^M_{k_{xx}} + \varepsilon^C_{k_{xx}} + \varepsilon^B_{k_{xx}} \\ \varepsilon^M_{k_{yy}} + \varepsilon^C_{k_{yy}} + \varepsilon^B_{k_{yy}} \\ \gamma^M_{k_{xy}} + \gamma^C_{k_{xy}} + \gamma^B_{k_{xy}} \\ \gamma^S_{k_{xz}} \\ \gamma^S_{k_{yz}} \end{Bmatrix} = \begin{bmatrix} \dfrac{\partial}{\partial x} & 0 & 0 \\ 0 & \dfrac{\partial}{\partial y} & 0 \\ \dfrac{\partial}{\partial y} & \dfrac{\partial}{\partial x} & 0 \\ \dfrac{\partial}{\partial z} & 0 & \dfrac{\partial}{\partial x} \\ 0 & \dfrac{\partial}{\partial z} & \dfrac{\partial}{\partial y} \end{bmatrix} \begin{Bmatrix} u_0 + \dfrac{h_1}{2}\beta_{1_x} + \sum\limits_{j=2}^{k-1} h_j\beta_{j_x} + \dfrac{h_k}{2}\beta_{k_x} + z_k\beta_{k_x} \\ v_0 + \dfrac{h_1}{2}\beta_{1_y} + \sum\limits_{j=2}^{k-1} h_j\beta_{j_y} + \dfrac{h_k}{2}\beta_{k_y} + z_k\beta_{k_y} \\ w_0 \end{Bmatrix} \tag{4.15}$$

Recalling Equation 4.11, it is possible to obtain an expression relating directly the generalized displacement field and the strain field, such as:

$$\{\varepsilon\}_k = [\mathcal{L}]\,[\mathcal{N}]_k\,\{d\} = [\mathcal{B}]_k\,\{d\} \tag{4.16}$$

where $[\mathcal{B}] = [\mathcal{L}]\,[\mathcal{N}]_k$ is the strain matrix of the layer k.

For convenience of formulation, the strain field vector is split into three partitions, where the first combines the membrane and coupling components, the second contemplates the bending terms and the final one represents the transverse shear components, as follows:

$$\{\varepsilon\}_k = \left\{\ \{\varepsilon\}^M_k + \{\varepsilon\}^C_k \quad ; \quad \{\varepsilon\}^B_k \quad ; \quad \{\gamma\}^S_k\ \right\}^{\mathrm{T}} \tag{4.17}$$

Thus, to obtain an expression similar to Equation 4.16 after rearranging of the strain field vector, the strain matrix must also be reorganized into three sub-matrices (one referring the membrane and coupling components, other the bending terms and the last one the transverse shear ones), as:

$$
[\mathcal{B}]_k = \begin{bmatrix} [\mathcal{B}]_k^{M+C} \\ \hdashline [\mathcal{B}]_k^{B} \\ \hdashline [\mathcal{B}]_k^{S} \end{bmatrix} =
$$

$$
= \left[\begin{array}{ccccccccccc:c}
\frac{\partial}{\partial x} & 0 & 0 & \frac{h_1}{2}\frac{\partial}{\partial x} & 0 & \cdots & h_j\frac{\partial}{\partial x} & 0 & \cdots & \frac{h_k}{2}\frac{\partial}{\partial x} & 0 & \\
0 & \frac{\partial}{\partial y} & 0 & 0 & \frac{h_1}{2}\frac{\partial}{\partial y} & \cdots & 0 & h_j\frac{\partial}{\partial y} & \cdots & 0 & \frac{h_k}{2}\frac{\partial}{\partial y} & [0] \\
\frac{\partial}{\partial y} & \frac{\partial}{\partial x} & 0 & \frac{h_1}{2}\frac{\partial}{\partial y} & \frac{h_1}{2}\frac{\partial}{\partial x} & \cdots & h_j\frac{\partial}{\partial y} & h_j\frac{\partial}{\partial x} & \cdots & \frac{h_k}{2}\frac{\partial}{\partial y} & \frac{h_k}{2}\frac{\partial}{\partial x} & \\
\hdashline
0 & 0 & 0 & 0 & 0 & \cdots & 0 & 0 & \cdots & z_k\frac{\partial}{\partial x} & 0 & \\
0 & 0 & 0 & 0 & 0 & \cdots & 0 & 0 & \cdots & 0 & z_k\frac{\partial}{\partial y} & [0] \\
0 & 0 & 0 & 0 & 0 & \cdots & 0 & 0 & \cdots & z_k\frac{\partial}{\partial y} & z_k\frac{\partial}{\partial x} & \\
\hdashline
0 & 0 & \frac{\partial}{\partial x} & 0 & 0 & \cdots & 0 & 0 & \cdots & 1 & 0 & 0\ldots0 \\
0 & 0 & \frac{\partial}{\partial y} & 0 & 0 & \cdots & 0 & 0 & \cdots & 0 & 1 & 0\ldots0
\end{array}\right] \tag{4.18}
$$

where $[\mathcal{B}]_k^{M+C}$ represents the membrane and coupling strain sub-matrix, $[\mathcal{B}]_k^{B}$ the bending strain sub-matrix and $[\mathcal{B}]_k^{S}$ the transverse shear strain sub-matrix.

4.3.3 Stress Field

The stress field of a generic layer k, $\{\sigma\}_k$, is related with the imposed strain field. Thus, after a simple analysis of Equation 4.13, it is possible to conclude that the resulting stress field can be defined by the vector:

$$
\{\sigma\}_k = \left\{\sigma_{k_{xx}}\ ;\ \sigma_{k_{yy}}\ ;\ \tau_{k_{xy}}\ ;\ \tau_{k_{xz}}\ ;\ \tau_{k_{yz}}\right\}^{\mathrm{T}} \tag{4.19}
$$

where such components can be rearranged as what was made with the strain field in Equation 4.17, that is, grouping the membrane and coupling terms, the bending components and the transverse shear ones, as:

$$
\{\sigma\}_k = \left\{\ \{\sigma\}_k^M + \{\sigma\}_k^C \quad ; \quad \{\sigma\}_k^B \quad ; \quad \{\tau\}_k^S\ \right\}^{\mathrm{T}} \tag{4.20}
$$

The relation between stress and strain fields is determined by the constitutive law of the layer's material, represented by the elasticity matrix, $[\mathcal{D}]$. The mathematical representation of this relation is given by:

$$\{\sigma\}_k = [\mathcal{D}]_k \{\varepsilon\}_k \tag{4.21}$$

Considering linear elasticity and isotropic material conditions, and assuming the strain and stress fields presented in Equations 4.17 and 4.20, respectively, the constitutive matrix can be defined as:

$$[\mathcal{D}]_k = \begin{bmatrix} [D]_k^{M+C} & [0] & [0] \\ & [D]_k^{B} & [0] \\ \text{sym.} & & [G]_k^{S} \end{bmatrix} \tag{4.22}$$

where $[D]_k^{M+C}$, $[D]_k^{B}$ and $[G]_k^{S}$ represent the membrane and coupling, bending and transverse shear constitutive matrices, respectively, defined, for isotropic materials, as:

$$[D]_k^{M+C} = [D]_k^{B} = \frac{E_k}{1-\nu_k^2} \begin{bmatrix} 1 & \nu_k & 0 \\ \nu_k & 1 & 0 \\ 0 & 0 & \dfrac{1-\nu_k}{2} \end{bmatrix} \tag{4.23a}$$

$$[G]_k^{S} = [G]_k = \frac{E_k}{2\left(1+\nu_k\right)} \begin{bmatrix} 1 & 0 \\ 0 & 1 \end{bmatrix} \tag{4.23b}$$

where E_k and ν_k represent the Young's modulus and the Poisson's ration of the generic layer k, respectively.

Note that when analyzing a viscoelastic material, the dependence of its constitutive properties with the frequency must be taken into account. In most cases, this is made by defining the corresponding matrices, $[\mathcal{D}(\omega)]_k$, using a reference isotropic Young's modulus and then updating them with the stiffness values, or complex modulus, for each frequency value. Nevertheless, as was seen in the previous Chapter, the finite element spatial model formulation is totally independent of this constitutive relations.

4.3.4 Elastic Strain Energy

The elastic strain energy, Π^P, stored in a multiple layer laminate is given by the integral evaluated over the volume domain of the whole n layers. Furthermore, it can also be obtained by the sum of the energy contribution of each layer, Π_k^P. That is:

$$\Pi^P = \frac{1}{2}\int_{\Omega} \{\varepsilon\}^{\mathrm{T}}\{\sigma\}\,\mathrm{d}\Omega = \sum_{k=1}^{n} \Pi_k^P = \sum_{k=1}^{n}\left[\frac{1}{2}\int_{\Omega_k} \{\varepsilon\}_k^{\mathrm{T}}\{\sigma\}_k\,\mathrm{d}\Omega_k\right] \tag{4.24}$$

Substituting the strain field's expression and considering that the volume integral might be substituted by two integrals, one evaluated over each layer's thickness and other evaluated over its area, the elastic strain energy expression can be written as follows:

$$\Pi^P = \sum_{k=1}^{n}\left[\frac{1}{2}\int_{A}\int_{z_k} \{\varepsilon\}_k^{\mathrm{T}}\,[\mathcal{D}]_k\,\{\varepsilon\}_k\,\mathrm{d}z_k\,\mathrm{d}A\right] \tag{4.25}$$

where A is the bi-dimensional space defined by the local x and y coordinates and $z_k \in \left[-\frac{h_k}{2}, \frac{h_k}{2}\right]$. This process is possible due to the constant thickness consideration for each layer. In case this is not verified, it is necessary to consider special procedures in the finite element formulation, namely the consideration of the average thickness of each layer.

Substituting Equation 4.16 in Equation 4.21 and then in Equation 4.25, the elastic strain energy expression can be written as:

$$\Pi^P = \sum_{k=1}^{n} \left[\frac{1}{2} \int_A \int_{z_k} \{d\}^{\mathrm{T}} \left[\mathcal{B}\right]_k^{\mathrm{T}} \left[\mathcal{D}\right]_k \left[\mathcal{B}\right]_k \{d\} \, \mathrm{d}z_k \, \mathrm{d}A \right] \tag{4.26}$$

Computing explicitly the integral over the layer's thickness, the strain energy is obtained from:

$$\Pi^P = \sum_{k=1}^{n} \left[\frac{1}{2} \int_A \{d\}^{\mathrm{T}} [\hat{\mathcal{B}}]_k^{\mathrm{T}} [\hat{\mathcal{D}}]_k [\hat{\mathcal{B}}]_k \{d\} \, \mathrm{d}A \right] \tag{4.27}$$

where $[\hat{\mathcal{D}}]_k$ is the modified constitutive matrix, which now includes the resulting integration terms and is defined as:

$$[\hat{\mathcal{D}}]_k = \begin{bmatrix} h_k \left[D\right]_k & [0] & [0] \\ & \dfrac{h_k^3}{12} \left[D\right]_k & [0] \\ \text{sym.} & & h_k \left[G\right]_k \end{bmatrix} \tag{4.28}$$

and $[\hat{\mathcal{B}}]_k$ represents the modified strain matrix, obtained from Equation 4.18, resulting on:

$$[\hat{\mathcal{B}}]_k = \begin{bmatrix} [\mathcal{B}]_k^{M+C} \\ \hdashline \dfrac{1}{z_k} \left[\mathcal{B}\right]_k^{B} \\ \hdashline [\mathcal{B}]_k^{S} \end{bmatrix} \tag{4.29}$$

4.3.5 Kinetic Energy

The total kinetic energy, Π^C, of a multiple layer laminate can be obtained from the integral evaluated over the volume of the whole set of n layers as:

$$\Pi^K = \frac{1}{2} \int_\Omega \{v\}^{\mathrm{T}} \left[\mathcal{J}\right] \{v\} \, \mathrm{d}\Omega \tag{4.30}$$

It can also be obtained by the sum of the energy contribution of each layer, Π_k^C, as was previously done for the strain energy. That is:

$$\Pi^K = \sum_{k=1}^{n} \Pi_k^K = \sum_{k=1}^{n} \left[\frac{1}{2} \int_{\Omega_k} \{v\}_k^{\mathrm{T}} \left[\mathcal{J}\right]_k \{v\}_k \, \mathrm{d}\Omega_k \right] \tag{4.31}$$

where $\left[\mathcal{J}\right]_k$ represents the inertia matrix of the kth layer, defined by:

$$\left[\mathcal{J}\right]_k = \begin{bmatrix} \rho_k & 0 & 0 \\ 0 & \rho_k & 0 \\ 0 & 0 & \rho_k \end{bmatrix} \tag{4.32}$$

where ρ_k is the mass density of the layer's material and $\{v\}_k$ represents the velocity field for the kth layer. For the rotating case, with a co-rotating referential, it is obtained by

the time derivation of the corresponding position vector, which generic result in matrix notation was previously presented by Equation 2.16. Applying to the present formulation, the velocity field can be written as follows:

$$
\begin{aligned}
\{v\}_k &= \{\dot{u}\}_k + \{\omega\} \times \{P\} = \{\dot{u}\}_k + [\Omega]\left(\{r\} + \{u\}\right) = \\
&= \begin{Bmatrix} \dot{u}_k(x,y,z) \\ \dot{v}_k(x,y,z) \\ \dot{w}_k(x,y) \end{Bmatrix} + \begin{bmatrix} 0 & -\omega_z & \omega_y \\ \omega_z & 0 & -\omega_x \\ -\omega_y & \omega_x & 0 \end{bmatrix} \left(\begin{Bmatrix} x \\ y \\ z \end{Bmatrix} + \begin{Bmatrix} u_k(x,y,z) \\ v_k(x,y,z) \\ w_k(x,y) \end{Bmatrix} \right) = \\
&= \begin{Bmatrix} \dot{u}_0 + \dfrac{h_1}{2}\dot{\beta}_{1_x} + \sum\limits_{j=2}^{k-1} h_j \dot{\beta}_{j_x} + \dfrac{h_k}{2}\dot{\beta}_{k_x} + z_k \dot{\beta}_{k_x} \\ \dot{v}_0 + \dfrac{h_1}{2}\dot{\beta}_{1_y} + \sum\limits_{j=2}^{k-1} h_j \dot{\beta}_{j_y} + \dfrac{h_k}{2}\dot{\beta}_{k_y} + z_k \dot{\beta}_{k_y} \\ \dot{w}_0 \end{Bmatrix} + \begin{Bmatrix} -\omega_z\left(y + v_k\right) + \omega_y\left(z + w_k\right) \\ \omega_z\left(x + u_k\right) - \omega_x\left(z + w_k\right) \\ -\omega_y\left(x + u_k\right) + \omega_x\left(y + v_k\right) \end{Bmatrix}
\end{aligned}
\tag{4.33}
$$

where $u_k(x,y,z)$, $v_k(x,y,z)$ and $w_k(x,y)$ are the displacement field components, given by Equation 4.9.

As was made for the displacement field in Equation 4.11, the time derivative of the displacement field, $\{\dot{u}\}$, can be obtained through the generalized velocity field, $\{\dot{d}\}$, which represents the time derivative of the generalized displacement field, and the matrix $[\mathcal{N}]$. Furthermore, as was presented in Section 2.3, the position vector, $\{r\}$, can also be obtained as a function of the nodal coordinates, $\{c\}$, and the coordinates shape function matrix, $[\mathcal{N}']$. Therefore:

$$
\{v\}_k = [\mathcal{N}]_k \{\dot{d}\} + [\Omega]\left(\left[\mathcal{N}'\right]\{c\} + [\mathcal{N}]\{d\}\right) \tag{4.34}
$$

where $[\mathcal{N}]$ is defined in the same way as before (Equation 4.12).

Substituting Equation 4.34 in Equation 4.31, and considering that the volume integral might be substituted by two integrals, one evaluated over each layer's thickness and other evaluated over its area, the kinetic energy expression can be written as follows:

$$
\begin{aligned}
\Pi^K = \sum_{k=1}^{n} \Bigg[& \frac{1}{2}\int_A \int_{z_k} \{\dot{d}\}_k^{\mathrm{T}} [\mathcal{N}]_k^{\mathrm{T}} [\mathcal{J}]_k [\mathcal{N}]_k \{\dot{d}\} \, \mathrm{d}z_k \, \mathrm{d}A + \frac{1}{2}\int_A \int_{z_k} \{r\}^{\mathrm{T}} [\mathcal{J}]_k [\Omega^2] \{r\} \, \mathrm{d}z_k \, \mathrm{d}A + \\
& + \frac{1}{2}\int_A \int_{z_k} \{d\}^{\mathrm{T}} [\mathcal{N}]_k^{\mathrm{T}} [\mathcal{J}]_k [\Omega^2] [\mathcal{N}]_k \{d\} \, \mathrm{d}z_k \, \mathrm{d}A + \int_A \int_{z_k} \{\dot{d}\}^{\mathrm{T}} [\mathcal{N}]_k^{\mathrm{T}} [\mathcal{J}]_k [\Omega] \{r\} \, \mathrm{d}z_k \, \mathrm{d}A + \\
& + \int_A \int_{z_k} \{r\}^{\mathrm{T}} [\mathcal{J}]_k [\Omega^2] \{d\} \, \mathrm{d}z_k \, \mathrm{d}A + \int_A \int_{z_k} \{\dot{d}\}^{\mathrm{T}} [\mathcal{N}]^{\mathrm{T}} [\mathcal{J}]_k [\Omega] [\mathcal{N}] \{d\} \, \mathrm{d}z_k \, \mathrm{d}A \Bigg]
\end{aligned}
\tag{4.35}
$$

Computing explicitly the integral over the layer's thickness, the kinetic energy may be obtained as:

$$
\begin{aligned}
\Pi^K = \sum_{k=1}^{n} \Bigg[& \frac{1}{2}\int_A \{\dot{d}\}_k^{\mathrm{T}} [\hat{\mathcal{N}}]_k^{\mathrm{T}} [\hat{J}]_k [\hat{\mathcal{N}}]_k \{\dot{d}\} \, \mathrm{d}A + \frac{1}{2}\int_A \{r\}^{\mathrm{T}} [\hat{J}]_k [\Omega^2] \{r\} \, \mathrm{d}A + \\
& + \frac{1}{2}\int_A \{d\}^{\mathrm{T}} [\hat{\mathcal{N}}]_k^{\mathrm{T}} [\hat{J}]_k [\Omega^2] [\hat{\mathcal{N}}]_k \{d\} \, \mathrm{d}A + \int_A \{\dot{d}\}^{\mathrm{T}} [\hat{N}]_k^{\mathrm{T}} [\hat{J}]_k [\Omega] \{r\} \, \mathrm{d}A + \\
& + \int_A \{r\}^{\mathrm{T}} [\hat{J}]_k [\Omega^2] \{d\} \, \mathrm{d}A + \int_A \{\dot{d}\}^{\mathrm{T}} [\hat{\mathcal{N}}]_k^{\mathrm{T}} [\hat{J}]_k [\Omega] [\hat{\mathcal{N}}]_k \{d\} \, \mathrm{d}A \Bigg]
\end{aligned}
\tag{4.36}
$$

where $[\hat{\mathcal{N}}]_k$ and $[\hat{J}]_k$ represent the modified shape and inertia matrices for the kth layer, respectively.

4.3.6 Variational Formulation - Hamilton's Principle

In the derivation of the variational statement equivalent to the governing differential equations, as well as the natural boundary conditions, the Hamilton's Principle is adopted, which can be described as:

$$\delta \int_{t_1}^{t_2} \left(\Pi^K - \Pi^P\right) \mathrm{d}t + \int_{t_1}^{t_2} \delta W \mathrm{d}t = 0 \tag{4.37}$$

where Π^K, Π^P and δW represent the kinetic and elastic strain energies of the multiple layer body and the virtual work done by the external applied forces.

Knowing that $\delta W = \int_S \{\delta d\}^{\mathrm{T}} \{q\} \mathrm{d}S$, where S is the surface area, $\{\delta d\}$ is the virtual displacement and $\{q\}$ is the load vector, substituting Equations 4.36 and 4.27 in 4.37, after mathematical manipulation and knowing that the previous expression must be satisfied for an arbitrary virtual displacement, $\{\delta d\}$, within any time interval from t_1 to t_2, the result is:

$$\begin{aligned}
&\sum_{k=1}^{n} \left[\int_A \{\delta d\}_k^{\mathrm{T}} [\hat{\mathcal{N}}]_k^{\mathrm{T}} [\hat{J}]_k [\hat{\mathcal{N}}] \{\ddot{d}\} \, \mathrm{d}A \right] + \sum_{k=1}^{n} \left[2 \int_A \{\delta d\}_k^{\mathrm{T}} [\hat{\mathcal{N}}]_k^{\mathrm{T}} [\hat{J}]_k [\Omega] [\hat{\mathcal{N}}]_k \{\dot{d}\} \, \mathrm{d}A \right] + \\
&+ \sum_{k=1}^{n} \left[\int_A \{\delta d\}^{\mathrm{T}} [\hat{\mathcal{B}}]_k^{\mathrm{T}} [\hat{\mathcal{D}}]_k [\hat{\mathcal{B}}]_k \{d\} \, \mathrm{d}A - \int_A \{\delta d\}_k^{\mathrm{T}} [\hat{\mathcal{N}}]_k^{\mathrm{T}} [\hat{J}]_k [\Omega^2] [\hat{\mathcal{N}}]_k \{d\} \, \mathrm{d}A \right] - \\
&- \sum_{k=1}^{n} \left[\int_A \{\delta d\}^{\mathrm{T}} [\hat{\mathcal{N}}]_k^{\mathrm{T}} [\hat{J}]_k [\Omega^2] [\hat{\mathcal{N}}']_k \{c\} \, \mathrm{d}A \right] + \int_S \{\delta d\}^{\mathrm{T}} \{q\} \, \mathrm{d}S = 0
\end{aligned} \tag{4.38}$$

for any virtual displacement ($\forall \{\delta d\}$).

4.3.7 Layerwise Plate Finite Element Formulation

The finite element studied and used throughout this dissertation consists on a four-node isoparametric quadrilateral element. This three-dimensional facet shell element is described in a global Cartesian coordinate system (X, Y, Z), being its stiffness and mass matrices computed in a local Cartesian coordinate system (x, y, z), where the $x - y$ plane is coplanar with the element face. Before assembling, the element matrices must be transformed into the global coordinate system, using the correspondent transformation matrix.

When described in a natural coordinate system (ξ, η, ζ), the element assumes square-like configuration, whose sides have a length of two times the unit (Figure 4.4). Furthermore, it is assumed that the nodes are numbered in the counter-clockwise direction. This representation in a natural coordinate system allows a simpler and more standard definition of a set of interpolation functions and the use of a numerical integration method, namely the Gauss-Legendre quadrature.

4.3.7.1 Geometric and Displacement Field Interpolation

The transformation from the local system to the natural one can be made through a geometric approximation with the interpolation functions, which allow the definition of

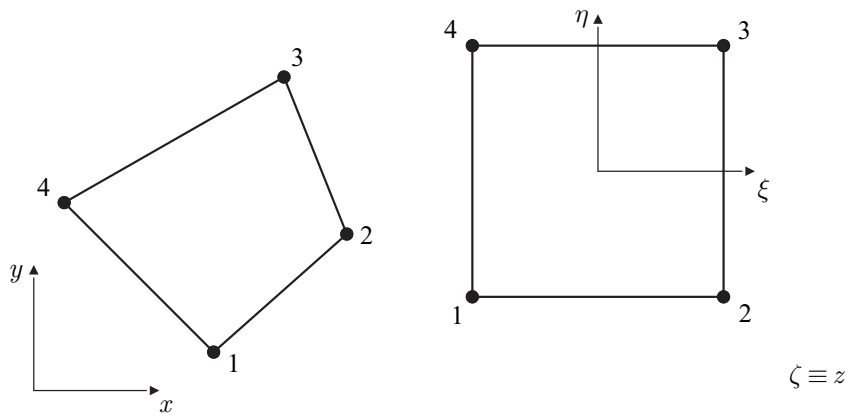

Figure 4.4: Four-node finite element for a facet shell configuration - local and natural coordinate systems.

the coordinates (x, y) within the element's domain from its natural coordinates (ξ, η) and the Cartesian coordinates of the nodes.

$$\begin{aligned} x(\xi,\eta) &= \sum_{i=1}^{4} N_i(\xi,\eta) x_i \\ y(\xi,\eta) &= \sum_{i=1}^{4} N_i(\xi,\eta) y_i \end{aligned} \tag{4.39}$$

where x_i and y_i represent the node's coordinates and $N_i(\xi, \eta)$ are the geometric interpolation functions of the element, usually named shape functions, evaluated at the corresponding point.

In addition, it is also necessary to interpolate the variables of a finite element problem (the displacements of each node) within the element, to define the displacement field. This process can be achieved by using the same set of interpolation functions used to interpolate the geometry, resulting on an isoparametric finite element formulation. Therefore, the generalized displacement vector of an element, $\{d\}^e = \{u_0, v_0, w_0, \beta_{1_x}, \beta_{1_y}, \ldots, \beta_{n_x}, \beta_{n_y}\}$, can be defined through the nodal displacement vector, $\{d_i\}^e = \{\ \{d_1\}^e\ \{d_2\}^e\ \{d_3\}^e\ \{d_4\}^e\ \}^{\mathrm{T}}$, and a set of interpolation functions, as:

$$\{d\}^e = \sum_{i=1}^{4} N_i(\xi,\eta)\{d_i\}^e \tag{4.40}$$

Using a matrix formulation, the previous expression can be written as:

$$\{d\}^e = [N]\{d_i\}^e \tag{4.41}$$

where $[N]$ is the shape functions matrix, defined by:

$$[N] = \left[\begin{array}{ccc|ccc|ccc|ccc} \ddots & & & \ddots & & & \ddots & & & \ddots & & \\ & N_1 & & & N_2 & & & N_3 & & & N_4 & \\ & & \ddots & & & \ddots & & & \ddots & & & \ddots \end{array}\right] \tag{4.42}$$

The shape functions are, usually, simple polynomial functions, that must satisfy the continuity condition within the element and allow the correct approximation of the interpolated variables. Generally, for four-node elements and $\mathbf{C^0}$ continuity, the applied shape functions present a bilinear form, as:

$$N_i = \frac{1}{4}\left(1+\xi_i\xi\right)\left(1+\eta_i\eta\right) \qquad (i = 1,\, 2,\, 3,\, 4) \tag{4.43}$$

whose derivatives in order to the natural coordinates ξ and η are:

$$\frac{\partial N_i}{\partial \xi} = \frac{1}{4}\xi_i\left(1+\eta_i\eta\right) \tag{4.44a}$$

$$\frac{\partial N_i}{\partial \eta} = \frac{1}{4}\eta_i\left(1+\xi_i\xi\right) \tag{4.44b}$$

where ξ_i and η_i are the nodal parameters defining the shape function expression for each node, according to what is presented in Table 4.1.

Table 4.1: Nodal parameters for the shape functions

Node	**1**	**2**	**3**	**4**
ξ_i	-1	1	1	-1
η_i	-1	-1	1	1

4.3.7.2 Weak Form Finite Element Discretization

The global weak form presented in Equation 4.38 can be expressed, after the domain discretization, as the sum of the elemental integral forms, leading to the definition of the elemental matrices and vectors. Considering the existence of n_e elements, the global weak form turns into:

$$\begin{aligned}\sum_{e=1}^{n_e}\Bigg(&\sum_{k=1}^{n}\left[\int_{A^e}\{\delta d^e\}_k^{\mathrm{T}}[\hat{\mathcal{N}}]_k^{\mathrm{T}}[\hat{J}]_k[\hat{\mathcal{N}}]\{\ddot{d}^e\}\,\mathrm{d}A^e\right]+\sum_{k=1}^{n}\left[2\int_{A^e}\{\delta d^e\}_k^{\mathrm{T}}[\hat{\mathcal{N}}]_k^{\mathrm{T}}[\hat{J}]_k[\Omega][\hat{\mathcal{N}}]_k\{\dot{d}^e\}\,\mathrm{d}A^e\right]+\\
&+\sum_{k=1}^{n}\left[\int_{A^e}\{\delta d^e\}^{\mathrm{T}}[\hat{\mathcal{B}}]_k^{\mathrm{T}}[\hat{\mathcal{D}}]_k[\hat{\mathcal{B}}]_k\{d^e\}\,\mathrm{d}A^e\right]-\sum_{k=1}^{n}\left[\int_{A^e}\{\delta d^e\}_k^{\mathrm{T}}[\hat{\mathcal{N}}]_k^{\mathrm{T}}[\hat{J}]_k[\Omega^2][\hat{\mathcal{N}}]_k\{d^e\}\,\mathrm{d}A^e\right]-\\
&-\sum_{k=1}^{n}\left[\int_{A^e}\{\delta d^e\}^{\mathrm{T}}[\hat{\mathcal{N}}]_k^{\mathrm{T}}[\hat{J}]_k[\Omega^2][\hat{\mathcal{N}}']_k\{c^e\}\,\mathrm{d}A^e\right]-\int_{S^e}\{\delta d^e\}^{\mathrm{T}}\{q\}\,\mathrm{d}S^e\Bigg)=0\end{aligned} \tag{4.45}$$

where the generalized variables, $\{d^e\}$, $\{\dot{d}^e\}$ and $\{\ddot{d}^e\}$, are restricted to the element domain of integration, A^e, and the interpolation stated in Equation 4.41 can be considered at a local level in each finite element. The same approximation can be done with the nodal coordinates, $\{c^e\}$. Substituting these approximation relations in Equation 4.45:

$$\sum_{e=1}^{n_e}\{\delta d_i^e\}_k^{\mathrm{T}}\Bigg(\sum_{k=1}^{n}\left[\int_{A^e}[N]_k^{\mathrm{T}}[\hat{\mathcal{N}}]_k\mathrm{T}[\hat{J}]_k[\hat{\mathcal{N}}]_k[N]_k\,\mathrm{d}A^e\right]\{\ddot{d}_i^e\}+$$
$$+\sum_{k=1}^{n}\left[2\int_{A^e}[N]_k^{\mathrm{T}}[\hat{\mathcal{N}}]_k^{\mathrm{T}}[\hat{J}]_k[\Omega][\hat{\mathcal{N}}]_k[N]_k\,\mathrm{d}A^e\right]\{\dot{d}_i^e\}+$$
$$+\left(\sum_{k=1}^{n}\left[\int_{A^e}[N]_k^{\mathrm{T}}[\hat{\mathcal{B}}]_k^{\mathrm{T}}[\hat{\mathcal{D}}]_k[\hat{\mathcal{B}}]_k[N]\,\mathrm{d}A^e-\int_{A^e}[N]_k^{\mathrm{T}}[\hat{\mathcal{N}}]_k^{\mathrm{T}}[\hat{J}]_k[\Omega^2][\hat{\mathcal{N}}]_k[N]_k\,\mathrm{d}A^e\right]\right)\{d_i^e\}-$$
$$-\sum_{k=1}^{n}\left[\int_{A^e}[N]_k^{\mathrm{T}}[\hat{\mathcal{N}}]_k^{\mathrm{T}}[\hat{J}]_k[\Omega^2][\hat{\mathcal{N}}']_k[N']_k\{c_i^e\}\,\mathrm{d}A^e\right]-\int_{S^e}[N]\{q_i^e\}\,\mathrm{d}S^e\Bigg)=0 \tag{4.46}$$

Considering $[\hat{N}]=[\hat{\mathcal{N}}][N]$, $[\hat{N}']=[\hat{\mathcal{N}}'][N']$ and $[\hat{B}]=[\hat{\mathcal{B}}][N]$, the previous expression can be written as:

$$\sum_{e=1}^{n_e}\{\delta d_i^e\}_k^{\mathrm{T}}\Bigg(\sum_{k=1}^{n}\left[\int_{A^e}[\hat{N}]_k^{\mathrm{T}}[\hat{J}]_k[\hat{N}]_k\,\mathrm{d}A^e\right]\{\ddot{d}_i^e\}+\sum_{k=1}^{n}\left[2\int_{A^e}[\hat{N}]_k^{\mathrm{T}}[\hat{J}]_k[\Omega][\hat{N}]_k\,\mathrm{d}A^e\right]\{\dot{d}_i^e\}+$$
$$+\left(\sum_{k=1}^{n}\left[\int_{A^e}[\hat{B}]_k^{\mathrm{T}}[\hat{\mathcal{D}}]_k[\hat{B}]_k\,\mathrm{d}A^e-\int_{A^e}[\hat{N}]_k^{\mathrm{T}}[\hat{J}]_k[\Omega^2][\hat{N}]_k\,\mathrm{d}A^e\right]\right)\{d_i^e\}-$$
$$-\sum_{k=1}^{n}\left[\int_{A^e}[\hat{N}]_k^{\mathrm{T}}[\hat{J}]_k[\Omega^2][\hat{N}']_k\{c_i^e\}\,\mathrm{d}A^e\right]-\int_{S^e}[N]\{q_i^e\}\,\mathrm{d}S^e\Bigg)=0 \tag{4.47}$$

Allowing the definition of the element mass, Coriolis, elastic stiffness and centrifugal softening matrices, $[m^e]$, $[c_c^e]$, $[k_e^e]$ and $[k_r^e]$ respectively, and the element centrifugal and external load vectors, $\{f_c^e\}$ and $\{f^{\mathrm{ext}^e}\}$, respectively, as:

$$[m^e]=\sum_{k=1}^{n}[m_k^e]=\sum_{k=1}^{n}\left[\int_{A^e}[\hat{N}]_k^{\mathrm{T}}[\hat{J}]_k[\hat{N}]_k\,\mathrm{d}A^e\right] \tag{4.48a}$$

$$[c_c^e]=\sum_{k=1}^{n}\left[c_{c_k}^e\right]=\sum_{k=1}^{n}\left[2\int_{A^e}[\hat{N}]_k^{\mathrm{T}}[\hat{J}][\Omega][\hat{N}]_k\,\mathrm{d}A^e\right] \tag{4.48b}$$

$$[k_e^e]=\sum_{k=1}^{n}\left[k_{e_k}^e\right]=\sum_{k=1}^{n}\left[\int_{A^e}[\hat{B}]_k^{\mathrm{T}}[\hat{\mathcal{D}}]_k[\hat{B}]_k\,\mathrm{d}A^e\right] \tag{4.48c}$$

$$[k_r^e]=\sum_{k=1}^{n}\left[k_{r_k}^e\right]=\sum_{k=1}^{n}\left[\int_{A^e}[\hat{N}]_k^{\mathrm{T}}[\hat{J}][\Omega^2][\hat{N}]_k\,\mathrm{d}A^e\right] \tag{4.48d}$$

$$\{f_c^e\}=\sum_{k=1}^{n}\{f_{c_k}^e\}=\sum_{k=1}^{n}\left[\int_{A^e}[\hat{N}]_k^{\mathrm{T}}[\hat{J}]\left[\Omega^2\right][\hat{N}']_k\{c_i^e\}\,\mathrm{d}A^e\right] \tag{4.48e}$$

$$\left\{f^{\mathrm{ext}^e}\right\}=\sum_{k=1}^{n}\left\{f^{\mathrm{ext}^e}\right\}=\sum_{k=1}^{n}\left[\int_{S^e}[N]\{q_i^e\}\,\mathrm{d}S^e\right] \tag{4.48f}$$

and recalling that the relation between elemental and global degrees of freedom can be established through a connectivity matrix, $[R^e]$, as: [Moreira et al., 2006]

$$\{d^e\} = [R^e]\{d\} \quad ; \quad \{\dot{d}^e\} = [R^e]\{\dot{d}\} \quad ; \quad \{\ddot{d}^e\} = [R^e]\{\ddot{d}\} \tag{4.49}$$

the assembled global system matrices and vectors are set as:

$$[M] = \sum_{e=1}^{n_e} [R^e]^{\mathrm{T}} [m^e] [R^e] \tag{4.50a}$$

$$[C_c] = \sum_{e=1}^{n_e} [R^e]^{\mathrm{T}} [c_c^e] [R^e] \tag{4.50b}$$

$$[K_e] = \sum_{e=1}^{n_e} [R^e]^{\mathrm{T}} [k_e^e] [R^e] \tag{4.50c}$$

$$[K_r] = \sum_{e=1}^{n_e} [R^e]^{\mathrm{T}} [k_r^e] [R^e] \tag{4.50d}$$

$$\{F_c\} = \sum_{e=1}^{n_e} [R^e]^{\mathrm{T}} \{f_c^e\} \tag{4.50e}$$

$$\left\{F^{\mathrm{ext}}\right\} = \sum_{e=1}^{n_e} [R^e]^{\mathrm{T}} \left\{f^{\mathrm{ext}^e}\right\} \tag{4.50f}$$

Remembering Equation 4.47, and the previous introduced relations, it is possible to write it in the global system formulation, as:

$$\{\delta d_i\}^T \left([M]\{\ddot{d}_i\} + [C_c]\{\dot{d}_i\} + ([K_e] - [K_r])\{d_i\} - \{F_c\} - \left\{F^{\mathrm{ext}}\right\}\right) = 0 \tag{4.51}$$

Finally, the previous equation must be verified to any $\{\delta d_i\}$. So, the global semi-discrete equations of motion are given to its non-trivial solution, yielding:

$$[M]\{\ddot{d}_i\} + [C_c]\{\dot{d}_i\} + ([K_e] - [K_r])\{d_i\} = \{F_c\} + \left\{F^{\mathrm{ext}}\right\} \tag{4.52}$$

4.3.7.3 Numerical Integration - Gauss Quadrature

Gauss quadrature is a very popular numerical integration method widely used in the finite element method, that overcomes the analytical evaluation of certain integrals that are impossible to solve in that way or that are highly time-consuming.

Considering the simple one-dimensional case, in the ξ direction, and allowing the function $f(\xi)$ to be integrated in the $[-1, 1]$ interval, the exact solution of the integral, I, is given by:

$$I = \int_{-1}^{1} f(\xi)\, \mathrm{d}\xi \tag{4.53}$$

According to the Gauss numeric integration rule, the previous result can be approximated by the sum of products between function values in specific, and well defined, points and the corresponding weight coefficients, as:

$$I \approxeq \sum_{j=1}^{n_{GP}} w_i f(\xi_i) \tag{4.54}$$

where n_{GP} and w_i represent, respectively, the number of integration points used (denominated Gauss points) and the weight coefficients associated with the ξ_i evaluation point.

Considering a bi-dimensional case such as the one in Equation 4.61, applying the Gauss numerical integration procedure results in:

$$\int_{-1}^{1}\int_{-1}^{1} \hat{f}(\xi,\eta)\,\mathrm{d}\xi\,\mathrm{d}\eta \approx \sum_{j=1}^{m_{GP}}\sum_{i=1}^{n_{GP}} w_j w_i \hat{f}(\xi_i,\eta_j) \tag{4.55}$$

where n_{GP} and m_{GP} represent the number of integration points considered in the ξ and η natural coordinates, respectively. In Table 4.2 it is possible to see the location of the different Gauss points and the correspondent weight coefficients.

Table 4.2: Location and weight coefficients of the integration points, according to the Gauss quadrature [Moreira, 2004]

$$\int_{-1}^{1} f(x)\,\mathrm{d}x = \sum_{g=1}^{n_g} H_g f\left(a_g\right)$$

n_g	a_g	H_g
1	0.000 000	2.000 000
2	±0.577 350	1.000 000
3	±0.774 597	0.555 556
	0.000 000	0.888 889
4	±0.861 136	0.347 854
	±0.339 981	0.652 154

The determination of the number of Gauss-points used in the numerical integration procedure takes into account that:

- To obtain the exact solution of the integral of a polynomial function of the $2m-1$ degree are necessary m integration points (or the integer number immediately above m);
- More integration points are usually related with more accurate results;
- More integration points lead to a more time-consuming procedure, so it is necessary to address a balance between the solution's precision and the computational effort.

As the used shape functions are bilinear, the exact solution of the elemental integrals is achieved through the use of two Gauss points in ξ and η, that is $n_{GP} = m_{GP} = 2$.

Remembering the elemental matrices and vectors presented in Equations 4.48, as the interpolation functions and their derivatives are defined in the natural coordinate system, it is necessary a transformation process that allows to obtain those derivatives in the Cartesian coordinate system. This process can be described based on the geometric interpolation of the coordinates (Equation 4.39). Thus, it can be presented the matrix $[J]$ as the *Jacobian matrix*, defined as:

$$[J] = \begin{bmatrix} \dfrac{\partial x}{\partial \xi} & \dfrac{\partial y}{\partial \xi} \\ \dfrac{\partial x}{\partial \eta} & \dfrac{\partial y}{\partial \eta} \end{bmatrix} \tag{4.56}$$

from which, substituting the expressions in Equation 4.39, results:

$$[J] = \begin{bmatrix} \sum_{i=1}^{4} x_i \dfrac{\partial N_i}{\partial \xi} & \sum_{i=1}^{4} y_i \dfrac{\partial N_i}{\partial \xi} \\ \sum_{i=1}^{4} x_i \dfrac{\partial N_i}{\partial \eta} & \sum_{i=1}^{4} y_i \dfrac{\partial N_i}{\partial \eta} \end{bmatrix} \tag{4.57}$$

Using the partial derivation rules, it is possible to define the shape functions derivatives written in the Cartesian coordinate system using the Equations 4.44a and 4.44b, as:

$$\begin{Bmatrix} \dfrac{\partial N_i}{\partial x} \\ \dfrac{\partial N_i}{\partial y} \end{Bmatrix} = \begin{Bmatrix} \dfrac{\partial N_i}{\partial \xi}\dfrac{\partial \xi}{\partial x} + \dfrac{\partial N_i}{\partial \eta}\dfrac{\partial \eta}{\partial x} \\ \dfrac{\partial N_i}{\partial \xi}\dfrac{\partial \xi}{\partial y} + \dfrac{\partial N_i}{\partial \eta}\dfrac{\partial \eta}{\partial y} \end{Bmatrix} = \begin{bmatrix} \dfrac{\partial \xi}{\partial x} & \dfrac{\partial \eta}{\partial x} \\ \dfrac{\partial \xi}{\partial y} & \dfrac{\partial \eta}{\partial y} \end{bmatrix} \begin{Bmatrix} \dfrac{\partial N_i}{\partial \xi} \\ \dfrac{\partial N_i}{\partial \eta} \end{Bmatrix} = [J]^{-1} \begin{Bmatrix} \dfrac{\partial N_i}{\partial \xi} \\ \dfrac{\partial N_i}{\partial \eta} \end{Bmatrix} \tag{4.58}$$

where $[J]^{-1}$ represents the inverse of the Jacobian matrix.

Note that in a layerwise finite element the transformation Jacobian matrix does not depend on the layer k considered, as it only depends on the element's geometry.

The element's volume must also be defined in the natural coordinate system to evaluate the aforementioned integrals. The infinitesimal portion of a generic layer's volume, $\mathrm{d}\Omega_k^e$, can be described as:

$$\mathrm{d}\Omega_k^e = \mathrm{d}x\ \mathrm{d}y\ h_k = \det[J]\ \mathrm{d}\xi\ \mathrm{d}\eta\ h_k \tag{4.59}$$

As was seen before, the integrations over the volume can be substituted by two integrations, one over the thickness, that is solved analytically, and one over the element's area. This way, considering a generalized function $f(x, y, z_k)$ evaluated over the volume, it gets:

$$\int_{\Omega_k^e} f(x, y, z_k)\ \mathrm{d}\Omega_k^e = \int_{A^e} \tilde{f}(x, y)\ \mathrm{d}A^e \tag{4.60}$$

where $\tilde{f}(x, y)$ represents the analytical integration of the function over the element's thickness. When considered in the natural coordinate system, with $\xi \in [-1, 1]$ and $\eta \in [-1, 1]$, the previous expression can be written as:

$$\int_{A^e} \tilde{f}(x, y)\ \mathrm{d}A^e = \int_{-1}^{1}\int_{-1}^{1} \hat{f}(\xi, \eta)\ \det[J]\ \mathrm{d}\xi\ \mathrm{d}\eta \tag{4.61}$$

Applying the Gauss numerical integration procedure results in:

$$\int_{A^e} \tilde{f}(x, y)\ \mathrm{d}A^e = \int_{-1}^{1}\int_{-1}^{1} \hat{f}(\xi, \eta)\ \det[J]\ \mathrm{d}\xi\ \mathrm{d}\eta \approxeq \sum_{j=1}^{m_{GP}}\sum_{i=1}^{n_{GP}} w_j w_i\ \det[J]\ \hat{f}(\xi_i, \eta_j) \tag{4.62}$$

where n_{GP} and m_{GP} represent the number of integration points considered in the ξ and η natural coordinates, respectively.

Finally, it is possible to present the expressions to numerically determine the element matrices and vectors:

$$[m^e] = \sum_{k=1}^{n}\sum_{j=1}^{m_{GP}}\sum_{i=1}^{n_{GP}} w_j w_i \det[J]\Big|_{\xi=\xi_i\ ;\ \eta=\eta_j}\ [\hat{N}]_k^{\mathrm{T}}\Big|_{\xi=\xi_i\ ;\ \eta=\eta_j}\ [\hat{J}]_k\ [\hat{N}]_k\Big|_{\xi=\xi_i\ ;\ \eta=\eta_j} \tag{4.63a}$$

$$[c_c^e] = \sum_{k=1}^{n} \sum_{j=1}^{m_{GP}} \sum_{i=1}^{n_{GP}} w_j w_i \det[J]\Big|_{\xi=\xi_i\ ;\ \eta=\eta_j} [\hat{N}]_k^{\mathrm{T}}\Big|_{\xi=\xi_i\ ;\ \eta=\eta_j} [\hat{J}]_k [\Omega] [\hat{N}]_k\Big|_{\xi=\xi_i\ ;\ \eta=\eta_j} \tag{4.63b}$$

$$[k_e^e] = \sum_{k=1}^{n} \sum_{j=1}^{m_{GP}} \sum_{i=1}^{n_{GP}} w_j w_i \det[J]\Big|_{\xi=\xi_i\ ;\ \eta=\eta_j} [\hat{B}]_k^{\mathrm{T}}\Big|_{\xi=\xi_i\ ;\ \eta=\eta_j} [\hat{\mathcal{D}}]_k [\hat{B}]_k\Big|_{\xi=\xi_i\ ;\ \eta=\eta_j} \tag{4.63c}$$

$$[k_r^e] = \sum_{k=1}^{n} \sum_{j=1}^{m_{GP}} \sum_{i=1}^{n_{GP}} w_j w_i \det[J]\Big|_{\xi=\xi_i\ ;\ \eta=\eta_j} [\hat{N}]_k^{\mathrm{T}}\Big|_{\xi=\xi_i\ ;\ \eta=\eta_j} [\hat{J}]_k \left[\Omega^2\right] [\hat{N}]_k\Big|_{\xi=\xi_i\ ;\ \eta=\eta_j} \tag{4.63d}$$

$$\{f_c^e\} = \sum_{k=1}^{n} \sum_{j=1}^{m_{GP}} \sum_{i=1}^{n_{GP}} w_j w_i \det[J]\Big|_{\xi=\xi_i\ ;\ \eta=\eta_j} [\hat{N}]_k^{\mathrm{T}}\Big|_{\xi=\xi_i\ ;\ \eta=\eta_j} [\hat{J}]_k \left[\Omega^2\right] [\hat{N}']_k\Big|_{\xi=\xi_i\ ;\ \eta=\eta_j} \{c_i^e\} \tag{4.63e}$$

$$\left\{f^{\mathrm{ext}^e}\right\} = \sum_{k=1}^{n} \sum_{j=1}^{m_{GP}} \sum_{i=1}^{n_{GP}} w_j w_i \det[J]\Big|_{\xi=\xi_i\ ;\ \eta=\eta_j} [N]_k\Big|_{\xi=\xi_i\ ;\ \eta=\eta_j} \{q_i^e\} \tag{4.63f}$$

4.3.7.4 Shear Locking Protection Through Selective Integration

The shear locking effect consists on the very significant numerical error when determining the elastic stiffness matrix shear terms when analysing thin plates or layers, even for simple geometries, and appears due to the representative limitation of the bilinear shape functions. Contrary to what happens when using Krichhoff-Love thin plates theory, when analysing a pure bending state, the shear components will not be null in all domain. Thus, when using the present plate theory with thin geometries, the shear strain energy will be generally overestimated and preponderant over others and, consequently, the associated calculated displacements are lower than the exact solution [Moreira, 2004]. There are many techniques that can be used to overcome this problem, being the *selective integration* the one studied and used in throughout the present dissertation.

This method is based on the calculation of the shear stiffness components differently from the coupling/membrane and bending terms. In fact, the numerical integration of the shear components is made using a lower number of Gauss points, namely one less in each direction, and the other terms are determined as previously presented (with two Gauss points in each isoparametric component). In addition, a correction coefficient of 5/6 is multiplied by the values obtained through the selective integration process in order to achieve more accurate results [Moreira, 2004; Oñate, 2013].

Despite being a very efficient method, the selective integration technique can induce extra null energy and rigid body natural vibration modes [Moreira, 2004].

4.3.8 Centrifugal Stiffness Matrix

As presented in Section 2.3.3, the centrifugal stiffening effects can be accounted for through a centrifugal stiffness matrix, $[K_g]$, instead the centrifugal force vector. Cook et al. [2007] present a general formulation for the determination of this stress stiffening matrix following the same procedure.

The large (non-linear) strain Green-Lagrange strain-displacement relations are given by:

$$
\begin{aligned}
\varepsilon_{xx} &= \frac{\partial u}{\partial x} + \frac{1}{2}\left[\left(\frac{\partial u}{\partial x}\right)^2 + \left(\frac{\partial v}{\partial x}\right)^2 + \left(\frac{\partial w}{\partial x}\right)^2\right] \\
\varepsilon_{yy} &= \frac{\partial v}{\partial y} + \frac{1}{2}\left[\left(\frac{\partial u}{\partial y}\right)^2 + \left(\frac{\partial v}{\partial y}\right)^2 + \left(\frac{\partial w}{\partial y}\right)^2\right] \\
\varepsilon_{zz} &= \frac{\partial w}{\partial z} + \frac{1}{2}\left[\left(\frac{\partial u}{\partial z}\right)^2 + \left(\frac{\partial v}{\partial z}\right)^2 + \left(\frac{\partial w}{\partial z}\right)^2\right] \\
\gamma_{xy} &= \frac{\partial u}{\partial y} + \frac{\partial v}{\partial x} + \left(\frac{\partial u}{\partial x}\frac{\partial u}{\partial y} + \frac{\partial v}{\partial x}\frac{\partial v}{\partial y} + \frac{\partial w}{\partial x}\frac{\partial w}{\partial y}\right) \\
\gamma_{xz} &= \frac{\partial u}{\partial z} + \frac{\partial w}{\partial x} + \left(\frac{\partial u}{\partial x}\frac{\partial u}{\partial z} + \frac{\partial v}{\partial x}\frac{\partial v}{\partial z} + \frac{\partial w}{\partial x}\frac{\partial w}{\partial z}\right) \\
\gamma_{yz} &= \frac{\partial v}{\partial z} + \frac{\partial w}{\partial y} + \left(\frac{\partial u}{\partial y}\frac{\partial u}{\partial z} + \frac{\partial v}{\partial y}\frac{\partial v}{\partial z} + \frac{\partial w}{\partial y}\frac{\partial w}{\partial z}\right)
\end{aligned}
\tag{4.64}
$$

The initial terms of Equation 4.64 are the customary linear normal and shear strain-displacement relations, used in the elastic potential energy determination and are contemplated in the elastic stiffness matrix, while the non-linear ones become significant if the displacement gradients are not small. On the other hand, remembering the layerwise plate theory assumptions, it is possible to conclude that $\varepsilon_{zz} = 0$ and, for that reason, can not be considered from now on, as well as the $\frac{\partial w}{\partial z}$ term.

Considering the pre-stress potential energy as the elastic strain energy resulting from the imposed loadings, it can be written as:

$$
\Pi^{P\,NL} = \int_{\Omega} \{\varepsilon_{NL}\}^{\mathrm{T}} \{\sigma_0\}\, \mathrm{d}\Omega \tag{4.65}
$$

where $\{\varepsilon_{NL}\}$ represents the strain non-linear components and $\{\sigma_0\}$ the stresses imposed by the loadings (in this case the centrifugal force), that is:

$$
\{\varepsilon_{NL}\} = \begin{Bmatrix} \varepsilon_{xx}^{NL} \\ \varepsilon_{yy}^{NL} \\ \gamma_{xy}^{NL} \\ \gamma_{xz}^{NL} \\ \gamma_{yz}^{NL} \end{Bmatrix} = \begin{Bmatrix} \frac{1}{2}\left[\left(\frac{\partial u}{\partial x}\right)^2 + \left(\frac{\partial v}{\partial x}\right)^2 + \left(\frac{\partial w}{\partial x}\right)^2\right] \\ \frac{1}{2}\left[\left(\frac{\partial u}{\partial y}\right)^2 + \left(\frac{\partial v}{\partial y}\right)^2 + \left(\frac{\partial w}{\partial y}\right)^2\right] \\ \frac{\partial u}{\partial x}\frac{\partial u}{\partial y} + \frac{\partial v}{\partial x}\frac{\partial v}{\partial y} + \frac{\partial w}{\partial x}\frac{\partial w}{\partial y} \\ \frac{\partial u}{\partial x}\frac{\partial u}{\partial z} + \frac{\partial v}{\partial x}\frac{\partial v}{\partial z} \\ \frac{\partial u}{\partial y}\frac{\partial u}{\partial z} + \frac{\partial v}{\partial y}\frac{\partial v}{\partial z} \end{Bmatrix} \quad ; \quad \{\sigma_0\} = \begin{Bmatrix} \sigma_{xx_0} \\ \sigma_{yy_0} \\ \tau_{xy_0} \\ \tau_{xz_0} \\ \tau_{yz_0} \end{Bmatrix} \tag{4.66}
$$

Equation 4.65 can be written after applying the cross product as:

$$\Pi^{P\,NL} = \int_\Omega \left[\frac{1}{2} \left[\left(\frac{\partial u}{\partial x}\right)^2 + \left(\frac{\partial v}{\partial x}\right)^2 + \left(\frac{\partial w}{\partial x}\right)^2 \right] \sigma_{xx_0} + \frac{1}{2} \left[\left(\frac{\partial u}{\partial y}\right)^2 + \left(\frac{\partial v}{\partial y}\right)^2 + \left(\frac{\partial w}{\partial y}\right)^2 \right] \sigma_{yy_0} + \right.$$
$$+ \left(\frac{\partial u}{\partial x}\frac{\partial u}{\partial y} + \frac{\partial v}{\partial x}\frac{\partial v}{\partial y} + \frac{\partial w}{\partial x}\frac{\partial w}{\partial y} \right) \tau_{xy_0} + \left(\frac{\partial u}{\partial x}\frac{\partial u}{\partial z} + \frac{\partial v}{\partial x}\frac{\partial v}{\partial z} \right) \tau_{xz_0} +$$
$$\left. + \left(\frac{\partial u}{\partial y}\frac{\partial u}{\partial z} + \frac{\partial v}{\partial y}\frac{\partial v}{\partial z} \right) \tau_{yz_0} \right] \mathrm{d}\Omega \tag{4.67}$$

After a mathematical rearrange, it can be expressed as a product of a vector with the partial derivations of the displacement field components and a matrix with the stress components:

$$\Pi^{P\,NL} = \sum_{k=1}^{n} \Pi_k^{P\,NL} = \sum_{k=1}^{n} \left[\frac{1}{2} \int_{\Omega_k} \{\delta\}_k^{\mathrm{T}} \begin{bmatrix} [S_k^1] & [0] & [0] \\ [0] & [S_k^1] & [0] \\ [0] & [0] & [S_k^2] \end{bmatrix} \{\delta\}_k \, \mathrm{d}\Omega_k \right] \tag{4.68}$$

where these are given by:

$$\{\delta\}_k^{\mathrm{T}} = \begin{bmatrix} \frac{\partial u_k}{\partial x} & \frac{\partial u_k}{\partial y} & \frac{\partial u_k}{\partial z} & \frac{\partial v_k}{\partial x} & \frac{\partial v_k}{\partial y} & \frac{\partial v_k}{\partial z} & \frac{\partial w_k}{\partial x} & \frac{\partial w_k}{\partial y} \end{bmatrix}$$
$$S_k^1 = \begin{bmatrix} \sigma_{xx_0\,k} & \tau_{xy_0\,k} & \tau_{xz_0\,k} \\ \tau_{xy_0\,k} & \sigma_{yy_0\,k} & \tau_{yz_0\,k} \\ \tau_{xz_0\,k} & \tau_{yz_0\,k} & 0 \end{bmatrix} \; ; \; S_k^2 = \begin{bmatrix} \sigma_{xx_0\,k} & \tau_{xy_0\,k} \\ \tau_{xy_0\,k} & \sigma_{yy_0\,k} \end{bmatrix} \tag{4.69}$$

Remembering the layerwise plate displacement field (Equation 4.9) it is possible to write the vector $\{\delta\}$ as a function of the generalized variables (Equation 4.11) as follows:

$$\{\delta\}_k = [\mathcal{G}]_k \{d\}_k \tag{4.70}$$

where $[\mathcal{G}]_k$ is the non-linear strain-displacement matrix of the layer k, given by:

$$[\mathcal{G}]_k = \left[\begin{array}{cccccccccc:c} \frac{\partial}{\partial x} & 0 & 0 & \frac{h_1}{2}\frac{\partial}{\partial x} & 0 & \cdots & h_j\frac{\partial}{\partial x} & 0 & \cdots & \left(\frac{h_k}{2}+z_k\right)\frac{\partial}{\partial x} & 0 & [0] \\ \frac{\partial}{\partial y} & 0 & 0 & \frac{h_1}{2}\frac{\partial}{\partial y} & 0 & \cdots & h_j\frac{\partial}{\partial y} & 0 & \cdots & \left(\frac{h_k}{2}+z_k\right)\frac{\partial}{\partial y} & 0 & [0] \\ 0 & 0 & 0 & 0 & 0 & \cdots & 0 & 0 & \cdots & 1 & 0 & [0] \\ 0 & \frac{\partial}{\partial x} & 0 & 0 & \frac{h_1}{2}\frac{\partial}{\partial x} & \cdots & 0 & h_j\frac{\partial}{\partial x} & \cdots & 0 & \left(\frac{h_k}{2}+z_k\right)\frac{\partial}{\partial x} & [0] \\ 0 & \frac{\partial}{\partial y} & 0 & 0 & \frac{h_1}{2}\frac{\partial}{\partial y} & \cdots & 0 & h_j\frac{\partial}{\partial y} & \cdots & 0 & \left(\frac{h_k}{2}+z_k\right)\frac{\partial}{\partial y} & [0] \\ 0 & 0 & 0 & 0 & 0 & \cdots & 0 & 0 & \cdots & 0 & 1 & [0] \\ 0 & 0 & \frac{\partial}{\partial x} & 0 & 0 & \cdots & 0 & 0 & \cdots & 0 & 0 & [0] \\ 0 & 0 & \frac{\partial}{\partial y} & 0 & 0 & \cdots & 0 & 0 & \cdots & 0 & 0 & [0] \end{array} \right] \tag{4.71}$$

It is possible to identify the resemblances between the non-linear strain-displacement matrix, $[\mathcal{G}]_k$ (Equation 4.71), and the strain matrix, $\mathcal{B}$ (Equation 4.18). After considering the finite element discretization and the geometric and displacement field interpolations (Section 4.3.7), Equation 4.68 can be written as:

$$\begin{aligned}
\Pi^{P\,NL} &= \sum_{k=1}^{n} \Pi_k^{P\,NL} = \sum_{e=1}^{n_e} \left(\sum_{k=1}^{n} \left[\frac{1}{2} \int_{\Omega_k} \{d^e\}^{\mathrm{T}} [\mathcal{G}]_k^{\mathrm{T}} [\tau]_k [\mathcal{G}]_k \{d^e\} \, \mathrm{d}\Omega_k \right] \right) = \\
&= \sum_{e=1}^{n_e} \left(\sum_{k=1}^{n} \left[\frac{1}{2} \int_{\Omega_k} \{d_i^e\}^{\mathrm{T}} [N]_k^{\mathrm{T}} [\mathcal{G}]_k^{\mathrm{T}} [\tau]_k [\mathcal{G}]_k [N]_k \{d_i^e\} \, \mathrm{d}\Omega_k \right] \right) = \\
&= \sum_{e=1}^{n_e} \left(\sum_{k=1}^{n} \left[\frac{1}{2} \int_{\Omega_k} \{d_i^e\}^{\mathrm{T}} [G]_k^{\mathrm{T}} [\tau]_k [G]_k \{d_i^e\} \, \mathrm{d}\Omega_k \right] \right) = \\
&= \sum_{e=1}^{n_e} \{d_i^e\}^{\mathrm{T}} \left(\sum_{k=1}^{n} \left[\frac{1}{2} \int_{\Omega_k} [G]_k^{\mathrm{T}} [\tau]_k [G]_k \, \mathrm{d}\Omega_k \right] \right) \{d_i^e\}
\end{aligned} \tag{4.72}$$

where $[\tau]_k$ represents the matrix with the stress field terms and $[G]_k = [\mathcal{G}]_k [N]_k$.

Regarding the previously affirmed resemblances, after a energetic variational formulation and the weak form considerations, it is possible to define the element centrifugal stiffness matrix as:

$$\left[k_g^e\right] = \sum_{k=1}^{n} \left[k_{g_k}^e\right] = \sum_{k=1}^{n} \left[\frac{1}{2} \int_{\Omega_k} [G]_k^{\mathrm{T}} [\tau]_k [G]_k \, \mathrm{d}\Omega_k \right] \tag{4.73}$$

While in the previously presented calculation processes the strain and inertia matrices were analytically integrated over the element's thickness and then the numerical integration procedure was performed over the element's area, in the present case the Gauss quadrature is applied in all three orthogonal natural coordinates (ξ, η, ζ). By doing so, the expression to numerically determine the element matrix is given by:

$$\begin{aligned}
\left[k_g^e\right] = \frac{1}{2} \sum_{k=1}^{n} \sum_{l=1}^{p_{GP}} \sum_{j=1}^{m_{GP}} \sum_{i=1}^{n_{GP}} w_l w_j w_i \det[J]\Big|_{\xi=\xi_i\,;\,\eta=\eta_j\,;\,\zeta=\zeta_l} \\
[G]_k^{\mathrm{T}}\Big|_{\xi=\xi_i\,;\,\eta=\eta_j\,;\,\zeta=\zeta_l} [\tau]_k\Big|_{\xi=\xi_i\,;\,\eta=\eta_j\,;\,\zeta=\zeta_l} [G]_k\Big|_{\xi=\xi_i\,;\,\eta=\eta_j\,;\,\zeta=\zeta_l}
\end{aligned} \tag{4.74}$$

Recalling that the relation between the elemental and global degrees of freedom can be established through the connectivity matrix, $[R^e]$ (Equation 4.49), the assembled global centrifugal stiffness matrix is defined as:

$$[K_g] = \sum_{e=1}^{n_e} [R^e]^{\mathrm{T}} \, [k_{g_e}] \, [R^e] \tag{4.75}$$

Finally, considering the absence of external loads, $\left\{F^{\mathrm{ext}}\right\} = \{0\}$, the global static problem presented in Equation 2.29 can also be represented as:

$$[M]\{\ddot{d}_i\} + [C_c]\,\{\dot{d}_i\} + ([K_e] - [K_r] + [K_g])\,\{d_i\} = \{0\} \tag{4.76}$$

since the centrifugal force stiffening effects are now considered in the matrix $[K_g]$.

Chapter 5

Numerical Simulation Methods

The present chapter will address some simulation methods used to study the dynamic behaviour of a gearwheel with superficial viscoelastic damping treatments through a numerical simulation using a layerwise finite element. Initially, the process to obtain the geometric model of the present case will be shown and explained. Then, the most important features and procedures of the developed finite element method software will be presented, as well as some simplifying assumptions that significantly reduce the computing time are exposed and explained. Finally, some results obtained with the developed program are compared with results presented in the literature or obtained using a commercial finite element method software, namely ANSYS®, as a validation procedure.

5.1 Geometrical Modeling

As initially presented in Chapter 1, the main motivation behind the present dissertation is a patent proposed by Marsaudon and Cutuli [2014], where a viscoelastic damping device was used in a gearwheel to reduce its vibrations. So, one of the primarily objectives of the developed software was to conveniently geometrically represent said setup, so that in a later stage the damping capacity of different treatment configurations could be evaluated.

5.1.1 Gearwheel

First it was necessary to obtain the characteristics of the studied gearwheel, used in the *Arriel* engine. Consulting this engine's sale's brochure (Safran Helicopter Engines [2012]), where Figure 5.1 was taken from, it is possible to conclude that the maximum working output power is $\dot{W} = 531$ kW and that it rotates at $\Omega = 6000$ rpm.

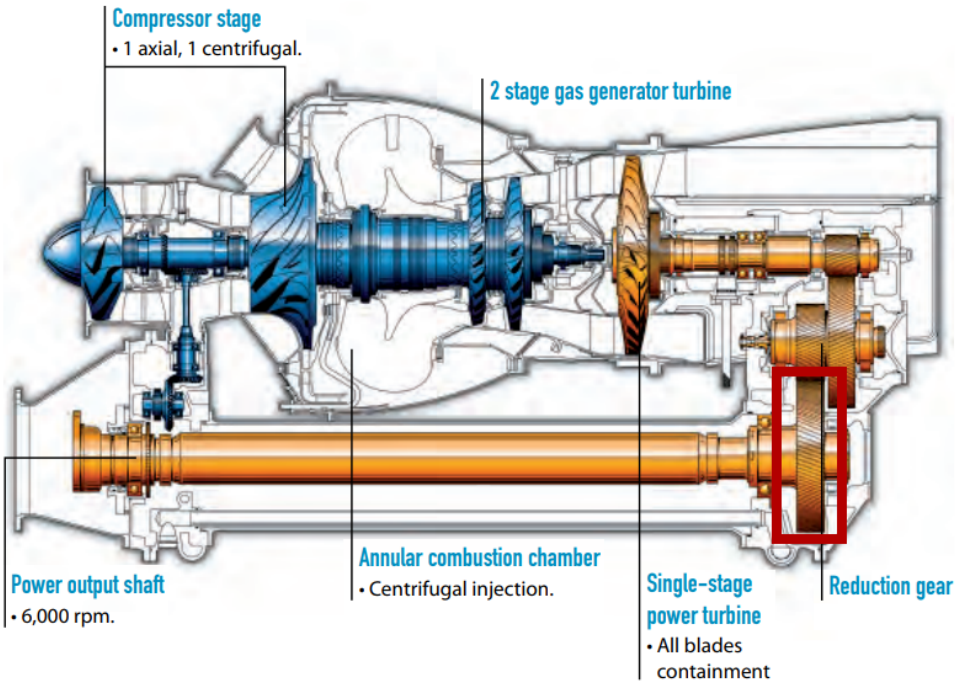

Figure 5.1: Representation of the *Arriel 1*® turbine engine with the studied gearwheel marked with a red box [Safran Helicopter Engines, 2012].

However, the dimensions of the gearwheel could not be found. This leaded to the usage of a gear design software, namely KISSsoft®, that allows its dimensioning when given some informations about the operation conditions. In this case, the calculation for a helical gear pair, where the wheels' webs had a smaller thickness than the hub, was performed.

One of the assumptions throughout this process was to consider that Figures 1.2, 1.3 and 5.1 were obtained from a scaling and simplification process from the real detailed design of the *Arriel 1* engine and the treated gearwheel. Thus, by measuring the ratio between the gearwheels outer diameter it was possible to determine the gear ratio $i = 2.04$. Furthermore, a helix angle of $\beta = 15°$, a safety factor of $SF = 1.4$, an application factor (coefficient that compensates for any uncertainties in loads and impact) of $KA = 1.25$ and a required service life of $H = 20\,000$ hours were considered for dimensioning purposes, as well as the case-carburized and hardened 18CrNiMo7-6 steel for both wheels material.

Defining all these inputs in KISSsoft®, the dimensions of the correspondent driven gearwheel (Figure 5.2) were obtained, from where resulted $\phi_{\text{ext}} = 138.00\,\text{mm}$, $b_{\text{web}} = 6.00\,\text{mm}$, $b_{\text{rim}} = 36.00\,\text{mm}$ and $s = 5.67\,\text{mm}$.

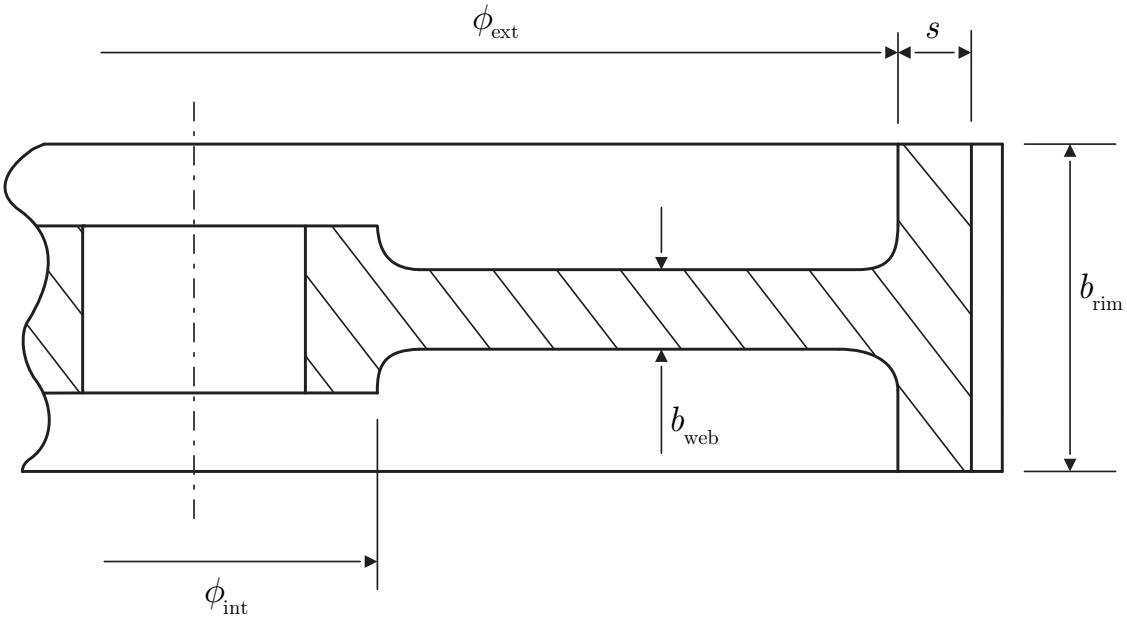

Figure 5.2: Schematic representation of the gear designed with the KISSsoft® software.

The ratios between the web's outer diameter, ϕ_{ext}, the web's thickness, b_{web}, the facewidth, b_{rim}, and the gear rim thickness, s, obtained through KISSsoft® agree with the same ratios verified in Figure 1.3, which means that, according to the previously presented assumption, the designed gearwheel is representative of the present case being studied.

There are, however, three facts that must be addressed:

- The gearwheel's teeth are not considered for simulation purposes, but only the rim were they are attached;
- The hub is considered to be cylindrical, thus the web is continuous and is not connected to it in more than one place, contrarily to what can be seen in the gearwheel presented on the patent under analysis (Figure 1.3). However, this feature of the patent's gearwheel will be considered when studying the viscoelastic damping device, since it constraints the possibly treated area to a radius in the range $r_{damping} = 34.00\,\text{mm}$ to $69.00\,\text{mm}$;
- There was no available information about the hub's diameter. Yet, recalling the scale assumption, a value for this dimension was obtained in agreement with the designed gearwheel and the one being studied, from what resulted $\phi_{\text{int}} = 31.00\,\text{mm}$.

Furthermore, the patent considers a wheel that presents a truncated cone (frustoconical) shape, meaning that its web is not perpendicular to the shaft, and, consequently, the rotation axis. In fact, it presents a slope angle, α, (Figure 5.3) that in the representations presented in the patent is $\alpha = 70°$. So, when analyzing a sloped gearwheel throughout this dissertation, this will be the considered value for the inclination of the web, whereas

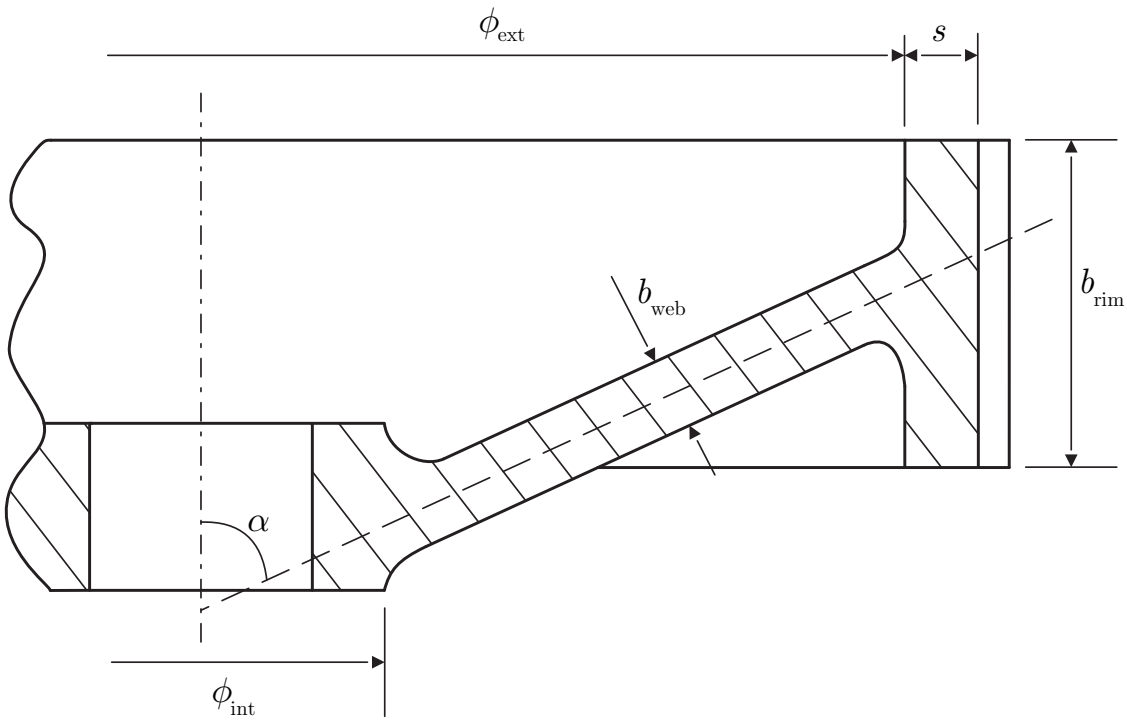

Figure 5.3: Schematic representation of the frustoconical designed gear.

when analyzing a plane gearwheel this angle will naturally be $\alpha = 90°$. Note that in both cases the diameters and the thicknesses remain the same.

Table 5.1 presents all the relevant dimensions of the component used to study the case presented on the patent.

Table 5.1: Considered gearwheel dimensions

$\phi_{\mathbf{ext}}$ [mm]	$b_{\mathbf{web}}$ [mm]	$b_{\mathbf{rim}}$ [mm]	s [mm]	α [°]
138.00	6.00	36.00	5.67	70 or 90

5.1.2 Viscoelastic Damping Device

Concerning the viscoelastic damping device, it was also necessary to define some basic characteristics that remained constant throughout the present dissertation despite the different tested configurations. These were, essentially, the materials and thicknesses of each layer.

The viscoelastic material considered in this study was the 3M^{TM} ISD112, mainly because it is a very commonly used material in viscoelastic damping devices with CLD configuration for automotive, aerospace, electrical and mechanical applications, such as disk drives, automotive covers, panel dampers and wing dampers. This is an acrylic based material, characterized by its excellent damping performance and thermal stability for long term applications at moderate temperatures, and also the ones that experience short high temperature excursions (below 120 °C), which may correspond to the case being studied [3M, 2017].

Figure 5.4 represents this material's shear storage modulus and the loss factor variations with the loading frequency and the service temperature. To find these properties for the correspondent working conditions, first one must find the intersection point between the horizontal constant frequency and the isothermal lines, then extend a vertical line from this point so that it intersects the storage modulus and loss factor curves. Finally, these parameters' values can be found on the left-hand axis by extending a horizontal line from these second intersection points [3M, 2017].

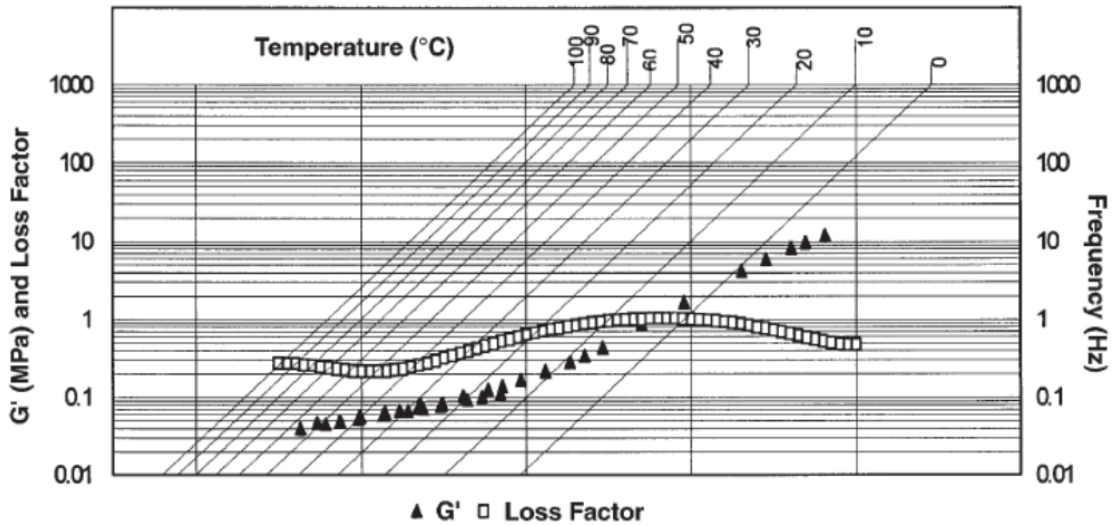

Figure 5.4: 3M^{TM} ISD112 shear storage modulus and loss factor temperature and frequency dependence [3M, 2017].

Throughout the present dissertation, the constitutive properties of the viscoelastic material are determined using the anelastic displacement field (ADF) model, presented previously in Section 3.4.1.2, using three terms of the series. Vasques et al. [2010a] identified the necessary parameters for the 3M^{TM} ISD112 at 27 °C, which can be seen in Table 5.2.

Table 5.2: 3M^{TM} ISD112 ADF parameters using three series ($n = 3$) [Vasques et al., 2010a]

i	G_0 [Mpa]	Δ_i	Ω_i
1		3.5286	504.20
2	0.1789	8.7533	4286.5
3		60.324	39313

In Figure 5.5 the storage modulus and the loss factor dependencies with the loading frequency obtained through this model are plotted.

In what concerns the backing layer, the material considered for this purpose was the same as used in the gearwheel, regular steel, because it is an elastic material with reasonably high elastic modulus, thus allowing good performance of the present CLD configured damping device.

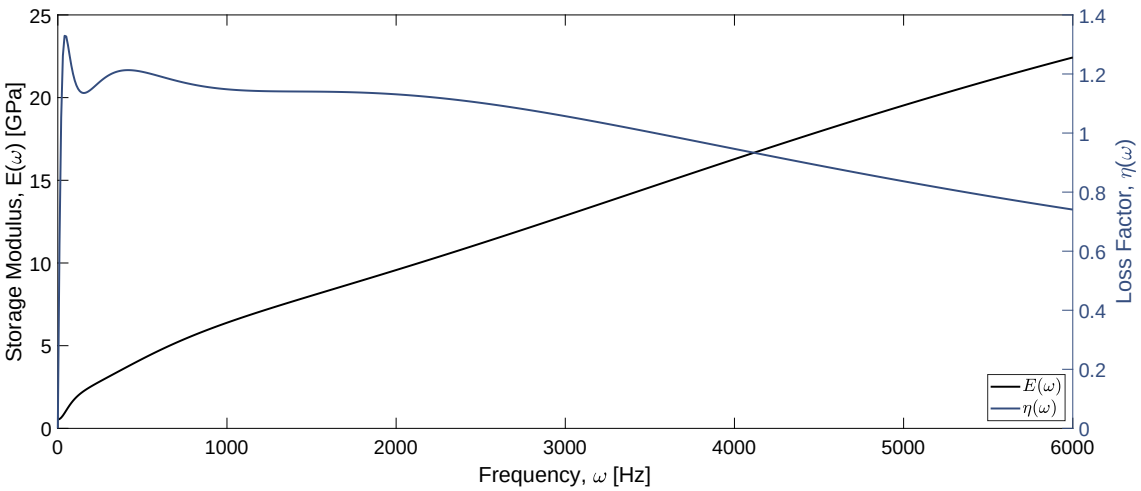

Figure 5.5: 3M^{TM} ISD112 storage modulus and loss factor at 27 °C obtained trough the three term series ADF model.

Finally, the thicknesses of both viscoelastic and elastic layers, e_1 and e_2, respectively, were defined in agreement with the ranges presented on the patent (and in Section 1.1). Table 5.3 shows these values, as well each layer's Poisson's ratio and density. Note that, contrary to what is shown in Figures 1.3 and what is proposed in the patent, the considered viscoelastic material thickness is lower than the one of the backing layer. In fact, the studied document suggests that a thicker viscoelastic layer should be used. This has not been implemented mainly because in the common usage of the 3M^{TM} ISD112 the involved thickness is lower and around the considered value. However, the considered constraining layer's thickness is equal to the value that Marsaudon and Cutuli [2014] refer as preferable for the damping device being studied.

Table 5.3: Viscoelastic and constraining layers' thicknesses, Poisson's ratios and densities considered

Layer	i	e_i [mm]	ν_i	ρ_i [kg/m^3]
Viscoelastic	1	0.50	0.49	1140
Constraining	2	1.00	0.30	7850

5.1.3 Mesh Parameters

Using the finite element method to perform the necessary analysis, it requires a domain discretization using the four noded quadrilateral shell facet elements studied previously in Chapter 4. Throughout the present dissertation a structured circular mesh is used, characterized by the number of radial and circumferential divisions, n_{er} and n_{ec} respectively. As can be easily understood, the finer the mesh (more divisions and, consequently, more elements), the closer the results become to the real values, once the global structure behavior gets closer to a continuous one and the interpolation processes are carried out in smaller domains, reducing the associated error. However, the greater the number of elements, the greater the computing effort and, consequently, the greater the time required to execute the numerical simulation.

In the present work, the mesh parameters were chosen based on these two principles. In fact, the used mesh should allow obtaining accurate values, and since the representation

and modal analysis of the studied viscoelastic damper device is required, the mesh should be able to correctly represent the treatment configurations and the resulting mode shapes (rough circular meshes are associated with the lack of determination and thus representation of some normal modes). A mesh convergence analysis was performed (Section 5.3) and it was concluded that the values:

$$n_{er} = 20 \quad ; \quad n_{ec} = 50 \tag{5.1}$$

enable the best compromise solution between the obtained results and the simulation time. Figure 5.6 presents the resulting mesh, from which one can easily determine the total number of elements, N_e, and nodes, N_n, as follows:

$$N_e = n_{er} \times n_{ec} = 1000 \quad ; \quad N_n = n_{ec} \times (n_{er} + 1) = 1050 \tag{5.2}$$

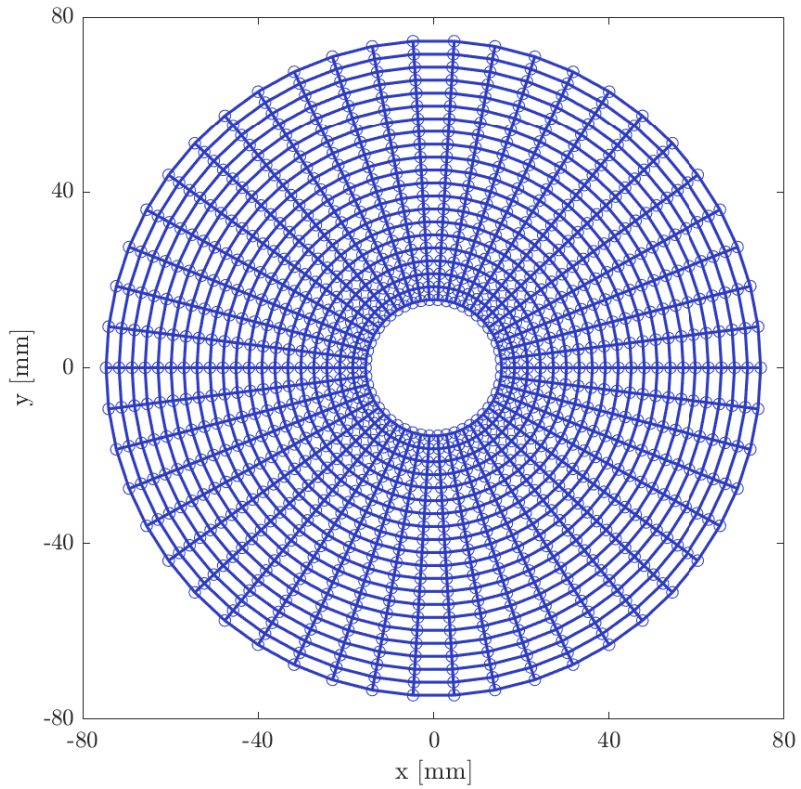

Figure 5.6: Structured circular mesh used.

The exceptions to the use of these parameters are verified when analyzing circumferential treatments with three, four and six sections, where $n_{ec} = 48$ circumferential elements are considered, remaining $n_{er} = 20$, to ensure full symmetry of the geometry. One must note that this change does not lead to significant variations on the results neither reduces the simulation time significantly.

Figure 5.7 shows the three-dimensional mesh used in the analysis of the frustoconical shaped cases. This is obtained through the plane case mesh, presented previously, adding each node the correspondent z coordinate.

Note that the elements positioned in the outer rim zone are not sloped, i.e. are parallel to the xOy coordinate plane. This strategy allows the correct geometrical modeling of this gearwheel's element just by attributing the correspondent thickness, b_{rim}, to the matching

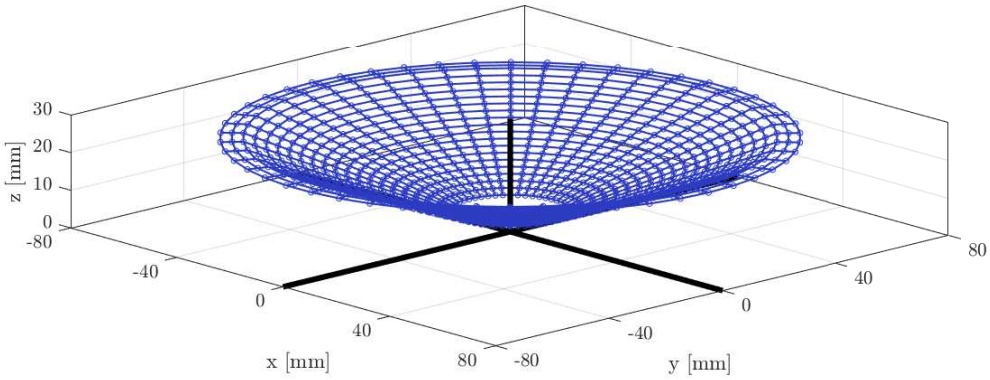

Figure 5.7: Structured three-dimensional circular mesh used.

elements, different from the others' value, b_{web}. Despite nothing has been said and not being perceptible in the mesh representation, this method of different thickness depending on the element's place is also applied in the plane gearwheel analysis to properly represent both zones.

Finally, it is important to refer that the only boundary condition considered in all the performed analysis is clamping in the inner circumference nodes, because when deformed the web is not allowed to move or rotate relative to the hub and all other nodes are constraint-free.

5.2 Finite Element Method Software

In order to study the dynamic response of rotating plane and sloped disks with viscoelastic damping treatments, a proper finite element method software was programmed in the MATLAB® environment. A previously developed base algorithm to the analysis of static circular layerwise plates was modified to ensure the correct simulation of the studied geometry and to include the rotational effects. In the present Section, the program procedures from an user point of view will be briefly presented and then the most important implemented features explained.

5.2.1 Basic Procedure

The obtained finite element method program procedure can be divided into three principal categories, same as most commercial softwares, namely the *data input*, *processing* and *post-processing*.

Data Input

In the data input stage the user first defines the analysis that wants to perform, namely static, modal or frequency response analysis. Then defines a set of characteristics of the system, its dimensions and some other important parameters dependent on the selected analysis. It is also in this stage that the viscoelastic damping treatment properties are defined, namely the system's total number of layers in the treated area (if a damping device as the one presented in the patent is being studied, there will be three total layers, the host, the viscoelastic and the constraining one), their thickness, their materials' properties and the treatment's configuration. This last characteristic can be generated manually,

defining the treated elements, or automatically, if a circumferential or a radial setup is intended, the user just needs to define the correspondent parameters. Before finishing this stage, the mesh is automatically defined and plotted.

Processing

Moving on to the processing stage, this is where/when all the necessary matrices for the selected analysis are determined, according to what is presented in Sections 4.3.7.2 and 4.3.7.3, and the solution to the defined analysis obtained.

Concerning the matrices calculation, some important aspects can be addressed more carefully, such as the definition of a local coordinate system in the elemental matrix calculation, which follows a similar methodology to the one proposed by Oñate [2013] for flat shell elements. In fact, as presented in Figure 5.8, the considered local frame is defined by the three unit directory vectors $\vec{\nabla}_{x^e}$, $\vec{\nabla}_{y^e}$ and $\vec{\nabla}_{z^e}$.

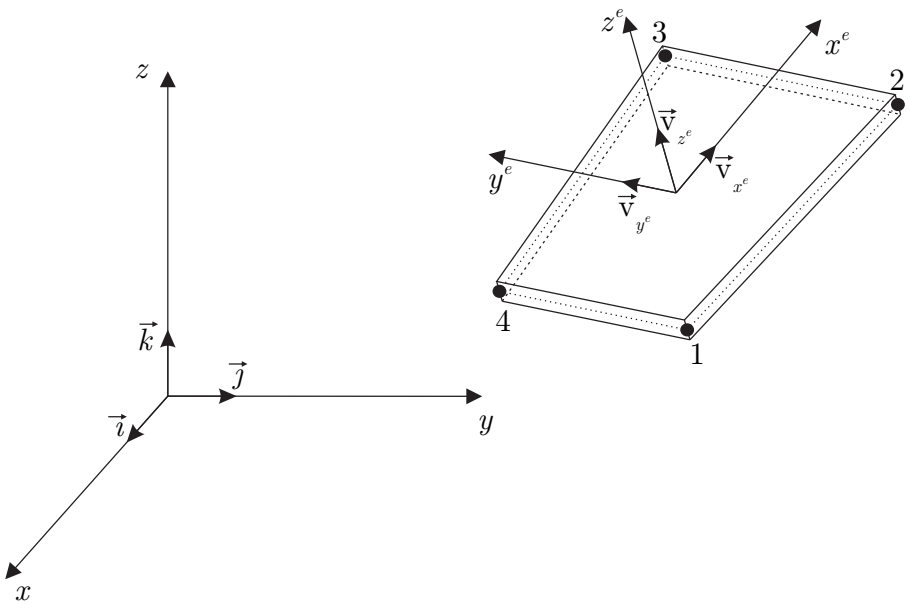

Figure 5.8: Local elemental coordinate system.

The first one is obtained trough the directions of the sides 1-2 and 4-3 in such a way that the x^e axis represents a symmetry line for the element.

$$\vec{\nabla}_{x^e} = \frac{\vec{\nabla}_{1-2} + \vec{\nabla}_{4-3}}{\|\vec{\nabla}_{1-2} + \vec{\nabla}_{4-3}\|} \tag{5.3}$$

Next the direction cosines of the z^e axis are obtained through the normal property of the cross product between two vectors. In fact, being the element flat, it is known that the cross product between the $\vec{\nabla}_{x^e}$ vector and the vector that defines the direction 1-4 results in a normal vector, as wanted. So, $\vec{\nabla}_{z^e}$ is obtained as:

$$\vec{\nabla}_{z^e} = \frac{\vec{\nabla}_{x^e} \times \vec{\nabla}_{1-4}}{\|\vec{\nabla}_{x^e} \times \vec{\nabla}_{1-4}\|} \tag{5.4}$$

Finally, the directory vector of the y^e axis is determined using the cross product property again:

$$\overrightarrow{\nabla}_{y^e} = \frac{\overrightarrow{\nabla}_{z^e} \times \overrightarrow{\nabla}_{x^e}}{\|\overrightarrow{\nabla}_{z^e} \times \overrightarrow{\nabla}_{x^e}\|} \tag{5.5}$$

After calculating a elemental matrix using the correspondent local coordinate system, a transformation matrix to the global system is used and finally it is assembled in the correspondent global matrix.

Another aspect that is important to note is the calculation of the centrifugal stiffness matrix for the modal and frequency response analysis of the damped systems. In fact, once the viscoelastic material's properties, namely the storage modulus, depend on the frequency, it would be necessary to solve the static problem and to determine this matrix for every evaluated value, which would be very time consuming. However, a simplification process of considering this matrix constant throughout the aforementioned analysis was implemented and validated, since were not verified significant differences on the obtained results.

According to Figure 5.5, the storage modulus of the 3M^{TM} ISD112 viscoelastic material presents a nearly linear evolution with the frequency and the values it takes are small (nearly 10% or below) when compared to the steel considered for the gearwheel and the backing layer ($E_{steel} = 200\,\text{GPa}$). Thus, it can be questioned if its stiffness will play a major role on the determination of the centrifugal stiffness matrix. To do so, an average value for the storage modulus can be considered, that is used for the determination of said matrix, that will be taken as constant throughout the analysis. Then, the obtained results can be compared with the values corresponding to the calculation of the centrifugal stiffness matrix at each evaluated frequency.

Looking more specifically at the modal analysis implemented process, first the static storage modulus for the viscoelastic material is considered, $E_0 = 533122\,\text{Pa}$, and the elastic stiffness matrix is updated, that is:

$$[K_e] = [K_{e,\,\text{E}}] + E_0[K_{e,\,\text{V}}] \tag{5.6}$$

where $[K_{e,\,\text{E}}]$ represents the stiffness matrix considering only the elastic layers, using the correspondent Young's modulus in its determination, and $[K_{e,\,\text{V}}]$ represents the stiffness matrix considering only the viscoelastic layer, using an unitary storage modulus in its determination to allow the update of this property with the evaluated frequencies.

This matrix is used to solve the static problem presented previously in Equation 2.29 and the centrifugal stiffness matrix is calculated. The eigenproblem is then solved and the correspondent natural frequencies and normal modes, ω_{n_i} and $\{\phi_i\}$, $i = 1, 2, \cdots, n$, respectively, determined. Considering the frequency range between the minimum and the maximum calculated natural frequencies and determining the constitutive properties of the viscoelastic material for p equally spaced frequencies within this interval, an average value for the storage modulus can be obtained as:

$$E_{\text{average}} = \frac{E(\omega_1 = \omega_{n_{\min}}) + \sum_{i=2}^{p-1} E(\omega_i) + E(\omega_p = \omega_{n_{\max}})}{p} \tag{5.7}$$

Throughout the present document the modal analysis were performed using $p = 10000$.

Considering the storage modulus of the viscoelastic material as the average value calculated, the previous process of updating the elastic stiffness matrix, determining the centrifugal stiffness matrix, obtaining the natural frequencies and calculating the average storage modulus of the range, is iteratively repeated until the maximum difference in the frequencies values between iterations is less than 0.1 Hz, or if more than 30 iterations take

place, since in this case the process does not show a convergent behavior. The last calculated centrifugal stiffness matrix is then taken as constant and the one that will be used in the next step of the modal analysis, namely the IMSE method (Step 2. in Figure 3.14) to obtain the updated natural frequencies values and the modal loss factors. To simplify its understanding, the algorithm behind this iterative simplification process can be seen in Figure 5.9.

1. Calculation of the mass, centrifugal softening and elastic stiffness matrices, considering the static viscoelastic material's storage modulus, $E_{\text{visco}} = E_0$;

$$[M] \;\; ; \;\; [K_r] \;\; ; \;\; [K_e] = [K_{e,\,\text{E}}] + E_0[K_{e,\,\text{V}}]$$

2. Determination of the centrifugal stiffness matrix, $[K_g]$, and solving of the corresponding eigenproblem;

$$\text{Re}\left([K_e] + [K_g] - [K_r]\right)\{\phi\}_r = \omega_r^2[M]\{\phi\}_r$$

3. Loop until convergence;

   - Determination of the average storage modulus in the calculated natural frequencies range;

$$E_{\text{average}} = \frac{E(\omega_1 = \omega_{n_{\min}}) + \sum_{i=2}^{p-1} E(\omega_i) + E(\omega_p = \omega_{n_{\max}})}{p}$$

   - Update the elastic stiffness matrix for that value;

$$[K_e] = [K_{e,\,\text{E}}] + E_{\text{average}}[K_{e,\,\text{V}}]$$

   - Determination of the centrifugal stiffness matrix and solving of the corresponding eigenproblem;
   - Convergence condition test;

$$\max\left(\Delta_\omega\right) = \max\left(\mid \omega_r^{j+1} - \omega_r^j \mid\right) \leq \Delta_{\max}$$

4. Application of the IMSE method for the update of the natural frequency values and determination of the modal loss factors.

Figure 5.9: Simplified modal analysis algorithm.

Concerning the direct frequency response implemented process, the process is simpler but somewhat similar to the one presented previously. In fact, being necessary to define the n frequency values at which the response will be evaluated, $(\omega_1, \omega_2, \cdots, \omega_i, \cdots, \omega_n)$, the average storage modulus is simply calculated as:

$$E_{\text{average}} = \frac{\sum_{i=1}^{n} E(\omega_i)}{n} \tag{5.8}$$

Then, this value is directly used to update the elastic stiffness matrix,

$$[K_e] = [K_{e,\,\mathrm{E}}] + E_{\mathrm{average}}[K_{e,\,\mathrm{V}}] \tag{5.9}$$

and the centrifugal stiffness matrix is determined through the previously presented method, being then considered constant throughout the solving of the system of equations of motion used to determine the frequency responses, presented in Section 3.4.3.1. Thus, there is no iterative process to determine the centrifugal stiffness matrix, it is done with only one step, contrary to what was implemented in the modal analysis. Figure 5.10 presents the algorithm of what was previously mentioned.

1. Determination of the average storage modulus in the defined frequency range;

$$E_{\mathrm{average}} = \frac{\sum_{i=1}^{n} E(\omega_i)}{n}$$

2. Calculation of the mass, centrifugal softening and elastic stiffness matrices, considering the static viscoelastic material's storage modulus, $E_{\mathrm{visco}} = E_0$;

$$[M] \;\; ; \;\; [K_r] \;\; ; \;\; [K_e] = [K_{e,\,\mathrm{E}}] + E_{\mathrm{average}}[K_{e,\,\mathrm{V}}]$$

3. Calculation of the centrifugal stiffness matrix, $[K_g]$;

4. Determination of the frequency responce, $\alpha_{jl}\,(\omega_i)$, for each evaluation frequency, ω_i;

$$\left([K_{e,\,\mathrm{E}}] + \bar{E}\,(\omega_i)\,[K_{e,\,\mathrm{V}}] + [K_g] - [K_r] - \omega_i^2[M]\right)\left\{\bar{X}(\omega_i)\right\}_l = \{F_l(\omega_i)\}$$

$$\{\alpha\,(\omega_i)\}_l = \frac{\left\{\bar{X}\,(\omega_i)\right\}_l}{F_l} \Longrightarrow \alpha_{jl}\,(\omega_i) \Longrightarrow \{\alpha_{jl}(\omega)\}$$

Figure 5.10: Simplified modal analysis algorithm.

Post-Processing

In the post-processing stage, the obtained results are treated and shown to the user, mainly in a graphical form. In fact, when a modal analysis is executed, the natural frequencies and the modal loss factors are presented in the command window and the mode shapes can be plotted as the normalized three-dimensional deformed mesh or a normalized color map either of the total displacement or of each directional displacement. When a direct frequency response analysis is executed the Bode diagram of the selected frequency response function is plotted

5.3 Implemented Finite Element and Numerical Method Validation

In order to validate the implemented rotating layerwise facet shell finite element, some results obtained using the developed software were compared with data presented in the literature, for the plane gearwheel, or values obtained using a commercial finite element method software, namely ANSYS®, for the sloped case.

Note that when studying axisymmetric stationary (or rotative without considering the Coriolis effect) structures occurs the natural frequencies' multiplicity phenomenon, which corresponds to the cases when two modes present equal natural frequency value but different mode shapes, generally rotated by 90°. However, these normal modes have the same number of nodes, that in the disk case can be circumferential or diametral. Thus, to make it easier and more comprehensible, the designation "mode (m,n)" or "(m,n) mode" will be used throughout the present dissertation to refer the pair of natural modes characterized by the same number of nodal diameters, m, and nodal circumferences, n.

5.3.1 Plane Disk

To validate the implemented finite element in the study of plane disks, the obtained results were compared to some data found in the literature, namely from Sinha [1987], D'Angelo and Mote [1993] and Hsieh and Abel [1995].

5.3.1.1 Stationary Case

Firstly, the stationary plane disk case was validated with the results obtained by D'Angelo and Mote [1993], where both experimental and analytical (through an one-term Galerkin expansion) modal analysis were presented for a regular steel plane disk, whose characteristics can be summarized in Table 5.4, where ϕ_i represents the inner diameter, ϕ_e the outer diameter, b its thickness, E the material's Young modulus, ν its Poisson's ration and ρ its density.

Table 5.4: Dimensions and constitutive properties of the disk analyzed by D'Angelo and Mote [1993]

ϕ_i [mm]	ϕ_e [mm]	b [mm]	E [GPa]	ν	ρ [kg/m^3]
106.7	356	0.775	200	0.3	7840

Different meshes were used as a way to study their convergence. The results obtained for the first 10 modes with 5×20, 10×20, 10×30, 10×40 and 20×50 meshes (where the first number indicates the number of radially distributed elements and the second corresponds to the number of circumferential distributed elements) are presented in Tables 5.5 to 5.9. Note that in Table 5.5 the natural frequency multiplicity phenomenon is present, whereas in the others it is only referred one value for each mode once the repetition would not reflect new nor valuable information. Moreover, Figures 5.11, 5.12 and 5.13 represent this convergence study graphically. Note that $|\Delta_r|$ represents the absolute value of the relative difference of the obtained results in respect to the ones presented in the literature.

Table 5.5: Stationary plane disk, 5×20 Mesh (100 Elements)

Mode	Present Model	D'Angelo and Mote [1993] Experimental Approach		D'Angelo and Mote [1993] Analytical Approach	
(m,n)	ω_n [Hz]	ω_n [Hz]	$\lvert\Delta_r\rvert$ [%]	ω_n [Hz]	$\lvert\Delta_r\rvert$ [%]
(1,0)	40.59	37.19	9.14	39.08	3.86
	40.59	37.19	9.14	39.08	3.86
(0,0)	41.31	38.40	7.58	39.08	3.98
	41.31	38.40	7.58	39.08	3.98
(2,0)	48.49	47.10	2.95	48.46	2.17
	48.49	47.10	2.95	48.46	2.17
(3,0)	83.71	79.78	4.93	79.18	5.72
	83.71	79.78	4.93	79.18	5.72
(4,0)	151.02	133.08	13.48	131.64	14.72
	151.02	133.08	13.48	131.64	14.72
(5,0)	256.16	202.18	26.70	200.16	27.98
	256.16	202.18	26.70	200.16	27.98
(0,1)	291.30	250.36	16.35	254.18	14.60
	291.30	250.36	16.35	254.18	14.60
(1,1)	302.26	262.38	15.20	266.23	13.53
	302.26	262.38	15.20	266.23	13.53
(6,0)	420.02	285.71	47.01	282.68	48.58
	420.02	285.71	47.01	282.68	48.58
(2,1)	338.45	304.76	11.06	303.88	11.38
	338.45	304.76	11.06	303.88	11.38

Table 5.6: Stationary plane disk, 10×20 Mesh (200 Elements)

Mode	Present Model	D'Angelo and Mote [1993] Experimental Approach		D'Angelo and Mote [1993] Analytical Approach	
(m,n)	ω_n [Hz]	ω_n [Hz]	$\lvert\Delta_r\rvert$ [%]	ω_n [Hz]	$\lvert\Delta_r\rvert$ [%]
(1,0)	40.22	37.19	8.16	39.08	2.93
(0,0)	40.78	38.40	6.19	39.08	2.64
(2,0)	48.50	47.10	2.98	48.46	2.20
(3,0)	83.69	79.78	4.89	79.18	5.69
(4,0)	150.49	133.08	13.07	131.64	14.31
(5,0)	254.96	202.18	26.11	200.16	27.38
(0,1)	267.23	250.36	6.74	254.18	5.13
(1,1)	279.53	262.38	6.54	266.23	4.99
(6,0)	417.78	285.71	46.22	282.68	47.79
(2,1)	319.55	304.76	4.85	303.88	5.16

Table 5.7: Stationary plane disk, 10×30 Mesh (300 Elements)

Mode	Present Model	D'Angelo and Mote [1993] Experimental Approach		D'Angelo and Mote [1993] Analytical Approach	
(m,n)	ω_n [Hz]	ω_n [Hz]	$\lvert\Delta_r\rvert$ [%]	ω_n [Hz]	$\lvert\Delta_r\rvert$ [%]
(1,0)	39.55	37.19	6.35	39.08	1.21
(0,0)	40.20	38.40	4.70	39.08	1.19
(2,0)	47.78	47.10	1.43	48.46	0.66
(3,0)	80.88	79.78	1.38	79.18	2.14
(4,0)	139.06	133.08	4.49	131.64	5.64
(5,0)	220.96	202.18	9.29	200.16	10.39
(0,1)	263.40	250.36	5.21	254.18	3.63
(1,1)	275.31	262.38	4.93	266.23	3.41
(6,0)	330.01	285.71	15.51	282.68	16.74
(2,1)	313.33	304.76	2.81	303.88	3.11

Table 5.8: Stationary plane disk, 10×40 Mesh (400 Elements)

Mode	Present Model	D'Angelo and Mote [1993] Experimental Approach		D'Angelo and Mote [1993] Analytical Approach	
(m,n)	ω_n [Hz]	ω_n [Hz]	$\lvert\Delta_r\rvert$ [%]	ω_n [Hz]	$\lvert\Delta_r\rvert$ [%]
(1,0)	39.32	37.19	5.74	39.08	0.62
(0,0)	40.00	38.40	4.18	39.08	0.69
(2,0)	47.52	47.10	0.90	48.46	0.14
(3,0)	79.95	79.78	0.21	79.18	0.97
(4,0)	135.49	133.08	1.81	131.64	2.92
(5,0)	211.08	202.18	4.40	200.16	5.46
(0,1)	262.08	250.36	4.68	254.18	3.11
(1,1)	273.87	262.38	4.38	266.23	2.87
(6,0)	307.26	285.71	7.54	282.68	8.69
(2,1)	311.26	304.76	2.13	303.88	2.43

Table 5.9: Stationary plane disk, 20×50 Mesh (1000 Elements)

Mode	Present Model	D'Angelo and Mote [1993] Experimental Approach		D'Angelo and Mote [1993] Analytical Approach	
(m,n)	ω_n [Hz]	ω_n [Hz]	$\lvert\Delta_r\rvert$ [%]	ω_n [Hz]	$\lvert\Delta_r\rvert$ [%]
(1,0)	39.14	37.19	5.23	39.08	0.14
(0,0)	39.78	38.40	3.59	39.08	0.12
(2,0)	47.45	47.10	0.75	48.46	0.02
(3,0)	79.60	79.78	0.23	79.18	0.52
(4,0)	133.89	133.08	0.61	131.64	1.71
(5,0)	206.64	202.18	2.21	200.16	3.24
(0,1)	255.97	250.36	2.24	254.18	0.71
(1,1)	267.95	262.38	2.12	266.23	0.64
(6,0)	297.38	285.71	4.08	282.68	5.20
(2,1)	305.70	304.76	0.31	303.88	0.60

Interpreting the presented data, it is clear that the finer the used mesh the better the results, since it leads to lower relative differences, $|\Delta_r|$, and it allows the correct calculation of the natural modes. In fact, it is possible to identify that coarser meshes lead to frequency values distant from the ones presented by D'Angelo and Mote [1993], as well as swapping (e.g. the 9th mode in 5×20, 10×20 and 10×30 meshes present a higher frequency than the 10th mode) and skipping modes (despite not being represented here, coarser meshes "skip" more energetic modes, as if they don't exist, because they do not have the necessary resolution to represent them).

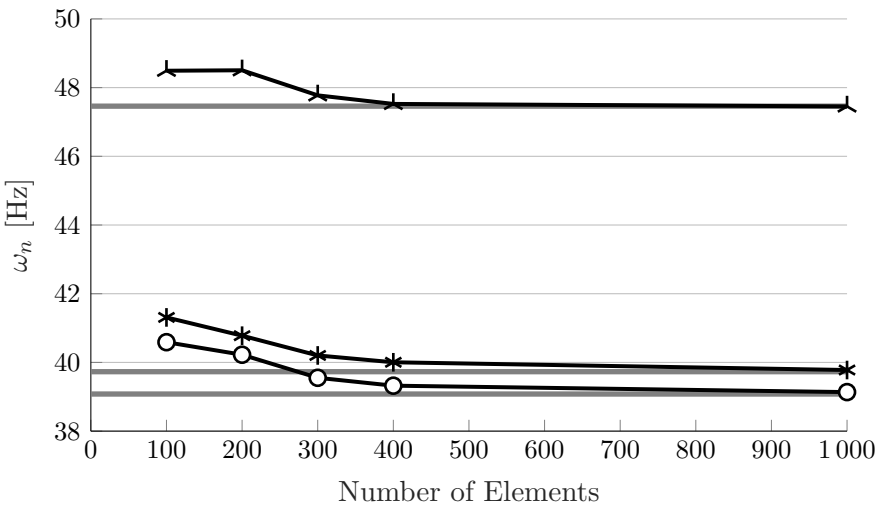

Figure 5.11: Modes 1 to 3 natural frequencies convergence representation.
1st Mode — 2nd Mode — 3rdMode — Analytical values by D'Angelo and Mote [1993].

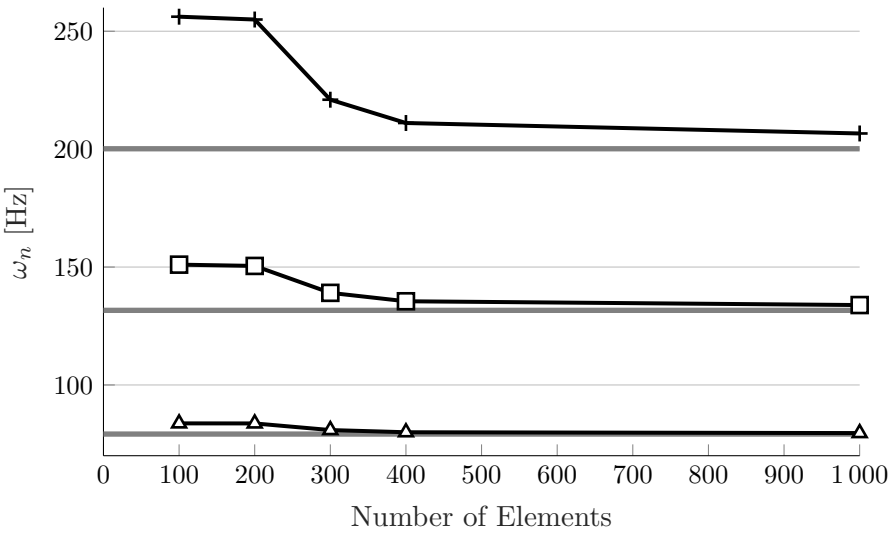

Figure 5.12: Modes 4 to 6 natural frequencies convergence representation.
4th Mode 5th Mode 6th Mode Analytical values by D'Angelo and Mote [1993].

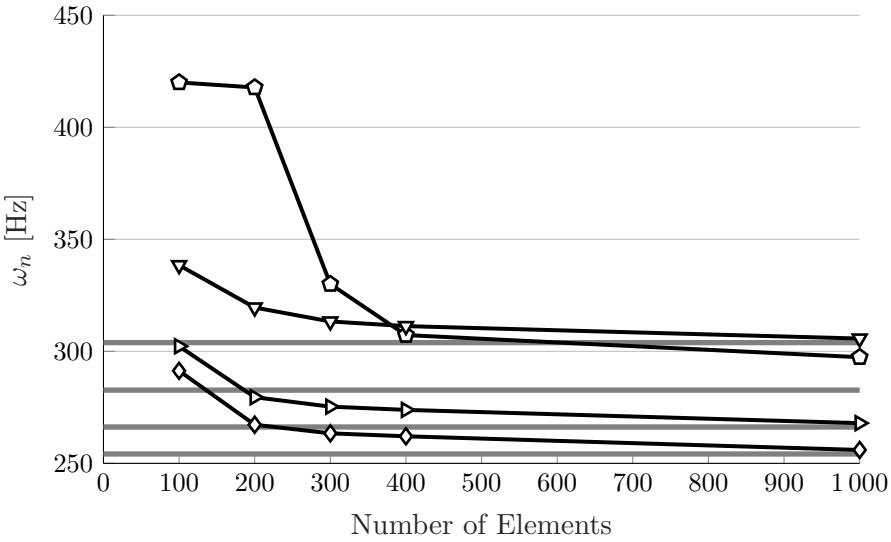

Figure 5.13: Modes 6 to 10 natural frequencies convergence representation.
7th Mode 8th Mode 9th Mode 10th Mode Analytical values by D'Angelo and Mote [1993].

Furthermore, it is possible to conclude that the mesh having 50 circumferential and 20 radial elements is the only one achieving accurate results, with relative differences in an acceptable range (0-5%), which leads to the validation of the developed model to the study of one-layer stationary plane disks (circular plates).

A validation test to a multi-layer stationary case was also made with the same structure. In fact, different numbers of layers with the same material and equal thicknesses (whose sum equals the original global thickness $b = 0.775\,\text{mm}$) were considered and the modal analysis performed. Plane disks with two, five and ten layers were studied (Table 5.10).

Table 5.10: Stationary plane disk with multiple layers

Mode	One Layer	Two Layers		Five Layers		Ten Layers	
(m,n)	ω_n [Hz]	ω_n [Hz]	$\lvert\Delta_r\rvert$ [$\times 10^{-3}\%$]	ω_n [Hz]	$\lvert\Delta_r\rvert$ [$\times 10^{-3}\%$]	ω_n [Hz]	$\lvert\Delta_r\rvert$ [$\times 10^{-3}\%$]
(1,0)	39.1359	39.1359	0	39.1353	1.53	39.1352	1.79
(0,0)	39.7789	39.7789	0	39.7787	5.04	39.7786	0.75
(2,0)	47.4520	47.4520	0	47.4502	3.79	47.4498	4.64
(3,0)	79.5957	79.5957	0	79.5921	4.52	79.5915	5.28
(4,0)	133.8870	133.8870	0	133.8800	5.23	133.8790	5.98
(5,0)	206.6450	206.6450	0	206.6320	6.29	206.6300	7.26
(0,1)	255.9729	255.9730	0.12	255.9640	3.40	255.9630	3.79
(1,1)	267.9461	267.9461	0	267.9350	4.14	267.9330	4.89
(6,0)	297.3826	297.3830	3.50	297.3600	7.60	297.3560	8.95
(2,1)	305.7000	305.7000	0	305.6820	5.89	305.6768	7.20

Analyzing the results, it is possible to conclude that the consideration of more than one layer does not induce significant variations on the obtained natural frequencies. It is interesting to note that as the number of layers increases, the natural frequencies values slightly decrease, as a result of a finer discretization of the domain, since the number of layers can be interpreted as divisions in the structure's thickness. However, these differences are so small that the relative variations between these results and the ones of the single layer previously validated never exceed $1 \times 10^{-2}\%$, leading to the validation of the present model to the simulation of multilayer static plane cases.

5.3.1.2 Spinning Case

It is also important to ensure that the implemented finite element is able to correctly represent a rotating plane disk. To do so, the results presented by Sinha [1987] and Hsieh and Abel [1995] were used. The first work uses numerical Rayleigh-Ritz's trial functions to parametrically determine the natural frequencies of thick spinning annular disks, while the second one proposes two different finite element approaches to the study of rotating plate structures, one considering the continuous distribution of the elements' mass (DM - distributed mass approach) and the other considering that it is concentrated in the nodes (LM - lumped masses approach).

A spinning annular ring made of steel was numerically simulated at three different rotational speeds, namely 0 (static case), 16 387 and 32 773 rpm. Its characteristics are presented in Table 5.11. Three-dimensional 20-node brick elements with a $4 \times 12 \times 1$ (the last number representing the thickness discretization) mesh was used by Hsieh and Abel [1995], while the previously validated 20×50 plate mesh was used in the developed model.

Table 5.11: Dimensions and constitutive properties of the annular plate studied by Hsieh and Abel [1995]

ϕ_i [mm]	ϕ_e [mm]	b [mm]	E [GPa]	ν	ρ [kg/m^3]
250	1000	200	196	0.3	7800

Table 5.12 presents this annular plate's modal analysis results with the implemented finite element. Note that, once again, Δ_r represents the relative difference of the obtained results comparatively to the correspondent values presented in the literature, and that the multiplicity of the natural frequencies was neglected.

Table 5.12: Hsieh and Abel [1995] rotating annular plate's natural frequencies

Ω	Mode	Present Model	Sinha [1987]		Hsieh and Abel [1995] DM Approach		Hsieh and Abel [1995] LM Approach	
[rpm]	(m,n)	ω_n [Hz]	ω_n [Hz]	$\lvert\Delta_r\rvert$ [%]	ω_n [Hz]	$\lvert\Delta_r\rvert$ [%]	ω_n [Hz]	$\lvert\Delta_r\rvert$ [%]
	(1,0)	239.89	247.22	2.96	245.29	2.20	245.29	2.20
0	(0,0)	262.53	268.47	2.21	267.50	1.86	267.50	1.86
	(2,0)	302.10	304.20	0.67	299.85	0.75	299.85	0.75
	(0,0)	364.20	380.01	4.15	376.63	3.30	377.60	3.55
16 387	(1,0)	377.05	398.84	5.46	387.74	2.75	394.01	4.30
	(2,0)	481.28	494.93	2.76	486.24	1.02	493.96	2.57
	(0,0)	558.17	595.36	6.24	611.30	8.69	617.56	9.62
32 773	(1,0)	626.82	669.72	6.41	674.07	7.01	682.28	8.13
	(2,0)	815.42	827.14	1.42	851.76	4.26	871.08	6.39

Analyzing the values, it can be observed that the higher the spinning velocity, the higher the verified relative difference. On the other hand, it is possible to identify a swap on the natural modes from the stationary case to the $\Omega = 16\,387$ rpm one, that was correctly represented by the present model, resulting from the different response to the rotating effects.

From Table 5.12, it is possible to conclude that for the first two cases the implemented model is in accordance with the numerical results of Sinha [1987] and Hsieh and Abel [1995]. Despite being possible to identify a relative difference slightly out of the acceptable range (jut over 5 %), it can be considered that the developed finite element is able to correctly simulate rotating plane disks, with spinning velocities up to $\Omega = 16\,387$ rpm, which includes the studied case.

However, for the last tested velocity, $\Omega = 32\,773$ rpm, most of the relative differences far exceeded the acceptable values, being these bigger for the two finite element approaches. This significant difference may be due to the type of elements and the mesh used by Hsieh and Abel [1995], since when comparing to the values presented by Sinha [1987] the relative differences are smaller, although a bit off the acceptable range.

5.3.2 Sloped Disk

To validate the implemented finite element in the study of sloped disks, the obtained results were compared to modal analysis performed in the commercial finite element method software ANSYS®. Contrarily to what was done in the previous Section, the validation process for the inclined cases was not divided into stationary and rotating instances, it was all done at once. On the other hand, the Coriolis effects were also considered, so that all the spinning outcomes could be evaluated.

The studied geometry was very similar to the one presented in Section 5.1.1 for the sloped gearwheel, being the only difference the outer rim's thickness, that was considered equal to the web's thickness. Table 5.13 presents its dimensions and the material's properties.

Table 5.13: Dimensions and constitutive properties of the analyzed sloped disk

ϕ_i [mm]	ϕ_e [mm]	b_{web} [mm]	b_{rim} [mm]	s [mm]	α [°]	E [GPa]	ν	ρ [kg/m^3]
31	138	6	6	5.67	70	200	0.3	7840

Table 5.14 presents this sloped disk's first five natural modes results for various rotating speeds with the implemented finite element. Once again, Δ_r represents the relative difference of the obtained results comparatively to the correspondent values obtained from the ANSYS® simulations. However, since the Coriolis effects were taken into account, the natural frequency split phenomenon is present, thus being important to represent both values for each mode. On the other hand, Figure 5.14 presents the correspondent Campbell diagrams.

Table 5.14: Rotating sloped disk modal analysis

Ω	Mode	Present Model	ANSYS®	
[rpm]	(m,n)	ω_n [Hz]	ω_n [Hz]	$\lvert\Delta_r\rvert$ [%]
0	(1,0)	1677.62	1648.60	1.76
		1677.62	1648.60	1.76
	(1,0)	1726.68	1730.08	0.20
		1726.68	1730.08	0.20
	(3,0)	3281.48	3266.66	0.45
		3281.48	3266.66	0.45
	(0,0)	3446.06	3432.17	0.40
	(Torsion)	3968.83	3941.86	0.68
600	(1,0)	1666.13	1640.14	1.58
		1689.16	1657.11	1.93
	(1,0)	1705.93	1712.55	0.39
		1747.64	1747.80	0.01
	(3,0)	3251.03	3240.33	0.33
		3312.16	3293.22	0.58
	(0,0)	3446.06	3432.17	0.40

Table 5.14: Rotating sloped disk modal analysis *(Continued)*

Ω	Mode	Present Model	ANSYS®	
[rpm]	(m,n)	ω_n [Hz]	ω_n [Hz]	$\lvert\Delta_r\rvert$ [%]
600	(Torsion)	3968.84	3941.86	0.68
6000	(1,0)	1564.72	1565.90	0.08
		1795.06	1735.70	3.42
	(1,0)	1528.06	1562.80	2.22
		1945.14	1915.30	1.56
	(3,0)	2987.62	3012.90	0.84
		3599.00	3541.80	1.61
	(0,0)	3445.65	3432.20	0.39
	(Torsion)	3969.54	3941.90	0.70
10 000	(1,0)	1491.93	1513.10	1.40
		1875.86	1796.10	4.44
	(1,0)	1406.53	1461.10	3.73
		2101.66	2048.50	2.60
	(3,0)	2804.77	2855.50	1.78
		3823.73	3737.00	2.32
	(0,0)	3444.92	3432.20	0.37
	(Torsion)	3970.81	3941.90	0.73
20 000	(1,0)	1343.66	1389.50	3.30
		2061.08	1955.20	5.41
	(1,0)	1152.97	1239.60	6.99
		2514.83	2414.40	4.16
	(3,0)	2401.17	2502.00	4.03
		4420.16	4265.00	3.64
	(0,0)	3447.36	3432.20	0.44
	(Torsion)	3969.91	3941.90	0.71
30 000	(1,0)	1124.17	1277.40	12.00
		2276.59	2125.60	7.10
	(1,0)	800.48	1060.30	24.50
		2886.13	2822.30	2.26
	(3,0)	1896.31	2201.90	13.88
		4931.30	4846.40	1.75
	(0,0)	3453.29	3432.10	0.62
	(Torsion)	3970.39	3941.90	0.72

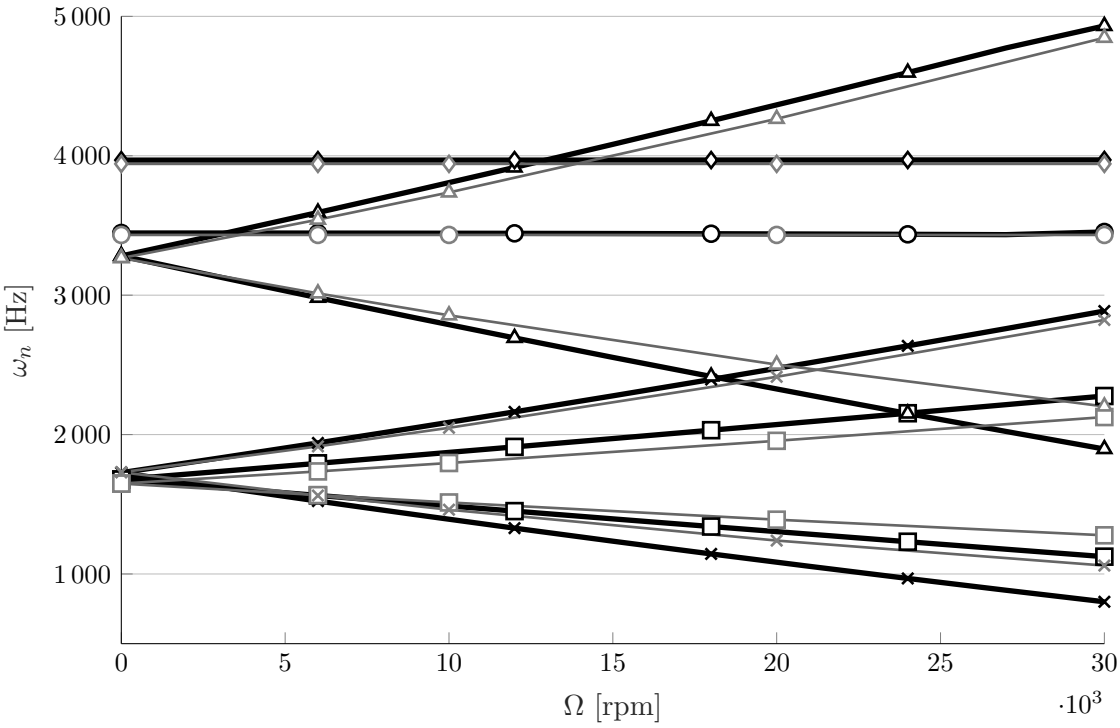

Figure 5.14: Sloped rotating disk's Campbell diagram. ━ Present model ── ANSYS® ─□─ 1st Mode ─×─ 2nd Mode ─△─ 3rdMode ─○─ 4thMode ─◇─ 5thMode.

From Table 5.14 it can be verified that the developed model achieves results that are very similar to the ones obtained with ANSYS® for spinning velocities up until 10 000 rpm. For $\Omega = 20\,000$ rpm there are two relative difference values that exceed the tolerable range and for $\Omega = 30\,000$ rpm it is clear that the implemented finite element leads to results that highly differ from the ones obtained with the commercial finite element software. Thus, once again, it is possible to conclude that the higher the spinning velocity, the bigger the associated results' relative difference and that the developed finite element is able to correctly simulate rotating sloped disks with spinning velocities up to $\Omega = 20\,000$ rpm, which includes the studied case.

The Campbell diagram in Figure 5.14 confirms what was previously mentioned, since most of the curves corresponding to the present model and the ANSYS® results are further apart for higher rotation velocities.

As a finishing note, the significant differences when comparing the results obtained with the developed model to the ones verified through the usage of a commercial finite element method software for high spinning velocities may be due to a slight discontinuity in the considered geometric model of the sloped disk, namely in the area of the connection between the rim and the web. On the other hand, the element considered in the ANSYS® simulations was a shell element which presents an additional degree of freedom, the rotation in the normal direction.

5.3.3 Numerical Simplifications

As presented in Section 5.2, some simplifications regarding the centrifugal stiffness matrix calculation were considered in order to reduce the computation time. Thus, once the non-treated plane and sloped cases results are validated, it is important to verify if these

abridgments entail significant deviations.

To do so, a steel plane disk treated all over its surface, which characteristics are presented in Table 5.15, was analyzed using both methodologies (simplified and exact) for three velocities, namely 0 (static case), 6000 and 10 000 rpm. The viscoelastic material used was the 3M^{TM} ISD112 and the treatment's configuration was CLD, with the backing layer made of the same material as the host structure and the dimensions e_1 and e_2 corresponding to the viscoelastic and the constraining layers, respectively.

Table 5.15: Treated plane disk characteristics

Host Structure						Viscoelastic Treatment			
ϕ_i [mm]	ϕ_e [mm]	b [mm]	E [GPa]	ν	ρ [kg/m^3]	Setup	Materials	e_1 [mm]	e_2 [mm]
31.00	149.34	6.00	200	0.3	7840	CLD Complete	ISD112 Steel	1.00	1.00

Note that the disk presents the same dimensions as the patent's studied case except for the rim's thickness, that is considered equal to the web (constant thickness plane disk). However, the damping treatment is considered to be applied all over the surface, which is not possible in the patent's configuration, and the viscoelastic layer presents double the thickness. These differences were considered so that the viscoelastic material's behavior had a bigger influence in the structure, and thus highlighting possible variations between approaches.

Table 5.16 presents the modal analysis' results, where η_n represents the modal loss factor, $\Delta_{r\,\omega_n}$ represents the relative difference between the simplified and exact approaches' natural frequencies values and $\Delta_{r\,\eta_n}$ represents the relative difference between the simplified and exact approaches' loss factor values.

Table 5.16: Modal analysis simplification validation

Ω [rpm]	Mode (m,n)	Simplified Approach ω_n [Hz]	Simplified Approach η_n [%]	Exact Approach ω_n [Hz]	Exact Approach $\lvert\Delta_{r\,\omega_n}\rvert$ [$\times 10^{-5}$%]	Exact Approach η_n [%]	Exact Approach $\lvert\Delta_{r\,\eta_n}\rvert$ [$\times 10^{-5}$%]
0	(1,0)	1168.8011	1.5581	1168.8011	0.01	1.5581	25.25
		1168.8011	1.5581	1168.8011	0.01	1.5581	25.25
	(0,0)	1266.8937	1.1089	1266.8937	0.00	1.1089	9.82
	(2,0)	1541.6282	1.9669	1541.6282	0.03	1.9669	18.54
		1541.6282	1.9669	1541.6282	0.03	1.9669	18.54
	(3,0)	3031.5492	1.3200	3031.5492	0.01	1.3200	19.21
		3031.5492	1.3200	3031.5492	0.01	1.3200	19.21
	(Torsion)	4122.0782	0.0418	4122.0782	0.00	0.0418	10.00
	(4,0)	5280.1663	0.8171	5280.1663	0.00	0.8171	5.58
		5280.1663	0.8171	5280.1663	0.00	0.8171	5.58
6000	(1,0)	1171.8358	1.5517	1171.8369	9.39	1.5517	0.79
		1171.8358	1.5517	1171.8369	9.39	1.5517	0.79

Table 5.16: Modal analysis simplification validation *(Continued)*

Ω [rpm]	Mode (m,n)	Simplified Approach ω_n [Hz]	Simplified Approach η_n [%]	Exact Approach ω_n [Hz]	Exact Approach $\lvert\Delta_r\,\omega_n\rvert$ [$\times 10^{-5}$%]	Exact Approach η_n [%]	Exact Approach $\lvert\Delta_r\,\eta_n\rvert$ [$\times 10^{-5}$%]
6000	(0,0)	1268.9718	1.1059	1268.9726	6.50	1.1059	9.07
	(2,0)	1545.7122	1.9594	1545.7133	7.28	1.9594	9.39
		1545.7122	1.9594	1545.7133	7.28	1.9594	9.39
	(3,0)	3035.0123	1.3177	3035.0128	1.73	1.3177	2.18
		3035.0123	1.3177	3035.0128	1.73	1.3177	2.18
	(Torsion)	4121.1567	0.0424	4121.1567	0.00	0.0424	75.25
	(4,0)	5283.1471	0.8162	5283.1472	0.20	0.8162	0.07
		5283.1471	0.8162	5283.1472	0.20	0.8162	0.07
10 000	(1,0)	1177.2112	1.5406	1177.2142	25.84	1.5406	19.08
		1177.2112	1.5406	1177.2142	25.84	1.5406	19.08
	(0,0)	1272.6571	1.1006	1272.6594	17.95	1.1006	24.05
	(2,0)	1552.9464	1.9461	1552.9495	20.07	1.9461	20.15
		1552.9464	1.9461	1552.9495	20.07	1.9461	20.15
	(3,0)	3041.1593	1.3137	3041.1608	4.81	1.3137	3.77
		3041.1593	1.3137	3041.1608	4.81	1.3137	3.77
	(Torsion)	4120.6576	0.0435	4120.6575	0.05	0.0435	0.01
	(4,0)	5288.4422	0.8147	5288.4425	0.54	0.8147	0.14
		5288.4422	0.8147	5288.4425	0.54	0.8147	0.14

From the previous results, it is clear that the variations induced by the simplified approach of initially determining the centrifugal stiffness matrix and considering it constant throughout the complex modal analysis using the IMSE method are not significant and, consequently, this process can be validated. Furthermore, while the analysis with the exact method took approximately four minutes to process and plot the results, the ones with the simplified method only took approximately one minute, which corresponds to a 75 % reduction and consequently justifies the application of this process.

On the other hand, Figure 5.15 presents the receptance's Bode diagram for the disk with no treatment and for the simplified and exact approaches spinning at $\Omega = 6000$ rpm. A direct frequency response function was selected, for an exterior node and for the degree of freedom correspondent to the transversal direction displacement.

From Figure 5.15, it is possible to verify that the treated system's receptances curves overlapped (the interrupted light gray curve of the exact method lays exactly on top of the continuum black curve of the simplified method). In fact, only if a significant amount of zoom is applied (Figure 5.16) the curves separation can be identified. Thus, it can be concluded that the implementation of the simplification method is not associated with significant differences on the results when compared to the ones obtained through the exact process, leading to its validation. Furthermore, while the analysis with the exact method took nearly six hours to process and plot the results, the one using the simplified method only took approximately 30 minutes, which corresponds to a 90 % time reduction and, consequently, justifies the application of this simplified process.

Although it does not correspond directly to the analysis made in the present Section, some interesting notes can be stated about the shown FRF, such as the graphic visualization of the expected damping phenomenon, since the magnitude's peaks significantly reduce and the curves' evolutions near the resonance frequencies are much more smooth. On the other hand, the problematic associated with the significant addition of a material with relatively low stiffness is also evident due to the natural frequencies values reduction. Finally, it is also important to note that the 5th mode, the torsion one, can not be identified in the presented Bode plot, once the degree of freedom considered for the application of the excitation corresponds to the transverse displacement, which does not excite this mode.

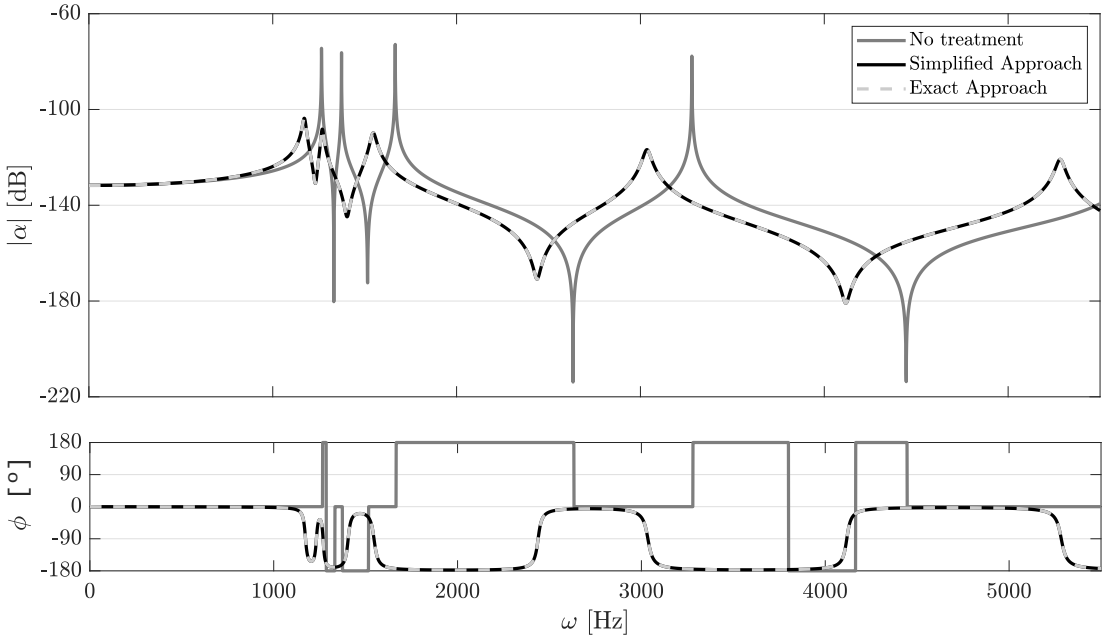

Figure 5.15: Plane disk's receptance Bode diagram - No treatment, exact approach and simplified approach.

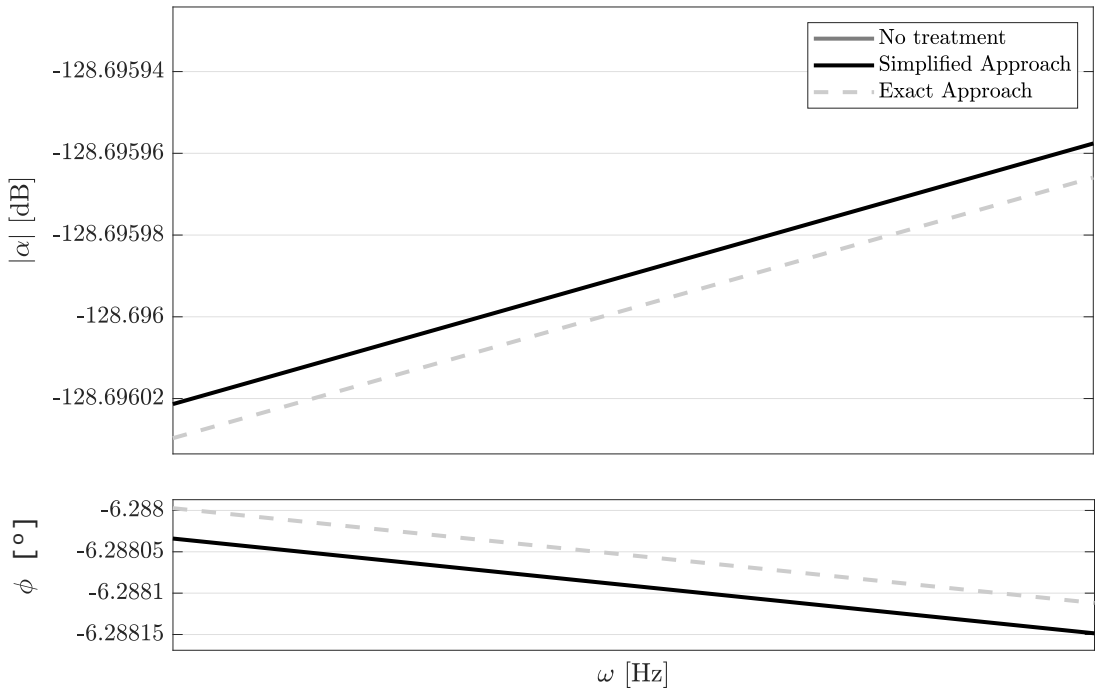

Figure 5.16: Zoom of the plane disk's receptance Bode diagram - No treatment, exact approach and simplified approach.

Chapter 6

Analysis of the Non-Treated Gearwheels

In the present chapter the numerical simulation results of the studied gearwheel without viscoelastic damping devices will be presented and discussed. Initially, the inclination angle influence on the modal analysis results is considered. Then, the thicker outer rim effects are presented and interpreted. Finally, the influence of each rotational effect on the natural frequencies, for both plane and sloped gearwheel, is analyzed.

6.1 Introduction

As said before, one of the main motivations for the present dissertation was the patent presented by Marsaudon and Cutuli [2014], where a sloped gearwheel with an annular shaped damping device based on viscoelastic materials was proposed. Thus, it is interesting to study the efficiency of the presented solution and, additionally, to propose and assay new treatment configurations.

However, before beginning to study the viscoelastic damping devices, an analysis of the simple gearwheels must be performed, so that their isolated behavior can be known and used as a basis for the treatments' performance evaluation. More than the sloped gearwheel, it is also important to analyze the plane case, so that it can be understood how the inclination angle affects its behavior. It is also important to determine the influence of the spinning effects on the dynamic behavior of the studied gearwheel, despite the velocity conditions being almost constant (Ω = 6000 rpm), because it leads to a better familiarization with all the present variables.

6.2 Non-Treated Gearwheel

The non-treated gearwheels' meshes used in the numerical simulations were previously analyzed and presented in Section 5.1.3 (Figures 5.6 and 5.7).

Table 6.1 presents the first five natural frequencies for the non-treated plane and sloped gearwheels spinning at 6000 rpm.

Table 6.1: Non-treated plane gearwheel modal analysis results

Plane Gearwheel			Sloped Gearwheel		
Mode	(m,n)	ω_n [Hz]	Mode	(m,n)	ω_n [Hz]
1	(1,0)	844.30	1	(1,0)	1099.08
2		844.30	2		1099.08
3	(0,0)	1293.17	3	(2,0)	2103.97
			4		2103.97
4	(2,0)	2071.09	5	(Torsion)	2564.21
5		2071.09			
6	(Torsion)	2636.55	6	(0,0)	2858.70
7	(3,0)	5565.10	7	(3,0)	5493.90
8		5565.10	8		5493.90

Figures 6.1 to 6.5 show the plane gearwheel mode shapes' displacement in each direction.

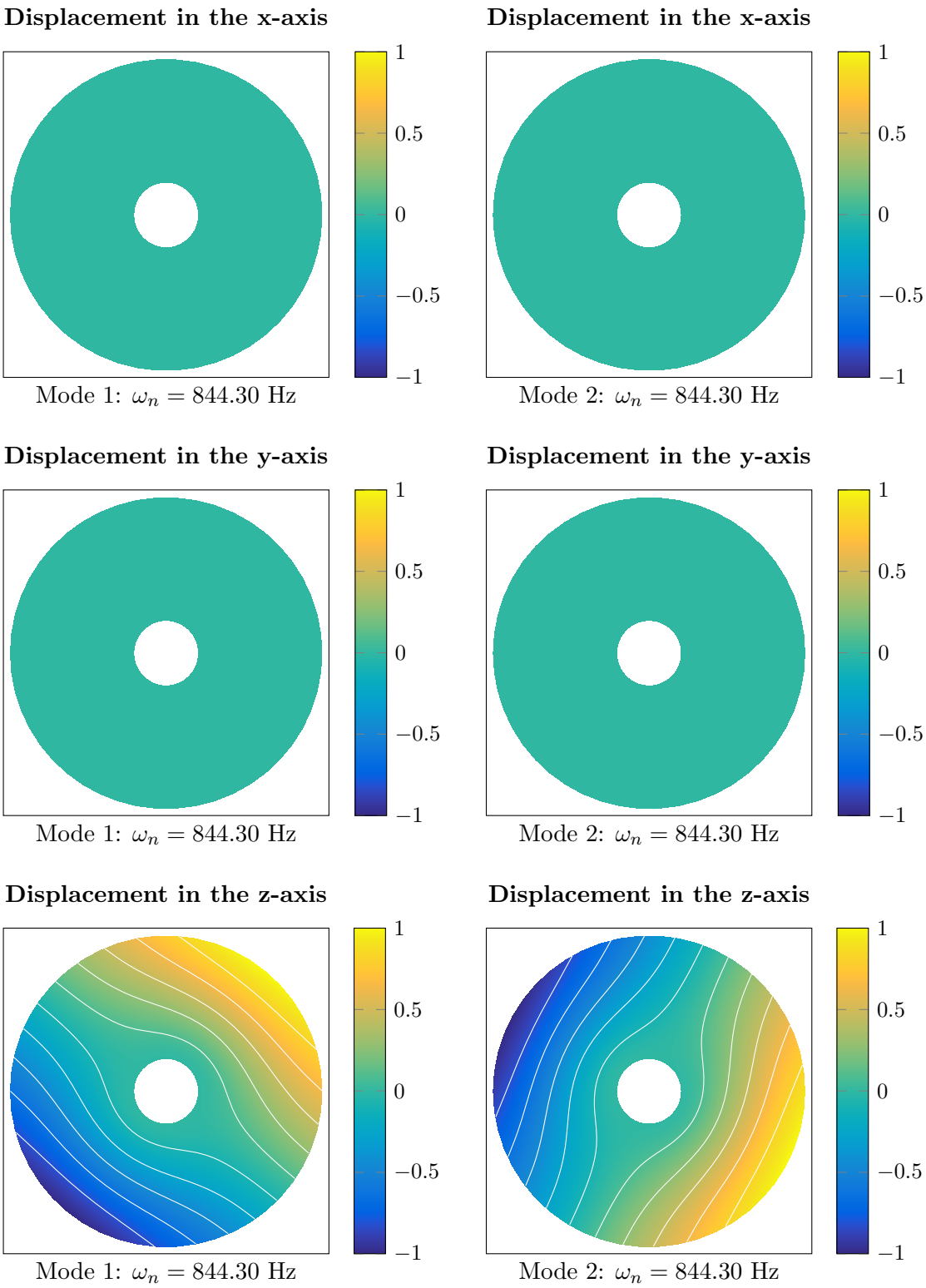

Figure 6.1: Non-treated plane gearwheel 1st mode shapes' displacement along each direction.

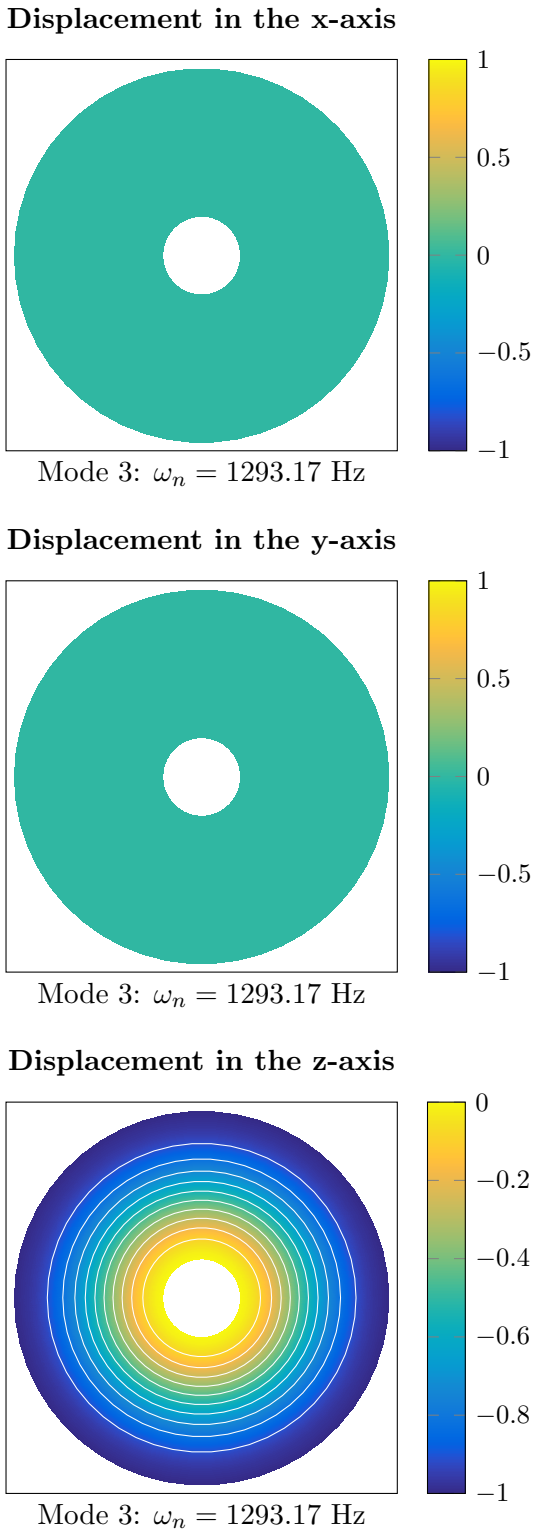

Figure 6.2: Non-treated plane gearwheel 2nd mode shape's displacement along each direction.

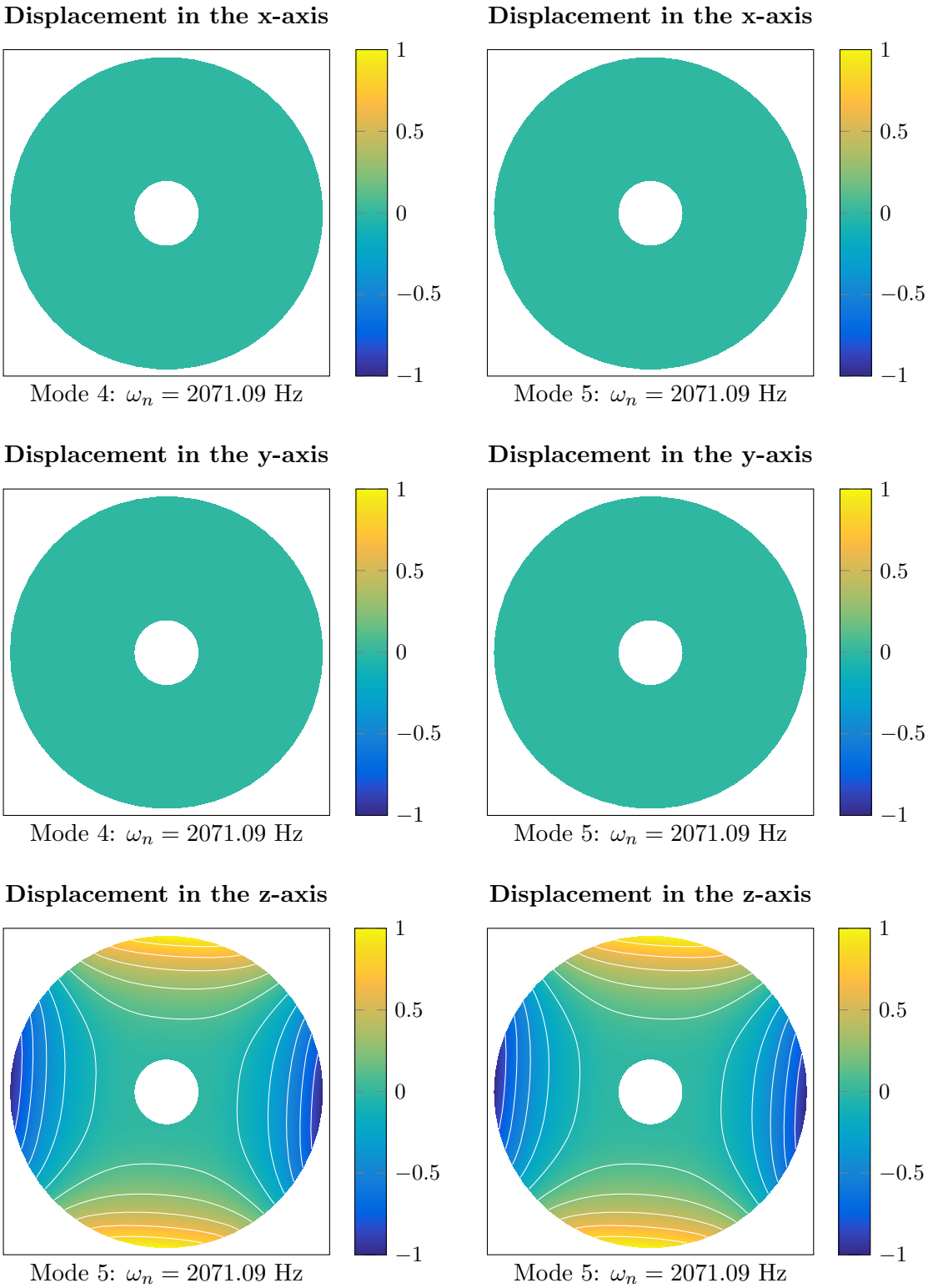

Figure 6.3: Non-treated plane gearwheel 3rd mode shapes' displacement along each direction.

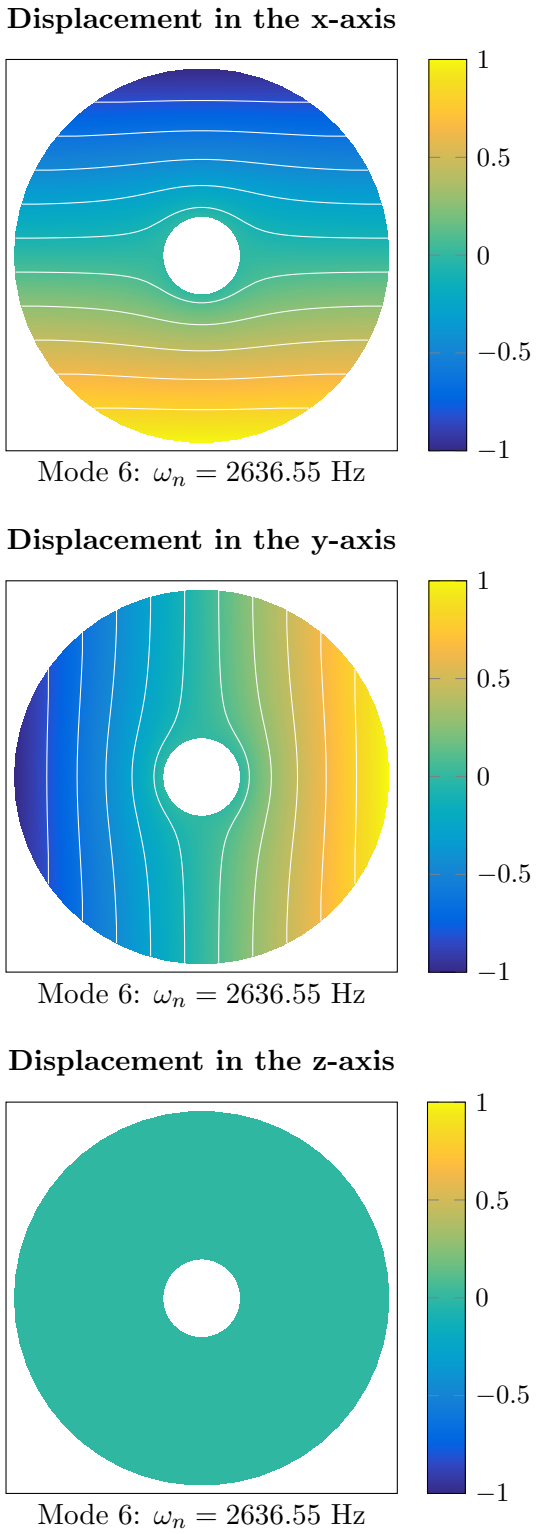

Figure 6.4: Non-treated plane gearwheel 4th mode shape's displacement along each direction.

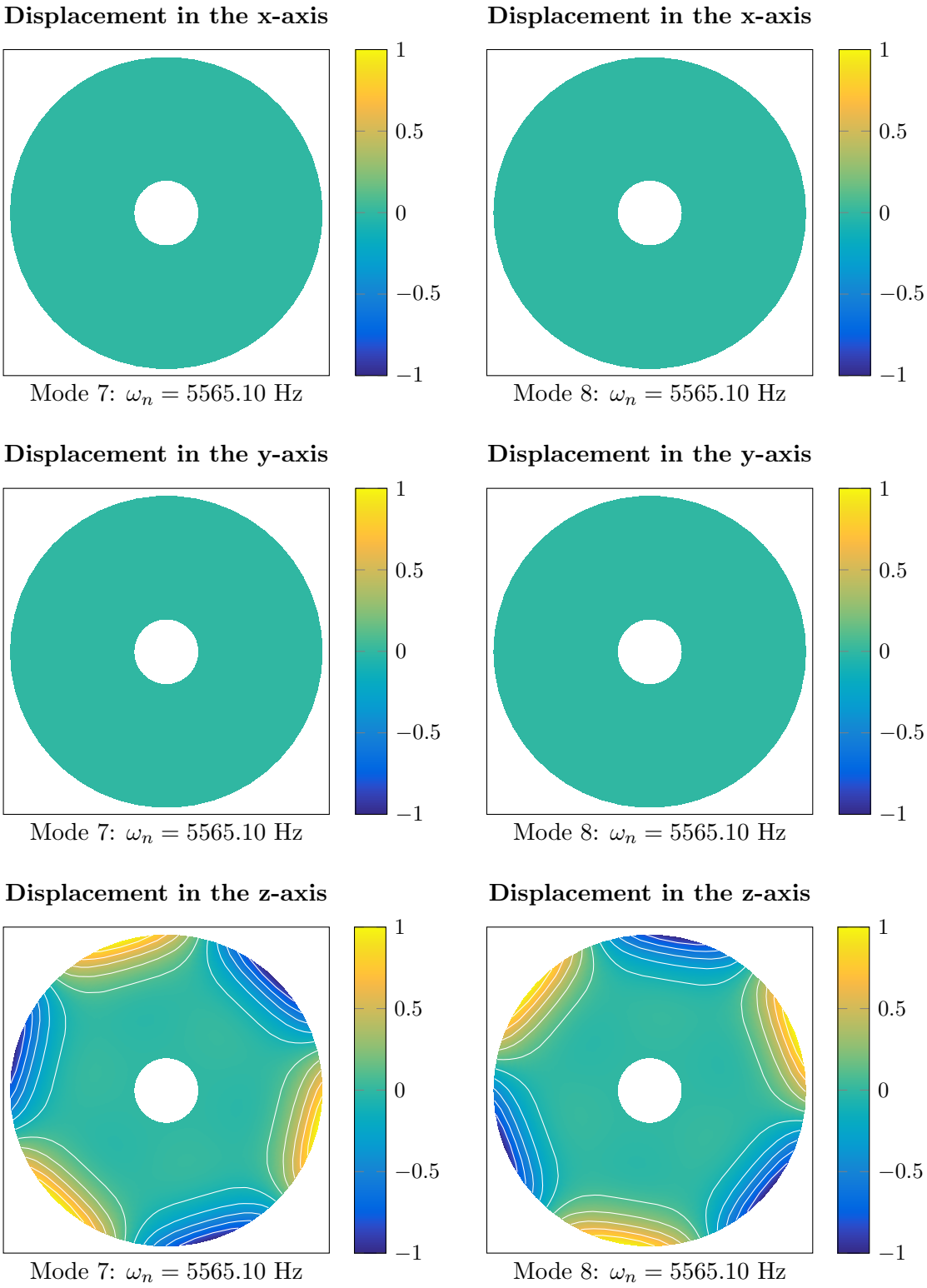

Figure 6.5: Non-treated plane gearwheel 5th mode shapes' displacement along each direction.

Figures 6.6 to 6.9 present the sloped gearwheel mode shapes' displacement in each direction.

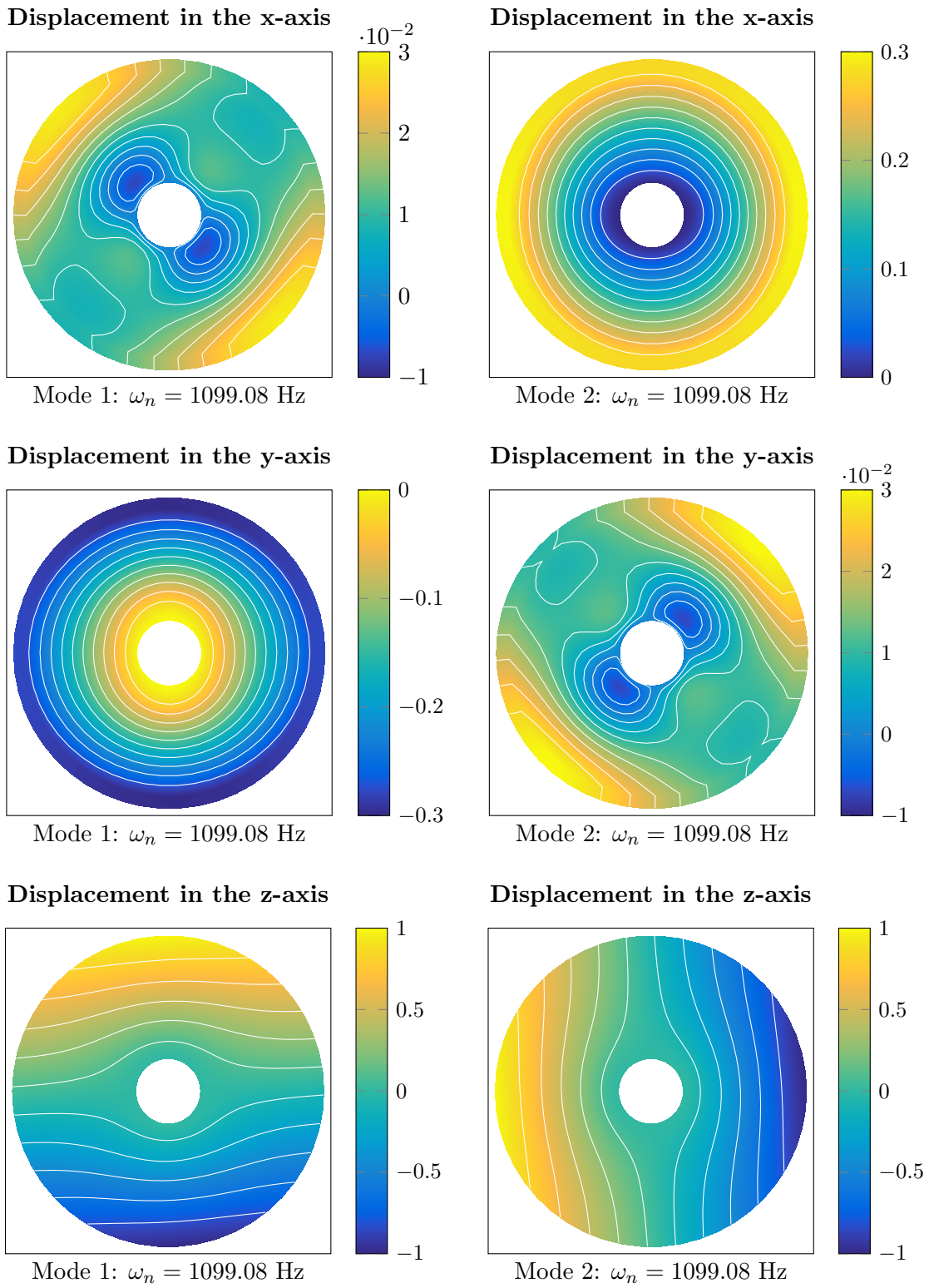

Figure 6.6: Non-treated sloped gearwheel 1st mode shapes' displacement along each direction.

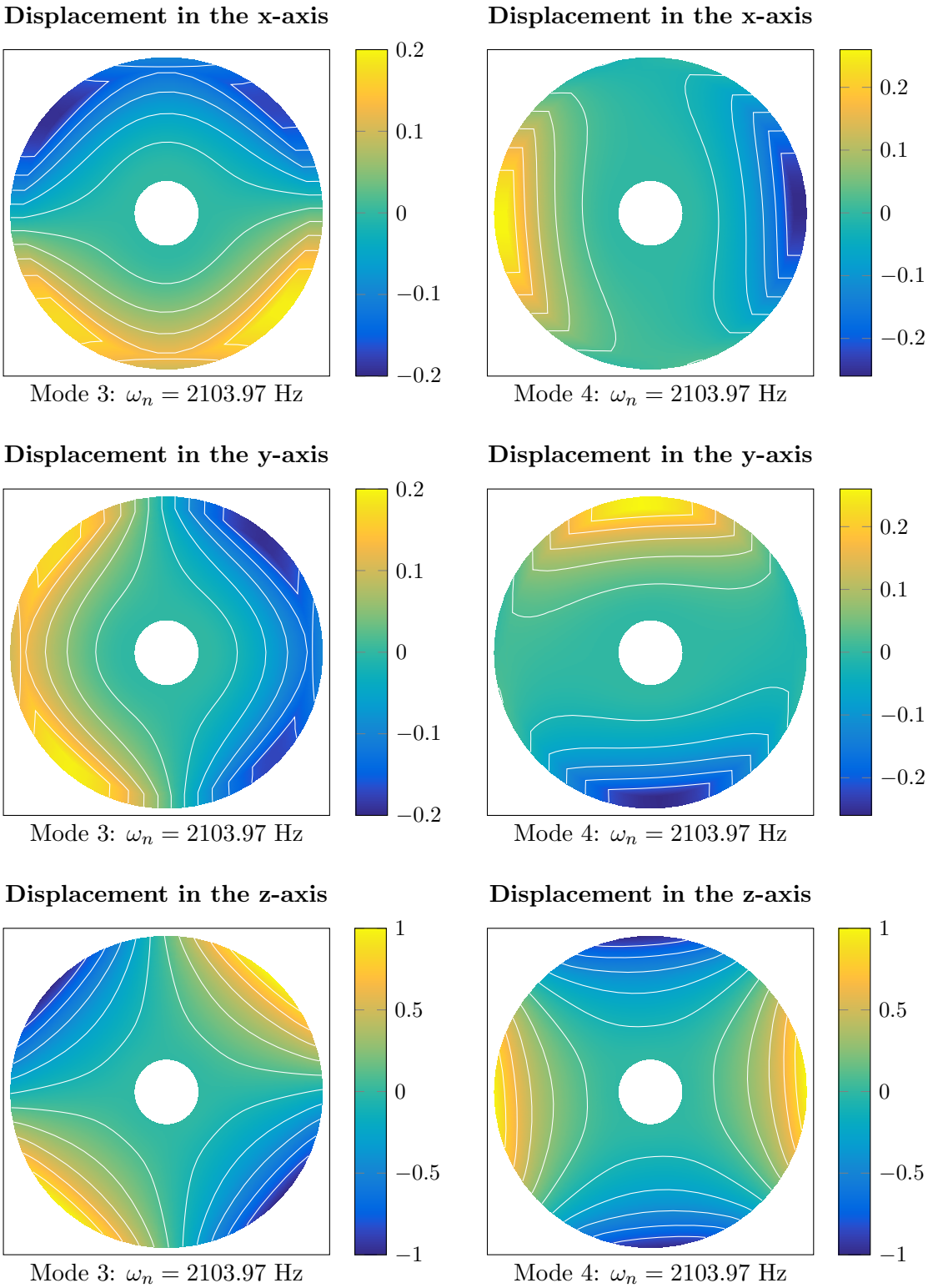

Figure 6.7: Non-treated sloped gearwheel 2nd mode shapes' displacement along each direction.

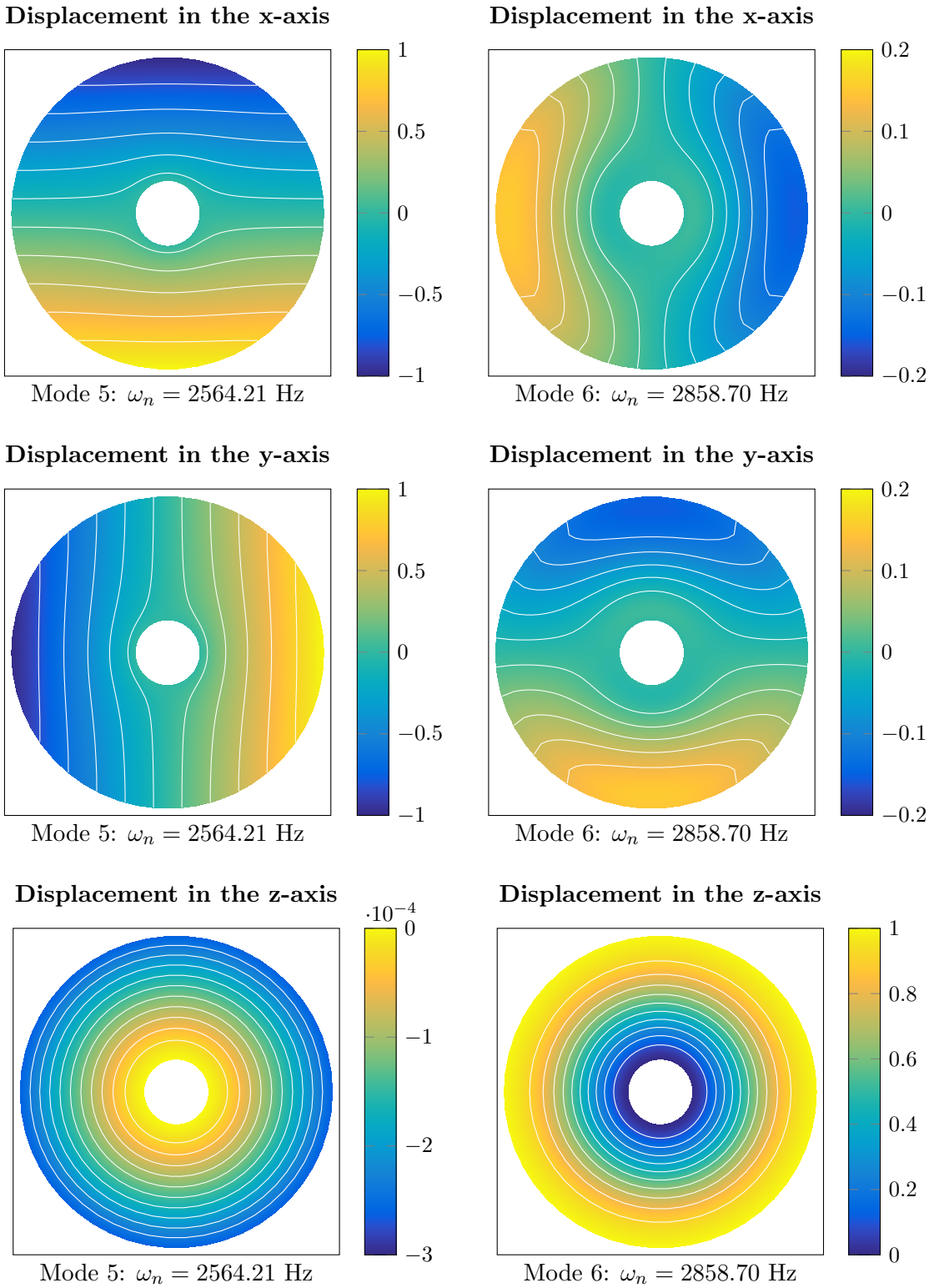

Figure 6.8: Non-treated sloped gearwheel 3rd and 4th mode shapes' displacement along each direction.

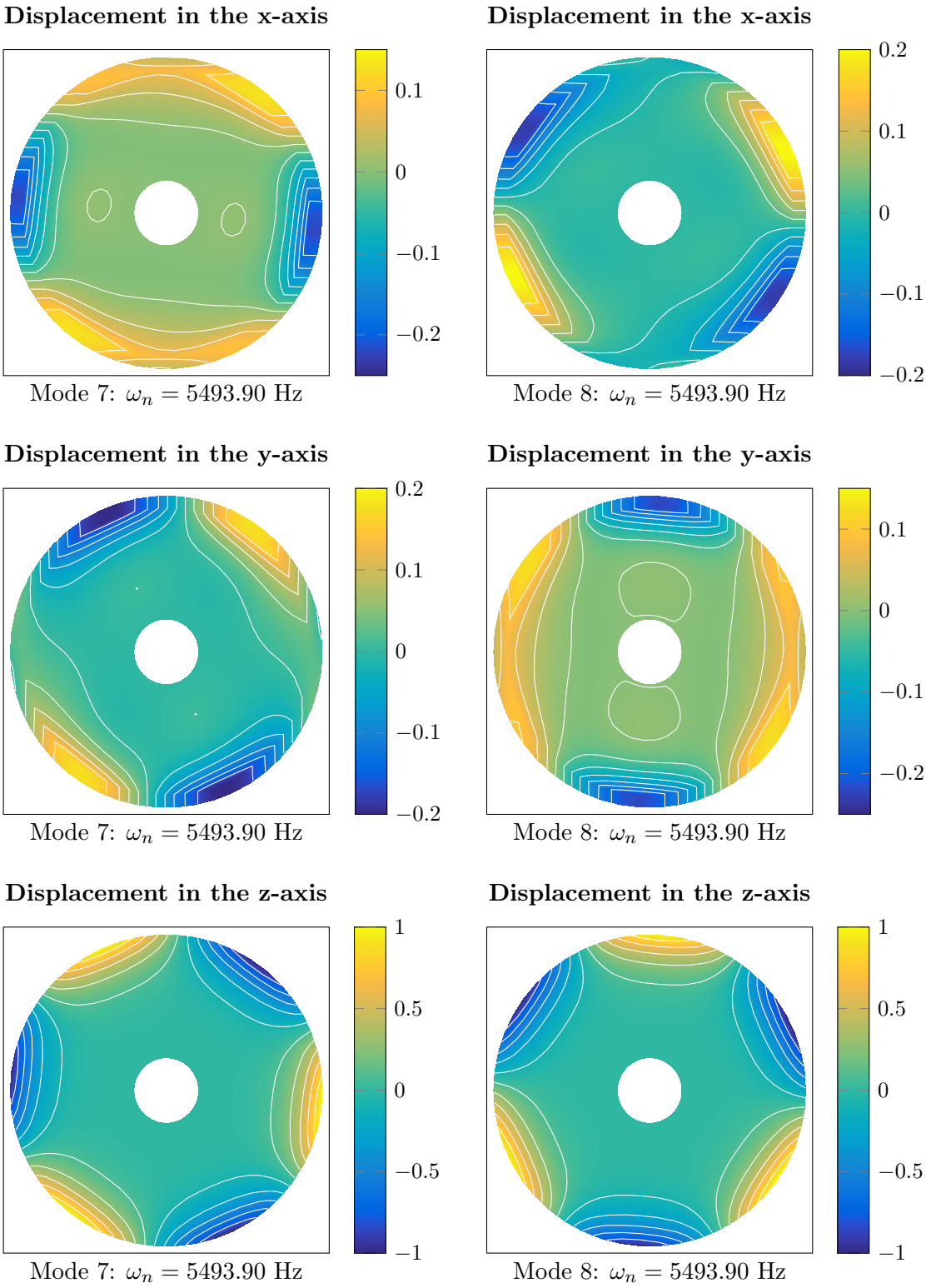

Figure 6.9: Non-treated sloped gearwheel 5th mode shapes' displacement along each direction.

From Table 6.1 it is possible to conclude that the inclination angle promotes the natural frequency increase of some natural modes and the decrease of others. In fact, the modes characterized by none, one and two nodal diameters (and zero nodal circumferences) verified a rise in their natural frequencies of 120 %, 30 % and 2 %, respectively, while the modes of torsion and the one characterized by three nodal diameters verified a reduction on their natural frequencies of 8 % and 1 %, respectively. This may be due to the mode shapes in each configuration. For example, for the (1,0) mode, the bending of the web requires more energy in the sloped gearwheel because it is necessary to counter its natural slope in essentially one-half and to increase the inclination angle in the other, which leads to the rise of the natural frequency. The same can be applied to the other natural modes.

Figure 6.10 presents the inclination angle influence on the natural frequencies values. Note that $\beta = 90 - \alpha$ corresponds to the angle between the web and a normal to the rotation axis, thus $\beta = 0°$ for the plane gearwheel and $\beta = 20°$ for the studied sloped case.

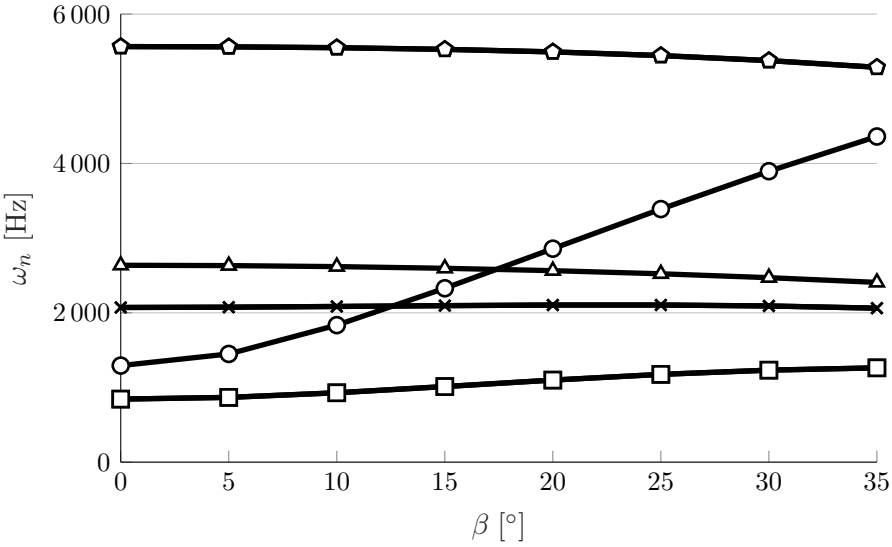

Figure 6.10: Inclination angle influence on the non-treated gearwheel's natural frequencies. Mode (1,0) Mode (0,0) Mode (2,0) Torsion Mode Mode (3,0).

It is possible to conclude that the aforementioned observed variation of the natural frequencies with the inclination angle is constant in the range proposed by Marsaudon and Cutuli [2014] in the studied patent.

The modal analysis of the plane gearwheel can be used to evaluate the influence of the outer rim much thicker than the web. In fact, remembering the presented results in Figure 5.15, where a non-treated constant-thickness disk with the same inner and outer diameters was also analyzed, it is possible to determine its natural frequencies and compare both results, as in Table 6.2. Note that the natural frequency multiplicity was neglected (since there are no variations), Δ represents the difference between the values with the outer rim and the values for the plane disk and Δ_r its relative value (when compared to the case with no outer rim).

Furthermore, the same comparison can also be made for the sloped gearwheel, using the results in Table 5.14 and adding the Coriolis effect to the modal analysis, as well as its representation in an inertial frame. Table 6.3 presents these results and the correspondent comparison.

For the plane case, it is possible to conclude that the outer rim resulted in a swap

Table 6.2: Outer rim influence for the plane case, $\Omega = 6000$ rpm

Mode	(m,n)	Thicker Outer Rim	No Outer Rim	
		ω_n [Hz]	ω_n [Hz]	Δ [Hz] (Δ_r [%])
1 & 2	(1,0)	844.30	1265.57	−421.27 (−33.29)
3	(0,0)	1293.17	1374.06	−80.89 (−5.89)
4 & 5	(2,0)	2071.09	1666.07	405.02 (24.31)
6	(Torsion)	2636.55	4165.00	−1528.45 (−36.70)
7 & 8	(3,0)	5565.10	3279.84	2285.26 (69.68)

Table 6.3: Outer rim influence for the sloped case, $\Omega = 6000$ rpm and Coriolis effect considered

Mode	(m,n)	Thicker Outer Rim	No Outer Rim	
		ω_n [Hz]	ω_n [Hz]	Δ [Hz] (Δ_r [%])
1	(1,0)	980.69	1564.72	−584.03 (−37.32)
2		1211.15	1795.06	−583.91 (−32.53)
3	(2,0)	1890.48	1528.06	362.42 (23.72)
4		2302.72	1945.14	357.58 (18.38)
5	(Torsion)	2562.34	3969.54	−1407.20 (−35.45)
6	(0,0)	2859.25	3445.65	−586.40 (−17.02)
7	(3,0)	5185.63	2987.62	2198.01 (73.57)
8		5790.69	3599.00	2191.69 (60.90)

between the torsion and the (3,0) modes. For the sloped case, both these modes switched places as well as the (0,0) mode. However, in both cases it is possible to conclude that the thicker outer rim led to the decrease of the (0,0), (1,0) and torsion modes' natural frequencies and to the increase of the (2,0) and (3,0) modes' natural frequencies. These evolutions can be explained by the relation between the added mass, the added stiffness and the correspondent natural shapes. In fact, for the decreasing cases it is possible to observe that the thicker geometry will not suffer significant bending and thus the mass addition is preponderant, leading to a less energy needs for these modes to occur. On the other hand, for the rising cases, it is possible to observe that the outer rim is forced to bend significantly, leading to a more meaningful stiffness increase than the mass addition, which requires more energy for them to occur.

Analyzing the mode shapes presented in Figures 6.1 to 6.9, for both plane and sloped gearwheels, it is possible to observe the node characterization previously given and the aforementioned normal modes' particularities when the natural frequency multiplicity phenomenon occurs. On the other hand, for the plane gearwheel, the absence of coupling between the membrane displacements, u and v, and the transverse displacement, w, is evident. In fact, for the bending modes the displacement along the x and y-axis is null and for the torsion mode the out-of-plane displacement, along the z-axis, is also null. However, for the sloped gearwheel, this does not occur, since the inclination leads to the coupling

between membrane and transverse displacements. Despite u and v displacements, for the bending modes, and w displacement, for the torsion mode, being smaller than the transverse and membrane displacements, respectively, they are not null, as verified for the plane gearwheel.

To complete the non-treated plane and sloped gearwheels analysis, Figure 6.11 presents the frequency response function receptance for both cases. A direct FRF was determined, where the considered node was an exterior one and the considered degree of freedom was the displacement along the z-axis.

From Figure 6.11, it is possible to observe the referred natural frequency evolution between cases and that the torsion mode is not presented, because it only occurs with a membrane excitation.

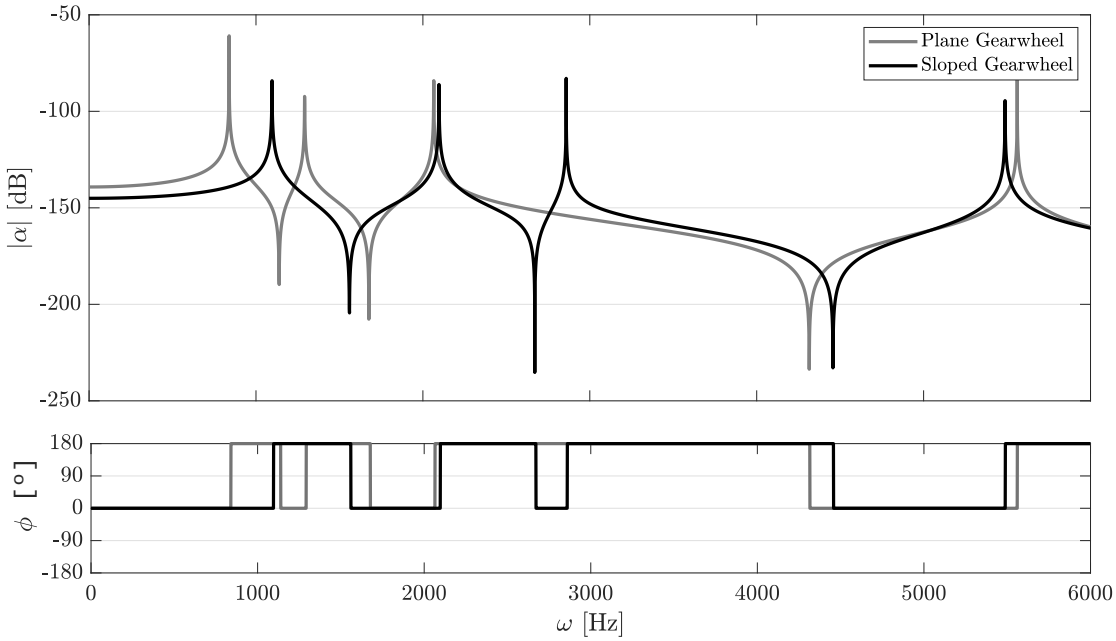

Figure 6.11: Non-treated plane and sloped gearwheel receptance FRF.

6.3 Individual Evaluation of the Spinning Effects

As presented in Chapter 2, the rigid body spinning motion of the gearwheel induces some effects that change the stiffness and dynamic characteristics of the structure, namely the centrifugal softening, centrifugal stiffening and Coriolis effects, so it is important to analyze the influence of each one separately for the studied cases (plane and sloped wheels).

6.3.1 Centrifugal Softening Effect

To comprehend the influence of the centrifugal softening effect, the evolution of the natural frequencies with the spinning velocity was plotted in Figure 6.12, for both plane and sloped gearwheels and in a range from 0 to 6000 rpm, discarding the centrifugal stiffening and the Coriolis effects.

Analyzing Figure 6.12, it is not possible to identify variations on the natural frequencies results in any of the studied cases. In fact, as aforementioned in Section 2.3.2, the centrifugal softening effect is reduced, only presenting significant influence at very high

rotation velocities. So, Figure 6.13 presents the same analysis but in a range from 0 to 100 000 rpm.

Analyzing Figure 6.13, the centrifugal softening effect can be identified, since there are some reductions on the natural frequencies. As also referred in Section 2.3.2, it is possible to verify that for the plane case only the torsion mode is affected, while for the sloped gearwheel the bending modes are also affected, most notably the (1,0) mode.

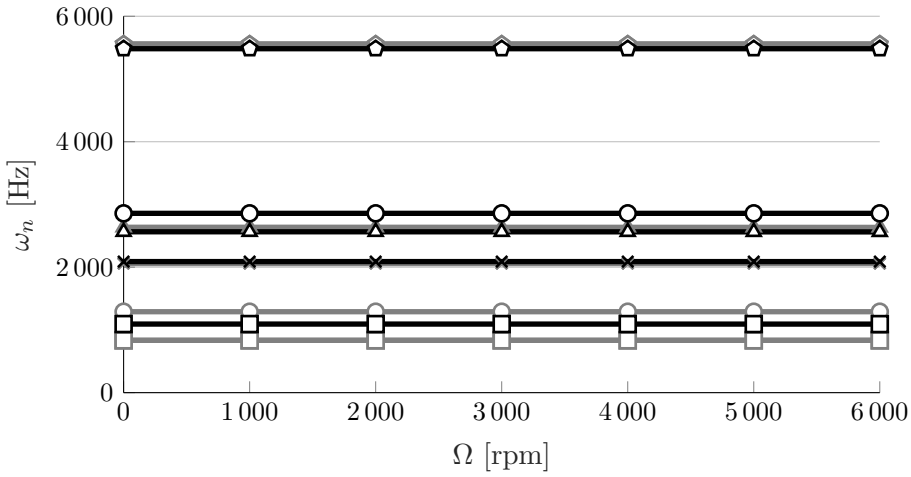

Figure 6.12: Centrifugal softening effect between 0 and 6000 rpm.
Plane gearwheel — Sloped gearwheel
Mode (1,0) — Mode (0,0) — Mode (2,0) — Torsion Mode — Mode (3,0)

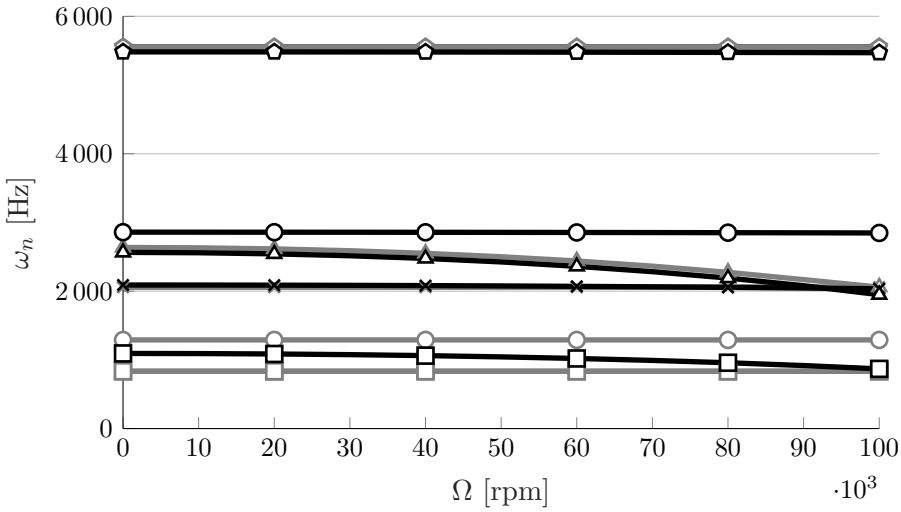

Figure 6.13: Centrifugal softening effect between 0 and 100 000 rpm.
Plane gearwheel — Sloped gearwheel
Mode (1,0) — Mode (0,0) — Mode (2,0) — Torsion Mode — Mode (3,0)

6.3.2 Centrifugal Stiffening Effect

To comprehend the influence of the centrifugal stiffening effect, the evolution of the natural frequencies with the spinning velocity was plotted in Figure 6.14, for both plane and sloped

gearwheels and in a range from 0 to 6000 rpm, discarding the centrifugal softening and Coriolis effects.

Once again, from Figure 6.14 it is not possible to identify graphically the centrifugal stiffening influence in the studied velocity range. So, Figure 6.15 presents the same analysis but in a range from 0 to 100 000 rpm.

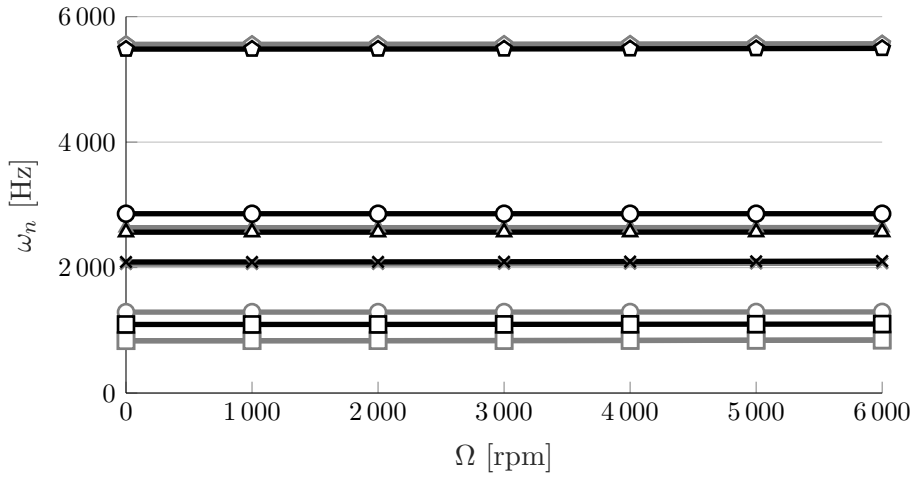

Figure 6.14: Centrifugal stiffening effect between 0 and 6000 rpm.
Plane gearwheel — Sloped gearwheel
Mode (1,0) — Mode (0,0) — Mode (2,0) — Torsion Mode — Mode (3,0)

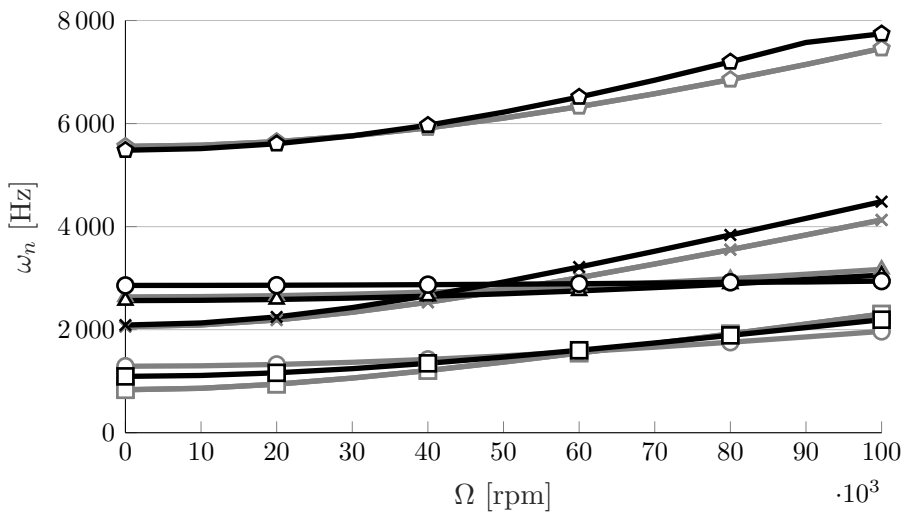

Figure 6.15: Centrifugal stiffening effect between 0 and 100 000 rpm.
Plane gearwheel — Sloped gearwheel
Mode (1,0) — Mode (0,0) — Mode (2,0) — Torsion Mode — Mode (3,0)

Analyzing Figure 6.15, the centrifugal stiffening effect can be identified, since all the natural frequencies increase. This rise is identical for each studied case but not the same for all modes. In fact, it is possible to conclude that the stiffening effect presents a greater influence on the bending modes with higher nodal diameters.

6.3.3 Combined Centrifugal Softening and Stiffening Effects

Once the influence of both centrifugal softening and stiffening effects were individually evaluated, it is important to study their effects when combined. Thus, the evolution of the natural frequencies with the spinning velocity was plotted in Figure 6.16, for both plane and sloped gearwheels and in a range from 0 to 100 000 rpm, since in the 0-6000 rpm range there were no visual changes, discarding only the Coriolis effect.

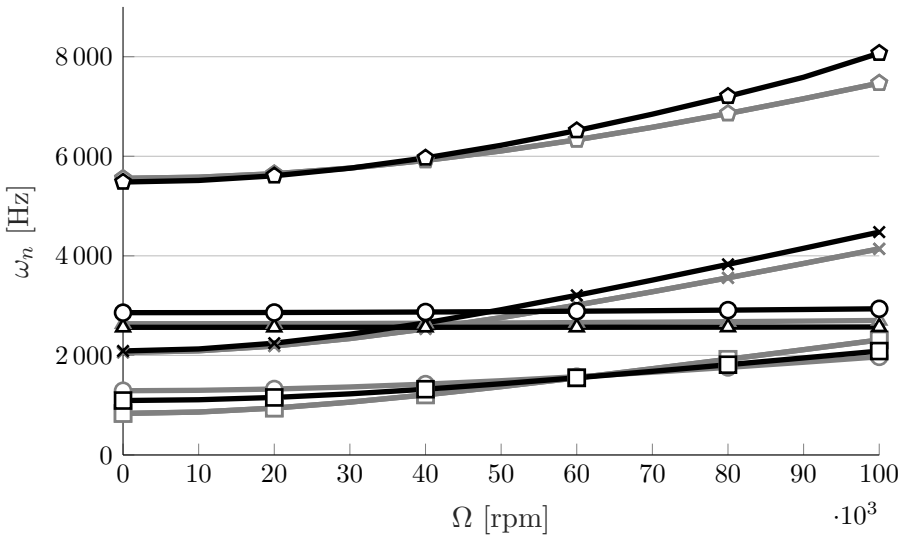

Figure 6.16: Combined centrifugal softening and stiffening effects between 0 and 100 000 rpm.
Plane gearwheel — Sloped gearwheel
Mode (1,0) — Mode (0,0) — Mode (2,0) — Torsion Mode — Mode (3,0)

Analyzing Figure 6.16, it is possible to conclude that the centrifugal stiffening effect is preponderant because the natural frequencies present an increasing evolution. The major difference to Figure 6.15, where only the centrifugal stiffening effect was studied, can be verified in the torsion mode, that reduced its rising tendency and tends to remain approximately constant.

6.3.4 Coriolis Effect

In order to comprehend the influence of the Coriolis effect, the Campbell diagram for the plane and sloped gearwheels was plotted in Figure 6.17, for an inertial reference frame and considering both centrifugal softening and stiffening effects. Note that an inertial system was considered because if a rotating frame was used, its influence would hardly be noticeable.

From Figures 6.17a and 6.17b it is possible to graphically identify the aforementioned split of the natural frequencies for the same natural mode. In fact, their values diverge with increasing rotational velocity, being this variation greater for the modes with higher number of diametrical nodes. It is also possible to conclude that in the working velocity range there are no critical cases, since all the natural frequencies values are greater than the rotating speed.

Figure 6.18 presents the same Campbell diagrams, but now from 0 to 100 000 rpm. In this velocity range it is possible to identify some critical cases for the (1,0) and (2,0) modes for both plane and sloped cases.

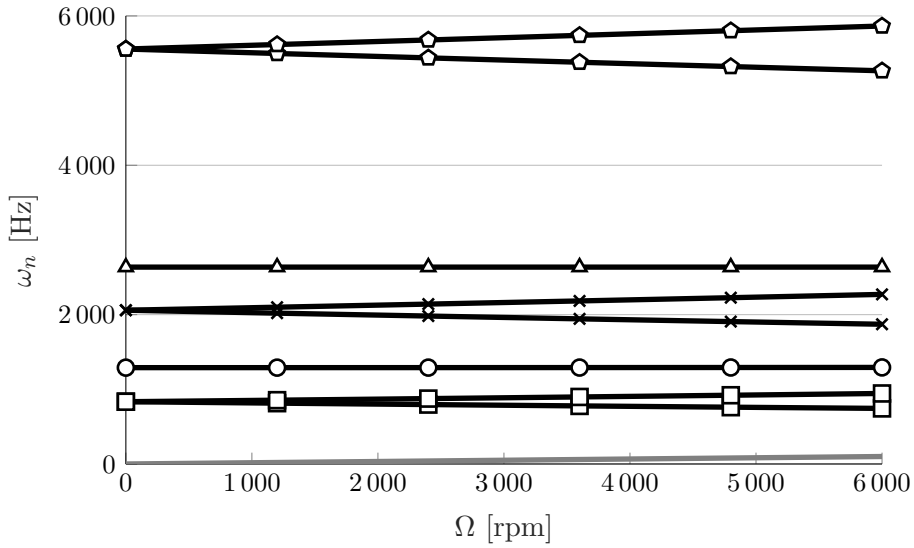

(a) Plane gearwheel.

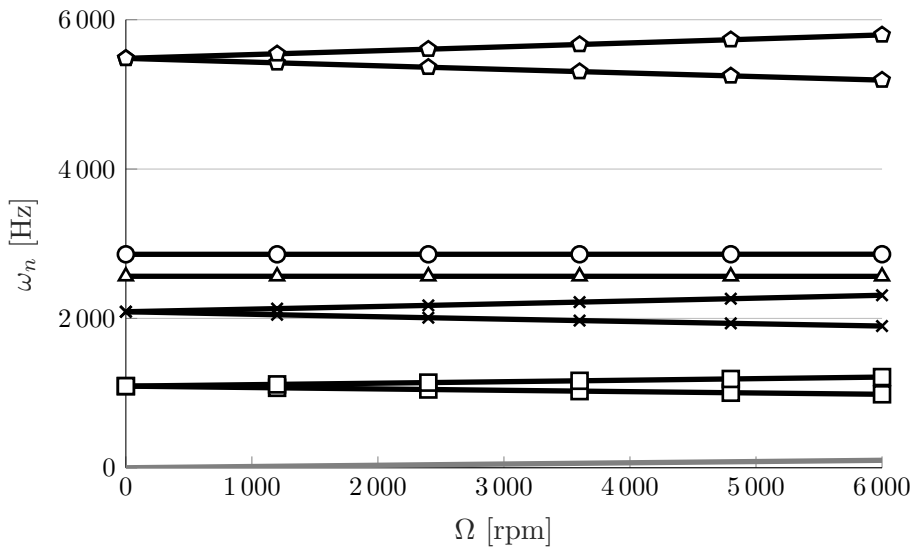

(b) Sloped gearwheel.

Figure 6.17: Campbell diagrams for the plane and sloped cases, between 0 and 6000 rpm.
Mode (1,0) Mode (0,0) Mode (2,0) Torsion Mode Mode (3,0)
$\omega_n = \Omega$

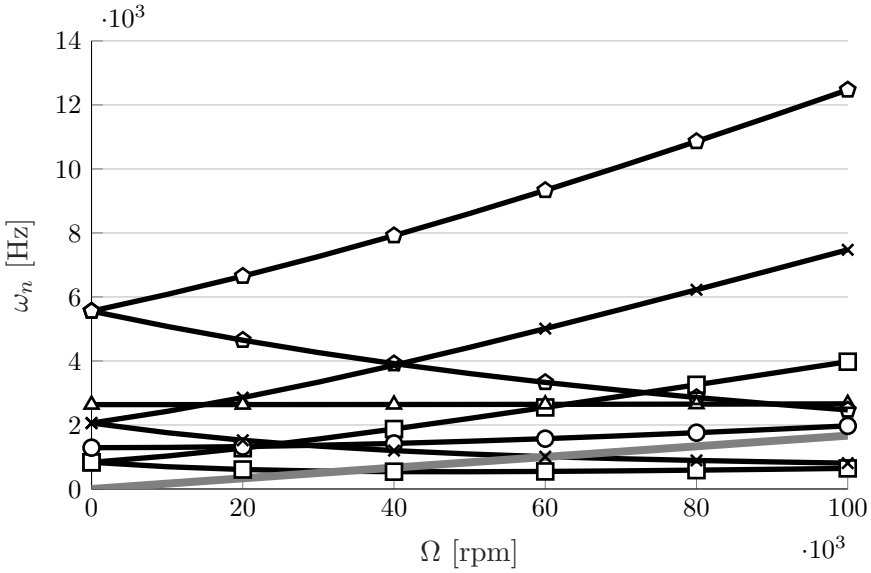

(a) Plane gearwheel.

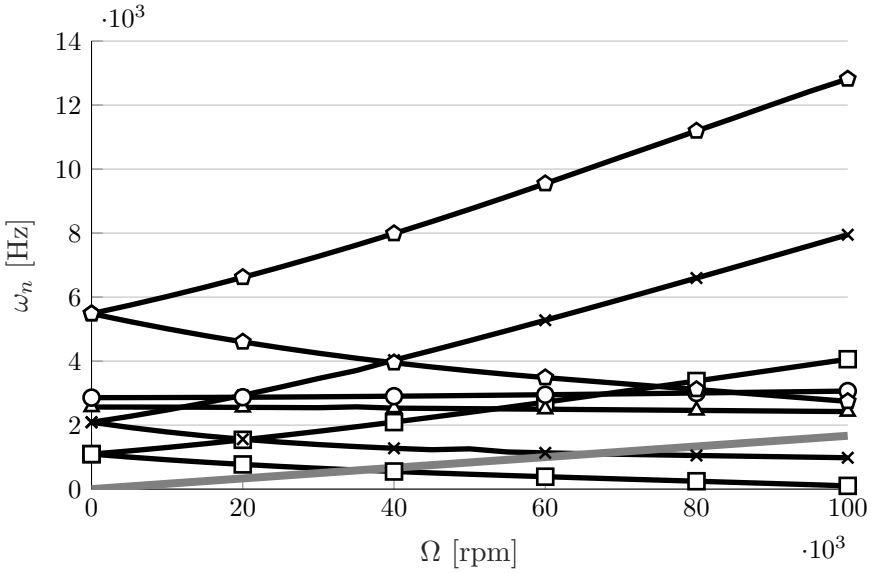

(b) Sloped gearwheel.

Figure 6.18: Campbell diagrams for the plane and sloped cases, between 0 and 100 000 rpm.
Mode (1,0) Mode (0,0) Mode (2,0) Torsion Mode Mode (3,0)
$\omega_n = \Omega$

Chapter 7

Analysis of Circumferentially Configured Viscoelastic Damping Devices

In the present chapter the numerical simulation results of the studied gearwheel with circumferential configured viscoelastic damping devices will be presented and discussed, for both plane and sloped gearwheels. Initially, complete annular shape treatments are considered and studied. Then, these are split into two, four and six segments and the same analysis is performed. Finally, the inclination angle effect is presented and discussed for some of the considered configurations.

7.1 Introduction

In the studied patent, Marsaudon and Cutuli [2014] proposed annular shaped viscoelastic damping devices, that could be continuous or segmented. Thus, the damping efficiency study of these configurations must be done.

The circumferential configured viscoelastic damping devices were defined by an inner and an outer diameter, $\phi_{i\ \text{treatment}}$ and $\phi_{e\ \text{treatment}}$, respectively, and the interruptions were implemented with a non-treated element break.

7.2 Plane Damped Gearwheel

For the plane gearwheel, the first circumferential configurations studied were complete annular shapes, one covering all the possible treated area, other corresponding to an exterior ring and the last corresponding to an interior ring with the same amount of added material as the second case (Figure 7.1, where the gray area corresponds to the damping device). Their diametral dimensions are presented in Table 7.1, since the thickness of each layer was previously presented in Table 5.3.

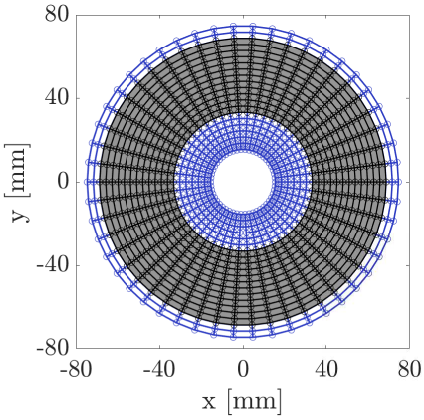

(a) Entire area.

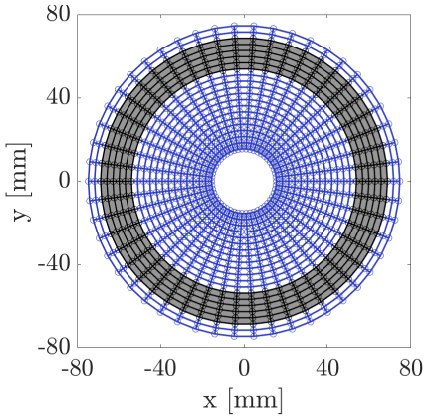

(b) Outer ring.

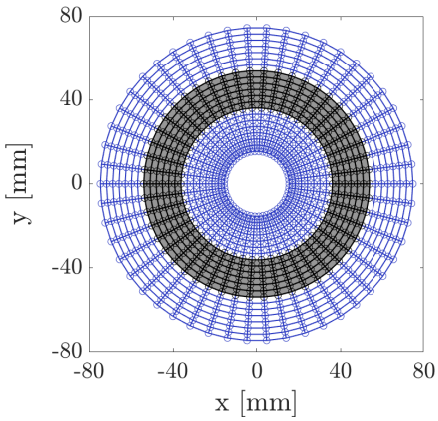

(c) Inner ring.

Figure 7.1: Complete circumferential damping devices' configurations.

The treatment covering all the treatable surface was studied more as a comparison case than a practical or applicable one, since it is associated with a significant added mass. The external damper ring's dimensions were determined in accordance to the ones presented

Table 7.1: Circumferential damping devices' dimensions

Entire Area		Outer Ring		Inner Ring	
ϕ_i treatment [mm]	ϕ_e treatment [mm]	ϕ_i treatment [mm]	ϕ_e treatment [mm]	ϕ_i treatment [mm]	ϕ_e treatment [mm]
68	138	108	138	68	110

by Marsaudon and Cutuli [2014] in the studied patent, since it is positioned closer to the outer teeth rim and presents a radial length of 15 mm. The inner annular configuration presents the same covered area as the previous one and was proposed in order to study the influence of the positioning of the circumferential damping device.

Table 7.2 presents the modal analysis results of these configurations. Note that the $\Delta_{r\ \eta_n}$ values represent the relative difference of the outer and inner circumferential dampers loss factors relatively to the complete treatment and Δm correspond to the added mass for each case. The relative difference values for the natural frequencies, $\Delta_{r\ \omega_n}$, were not presented once the variations were not significant.

Table 7.2: Complete circumferential damping devices' configurations modal analysis results for the plane gearwheel

Mode		Entire Area $\Delta m = 95.36$ g		Outer Ring $\Delta m = 48.80$ g			Inner Ring $\Delta m = 48.80$ g		
	(m,n)	ω_n [Hz]	η_n [%]	ω_n [Hz]	η_n [%]	$\Delta_{r\ \eta_n}$ [%]	ω_n [Hz]	η_n [%]	$\Delta_{r\ \eta_n}$ [%]
1	(1,0)	822.45	0.086	826.45	0.020	-77.341	835.47	0.057	-33.986
2		822.45	0.086	826.45	0.020	-77.341	835.47	0.057	-33.986
3	(0,0)	1261.60	0.364	1269.45	0.078	-78.663	1283.88	0.251	-31.239
4	(2,0)	2049.77	0.367	2048.67	0.032	-91.390	2065.11	0.044	-87.880
5		2049.77	0.367	2048.67	0.032	-91.390	2065.11	0.044	-87.880
6	(Torsion)	2545.80	3.416	2572.82	2.447	-28.363	2607.87	1.161	-66.026
7	(3,0)	5550.51	0.127	5547.63	0.035	-72.159	5573.07	0.005	-96.196
8		5550.51	0.127	5547.63	0.035	-72.159	5573.07	0.005	-96.196

Figures 7.2, 7.3 and 7.4 present the normal modes' factorized total displacement for each treatment configuration (entire treatable area covered, outer and inner complete annular shapes, respectively). The total displacement, u_t, corresponds to the Euclidean norm of the directional u, v and w displacements ($u_t = \sqrt{u^2 + v^2 + w^2}$).

However, an additional step was implemented to obtained the referred plots in order to consider the positive and negative direction of the transverse displacement. In fact, from the previous formula it is possible to verify that the total displacement, u_t, is always positive, from which one could easily conclude that in a bi-dimensional representation of this quantity all the variations from the null value would be positive, thus being impossible to fully comprehend the mode shape. Therefore, in the graphical representation of the total displacement, if the value is negative it means that the transverse movement occurs in the z-axis negative direction.

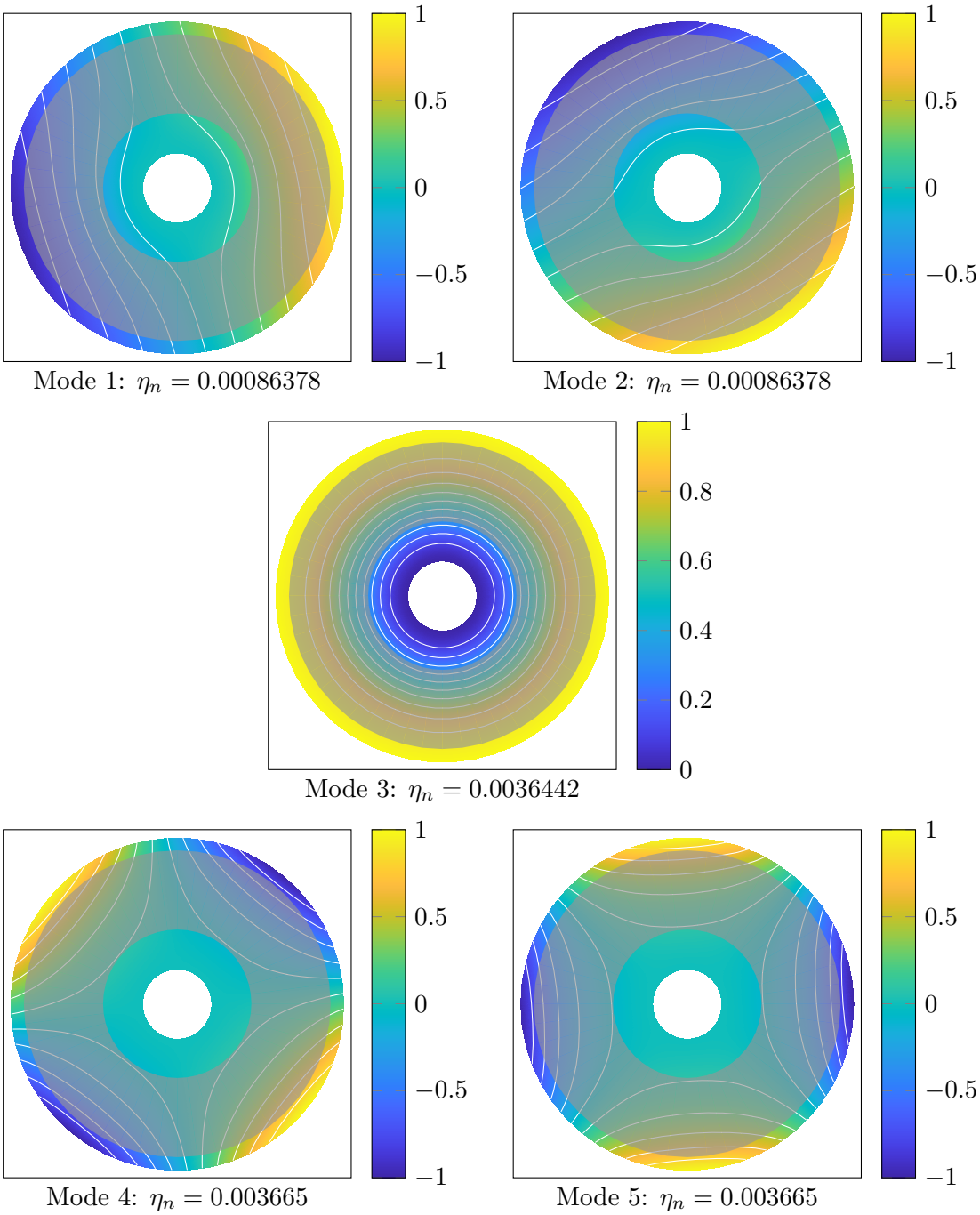

Figure 7.2: Mode shapes for the plane gearwheel with treatable surface completely covered.

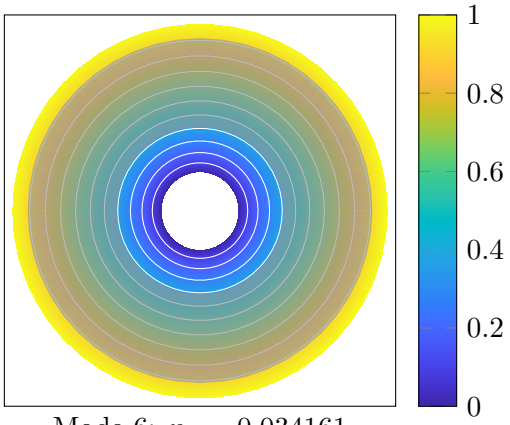

Mode 6: $\eta_n = 0.034161$

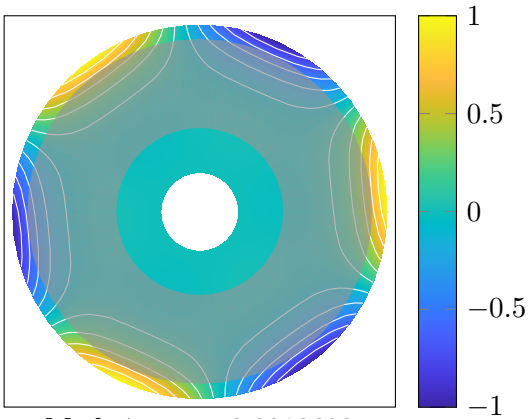

Mode 7: $\eta_n = 0.0012693$

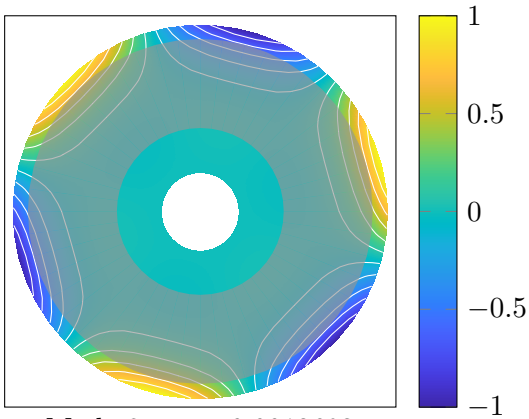

Mode 8: $\eta_n = 0.0012693$

Figure 7.2: Mode shapes for the plane gearwheel with treatable surface completely covered. *(Continued)*

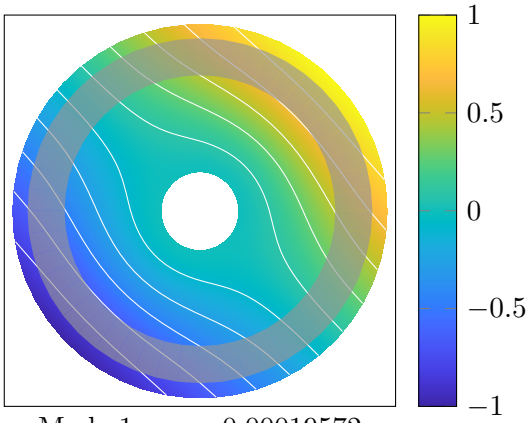

Mode 1: $\eta_n = 0.00019572$

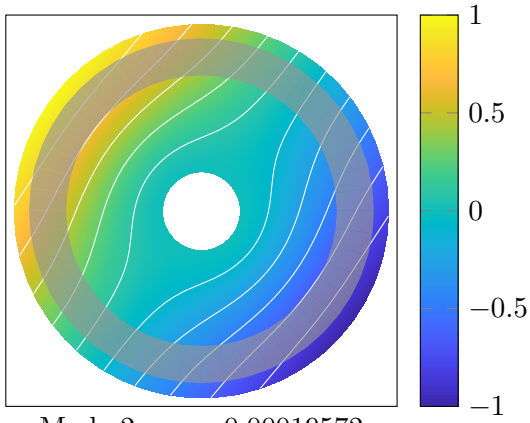

Mode 2: $\eta_n = 0.00019572$

Figure 7.3: Plane gearwheel with complete outer ring damping device mode shapes.

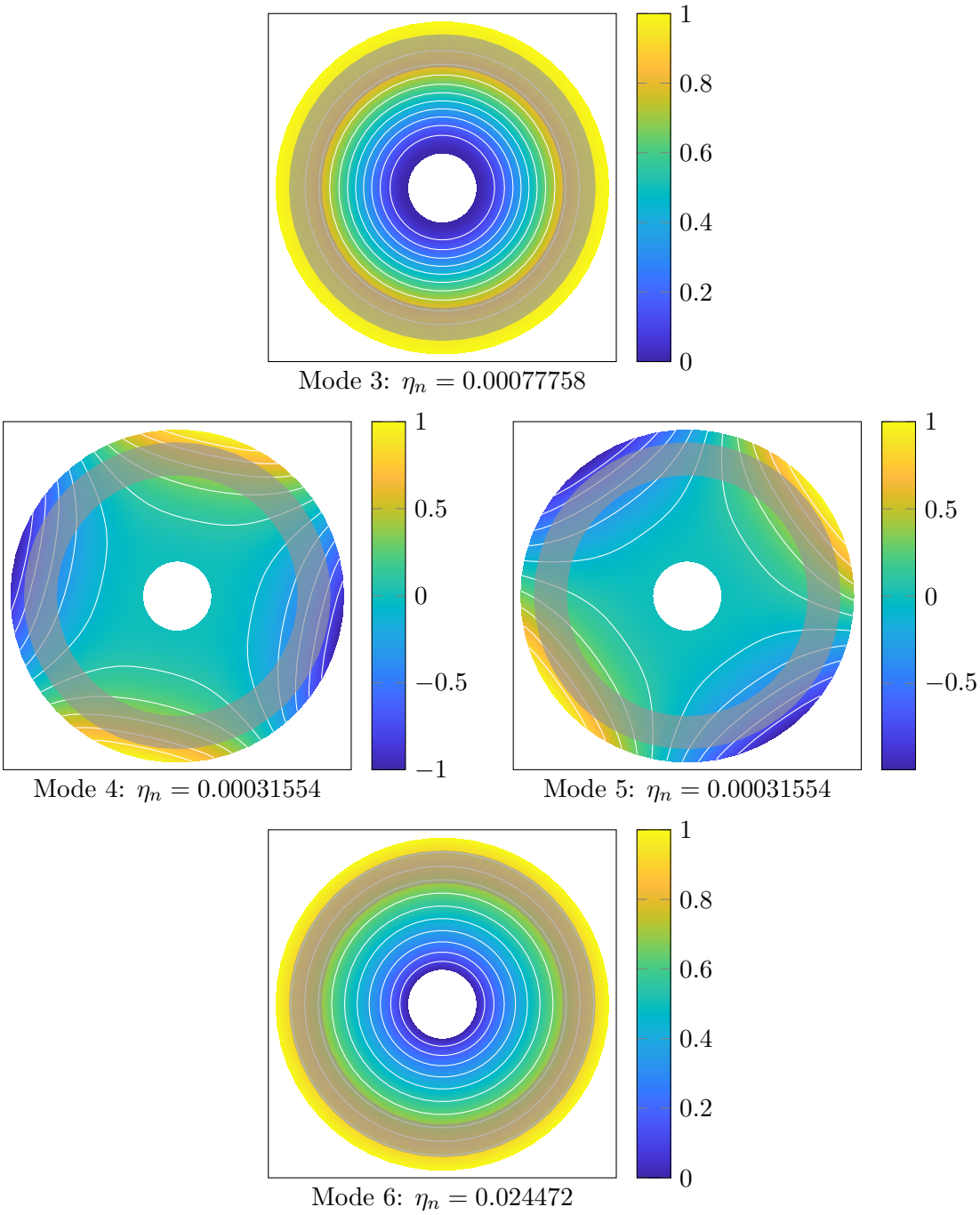

Figure 7.3: Plane gearwheel with complete outer ring damping device mode shapes. *(Continued)*

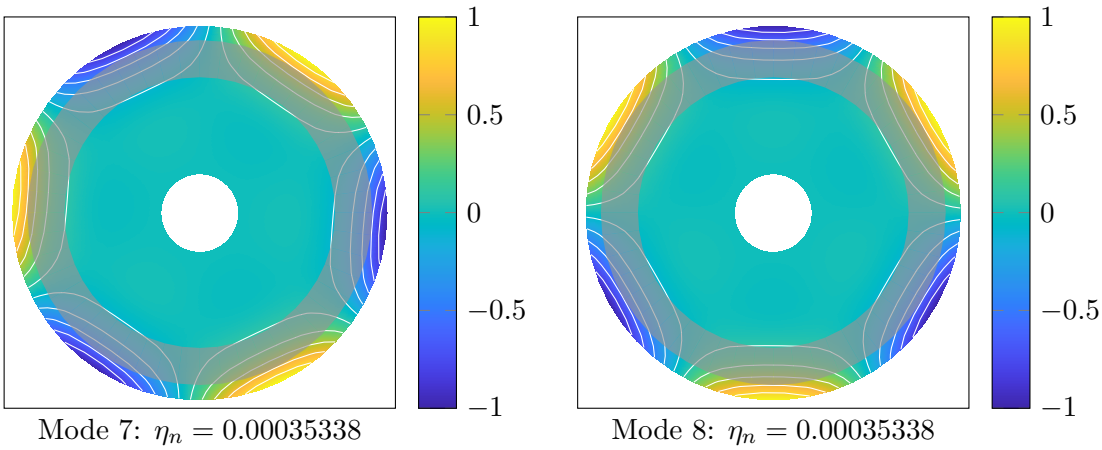

Mode 7: $\eta_n = 0.00035338$ Mode 8: $\eta_n = 0.00035338$

Figure 7.3: Plane gearwheel with complete outer ring damping device mode shapes. *(Continued)*

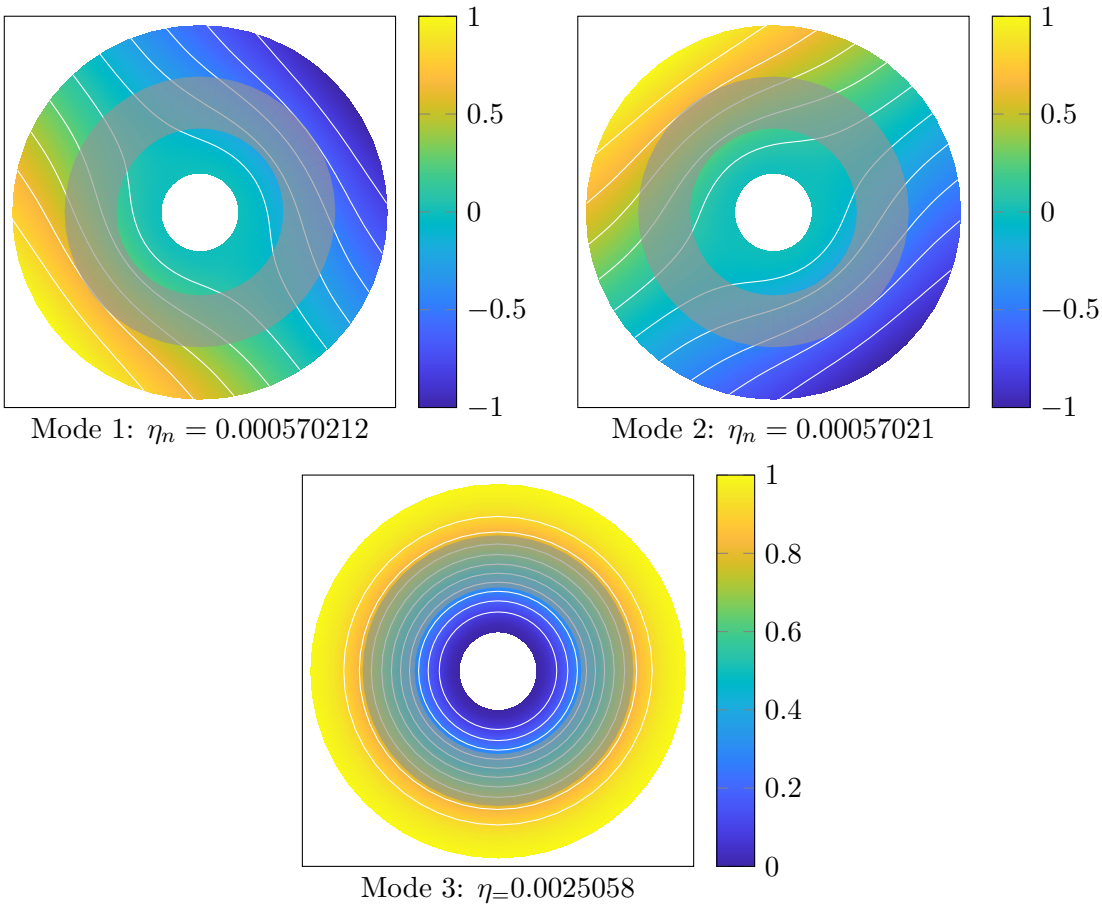

Mode 1: $\eta_n = 0.000570212$ Mode 2: $\eta_n = 0.00057021$

Mode 3: $\eta_{=}0.0025058$

Figure 7.4: Plane gearwheel with complete inner ring damping device mode shapes.

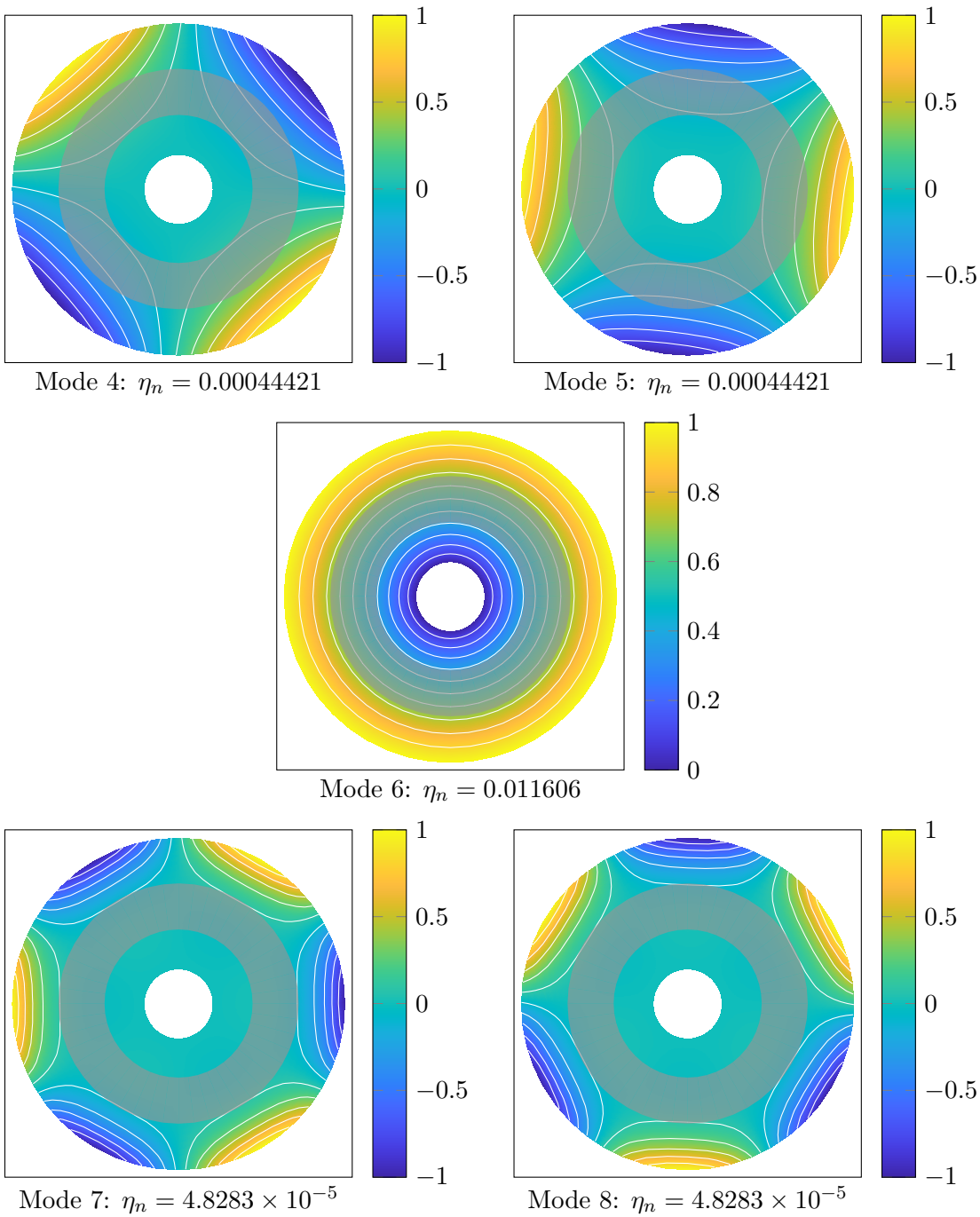

Figure 7.4: Plane gearwheel with complete inner ring damping device mode shapes. *(Continued)*

Finally, the receptance's Bode plot for these cases, as well as the non-treated plane gearwheel, can be seen in Figure 7.5. The considered node and degree of freedom for the excitation and the response record were the same considered in Section 6.2, i.e. an external node and the transverse displacement, w.

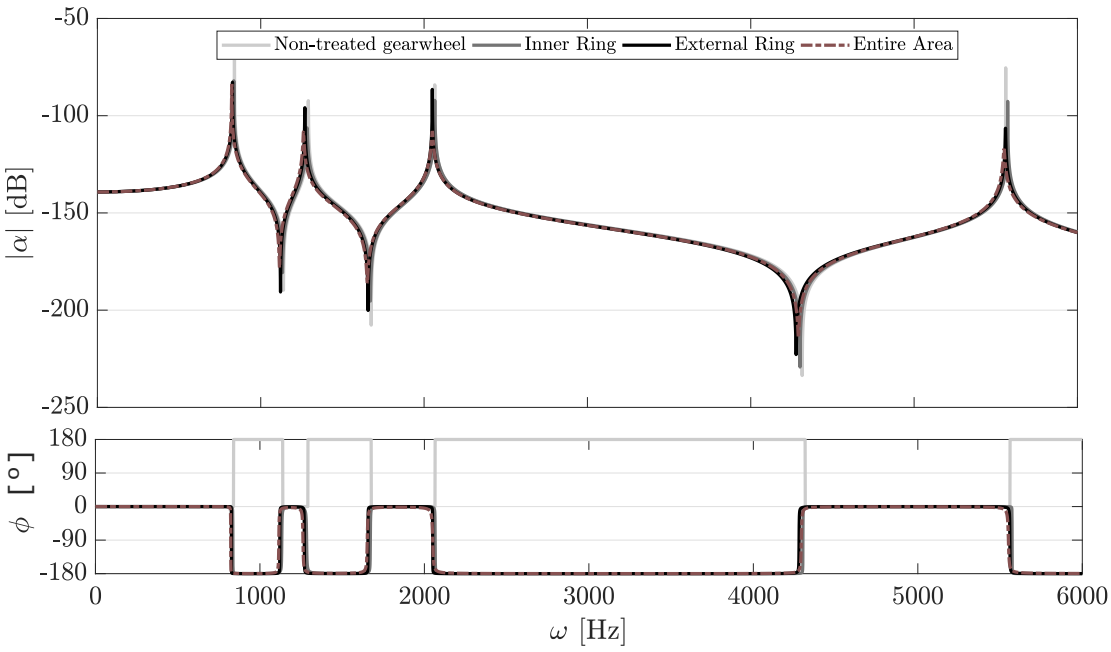

Figure 7.5: Receptance's Bode plot for the complete circumferential damping device configurations applied on the plane gearwheel.

Analyzing Table 7.2, it is possible to conclude that a damping device covering all the treatable surface of the gearwheel reveals the best damping capacity of all the analyzed configurations, since lower loss factor values were verified for the partial treatments. Figure 7.5 also reveals this same conclusion, as the peak amplitude values are smaller. This phenomenon results from the higher quantity of viscoelastic material, which increases the dissipation phenomena.

However, a larger covered area is associated with a greater amount of added mass to the gearwheel, which is not compensated by the necessary increase of stiffness, leading to the reduction of its natural frequencies, as can be seen in Table 7.2. As a more accurate and practical performance appraiser a dimensionless quantity representing the ratio between the loss factor and the relative added mass can be considered, as follows:

$$H = \frac{\eta_n}{\Delta_{r\,m}} \tag{7.1}$$

where $\Delta_{r\,m}$ is given by the ratio between the damping device's and gearwheel's masses ($m_{gearwheel} = 1.392\,\text{kg}$). This way, the weighting between the damping capacity and the induced mass modification can be studied. Table 7.3 presents these results for the studied cases, neglecting the multiplicity phenomenon.

From Table 7.3, it is possible to conclude that the previously mentioned superiority of the completely covered surface configuration was partially undone. In fact, the outer ring configuration presented a higher H value for the torsion mode, which can be explained by the fact that the greater displacements and strains in this case are verified in the outer

Table 7.3: Loss factor and added mass weighting, H, for the complete circumferential configurations in the plane gearwheel

Mode	(m,n)	Entire Area $\Delta_{r\,m} = 6.85\,\%$	Outer Ring $\Delta_{r\,m} = 3.50\,\%$		Inner Ring $\Delta_{r\,m} = 3.50\,\%$	
		H	H	$\Delta_{r\,H}$ [%]	H	$\Delta_{r\,H}$ [%]
1 & 2	(1,0)	0.013	0.006	-55.723	0.016	28.997
3	(0,0)	0.053	0.022	-58.304	0.071	34.366
4 & 5	(2,0)	0.053	0.009	-83.176	0.013	-76.316
6	(Torsion)	0.499	0.698	39.986	0.331	-33.612
7 & 8	(3,0)	0.019	0.010	-45.597	0.001	-92.567

region of the gearwheel and thus the viscoelastic material's influence closer to the center are minor. On the other hand, the inner ring configuration presented higher H values for the (1,0) and (0,0) modes, which can also be explained by the correspondent mode shapes. In fact, despite the total displacement increase with the distance to the center for these modes, in the plane gearwheel case, the higher strains occur closer to the inner clamped edge, resulting in greater energy dissipation phenomenon in these regions.

Note that an analysis based on the suggested parameter H can only be done when trying to determine the best compromise solution between damping capacity and mass modification. Some cases require a specific loss factor value that can only be obtained with a damper device with certain dimensions.

Since the inner ring configuration was determined to ensure the same amount of added material/covered surface, Table 7.3 can also be used to compare the efficiencies of the partial treatments. It can be easily concluded that the outer ring presents a better damping performance for the three last natural modes, while the inner ring configuration revealed better dissipation characteristics for the first five modes. This can be explained using the same arguments as previously presented when comparing the H parameter values of these configurations with the complete covered surface. Only the (3,0) mode was not addressed, but, from the mode shapes, it can be seen that the displacements are nearly constant and close to zero near the center and that the higher number of nodal diameters leads to significant strains in the regions close to the outer rim. From Table 7.2, it can also be noticed that the outer ring configuration is associated with lower natural frequencies, resultant from the fact that the low stiffness viscoelastic material is added further from the gearwheel's center.

Before moving on to the next analysis, it is important to note that the addition of the damping devices to the plane gearwheel led to the appearance of non-null membrane displacements in the bending modes and transverse displacement in the torsion mode. As an example, Figure 7.6 presents the mode shape's directional displacements for the mode 1.A and for the outer ring configuration.

It is possible to verify that the displacements in the x and y-axis, for the bending modes, are much smaller than the ones in z-direction, but they are not zero, as for the non-treated plane gearwheel. This fact results from the deviation of the neutral axis as a consequence of the non-symmetrical addition of material.

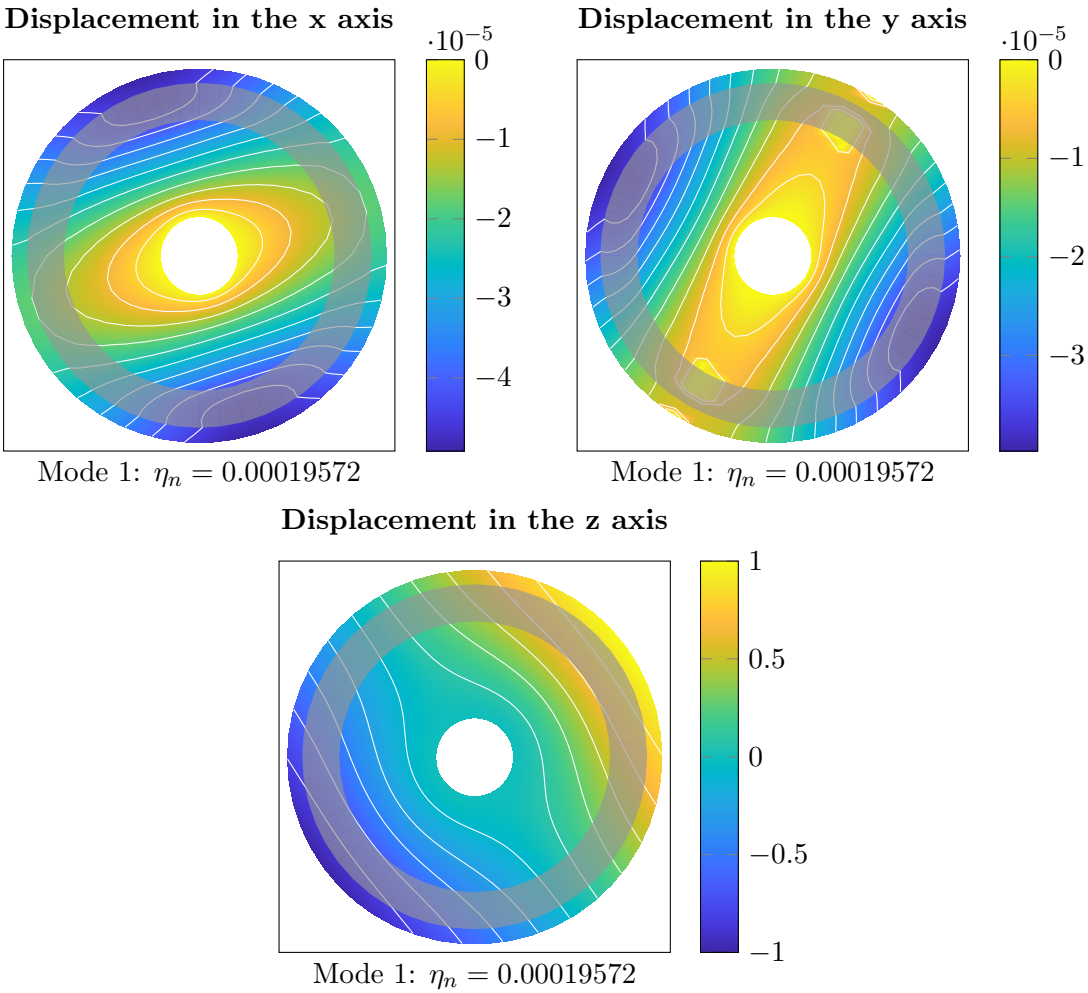

Figure 7.6: External ring configuration mode 1 mode shape's directional displacements.

7.2.1 Segmented Configurations

Split annular shapes were also studied. These consisted in the discontinuance of the previous outer and inner ring setups, leading to circumferential configurations segmented into two, four and six parts. Figure 7.7 presents the correspondent meshes, where again the gray area represents the areas with the damping treatment.

Starting their study with the split outer ring configurations, Table 7.4 presents their loss factor results. Note that $\Delta_{r\,\eta_n}$ values represent the relative difference of the sectioned setups relatively to the continuous one and that the natural frequency values are not presented in the referred Table 7.4, but in the correspondent mode shapes (Figures 7.8, 7.9 and 7.10). On the other hand, Table 7.5 presents the loss factor-added mass weighting results, H, for the present case.

Finally, Figure 7.11 presents the receptance's Bode plot for the split outer ring configurations.

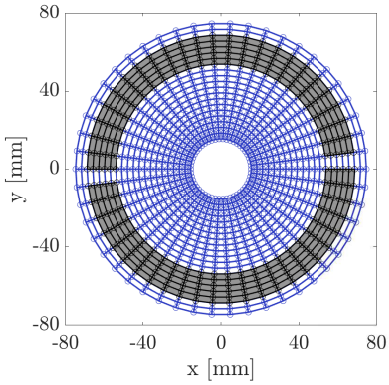

(a) Outer ring, 2 sections.

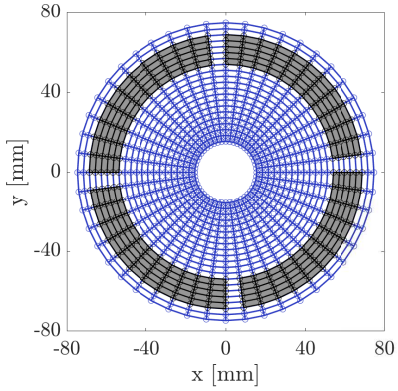

(b) Outer ring, 4 sections.

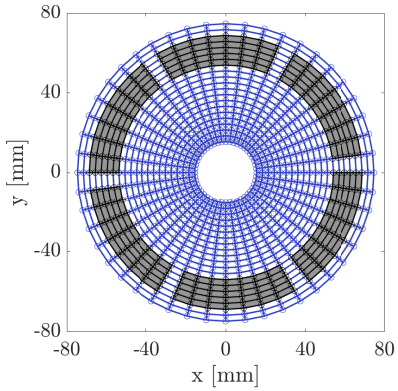

(c) Outer ring, 6 sections.

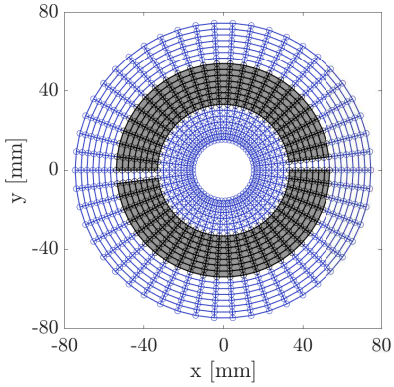

(d) Inner ring, 2 sections.

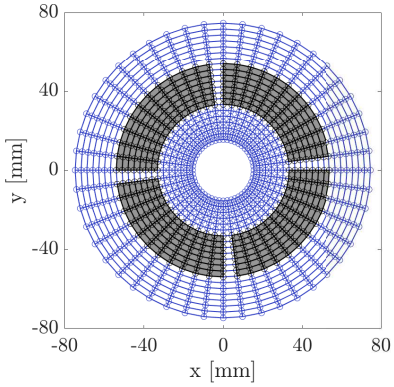

(e) Inner ring, 4 sections.

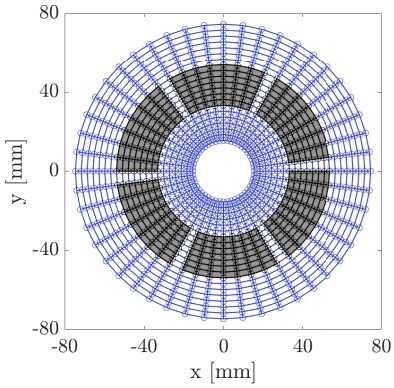

(f) Inner ring, 6 sections.

Figure 7.7: Split circumferential damping devices' configurations.

Table 7.4: Outer split ring damping devices' configurations loss factor results for the plane gearwheel.

Mode		Continuous $\Delta m = 48.80\,\mathrm{g}$	2 Sections $\Delta m = 46.85\,\mathrm{g}$		4 Sections $\Delta m = 44.90\,\mathrm{g}$		6 Sections $\Delta m = 42.94\,\mathrm{g}$	
	(m,n)	η_n [%]	η_n [%]	$\Delta_{r\,\eta_n}$ [%]	η_n [%]	$\Delta_{r\,\eta_n}$ [%]	η_n [%]	$\Delta_{r\,\eta_n}$ [%]
1	(1,0)	0.020	0.019	-3.467	0.009	-53.979	0.007	-65.372
2		0.020	0.009	-52.089	0.008	-59.089	0.007	-65.372
3	(0,0)	0.078	0.038	-50.806	0.020	-73.742	0.014	-82.548
4	(2,0)	0.032	0.089	182.026	0.080	152.645	0.061	94.403
5		0.032	0.047	49.154	0.064	103.000	0.061	94.403
6	(Torsion)	2.447	2.361	-3.538	2.268	-7.330	2.176	-11.0861
7	(3,0)	0.035	0.652	1744.649	2.089	5812.870	2.478	6913.328
8		0.035	0.179	406.514	2.089	5812.870	2.358	6572.986

Table 7.5: Loss factor and added mass weighting, H, for the complete and split outer ring configurations in the plane gearwheel

Mode		Continuous $\Delta_{r\,m} = 3.50\,\%$	2 Sections $\Delta_{r\,m} = 3.36\,\%$		4 Sections $\Delta_{r\,m} = 3.22\,\%$		6 Sections $\Delta_{r\,m} = 3.08\,\%$	
	(m,n)	H	H	$\Delta_{r\,H}$ [%]	H	$\Delta_{r\,H}$ [%]	H	$\Delta_{r\,H}$ [%]
1	(1,0)	0.006	0.006	0.551	0.003	-49.982	0.002	-60.647
2		0.006	0.003	-50.095	0.002	-55.535	0.002	-60.647
3	(0,0)	0.022	0.011	-48.759	0.006	-71.462	0.004	-80.167
4	(2,0)	0.009	0.026	193.765	0.025	174.590	0.020	120.933
5		0.009	0.014	55.362	0.020	120.633	0.020	120.933
6	(Torsion)	0.698	0.701	0.477	0.703	0.719	0.705	1.048
7	(3,0)	0.010	0.194	1821.427	0.648	6326.460	0.803	7870.434
8		0.010	0.053	427.596	0.648	6326.460	0.764	7483.646

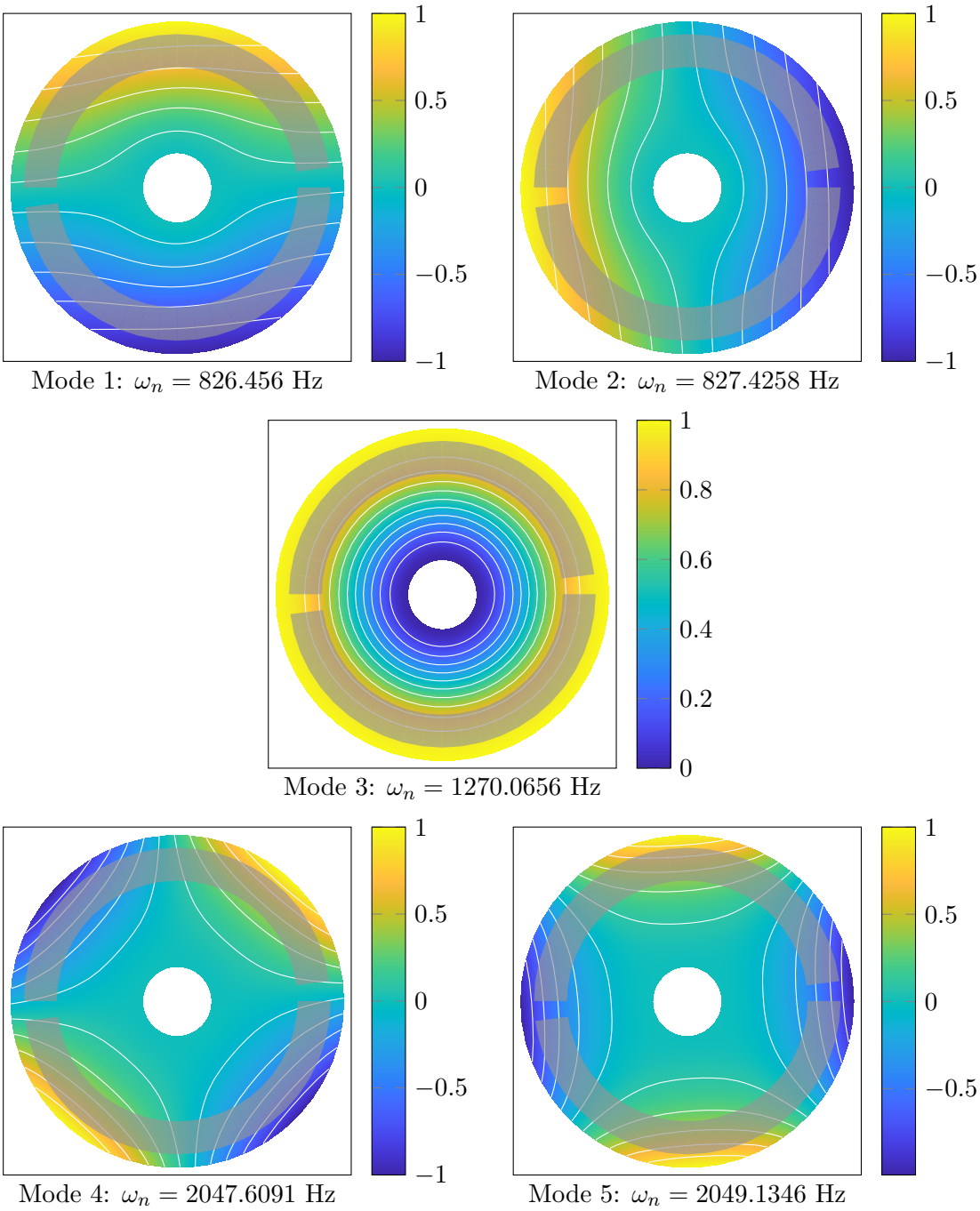

Figure 7.8: Plane gearwheel with outer ring configuration split into two sections mode shapes.

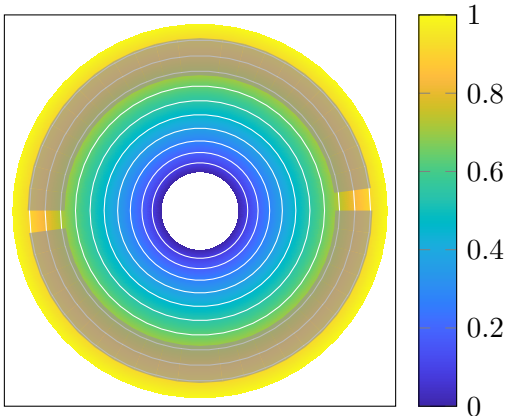

Mode 6: $\omega_n = 2575.2089$ Hz

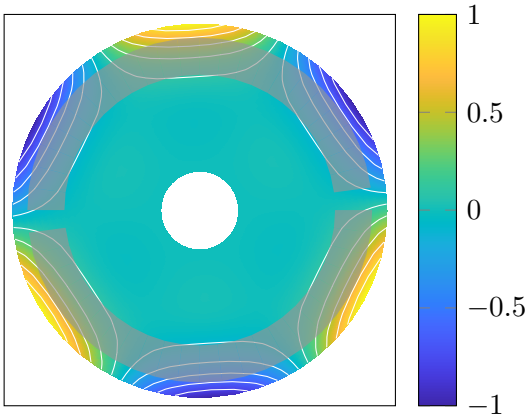

Mode 7: $\omega_n = 5539.2968$ Hz

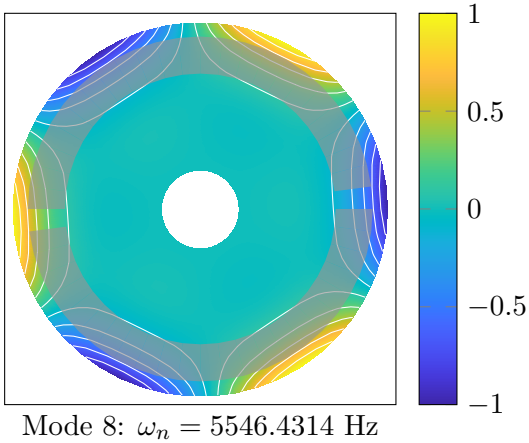

Mode 8: $\omega_n = 5546.4314$ Hz

Figure 7.8: Plane gearwheel with outer ring configuration split into two sections mode shapes. *(Continued)*

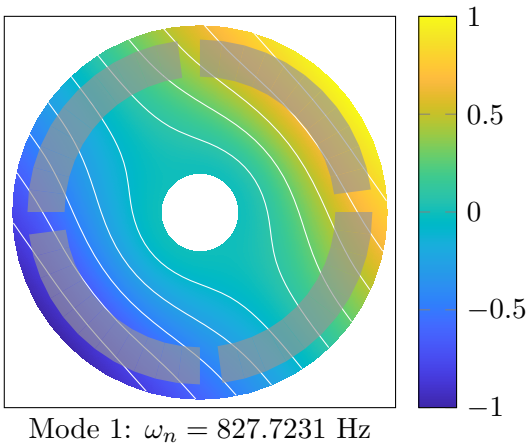

Mode 1: $\omega_n = 827.7231$ Hz

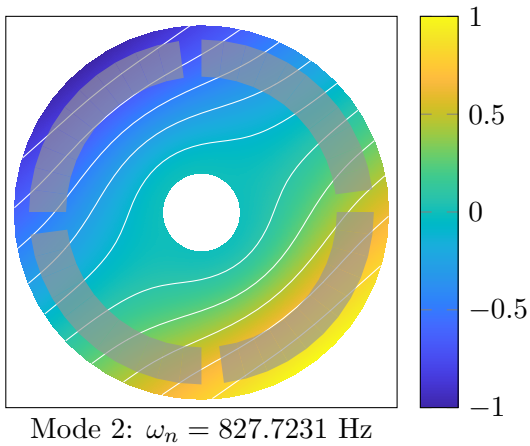

Mode 2: $\omega_n = 827.7231$ Hz

Figure 7.9: Plane gearwheel with outer ring configuration split into four sections mode shapes.

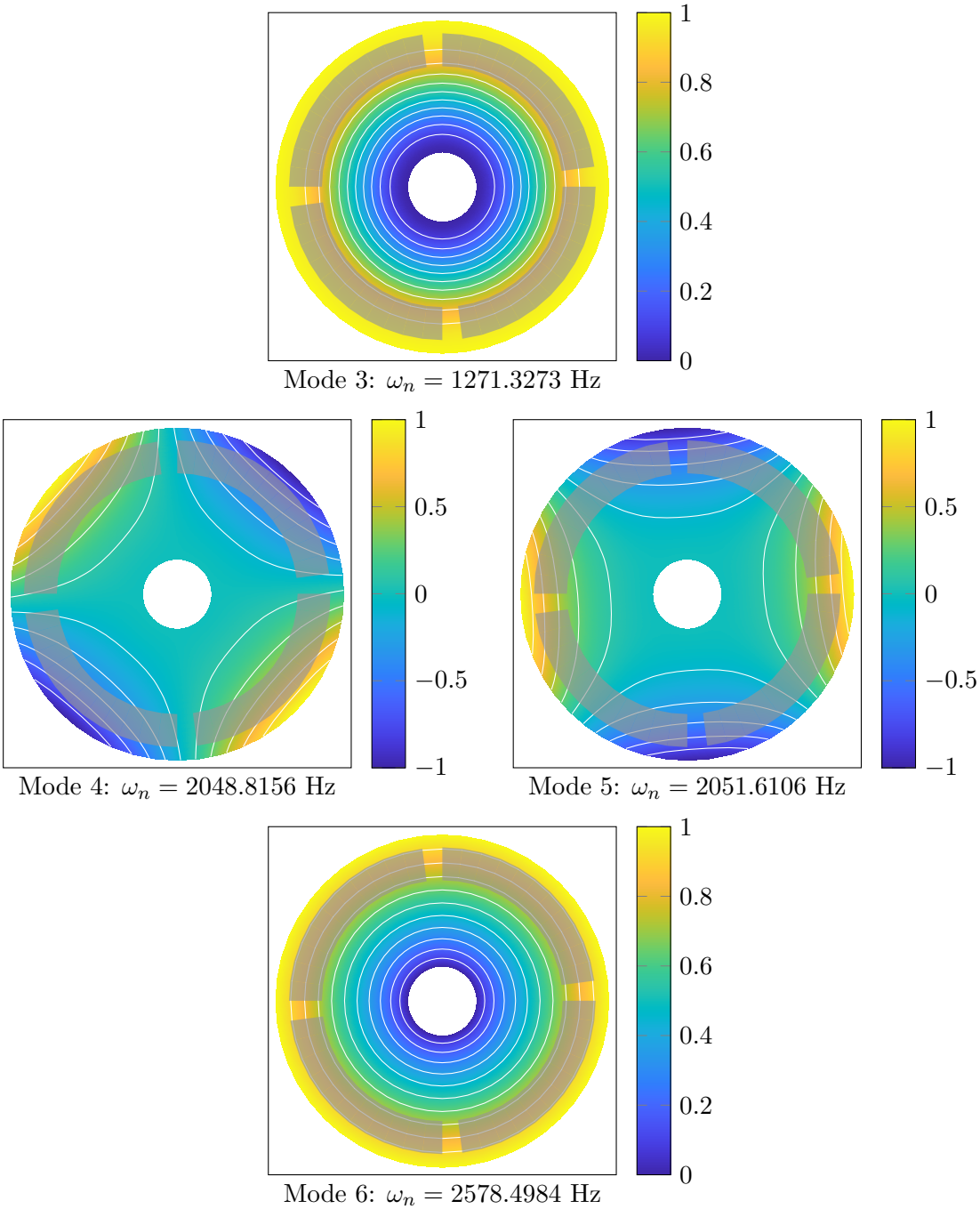

Figure 7.9: Plane gearwheel with outer ring configuration split into four sections mode shapes. *(Continued)*

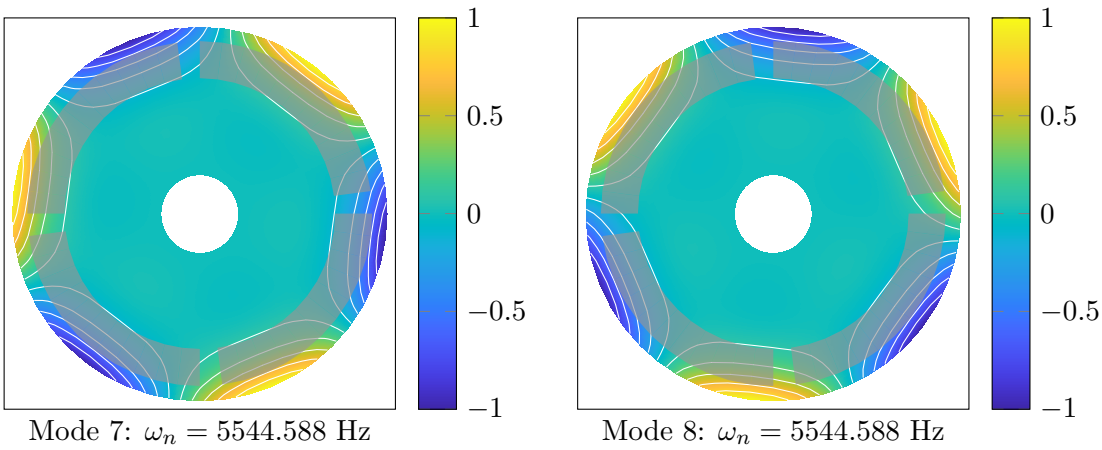

Mode 7: $\omega_n = 5544.588$ Hz

Mode 8: $\omega_n = 5544.588$ Hz

Figure 7.9: Plane gearwheel with outer ring configuration split into four sections mode shapes. *(Continued)*

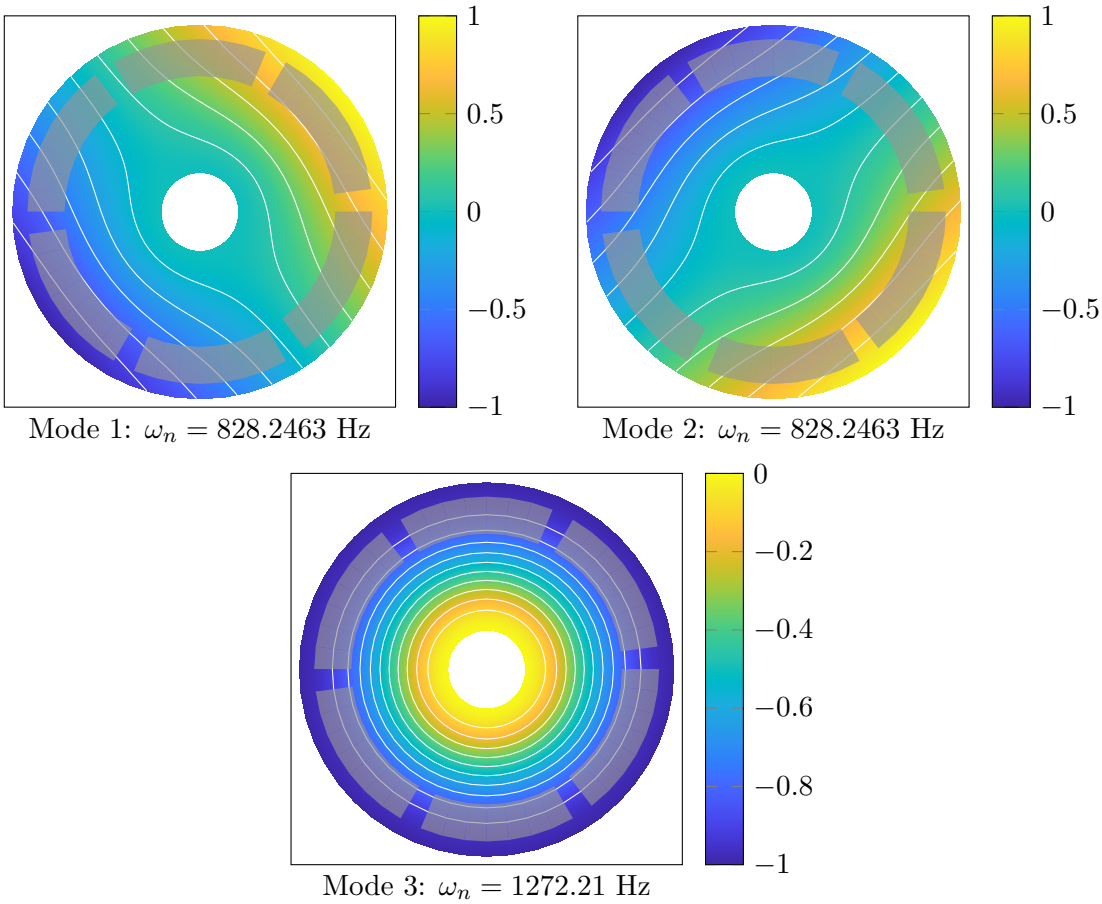

Mode 1: $\omega_n = 828.2463$ Hz

Mode 2: $\omega_n = 828.2463$ Hz

Mode 3: $\omega_n = 1272.21$ Hz

Figure 7.10: Plane gearwheel with outer ring configuration split into six sections mode shapes.

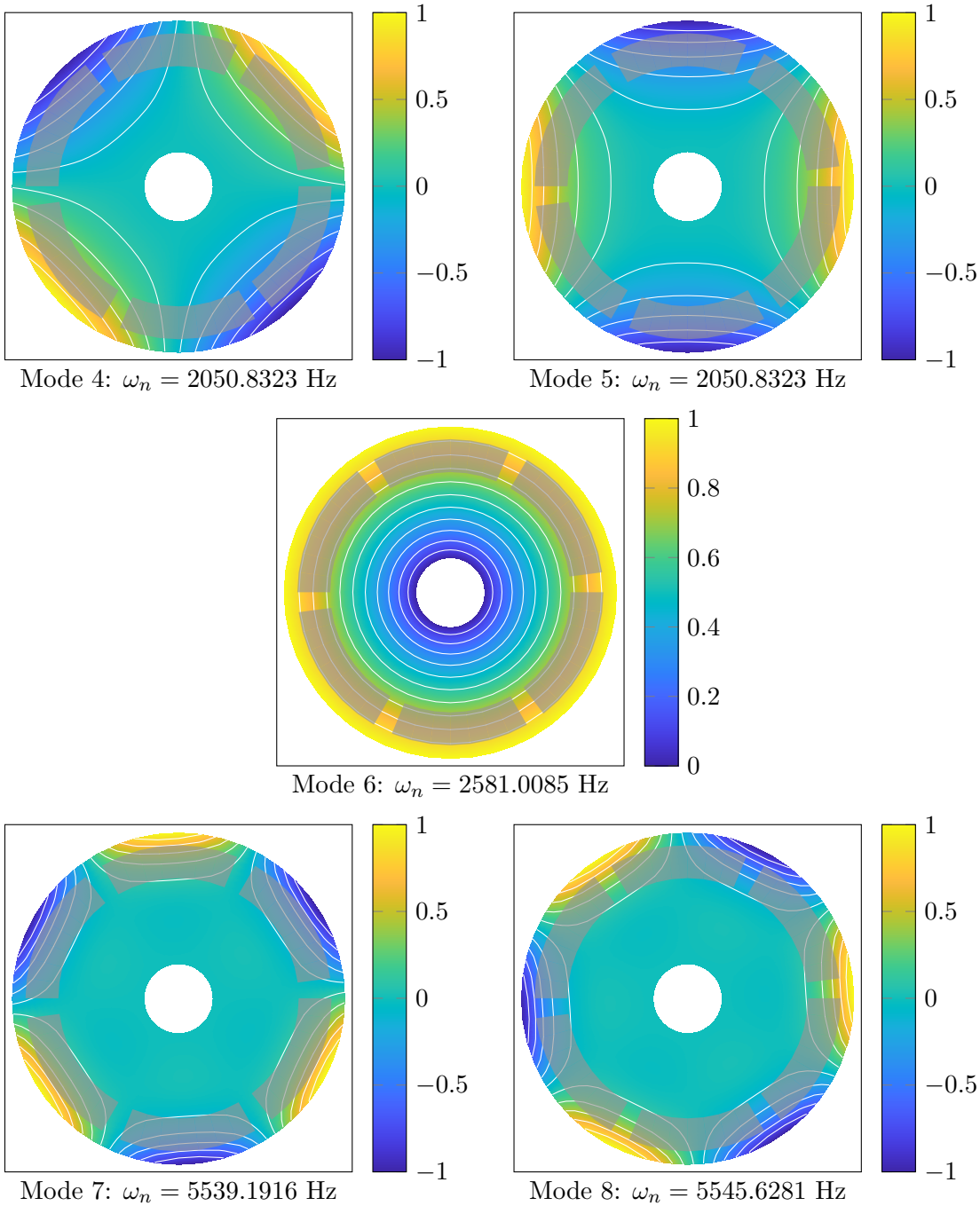

Figure 7.10: Plane gearwheel with outer ring configuration split into six sections mode shapes. *(Continued)*

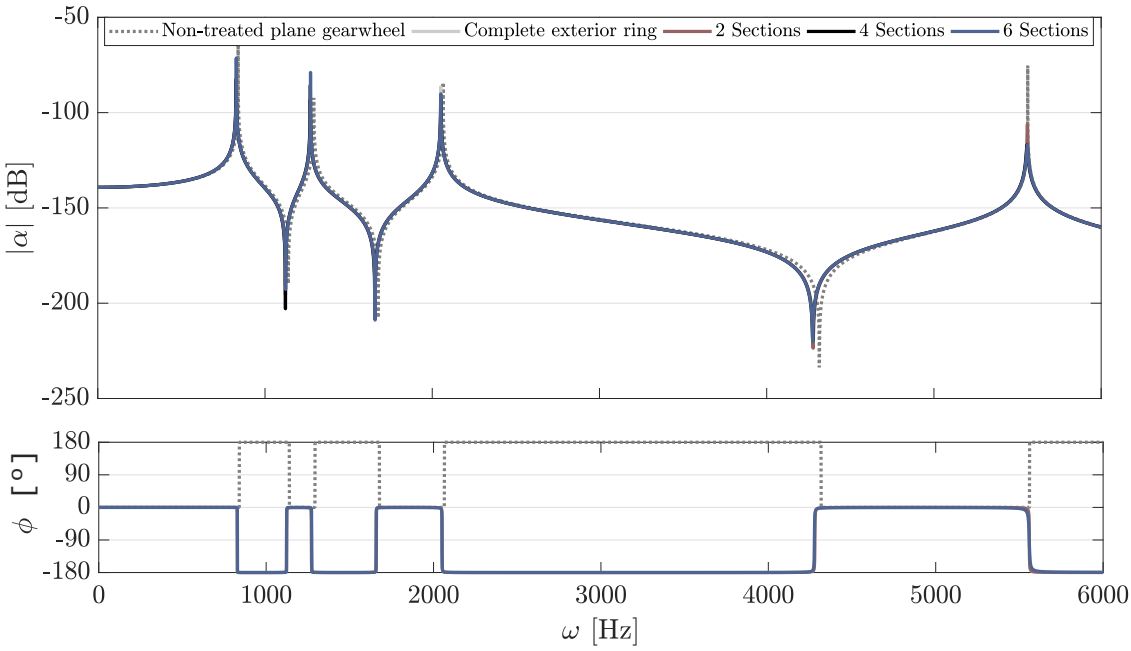

Figure 7.11: Receptance Bode plot for the split outer ring damping device configurations on the plane gearwheel.

Analyzing Table 7.4, it is possible to conclude that the continuous outer ring configuration presents better damping capacities for the (1,0), (0,0) and torsion modes, while the split configurations present higher loss factor values for the (2,0) and (3,0) modes. When considering the weighting between the loss factor and the added mass of the damping device, in Table 7.5, it is possible to verify that all the previous relations subsist, except for the torsion mode, where the performance of all configurations are nearly the same. These damping capacity variations between the continuous and the split configurations may be due to the appearance of the boundary effects in the discontinuity zones.

On the other hand, it is possible to conclude that the split configurations broke the geometrical axisymmetry of the global structure, leading to the end of the natural frequency and loss factor multiplicity phenomenon on some modes. From Figures 7.8, 7.9 and 7.10, it is possible to observe that the same mode can present a case with the diametral nodes coincident with the discontinuity and the other with the diametral nodes crossing the damping device. The first cases are associated with a lower natural frequency value, meaning that the setup deforms more easily, and a higher loss factor, meaning that a higher damping performance is achieved, while the second are associated with higher natural frequencies and lower loss factors.

The higher stiffness of the cases where the diametral nodes cross the damping device can be explained by the higher strains near the nodes when comparing with the zones where the displacement peaks. Thus, the added layers will act as an opposition to the development of said effects, leading to an increase of the required energy. On the other hand, the lower loss factor in these situations can possibly be explained by the zone where the boundary effects develop. In fact, in these cases the discontinuities' location correspond with the displacement peaks' area, while in the other cases they are situated in the nodal areas, which are associated with high strains, thus increasing the boundary effects.

Presenting now the split inner ring configuration analysis, Table 7.6 presents the associated loss factor results and Table 7.7 the H parameter values. Once again, the natural frequencies are presented along with the correspondent mode shape, in Figures 7.12, 7.13

and 7.14. Figure 7.15 presents the receptance's Bode plot for the split inner ring configurations.

Table 7.6: Inner split ring damping devices' configurations loss factor results for the plane gearwheel.

Mode		Continuous $\Delta m = 48.80\,\mathrm{g}$	2 Sections $\Delta m = 46.84\,\mathrm{g}$		4 Sections $\Delta m = 44.89\,\mathrm{g}$		6 Sections $\Delta m = 42.94\,\mathrm{g}$	
	(m,n)	η_n [%]	η_n [%]	$\Delta_{r\,\eta_n}$ [%]	η_n [%]	$\Delta_{r\,\eta_n}$ [%]	η_n [%]	$\Delta_{r\,\eta_n}$ [%]
1	(1,0)	0.057	0.065	13.988	0.026	-54.764	0.016	-71.236
2		0.057	0.027	-51.837	0.026	-54.764	0.016	-71.236
3	(0,0)	0.251	0.143	-42.783	0.053	-78.961	0.026	-89.590
4	(2,0)	0.044	0.037	-16.512	0.026	-41.880	0.021	-52.012
5		0.044	0.037	-15.974	0.026	-41.880	0.021	-52.012
6	(Torsion)	1.161	1.181	1.772	1.132	-2.491	1.083	-6.691
7	(3,0)	0.005	0.004	-20.042	0.064	1235.374	0.087	1705.791
8		0.005	0.007	37.888	0.064	1235.374	0.054	1010.765

Table 7.7: Loss factor and added mass weighting, H, for the complete and split inner ring configurations in the plane gearwheel

Mode		Continuous $\Delta_{r\,m} = 3.50\,\%$	2 Sections $\Delta_{r\,m} = 3.36\,\%$		4 Sections $\Delta_{r\,m} = 3.22\,\%$		6 Sections $\Delta_{r\,m} = 3.08\,\%$	
	(m,n)	H	H	$\Delta_{r\,H}$ [%]	H	$\Delta_{r\,H}$ [%]	H	$\Delta_{r\,H}$ [%]
1	(1,0)	0.016	0.019	18.743	0.008	-50.826	0.005	-67.308
2		0.016	0.008	-49.828	0.008	-50.826	0.005	-67.308
3	(0,0)	0.071	0.043	-40.396	0.016	-77.130	0.008	-88.168
4	(2,0)	0.013	0.011	-13.029	0.008	-36.819	0.007	-45.459
5		0.013	0.011	-12.469	0.007	-40.833	0.007	-45.459
6	(Torsion)	0.331	0.351	6.018	0.351	5.999	0.351	6.051
7	(3,0)	0.001	0.001	-16.706	0.020	1351.649	0.028	1952.380
8		0.001	0.002	43.640	0.020	1351.649	0.017	1162.445

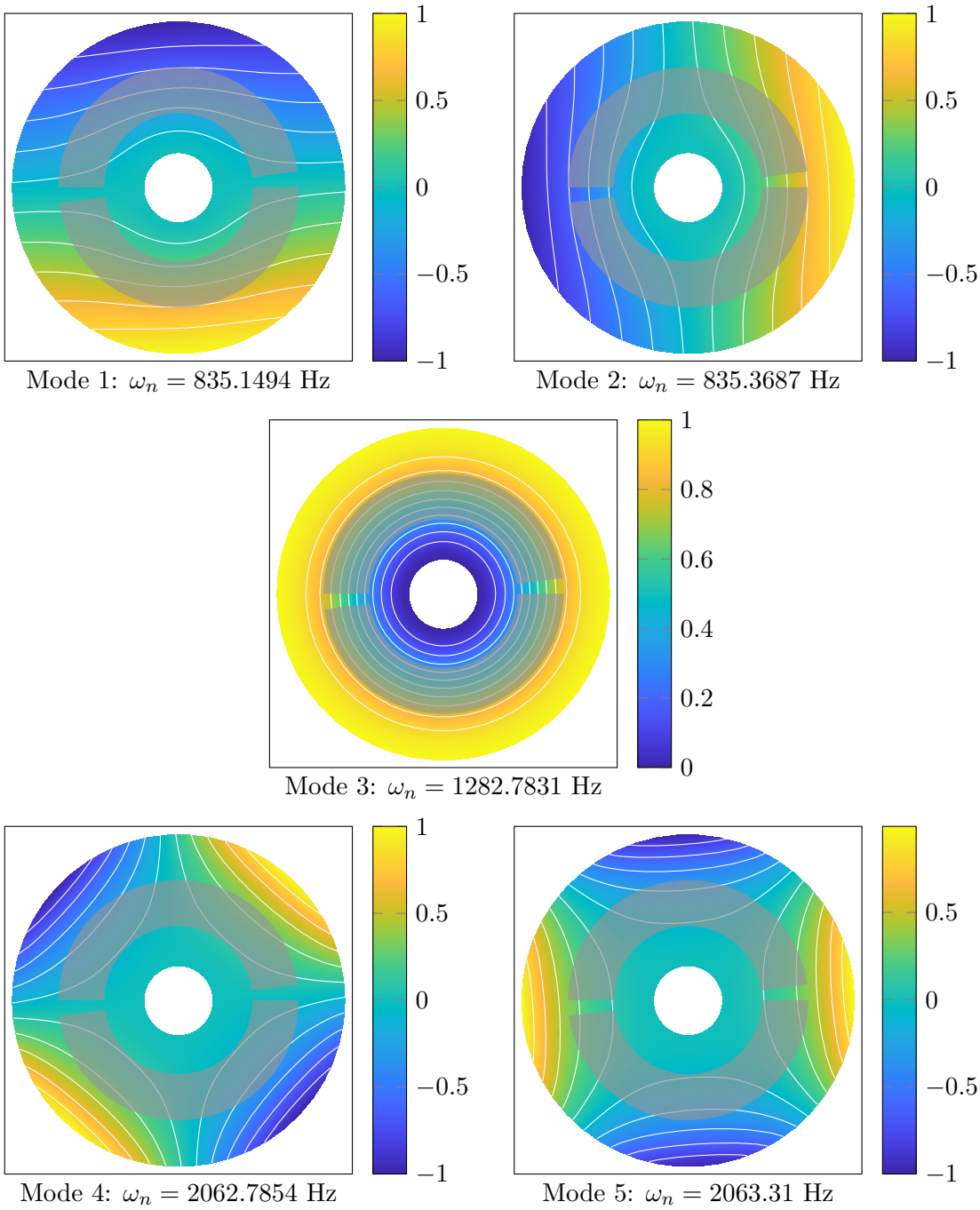

Figure 7.12: Plane gearwheel with inner ring configuration split into two sections mode shapes.

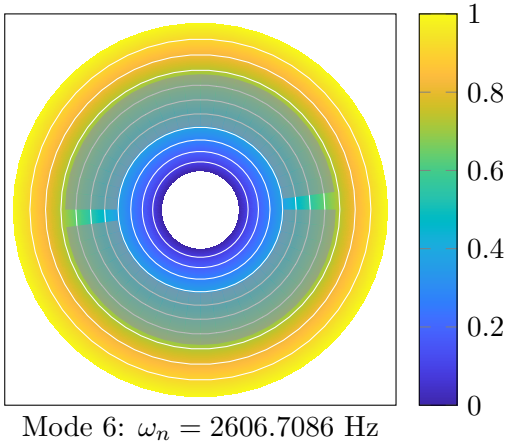

Mode 6: $\omega_n = 2606.7086$ Hz

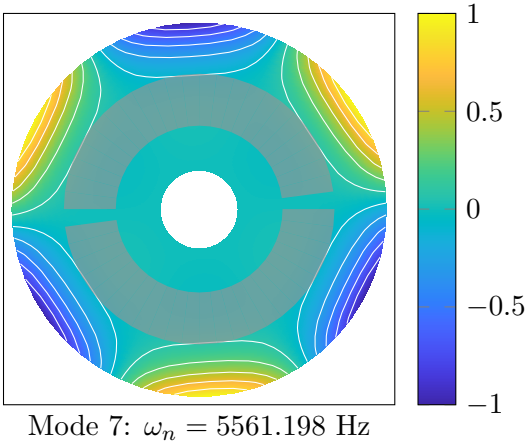

Mode 7: $\omega_n = 5561.198$ Hz

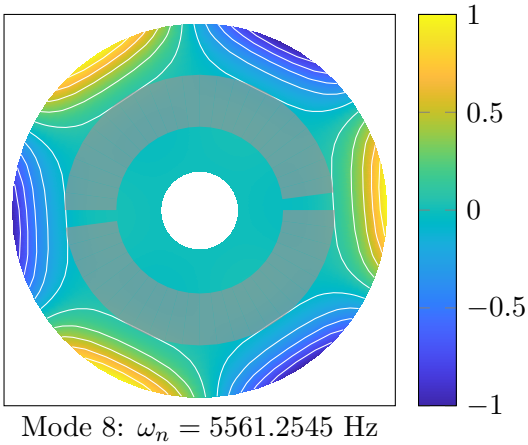

Mode 8: $\omega_n = 5561.2545$ Hz

Figure 7.12: Plane gearwheel with inner ring configuration split into two sections mode shapes. *(Continued)*

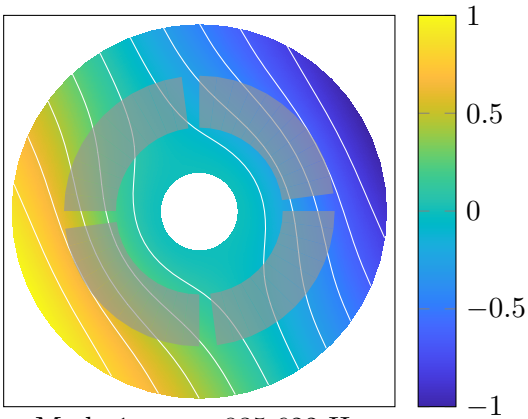

Mode 1: $\omega_n = 835.622$ Hz

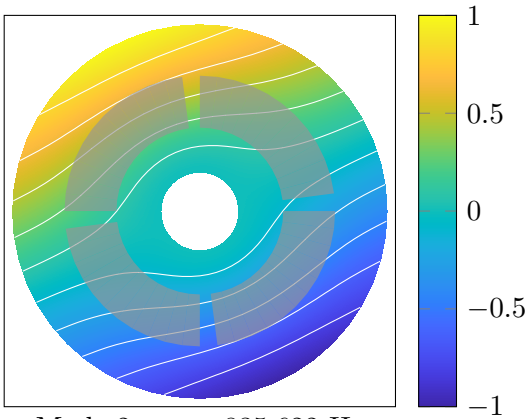

Mode 2: $\omega_n = 835.622$ Hz

Figure 7.13: Plane gearwheel with inner ring configuration split into four sections mode shapes.

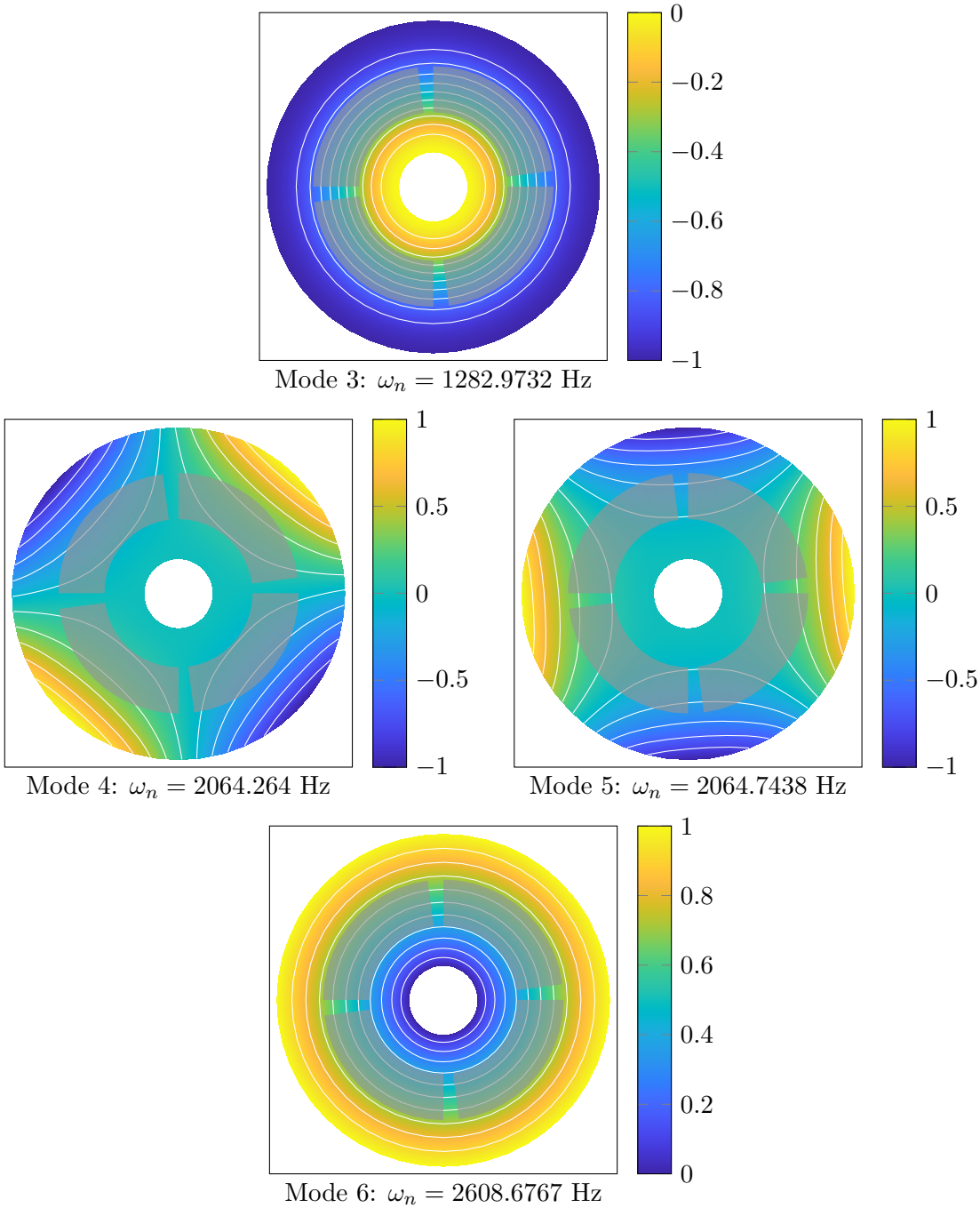

Figure 7.13: Plane gearwheel with inner ring configuration split into four sections mode shapes. *(Continued)*

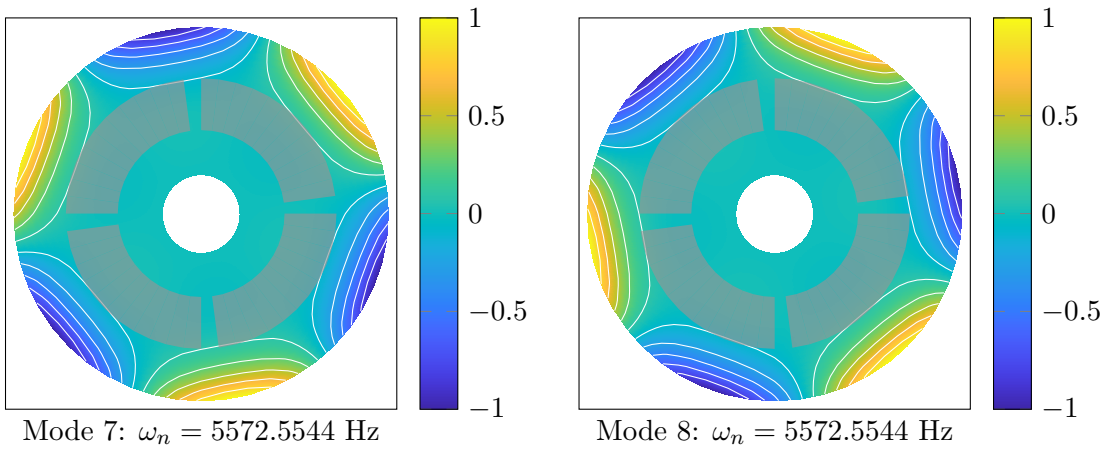

Figure 7.13: Plane gearwheel with inner ring configuration split into four sections mode shapes. *(Continued)*

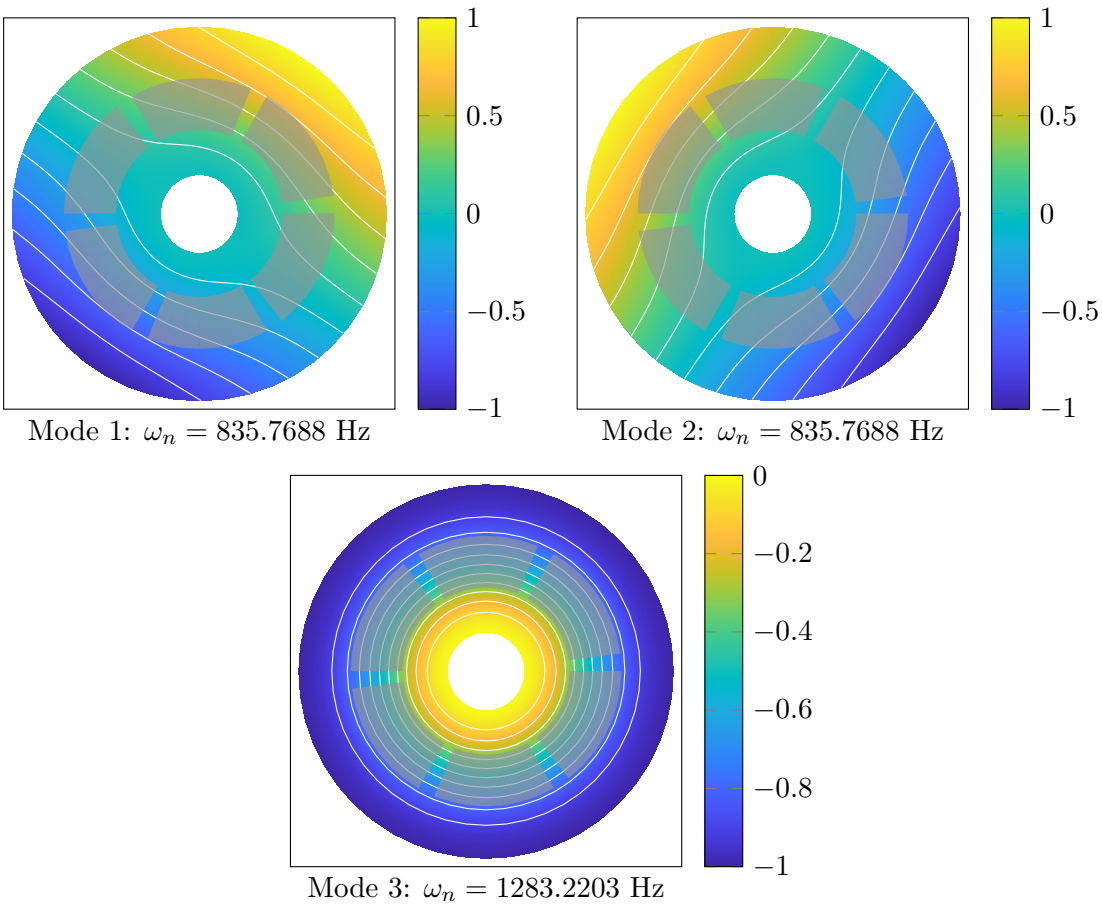

Figure 7.14: Plane gearwheel with inner ring configuration split into six sections mode shapes.

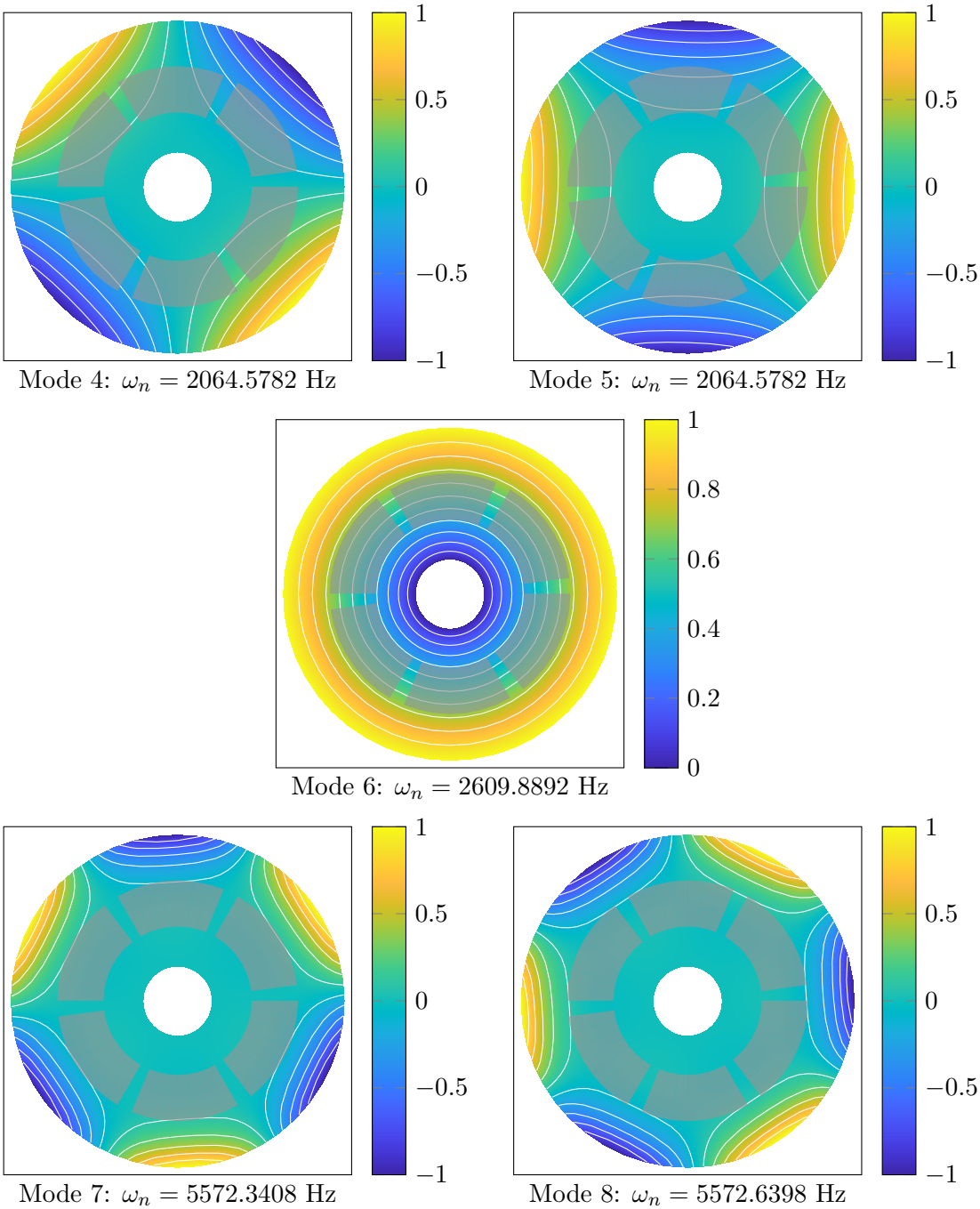

Figure 7.14: Plane gearwheel with inner ring configuration split into six sections mode shapes. *(Continued)*

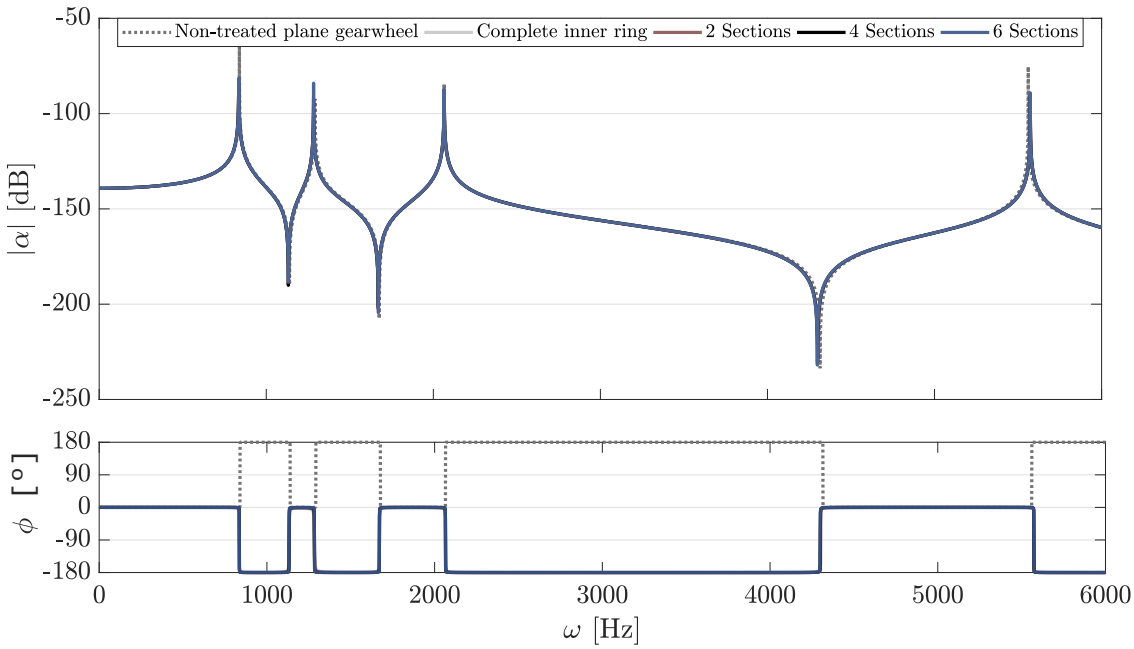

Figure 7.15: Receptance Bode plot for the split inner ring damping device configurations on the plane gearwheel.

Analyzing Table 7.6 it is possible to conclude that the complete inner ring configuration presents better damping capacities for all modes except for the (3,0), for which the split configurations presents higher loss factor values. There are, however, some exceptions, such as the modes 1 and 6 of the split configuration with 2 segments and the mode 7 of the continuous inner annular shape, that do not verify the previous relations. When considering the weighting between the loss factor and the added mas of the damping device, Table 7.7, it is possible to verify that all the previous differences subsist, except for the torsion mode, where the performance of all split configurations are almost the same and higher than the complete one. These damping capacity variations may, again, be due to a combination between the displacements and strains of the regions where the damping device is applied and the boundary effects, all parameters previously presented and explained.

Again, the geometrical axisymmetry was broken, leading to the end of the natural frequency and loss factor multiplicity phenomenon for some modes. However, it is possible to identify some cases where the relations between the modes with same number of nodal diameters were not verified. In fact, analyzing the two segments configuration, the cases with higher natural frequency (where the diametral nodes cross the damping device) present higher loss factors than the cases where the diametral nodes correspond with the discontinuities. This phenomenon may be due to the location of the treatment, where the verified high strains overcome the boundary effect influence.

Finally, the comparison between both split configurations can also be made in Table 7.8.

Analyzing the configurations with the same number of sections, it is possible to conclude that the inner split ring presents a better damping performance for the (1,0) and (0,0) modes, while the loss factor values of the outer split annulus are higher for the (2,0), torsion and (3,0) modes. The higher values for the inner configurations for the (1,0) and (0,0) modes can be explained by their mode shapes and the correspondent strain variation in the geometry, which is higher near the center. On the other hand, the other modes present an increasing strain spacial rates along the radial direction, leading to higher dis-

Table 7.8: Comparison between the loss factors of each split circumferential configuration for the plane gearwheel

Mode	(m,n)	2 Sections		4 Sections		6 Sections	
		Inner η_n [%]	Outer η_n [%]	Inner η_n [%]	Outer η_n [%]	Inner η_n [%]	Outer η_n [%]
1	(1,0)	0.065	0.019	0.026	0.009	0.016	0.007
2		0.027	0.009	0.026	0.008	0.016	0.007
3	(0,0)	0.143	0.038	0.053	0.020	0.026	0.014
4	(2,0)	0.037	0.089	0.026	0.080	0.021	0.061
5		0.037	0.047	0.026	0.064	0.021	0.061
6	(Torsion)	1.181	2.361	1.132	2.268	1.083	2.176
7	(3,0)	0.004	0.652	0.064	2.089	0.087	2.478
8		0.007	0.179	0.064	2.089	0.054	2.358

sipation effects in the viscoelastic layer. Again, the damping capacities variations were explained taking into account the strain and displacement distributions in the geometry.

Making a general evaluation and trying to choose the best circumferential damping device configuration for the plane gearwheel, if possible, since a performance appraisal must always take into account the specific needs, the outer ring split into four sections would be selected, since it revealed to be the best overall compromise solution for the damping of all modes.

7.3 Sloped Damped Gearwheel

The study of the circumferential viscoelastic damping devices applied in the sloped gearwheel also started with the complete annular shapes, with the same dimensions as the ones used for the plane damped gearwheel analysis (Table 7.1), whose resultant meshes were presented previously in Figure 7.1. The determination of the characteristics for these setups followed the same logic used for the plane case.

Table 7.9 presents the modal analysis results of these configurations, where again $\Delta_{r\,\eta_n}$ represents the relative difference of the outer and inner circumferential dampers' loss factors relatively to the complete treatment, Δm corresponds to the added mass for each case and the relative difference values for the natural frequencies, $\Delta_{r\,\omega_n}$, is not presented because the variations were not significant. On the other hand, Table 7.10 presents the loss factor-added mass weighting results, H, for the present configurations, neglecting the multiplicity phenomenon resulting from the axisymmetric geometry. Note that the sloped gearwheel mass is $m_{gearwheel} = 1.435\,\text{kg}$.

Figures 7.16, 7.17 and 7.18 present the normal modes' total displacement for each complete configuration.

Finally, the receptance's Bode plot for these cases, as well as the non-treated sloped gearwheel, can be presented in Figure 7.19. The considered node and degree of freedom for the excitation and the response record were the same as considered for the plane gearwheel.

Table 7.9: Complete circumferential damping devices configurations' modal analysis results for the sloped gearwheel

Mode		Entire Area $\Delta m = 98.82\,\mathrm{g}$		Outer Ring $\Delta m = 50.80\,\mathrm{g}$			Inner Ring $\Delta m = 50.80\,\mathrm{g}$		
	(m,n)	ω_n [Hz]	η_n [%]	ω_n [Hz]	η_n [%]	$\Delta_{r\,\eta_n}$ [%]	ω_n [Hz]	η_n [%]	$\Delta_{r\,\eta_n}$ [%]
1	(1,0)	1075.34	0.108	1077.14	0.059	-45.634	1090.45	0.046	-57.862
2		1075.34	0.108	1077.14	0.059	-45.634	1090.45	0.046	-57.862
3	(2,0)	2081.69	0.693	2080.24	0.105	-84.840	2096.57	0.101	-85.449
4		2081.69	0.693	2080.24	0.105	-84.840	2096.57	0.101	-85.449
5	(Torsion)	2477.47	3.225	2502.95	2.314	-28.227	2537.07	1.077	-66.608
6	(0,0)	2802.74	0.528	2807.52	0.393	-25.568	2841.48	0.260	-50.719
7	(3,0)	5475.96	0.177	5474.91	0.102	-42.285	5500.71	0.007	-95.955
8		5475.96	0.177	5474.91	0.102	-42.285	5500.71	0.007	-95.955

Table 7.10: Loss factor and added mass weighting, H, for the complete circumferential configurations in the sloped gearwheel

Mode	(m,n)	Entire Area $\Delta_{r\,m} = 6.88\,\%$	Outer Ring $\Delta_{r\,m} = 3.54\,\%$		Inner Ring $\Delta_{r\,m} = 3.54\,\%$	
		H	H	$\Delta_{r\,H}$ [%]	H	$\Delta_{r\,H}$ [%]
1 & 2	(1,0)	0.016	0.017	5.757	0.013	-18.031
3 & 4	(2,0)	0.101	0.030	-70.510	0.028	-71.695
5	(Torsion)	0.468	0.654	39.619	0.304	-35.042
6	(0,0)	0.077	0.111	44.792	0.074	-4.135
7 & 8	(3,0)	0.026	0.029	12.271	0.002	-92.131

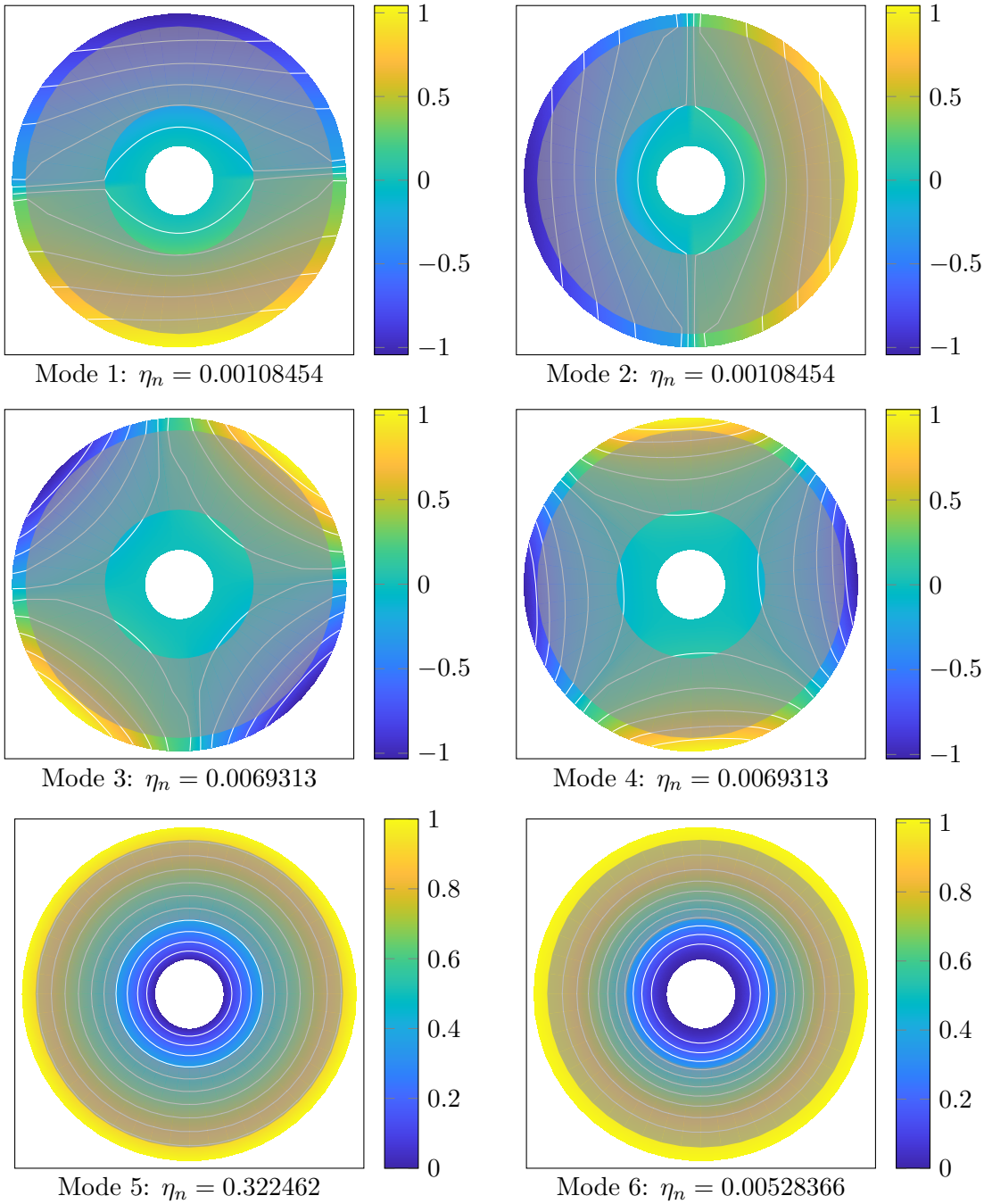

Figure 7.16: Sloped gearwheel treated area completely covered mode shapes.

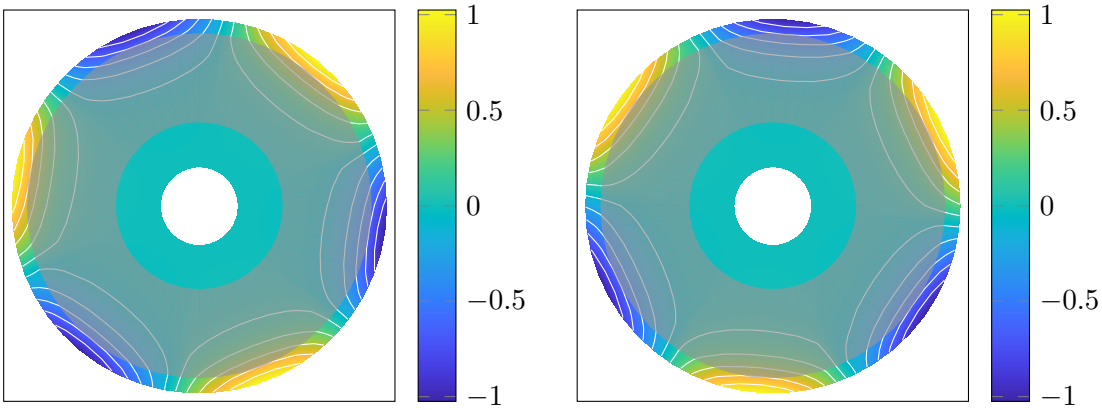

Mode 7: $\eta_n = 0.0017669$ Mode 8: $\eta_n = 0.0017669$

Figure 7.16: Sloped gearwheel treated area completely covered mode shapes. *(Continued)*

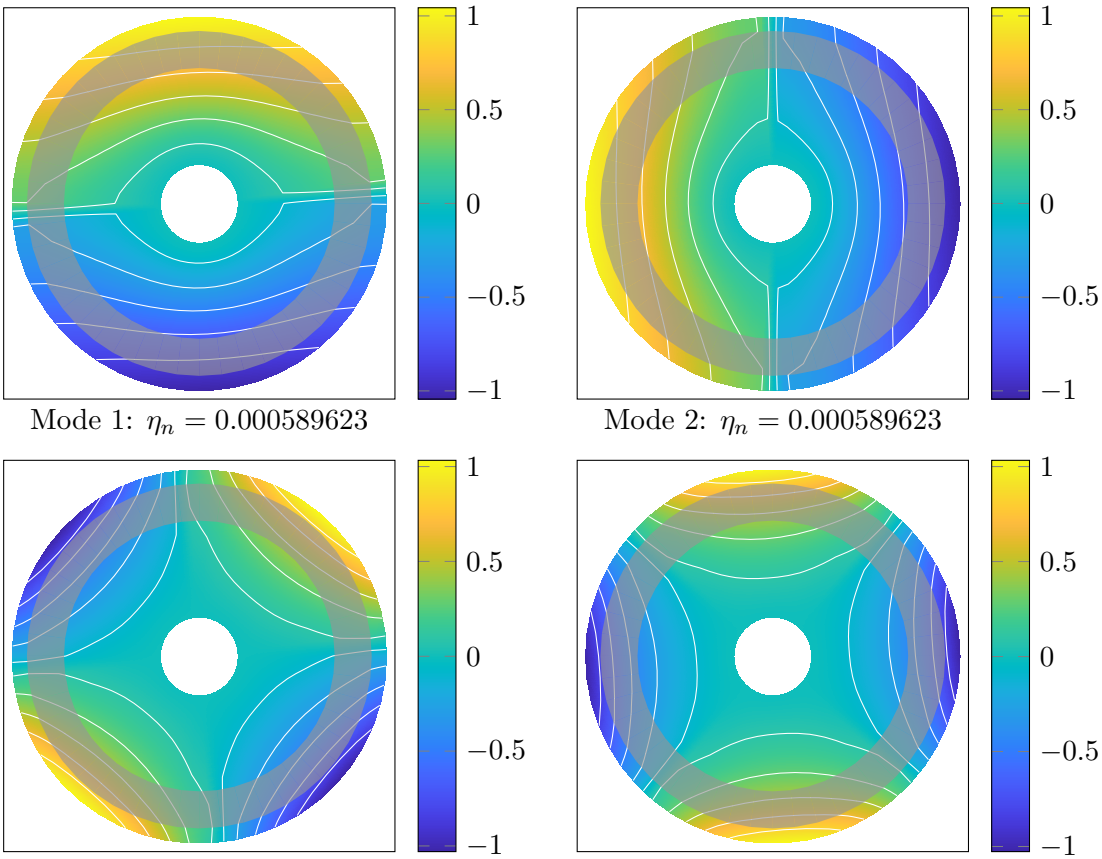

Mode 1: $\eta_n = 0.000589623$ Mode 2: $\eta_n = 0.000589623$

Mode 3: $\eta_n = 0.00105278$ Mode 4: $\eta_n = 0.00105078$

Figure 7.17: Sloped gearwheel with complete outer ring damping device mode shapes.

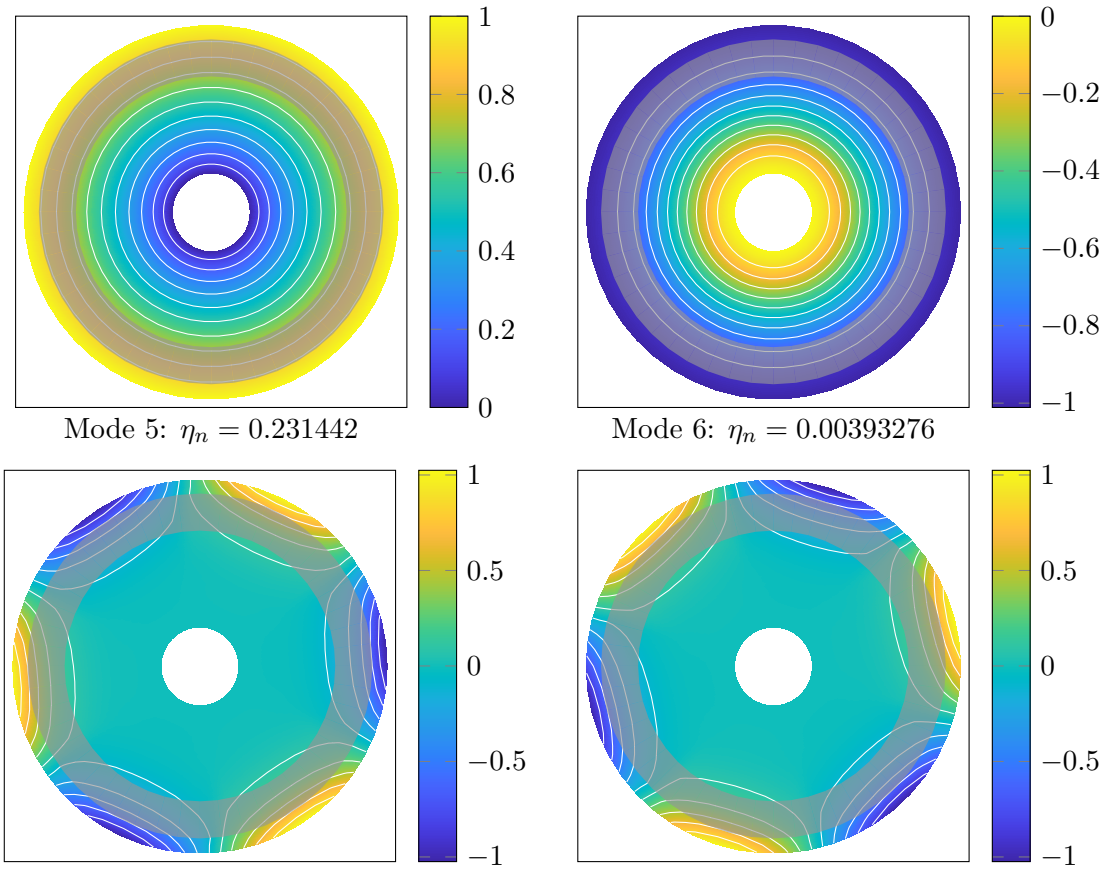

Mode 5: $\eta_n = 0.231442$ Mode 6: $\eta_n = 0.00393276$

Mode 7: $\eta_n = 0.00101976$ Mode 8: $\eta_n = 0.00101976$

Figure 7.17: Sloped gearwheel with complete outer ring damping device mode shapes. *(Continued)*

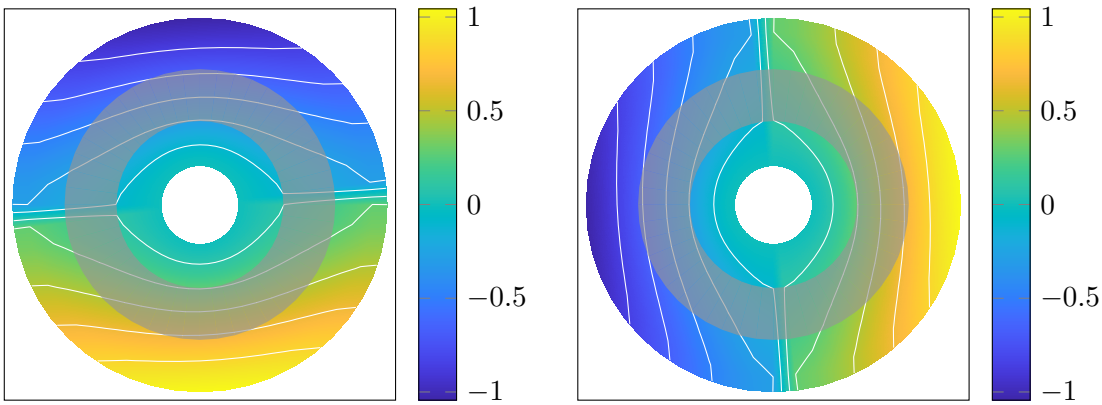

Mode 1: $\eta_n = 0.000456999$ Mode 2: $\eta_n = 0.000457$

Figure 7.18: Sloped gearwheel with complete inner ring damping device mode shapes.

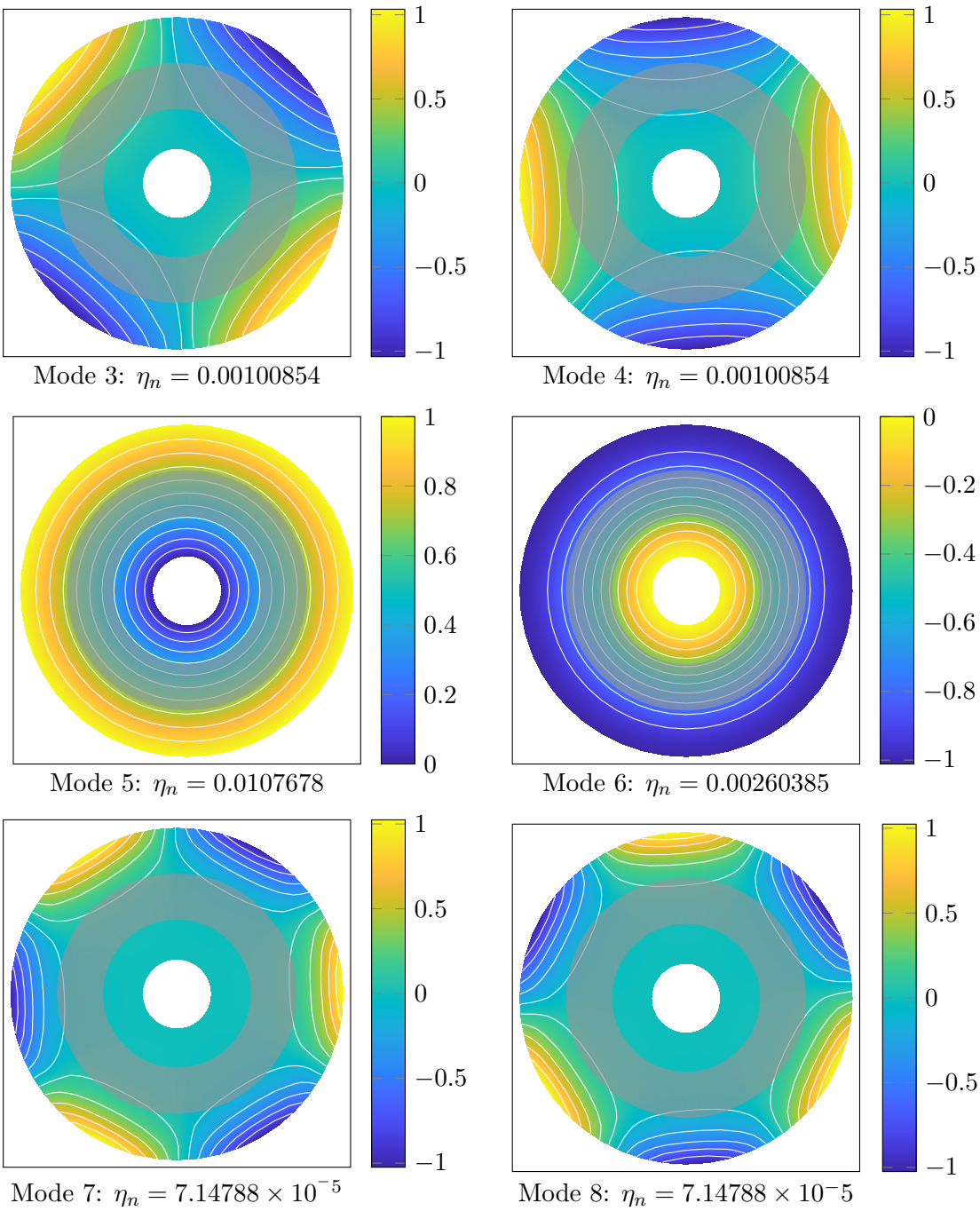

Figure 7.18: Sloped gearwheel with complete inner ring damping device mode shapes. *(Continued)*

Analyzing Table 7.9, it is possible to conclude that, such as for the plane gearwheel, the damping device covering all the treatable surface revealed the best damping capacity of all configurations, since lower loss factor values were verified for the partial treatments. The Bode plot (Figure 7.19) also revealed that information, since the peak amplitude values were smaller. Again, this phenomenon resulted from the higher quantity of viscoelastic material involved in the energy dissipation process. However, when considering the weighting between the loss factor and the added mass of the damping device, in Table 7.10, it is possible to conclude that the outer ring overcame the previous configuration, showing the best balance between damping performance and added mass for all modes except the (2,0). The inner ring configuration showed the worst behavior in both analysis.

These results can be explained by the combination of the correspondent mode shapes and the action of the coupling effects. Considering the variations in the mode shapes resultant from the inclination of the web, Figures 7.20 and 7.21 present the deformed meshes for one of the (1,0) modes in the plane and sloped gearwheels, respectively. It is possible to verify that the zones near the center in the first case are forced to deform more than in the second case, leading to higher strains, that will be "transmitted" to the viscoelastic material, increasing the damping effect of the treatment in these regions. Thus, it is comprehensible the decrease on the damping influence of the viscoelastic material in the inner zones of the sloped gearwheel for this mode. On the other hand, Figures 7.22 and 7.23 present the deformed meshes for one of the (2,0) modes in the plane and sloped gearwheels, respectively. In these cases, the previously presented variation is also possible to identify, but with smaller influence, which led to less significant changes in the damping efficiency.

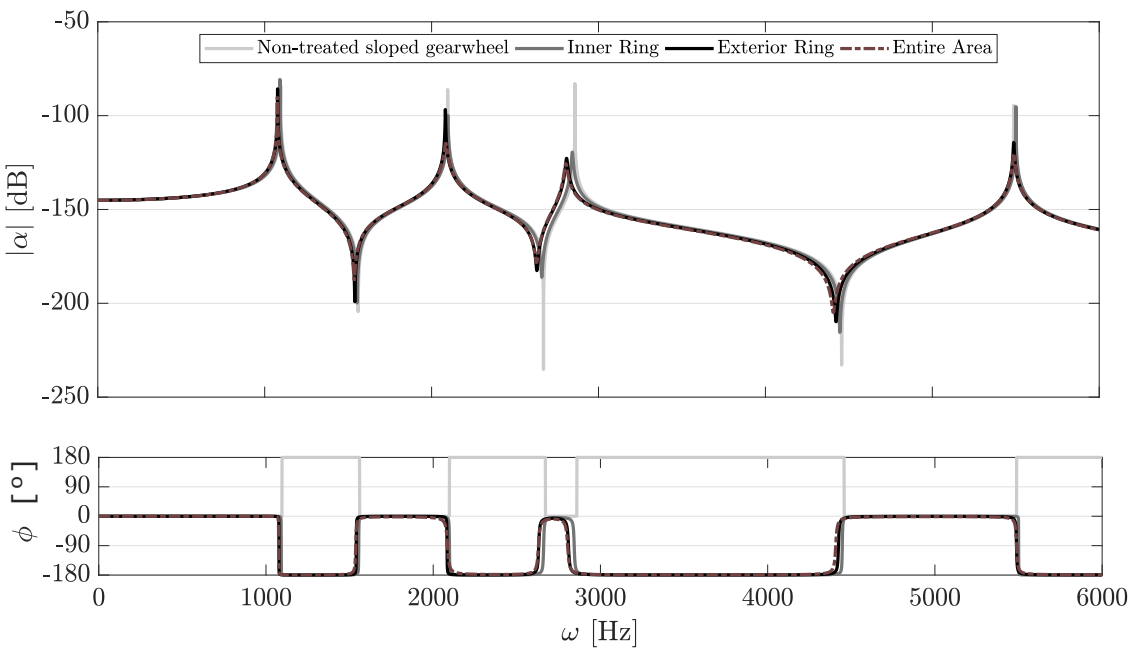

Figure 7.19: Receptance's Bode plot for the complete circumferential damping device configurations applied on the sloped gearwheel.

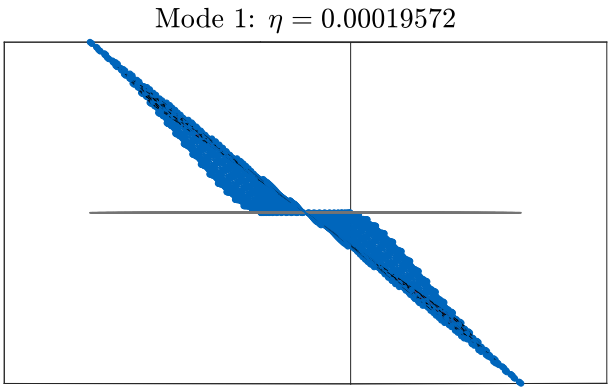

(a) Side view.

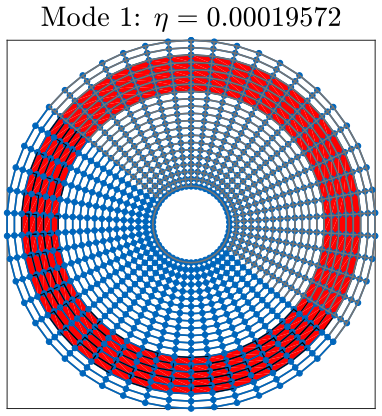

(b) Top view.

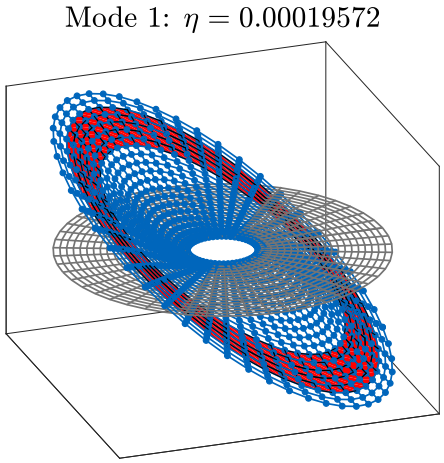

(c) Global view.

Figure 7.20: Mode (1,0) deformed mesh for the outer ring device configuration on the plane gearwheel.

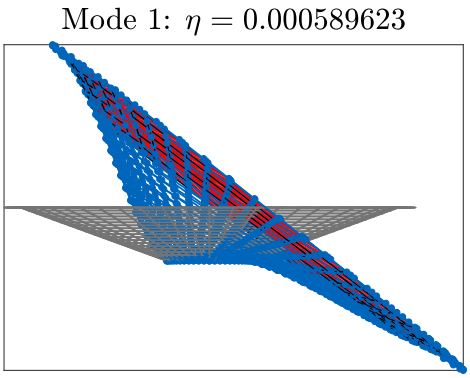

(a) Side view.

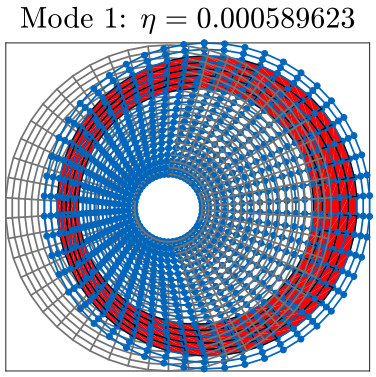

(b) Top view.

Figure 7.21: Mode (1,0) deformed mesh for the outer ring device configuration on the sloped gearwheel.

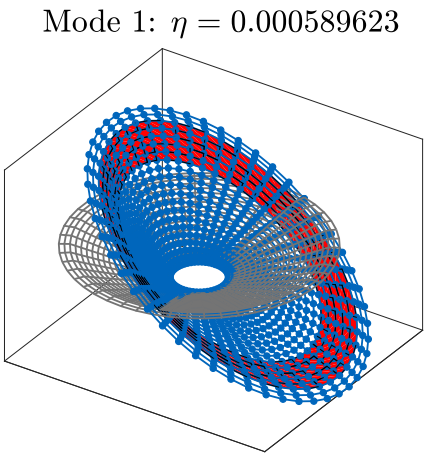

(c) Global view.

Figure 7.21: Mode (1,0) deformed mesh for the outer ring device configuration on the sloped gearwheel. *(Continued)*

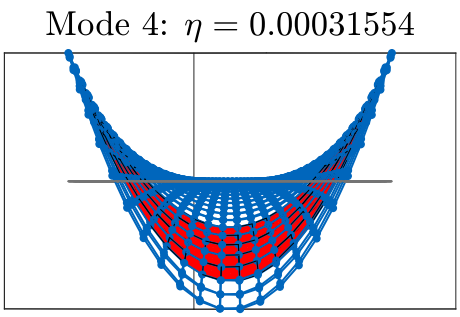

(a) Side view.

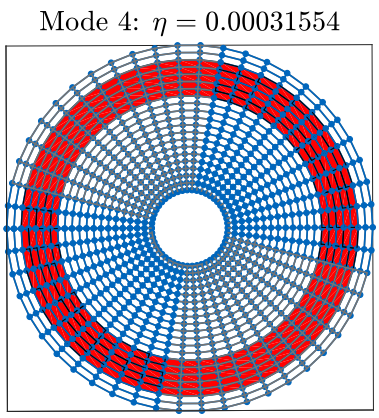

(b) Top view.

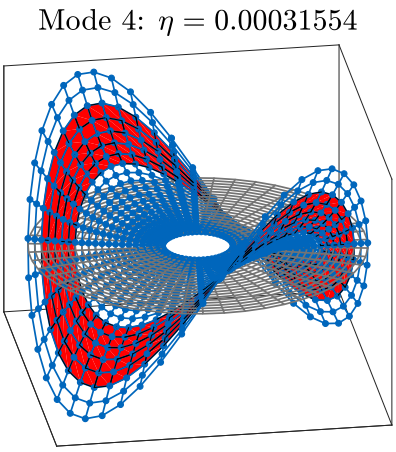

(c) Global view.

Figure 7.22: Mode (2,0) deformed mesh for the exterior ring device configuration on the plane gearwheel.

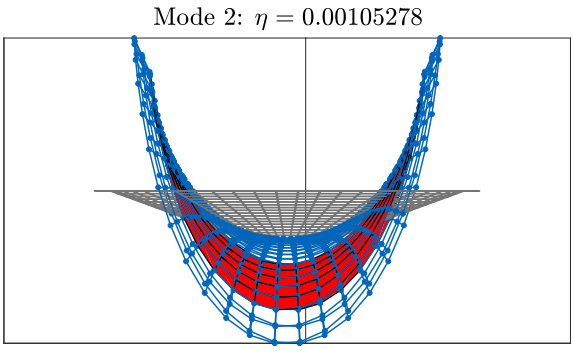

(a) Side view.

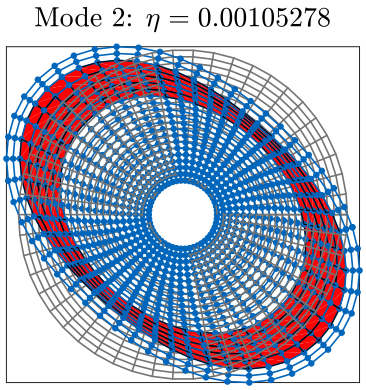

(b) Top view.

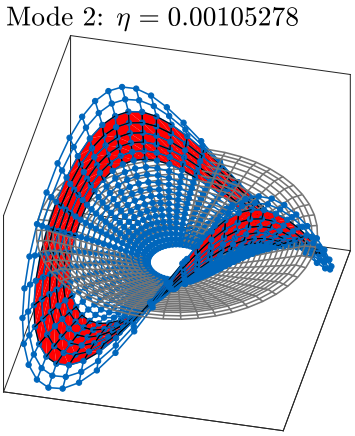

(c) Global view.

Figure 7.23: Mode (2,0) deformed mesh for the exterior ring device configuration on the sloped gearwheel.

Concerning the coupling effects, it was previously mentioned that the slope will induce significant coupling between the bending, the membrane displacements and the layers rotations. Thus, the action of the centrifugal force in the improvement of the shear strains developed in the viscoelastic material will be more significant. Note that, for the plane gearwheel, the centrifugal force will only lead to the appearance of shear loads in the damping device, while for the slope case this will present shear and compressive components. However, for the plane case the bending modes show negligible membrane displacements due to the reduced coupling, only resulting from the minor variation of the center of mass position. On the other hand, for the slope case the bending modes show significant membrane displacements. Thus, despite the centrifugal force having a minor shear component, the coupling effects in the sloped gearwheel may lead to the shear strain increase in the viscoelastic layer. It can also be easily understood that the further the damping device is located, the higher its damping capacity will be, since the centrifugal force and the coupling effects are higher.

Comparing the efficiencies of both partial treatments, it is obvious that the outer ring configuration presents a better performance in the damping of all studied natural modes, due to the reasons previously explained. When compared to the relations verified for the plane gearwheel, where the inner ring revealed benefits for the (1,0), (0,0) and (2,0) modes, it can be concluded that the coupling effects really affect the viscoelastic device's

behavior, since, for the present case, the outer ring configuration's efficiency overcomes the inner ring. However, from Table 7.9, it can be noticed that the outer annular shape is associated with lower natural frequencies, as for the plane case, because of the same reasons previously presented.

7.3.1 Segmented Configurations

As for the plane gearwheel, split annular shapes were also studied, but only the split outer ring configurations, since the correspondent continuous set showed a superior performance than the inner ring one. Table 7.11 presents their loss factor results, where again $\Delta_{r\,\eta_n}$ represents the relative difference of the sectioned setups relatively to the continuous one and that the frequency values are shown in the correspondent mode shapes (Figures 7.24, 7.25 and 7.26). On the other hand, Table 7.12 presents the loss factor-added mass weighting results, H, for the present case.

Finally, Figure 7.27 presents the receptance's Bode plot for the split outer ring configurations.

From Table 7.11, it is possible to conclude that the split configurations presented overall worse damping capacities than the complete one, except for the torsion and (3,0) modes, which can be explained by the combination of effects resulting from the strain decrease and the appearance of the boundary effects, both explained previously. However, when considering the weighting between loss factor and the added mass of the damping devices, in Table 7.12, the two sections outer ring configuration's interest increases, since its performance overcomes the continuous annular shape. In fact, all the split configurations improved their behavior, becoming better than the continuous ring for the (2,0) mode, but the two segments setup also did it for the (1,0) mode.

Once again, the split configurations broke the geometrical axisymmetry of the global structure, leading to the end of the natural and frequency loss factor multiplicity phenomenon for some modes. It is possible to identify that, for the same mode, the higher natural frequency cases are associated with lower loss factor values, as verified for the outer split ring in the plane gearwheel, for similar reasons.

As a conclusion, making a general evaluation and trying to choose the best circumferential damping device configuration for the sloped gearwheel, if possible, the outer ring split into two sections would be selected, since it revealed the best overall compromise solution for the damping of all modes.

Table 7.11: Outer split ring damping devices' configurations loss factor results for the sloped gearwheel.

Mode		Continuous $\Delta m = 50.80\,\mathrm{g}$	2 Sections $\Delta m = 48.77\,\mathrm{g}$		4 Sections $\Delta m = 46.74\,\mathrm{g}$		6 Sections $\Delta m = 44.70\,\mathrm{g}$	
	(m,n)	η_n [%]	η_n [%]	$\Delta_{r\,\eta_n}$ [%]	η_n [%]	$\Delta_{r\,\eta_n}$ [%]	η_n [%]	$\Delta_{r\,\eta_n}$ [%]
1	(1,0)	0.020	0.019	-3.467	0.009	-53.979	0.007	-65.372
2		0.020	0.009	-52.089	0.008	-59.089	0.007	-65.372
3	(2,0)	0.078	0.038	-50.806	0.020	-73.742	0.014	-82.548
4		0.078	0.038	-50.806	0.020	-73.742	0.014	-82.548
5	(Torsion)	2.447	2.361	-3.538	2.268	-7.330	2.176	-11.0861
6	(0,0)	0.032	0.089	182.026	0.080	152.645	0.061	94.403
7	(3,0)	0.035	0.652	1744.649	2.089	5812.870	2.478	6913.328
8		0.035	0.179	406.514	2.089	5812.870	2.358	6572.986

Table 7.12: Loss factor and added mass weighting, H, for the complete and split outer ring configurations in the sloped gearwheel

Mode		Continuous $\Delta_{r\,m} = 3.54\,\%$	2 Sections $\Delta_{r\,m} = 3.40\,\%$		4 Sections $\Delta_{r\,m} = 3.26\,\%$		6 Sections $\Delta_{r\,m} = 3.12\,\%$	
	(m,n)	H	H	$\Delta_{r\,H}$ [%]	H	$\Delta_{r\,H}$ [%]	H	$\Delta_{r\,H}$ [%]
1	(1,0)	0.017	0.018	5.234	0.016	-4.020	0.016	-6.283
2		0.017	0.017	0.751	0.016	-4.020	0.016	-6.283
3	(2,0)	0.030	0.058	95.985	0.044	49.687	0.036	21.940
4		0.030	0.034	13.903	0.040	33.107	0.036	21.940
5	(Torsion)	0.654	0.657	0.463	0.658	0.685	0.660	0.981
6	(0,0)	0.111	0.059	-47.138	0.036	-67.908	0.028	-74.936
7	(3,0)	0.029	0.157	446.213	0.619	2047.959	0.688	2288.541
8		0.029	0.124	331.551	0.619	2047.959	0.844	2828.965

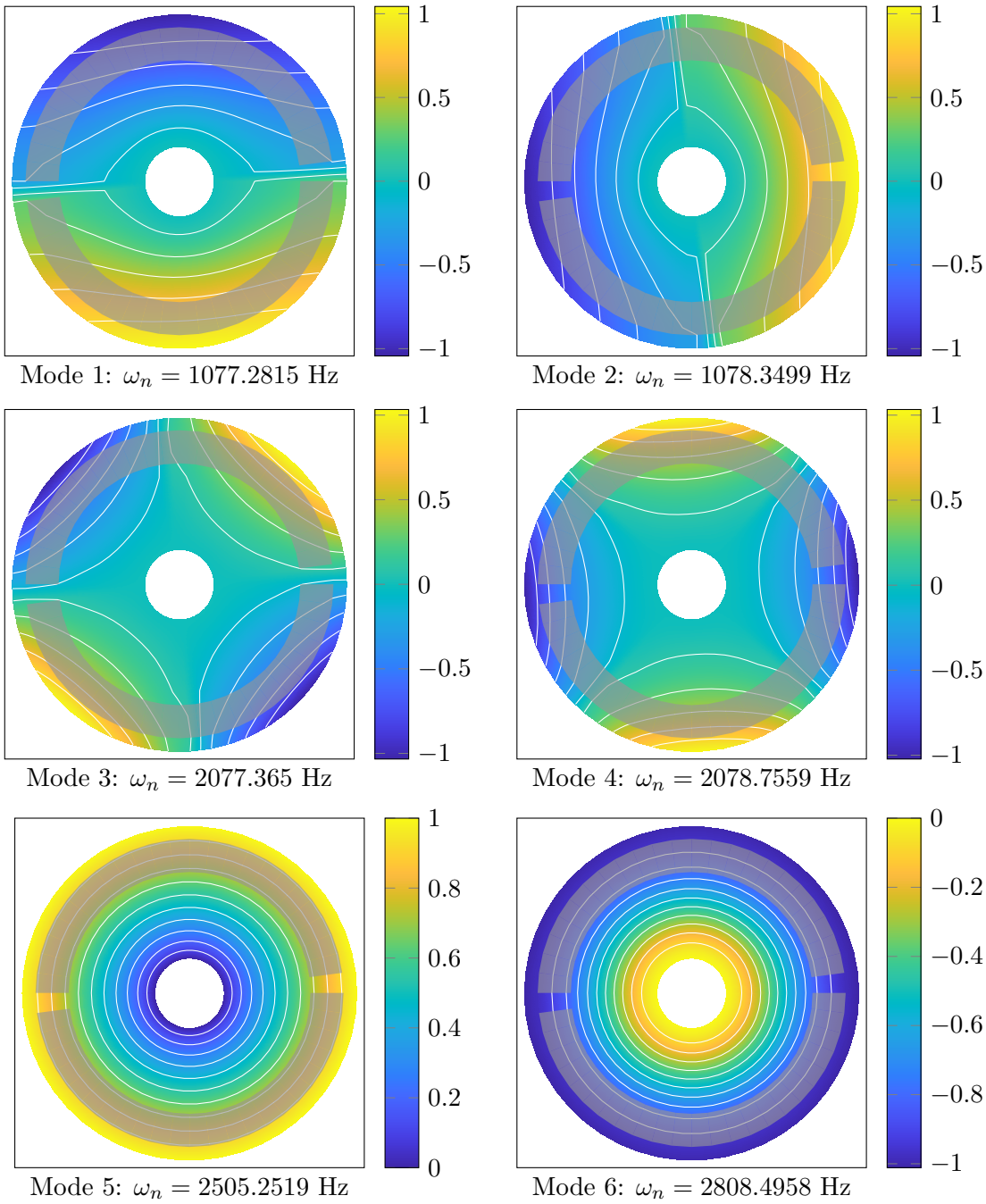

Figure 7.24: Outer ring configuration split into two sections mode shapes for the sloped gearwheel.

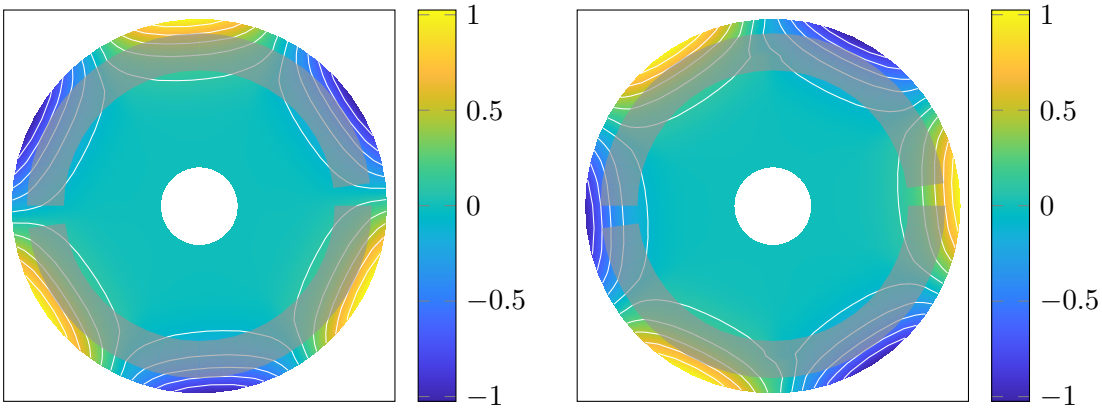

Mode 7: $\omega_n = 5465.7477$ Hz Mode 8: $\omega_n = 5471.7979$ Hz

Figure 7.24: Outer ring configuration split into two sections mode shapes for the sloped gearwheel. *(Continued)*

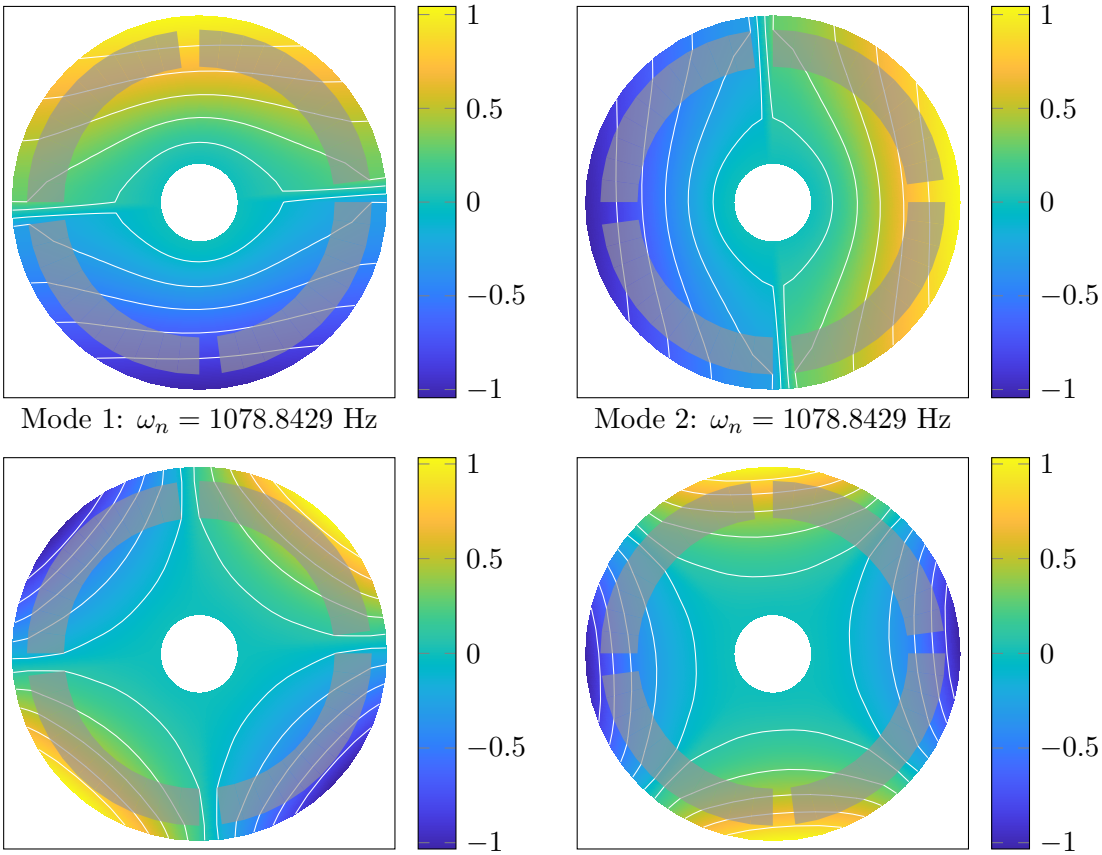

Mode 1: $\omega_n = 1078.8429$ Hz Mode 2: $\omega_n = 1078.8429$ Hz

Mode 3: $\omega_n = 2078.4159$ Hz Mode 4: $\omega_n = 2080.2252$ Hz

Figure 7.25: Outer ring configuration split into four sections mode shapes for the sloped gearwheel.

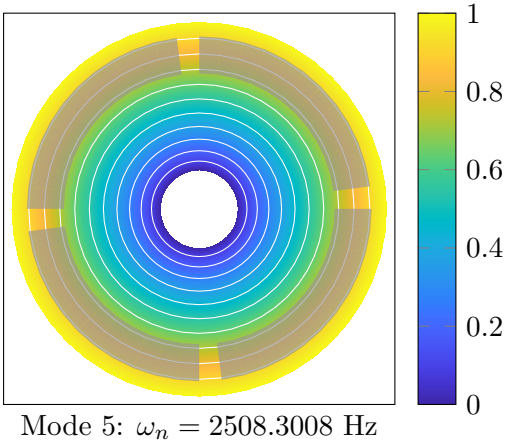

Mode 5: $\omega_n = 2508.3008$ Hz

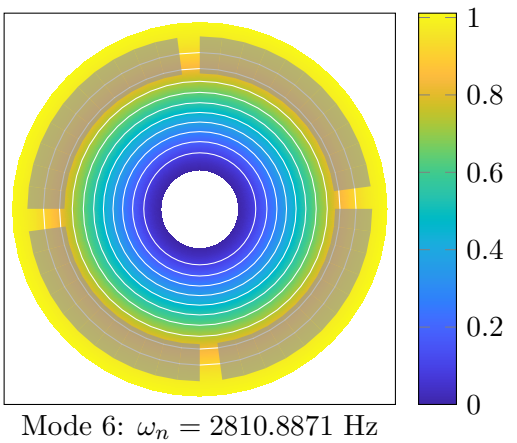

Mode 6: $\omega_n = 2810.8871$ Hz

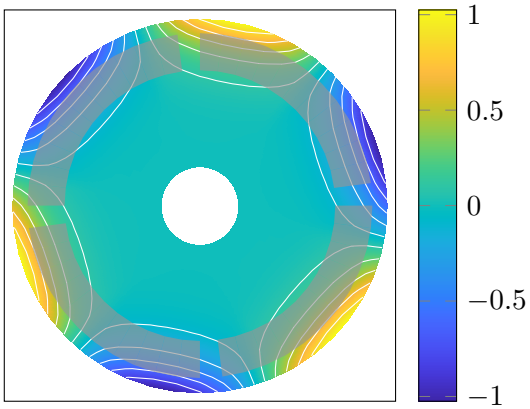

Mode 7: $\omega_n = 5469.5511$ Hz

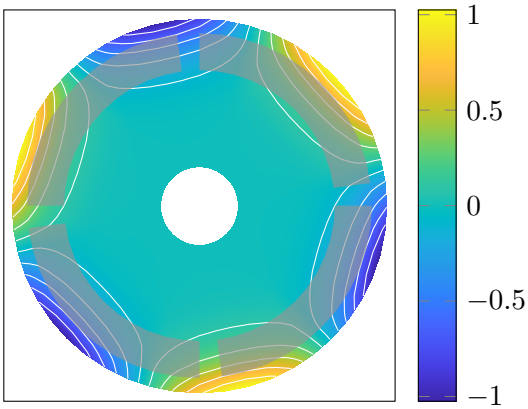

Mode 8: $\omega_n = 5469.5511$ Hz

Figure 7.25: Outer ring configuration split into four sections mode shapes for the sloped gearwheel. *(Continued)*

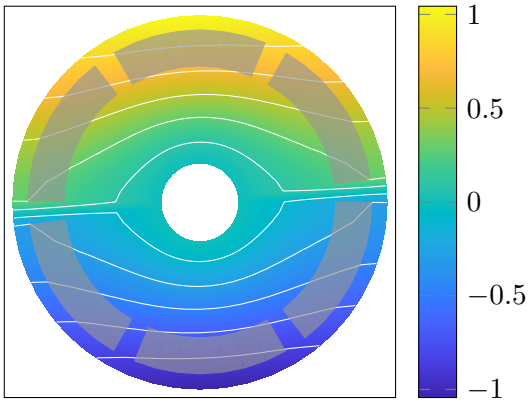

Mode 1: $\omega_n = 1079.6124$ Hz

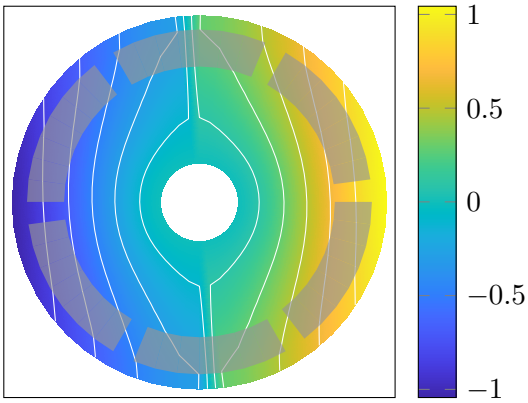

Mode 2: $\omega_n = 1079.6124$ Hz

Figure 7.26: Outer ring configuration split into six sections mode shapes for the sloped gearwheel.

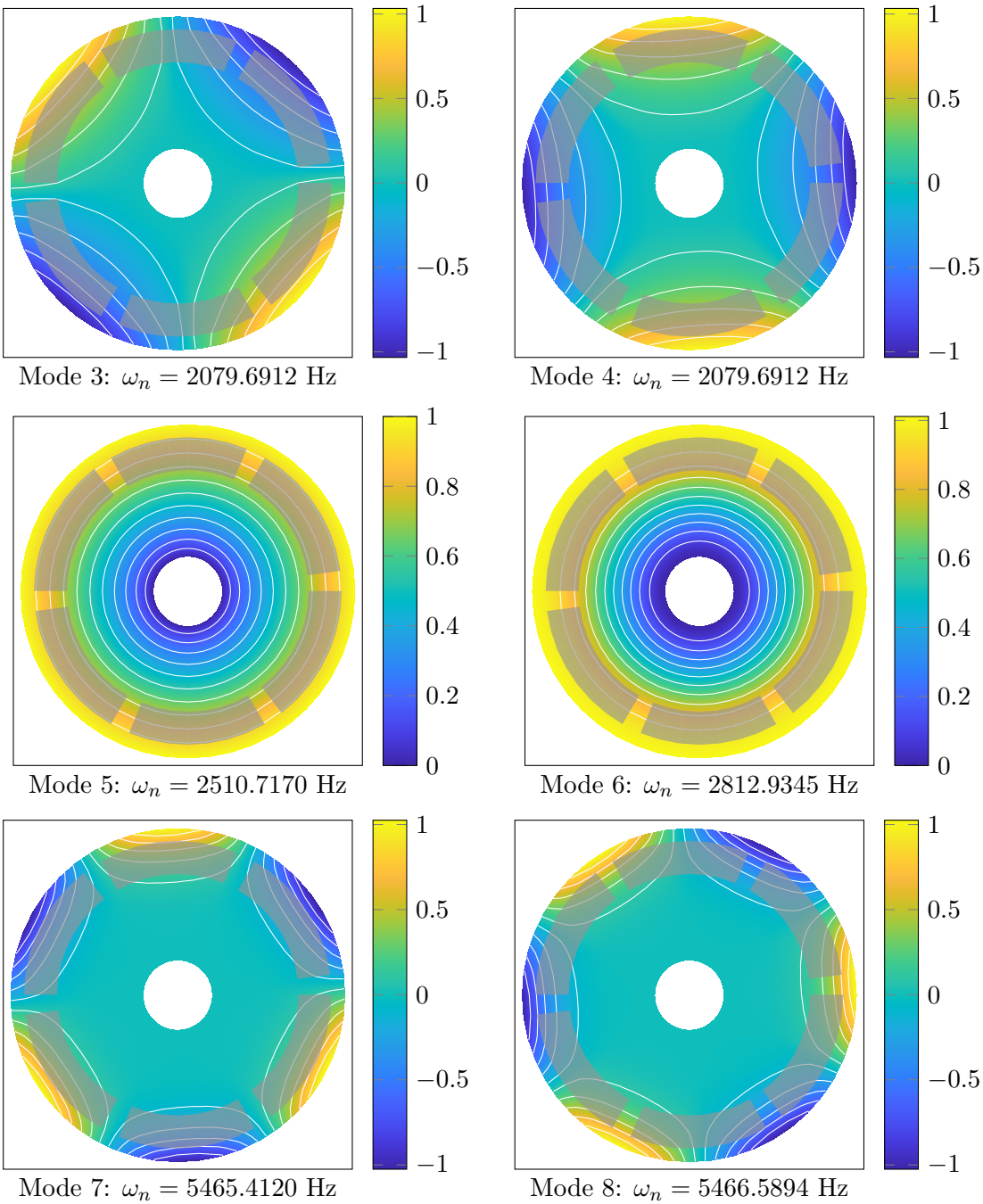

Figure 7.26: Outer ring configuration split into six sections mode shapes for the sloped gearwheel. *(Continued)*

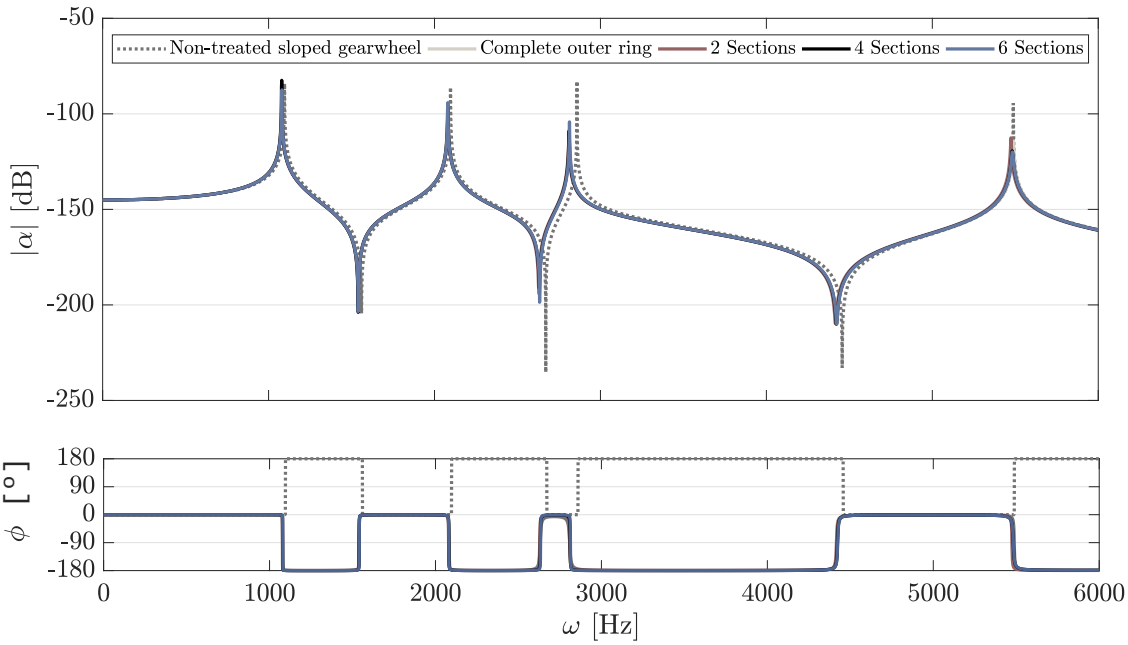

Figure 7.27: Receptance Bode plot for the split outer ring damping device configurations on the sloped gearwheel.

7.4 Inclination Effect

In order to better evaluate the inclination effect on the efficiency of the circumferentially configured damping devices, the variation of some setup's loss factors was plotted for α angles between 55° and 125°, which means $\beta \in [-35°, 35°]$. Note that the negative values of β can be seen as the application of the viscoelastic damping devices on the web's convex face (while the positive values were in the concave side), meaning that the influence of the side where the treatment is applied was also studied.

The studied circumferential configurations were all the continuous ones, that is the possibly treated area completely covered (Figure 7.28), the outer ring (Figure 7.29) and the inner ring (Figure 7.30). Note that the torsion modes' loss factors were not plotted because the much higher value would not allow a correct representation of the other modes' damping characteristics. On the other hand, the natural frequency values were not plotted also because their evolution is nearly the same as the one previously presented for the non-treated gearwheel (Figure 6.10).

Analyzing the previous Figures, it is possible to verify that the loss factors for positive values of β are always higher to the correspondent negative inclination angle, which means that it is possible to conclude that the viscoelastic damping device should always be applied over the concave face of the gearwheel. This follows what was proposed by Marsaudon and Cutuli [2014] in the studied patent and may be due to the coupling effects. In fact, when applied over the inner side of the frustoconical shape, the viscoelatic layer's rotations developed from the centrifugal force will be significantly constrained by the host structure, adding the influence of the backing layer, which results in the increase of the shear strains and, consequently, the energy dissipation phenomenon. On the other hand, if the damping device is applied over the convex side of the gearwheel, the influence of the thinner and more pliant backing layer will be dominant over the host structure, because of the direction of the centrifugal force, resulting in lower loss factors.

On the other hand, the decreasing of the involved strains for some modes with the inclination is also evident. In fact, for the inner ring configuration (Figure 7.30) and for the damping device applied over the concave side of the gearwheel ($\beta > 0$), it is possible to see that the curve for the (0,0) mode presents a local maximum, decreasing from there for higher inclination angles. This may be due to the fact that, for small values of β, the strain reduction is not significant, leading to the more important action of the centrifugal force. However, increasing the inclination angle, the strain field decreases in a such a way that the higher induced coupling effects are not sufficient to counterbalance it, leading to a reduction of the damping capabilities. For the (1,0) mode this can also be verified until some point (nearly $\beta = 20°$), from where the loss factor increases. This may, again, be due to a smaller reduction of the strain field and, consequently, a higher influence of the coupling effect of the centrifugal force. Both these evolutions can also be observed in the completely covered configuration (Figure 7.28).

7.5 Conclusion

As a conclusion for the present Chapter addressing the damping efficiency analysis of the circumferential damping treatments, the bar graphs in Figures 7.5 and 7.32 can be presented, where the values for the balancing parameter H are plotted for the plane and sloped gearwheels, respectively. Note that for the plane gearwheel only the split outer ring devices are considered.

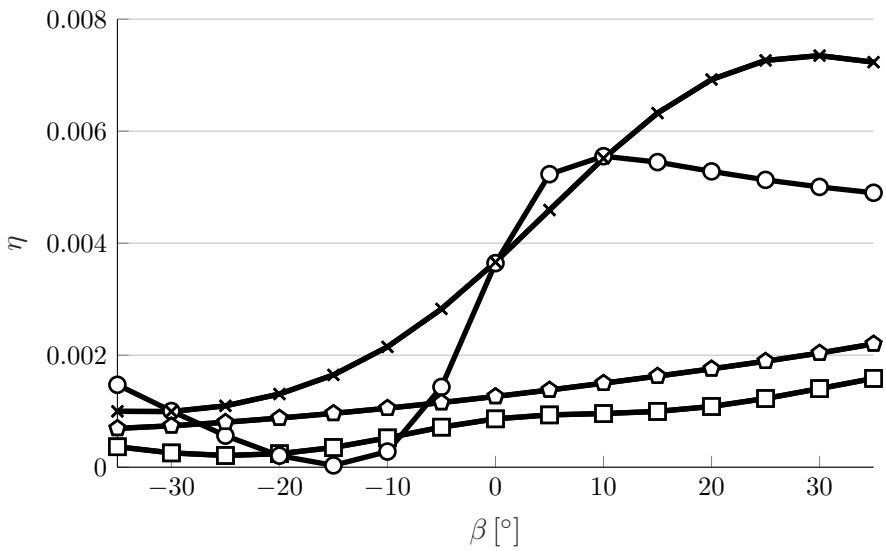

Figure 7.28: Inclination angle effect on the damping behavior of the completely covered area configuration.

Mode (1,0) Mode (0,0) Mode (2,0) Mode (3,0)

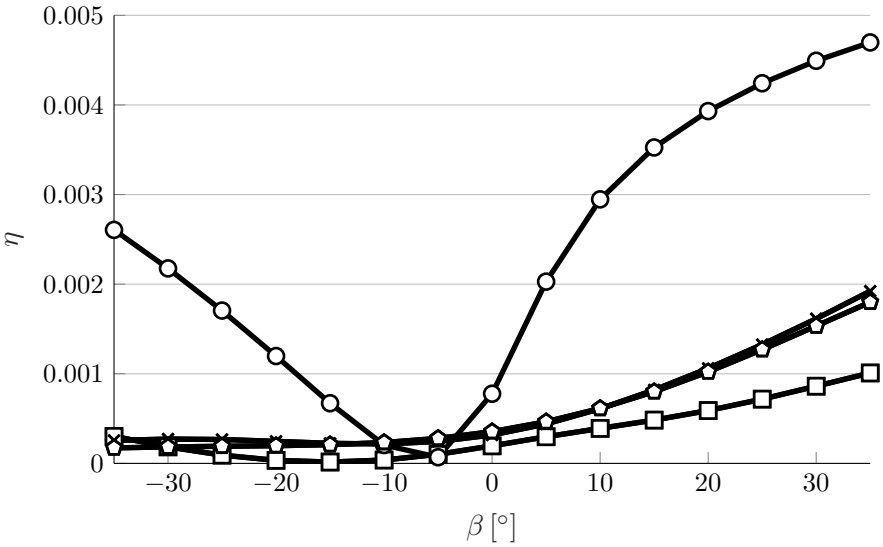

Figure 7.29: Inclination angle effect on the damping behavior of the outer ring configuration.
Mode (1,0) Mode (0,0) Mode (2,0) Mode (3,0)

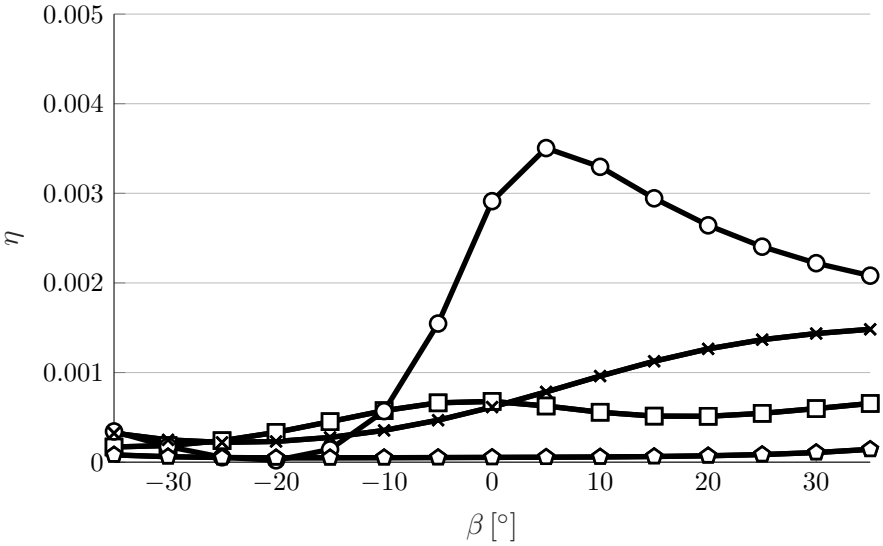

Figure 7.30: Inclination angle effect on the damping behavior of the inner ring configuration.
Mode (1,0) Mode (0,0) Mode (2,0) Mode (3,0)

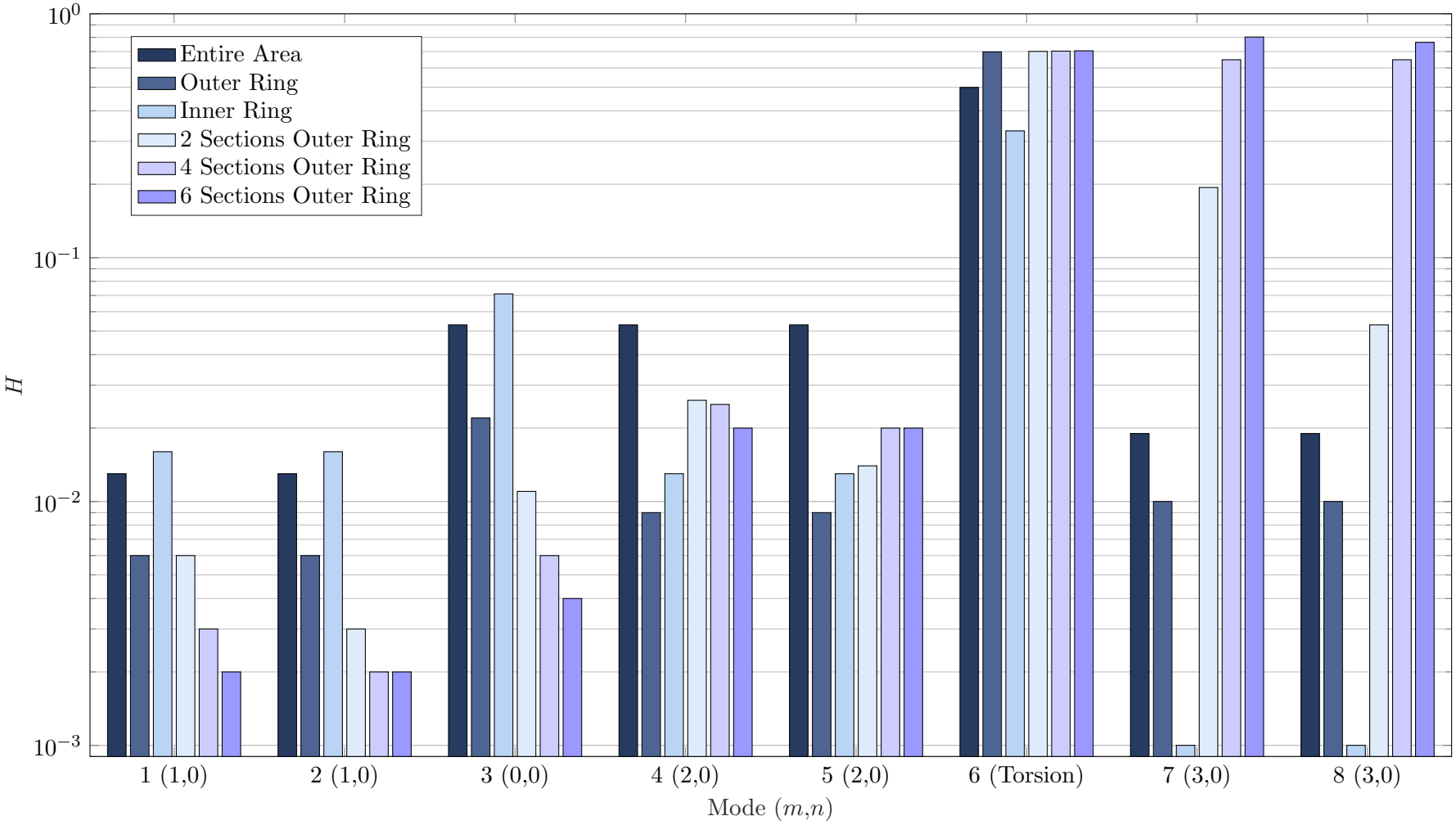

Figure 7.31: Loss factor-added mass weighting parameter, H, values for the circumferential damping treatments applied on the plane gearwheel.

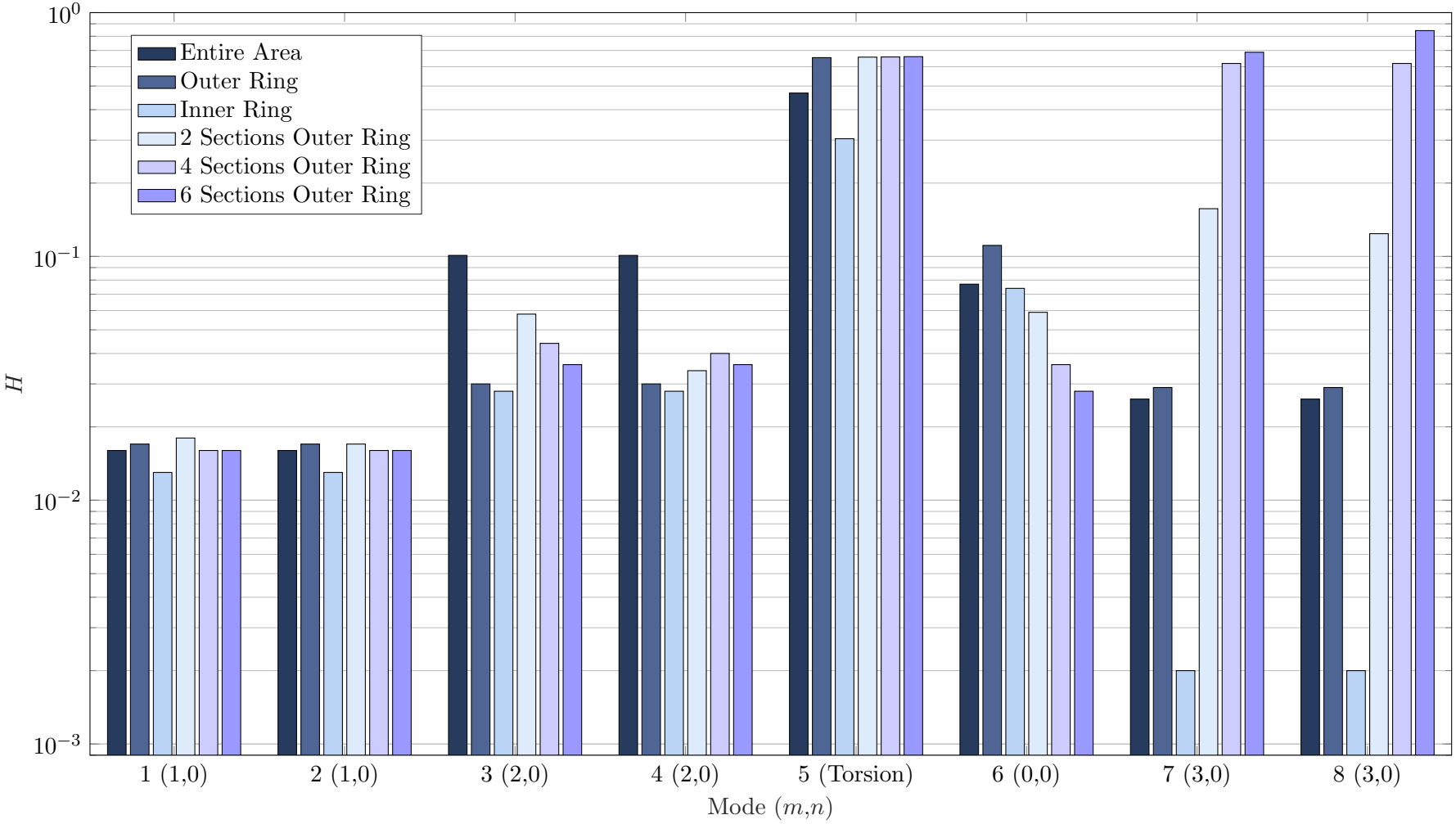

Figure 7.32: Loss factor-added mass weighting parameter, H, values for the circumferential damping treatments applied on the sloped gearwheel.

Chapter 8

Analysis of Radially Configured Viscoelastic Damping Devices

In the present chapter the numerical simulation results of the studied gearwheel with radial configured viscoelastic damping devices will be presented and discussed, for both plane and sloped gearwheels. Initially, complete circular sector shaped treatments are considered and studied. Then, these are radially split into two segments and the same analysis is performed. Finally, the inclination angle effect is presented and discussed for some of the considered configurations.

8.1 Introduction

As presented in Chapter 3, when considering a partial CLD configured viscoelastic damping treatment, the best location of the correspondent patches can be the nodal or the antinodal areas, depending on the relative thickness of the backing layer in respect to the host structure. So, a new set of damping devices for the present gearwheels, that would cover just these areas, neglecting the effect of the others, was suggested and assayed: the radial configurations.

These consist of circular sections characterized by an angle θ and inner, r_i, and outer, r_e, radii correspondent to the treated area. The numbers of considered sections were two, four and six, determined in accordance with the studied natural modes, since they present one, two and three nodal diameters. Table 8.1 presents the values of these characteristics. The layers' thicknesses were the same as presented in Table 5.3. The correspondent used meshes are presented in Figure 8.1, where the gray area corresponds to the damping device.

Split radial setups, materialized by a radial interruption of the patches, were also proposed and analyzed, as was performed for the circumferential configuration. The correspondent meshes are presented in Figure 8.2.

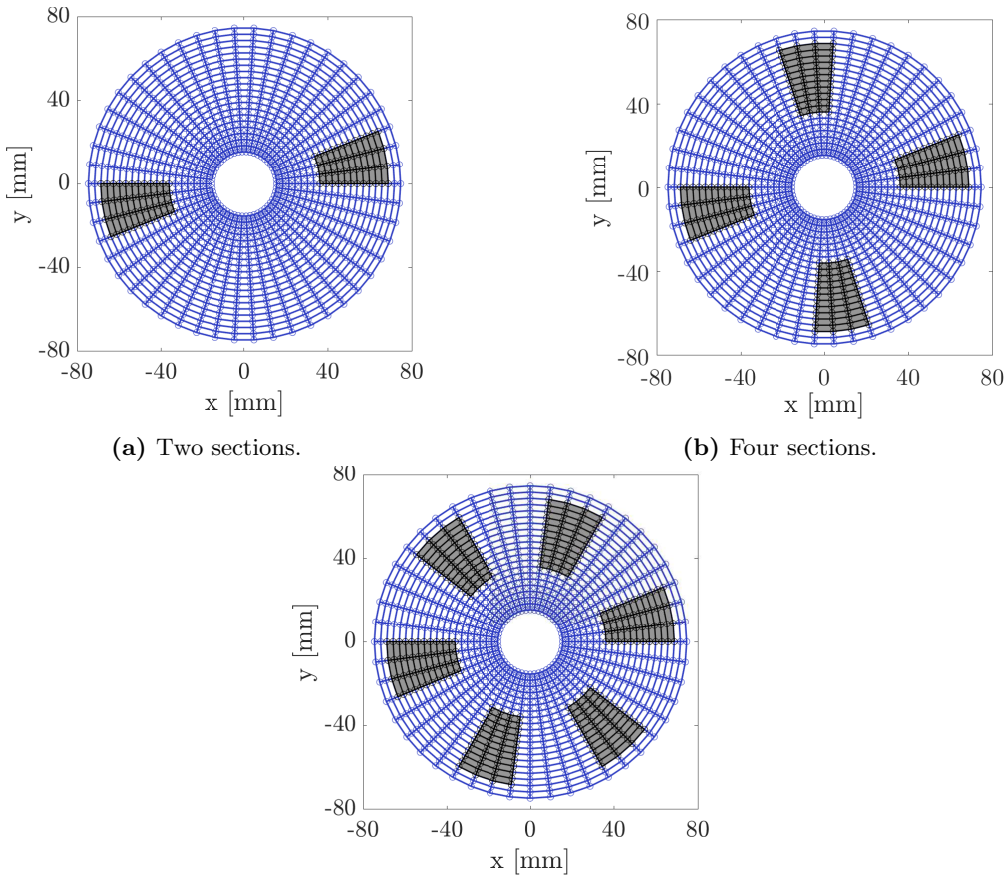

(a) Two sections.

(b) Four sections.

(c) Six sections.

Figure 8.1: Complete radial damping devices' configurations.

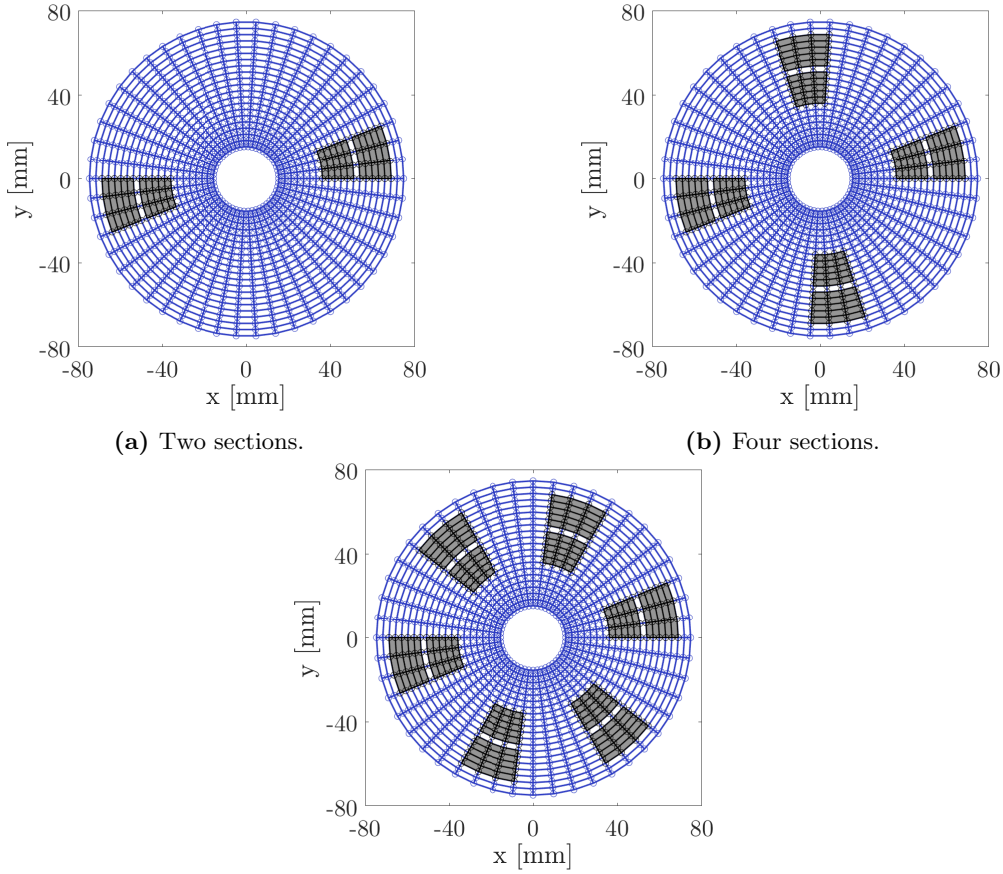

(a) Two sections.

(b) Four sections.

(c) Six sections.

Figure 8.2: Split radial damping devices' configurations.

Table 8.1: Radial damping devices' dimensions

θ [°]	r_i [mm]	r_e [mm]	Number of Radii
22	34	69	2, 4, 6

8.2 Plane Damped Gearwheel

The first radial configurations studied were the continuous ones. Table 8.2 presents the modal analysis results for these damping devices. Note that $\Delta_{r\,\eta_n}$ represents the relative difference of the four and six sections' loss factor values in respect to the two radii' results. Again, the values for the relative variation of the natural frequencies, $\Delta_{r\,\omega_n}$, were not presented once the differences were not significant. On the other hand, Table 8.3 presents the loss factor-added mass weighting results, H, for the present configurations.

Figures 8.3, 8.4 and 8.5 present the normal modes' total displacement for each treatment configuration.

Finally, the receptance's Bode plot for these cases, as well as for the non-treated plane gearwheel, can be presented in Figure 8.6. The considered node and degree of freedom for the excitation and the response record were the same as considered previously.

Table 8.2: Complete radial damping devices configurations' modal analysis results for the plane gearwheel

Mode		Two Radii $\Delta m = 11.66\,\mathrm{g}$		Four Radii $\Delta m = 23.31\,\mathrm{g}$			Six Radii $\Delta m = 34.96\,\mathrm{g}$		
	(m,n)	ω_n [Hz]	η_n [%]	ω_n [Hz]	η_n [%]	$\Delta_{r\,\eta_n}$ [%]	ω_n [Hz]	η_n [%]	$\Delta_{r\,\eta_n}$ [%]
1	(1,0)	835.208	0.003	835.247	0.005	65.374	833.082	0.007	147.146
2		839.336	0.002	835.247	0.005	194.595	833.082	0.007	340.262
3	(0,0)	1287.71	0.007	1283.92	0.014	110.620	1279.88	0.021	214.986
4	(2,0)	2060.51	0.020	2056.98	0.042	106.310	2059.15	0.046	129.082
5		2065.09	0.009	2066.53	0.020	112.349	2059.15	0.046	389.146
6	(Torsion)	2624.23	0.471	2612.91	0.958	103.526	2601.56	1.404	198.342
7	(3,0)	5554.84	0.437	5565.57	0.559	28.128	5553.72	1.289	195.113
8		5560.16	0.122	5565.57	0.559	360.111	5570.23	0.345	183.969

Table 8.3: Loss factor and added mass weighting, H, for the complete radial configurations in the plane gearwheel

Mode	(m,n)	Two Radii $\Delta_{r\,m} = 0.84\,\%$	Four Radii $\Delta_{r\,m} = 1.67\,\%$		Six Radii $\Delta_{r\,m} = 2.51\,\%$	
		H	H	$\Delta_{r\,H}$ [%]	H	$\Delta_{r\,H}$ [%]
1	(1,0)	0.003	0.003	-17.313	0.003	-17.618
2		0.002	0.003	47.298	0.003	46.754
3	(0,0)	0.008	0.008	5.310	0.008	4.995
4	(2,0)	0.024	0.025	3.155	0.018	-23.639
5		0.011	0.012	6.175	0.018	63.049
6	(Torsion)	0.562	0.572	1.768	0.559	-0.553
7	(3,0)	0.521	0.334	-35.936	0.513	-1.629
8		0.145	0.334	130.056	0.137	-5.344

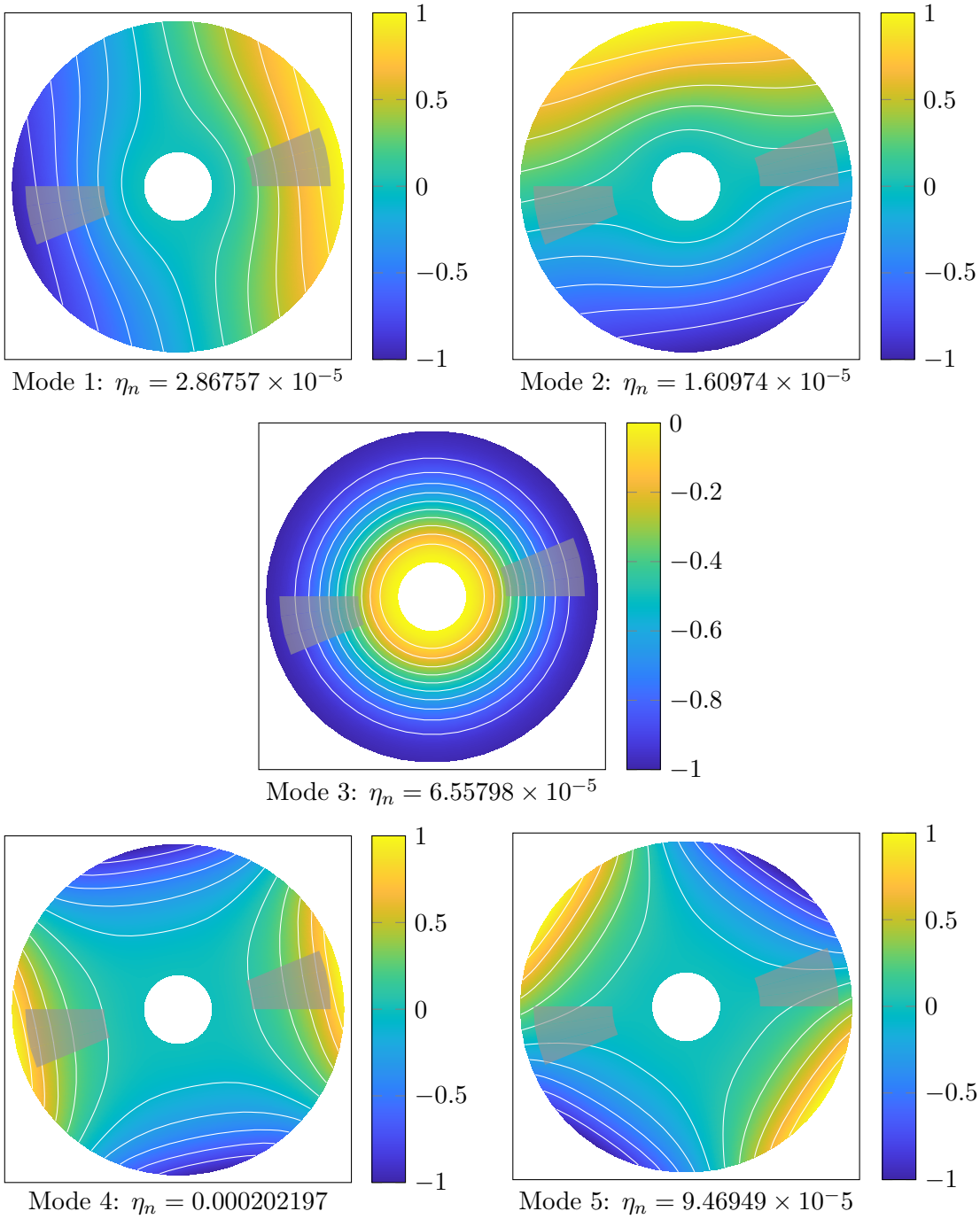

Figure 8.3: Plane gearwheel with two sections radial damping device mode shapes.

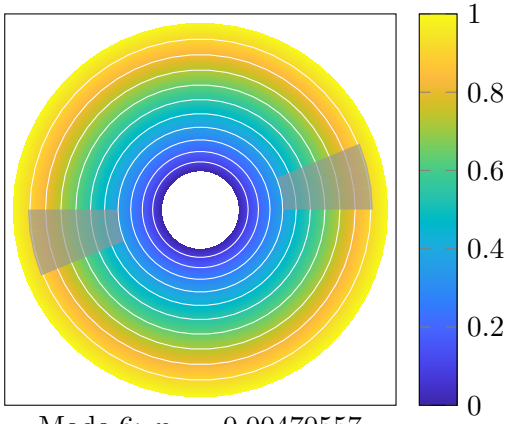

Mode 6: $\eta_n = 0.00470557$

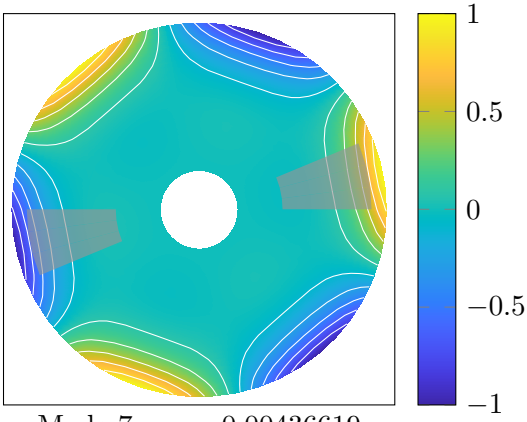

Mode 7: $\eta_n = 0.00436619$

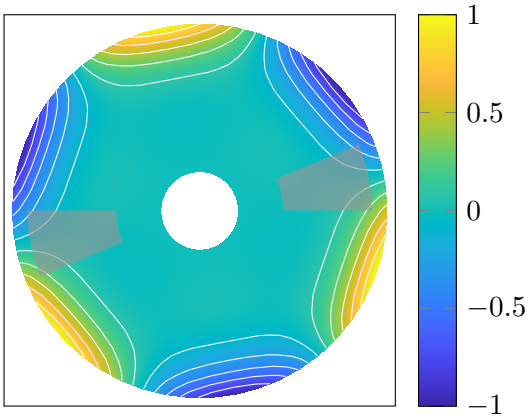

Mode 8: $\eta_n = 0.00121586$

Figure 8.3: Plane gearwheel with two sections radial damping device mode shapes. *(Continued)*

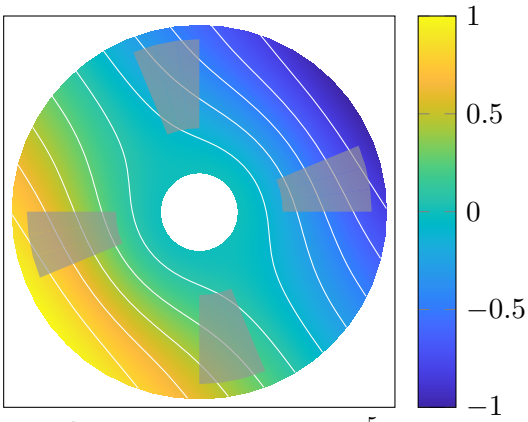

Mode 1: $\eta_n = 4.7422 \times 10^{-5}$

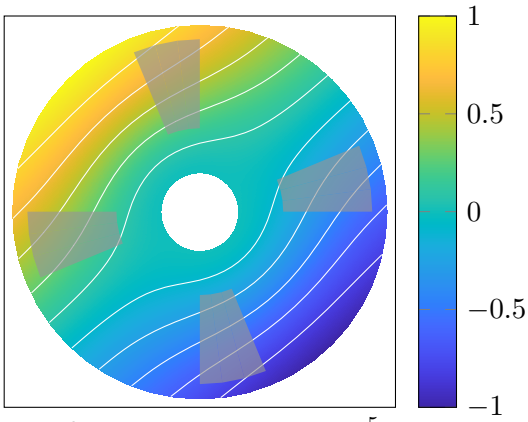

Mode 2: $\eta_n = 4.7422 \times 10^{-5}$

Figure 8.4: Plane gearwheel with four sections radial damping device mode shapes.

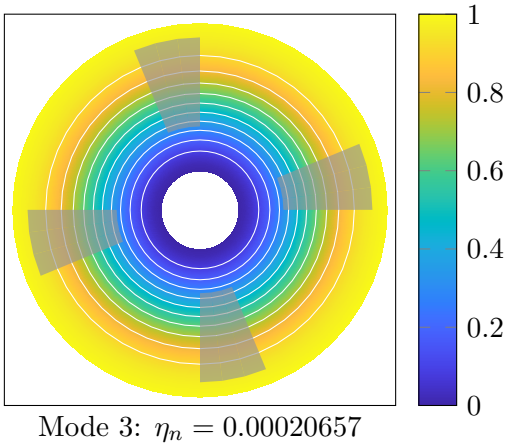

Mode 3: $\eta_n = 0.00020657$

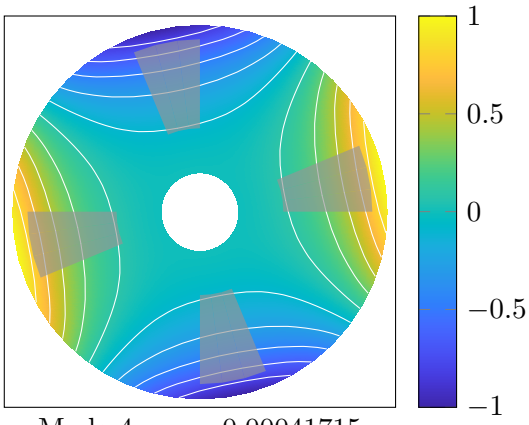

Mode 4: $\eta_n = 0.00041715$

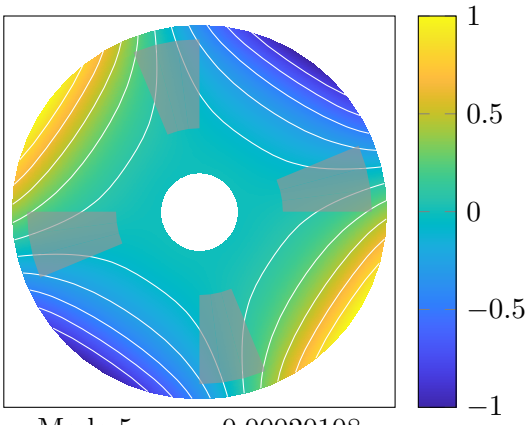

Mode 5: $\eta_n = 0.00020108$

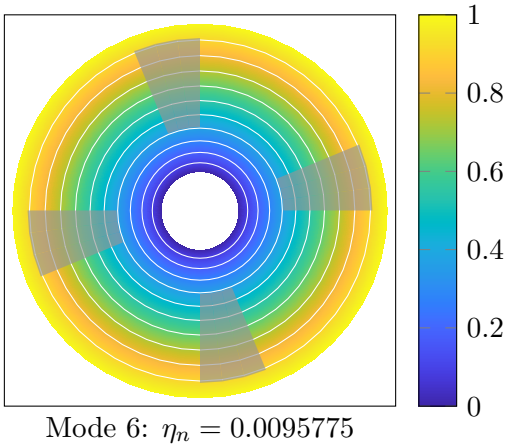

Mode 6: $\eta_n = 0.0095775$

Figure 8.4: Plane gearwheel with four sections radial damping device mode shapes. *(Continued)*

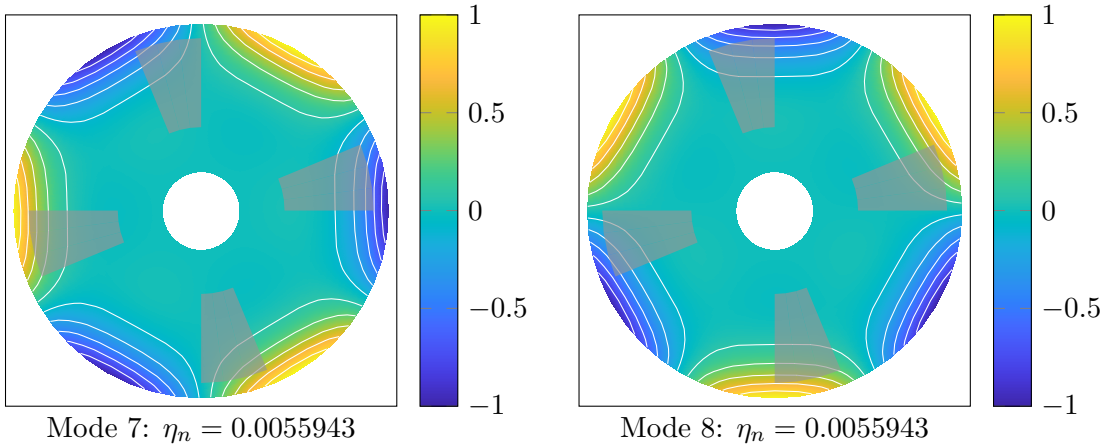

Figure 8.4: Plane gearwheel with four sections radial damping device mode shapes. *(Continued)*

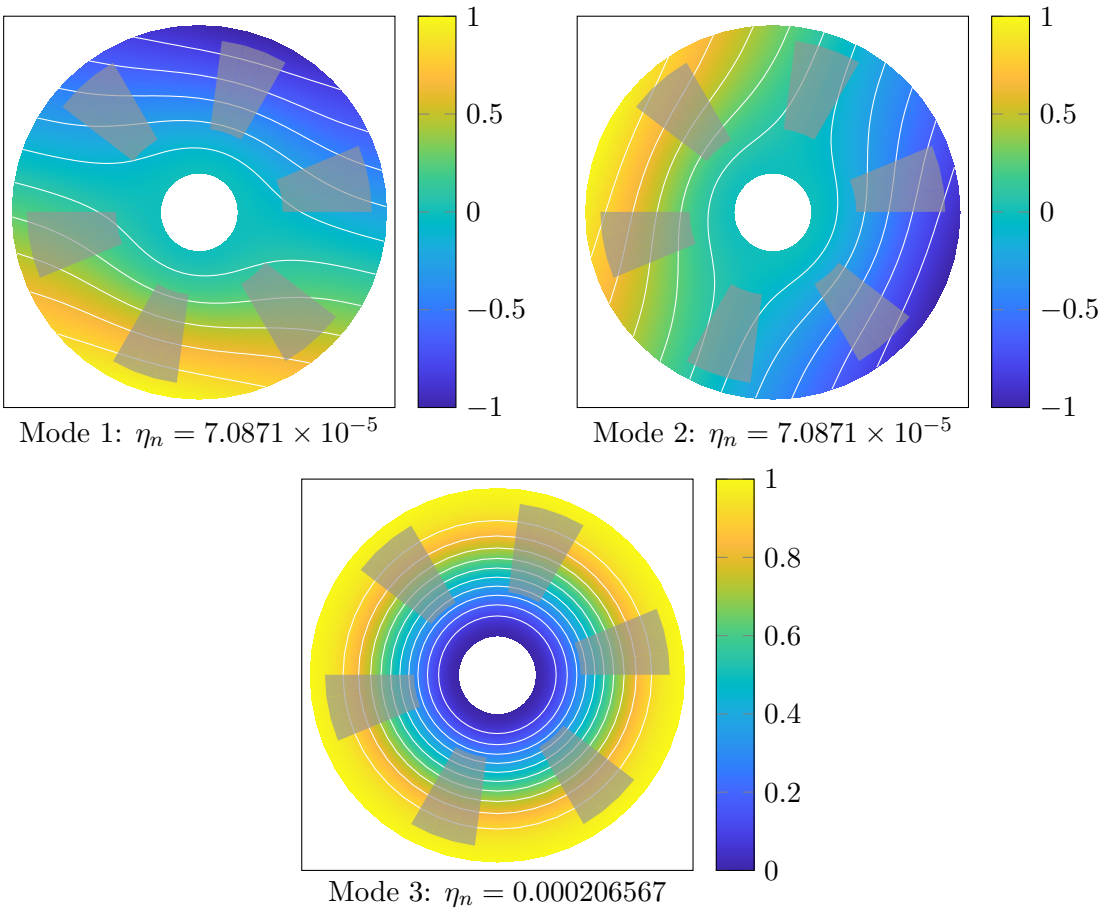

Figure 8.5: Plane gearwheel with six sections radial damping device mode shapes.

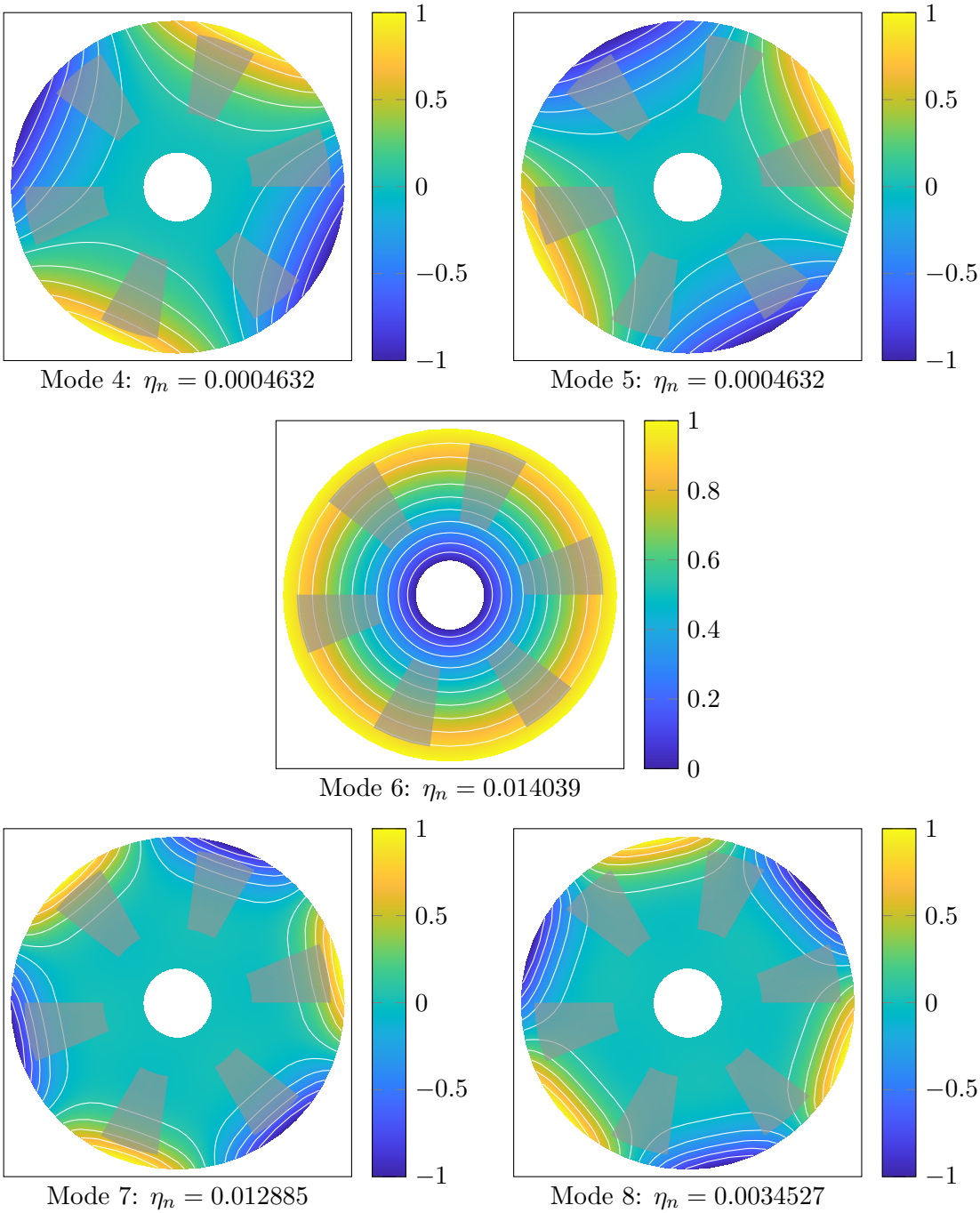

Figure 8.5: Plane gearwheel with six sections radial damping device mode shapes. *(Continued)*

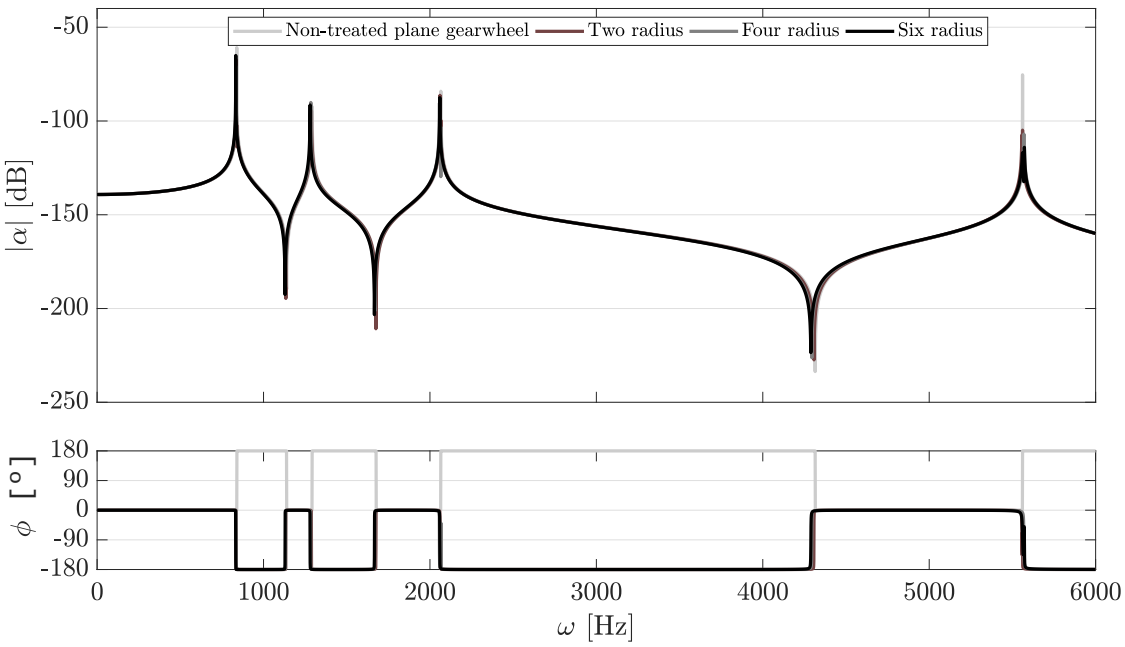

Figure 8.6: Receptance's Bode plot for the complete radial damping device configurations applied on the plane gearwheel.

Analyzing Table 8.2, it is clear that the higher number of sections is associated with a better damping capacity, since the loss factors are always superior, except for the eighth mode, where the higher loss factor value is verified for the configuration with four radii. This phenomenon can be explained together with the mode shapes, and may be due to the involved viscoelastic material's quantity. In fact, the four and six radii configurations present the double and the triple, respectively, of viscoelastic material than the two radii setup. So, even if the damping devices do not overlap the nodal nor the antinodal areas (occupying zones where neither the shear strains nor the transverse displacements reach the maximum absolute values), where the damping phenomena decreased, the higher quantity of the dissipative elements proved to be preponderant, leading to increasing damping capacity.

However, when considering the loss factor-added mass balancing parameter, H, in Table 8.3, the previously mentioned high superiority of the configurations with higher number of radial sections was partially undone. In fact, the results came closer and the two radii configuration's performance even surpassed the others for some modes, which reveals the previously mentioned effect of the extra viscoelastic material quantity.

On the other hand, it is possible to conclude that, for the plane gearwheel, the positioning of the damping devices in the antinodes led to better damping performances. In fact, analyzing, for example, the (1,0) mode for the two radii configuration, the higher loss factor value is verified for the case with lower natural frequency, corresponding to the placing of the treatment in the zones with maximum total displacement. The same occurs for the (2,0) mode in the four radii configuration and the (3,0) mode in the six radii configuration. This reveals that, for the plane gearwheel, the curvature and transverse displacements are more significant to damping than the higher shear strains developed in the nodal areas.

Comparing now the damping capacity of the radial configurations with the previously studied outer and inner continuous rings (Table 7.2), it can be verified that the suggested setup allowed to achieve higher loss factor values for the (2,0) and (3,0) modes, while

the circumferentially configured devices showed higher energy dissipation for the others. When comparing the loss factor-added mass weighting parameter, H, the same relations remained. These phenomena may due to the balance between the quantity of viscoelastic material and, thus, dissipative elements present in the device, and the boundary effects, that for the radial configurations develop in both sides of each circular sector. In fact, as seen before for the split circumferential configurations, these effects were also significant for the (2,0) and (3,0) modes, which reinforces its major influence on this comparison.

Considering now the split inner ring shaped devices and comparing their damping capacity (Table 8.4) with the correspondent present configurations (with the same number of sections), it is possible to verify that the energy dissipation is higher in the circumferential configurations with two and four sections, except for the (3,0) mode. However, in the setups with six segments, the radial configuration presents higher or nearly equal damping capacity for all modes, except for the (1,0). On the other hand, comparing the loss factor-added mass balanced performance (Table 8.5) of these configurations, it is possible to conclude that the radially shaped devices accomplished better results for the (2,0), torsion and (3,0) modes, regardless the number of sections.

Doing the same but for the split outer ring shaped devices, (Tables 8.6 and 8.7) it is possible to conclude that the obtained loss factors were all superior to the ones achieved with the radial configurations. However, for the balancing parameter H, different relations were obtained. In fact, the two radii radial configuration presented a better performance for the (3,0) mode and a worse performance for the other modes, while the four and six radii shaped devices presented better performances for the (1,0) and (0,0) modes, and worse for the others. This can be explained by the fact that the damping of these two modes is favored by the higher shear strains that occur near the center of the plane gearwheel, that affect the inner part of the radial patches but do not affect the outer circumferential segments. This may not be verified for the two section configurations once the importance of the higher amount of viscoelastic material and, consequent higher quantity of dissipative elements, prevailed in the split annular shape.

Table 8.4: Comparison between the damping capacities of the radial and inner split circumferential configurations for the plane gearwheel

Mode		Two Sections		Four Sections		Six Sections	
	(m,n)	Annular η_n [%]	Radial η_n [%]	Annular η_n [%]	Radial η_n [%]	Annular η_n [%]	Radial η_n [%]
1	(1,0)	0.065	0.003	0.026	0.005	0.016	0.007
2		0.027	0.002	0.026	0.005	0.016	0.007
3	(0,0)	0.143	0.007	0.053	0.014	0.026	0.021
4	(2,0)	0.037	0.020	0.026	0.042	0.021	0.046
5		0.037	0.009	0.024	0.020	0.021	0.046
6	(Torsion)	1.181	0.471	1.132	0.958	1.083	1.289
7	(3,0)	0.004	0.437	0.064	0.559	0.087	1.289
8		0.007	0.122	0.064	0.559	0.054	0.345

Table 8.5: Comparison between the loss factor-added mass weighting parameter of the radial and inner split circumferential configurations for the plane gearwheel

Mode		Two Sections		Four Sections		Six Sections	
	(m,n)	Annular H	Radial H	Annular H	Radial H	Annular H	Radial H
1	(1,0)	0.019	0.003	0.008	0.003	0.005	0.003
2		0.008	0.002	0.008	0.003	0.005	0.003
3	(0,0)	0.043	0.008	0.016	0.008	0.008	0.008
4	(2,0)	0.011	0.024	0.008	0.025	0.007	0.018
5		0.011	0.011	0.007	0.012	0.007	0.018
6	(Torsion)	0.351	0.562	0.351	0.572	0.351	0.559
7	(3,0)	0.001	0.521	0.020	0.334	0.028	0.513
8		0.002	0.145	0.020	0.334	0.017	0.137

Table 8.6: Comparison between the damping capacities of the radial and outer split circumferential configurations for the plane gearwheel

Mode		Two Sections		Four Sections		Six Sections	
	(m,n)	Annular η_n [%]	Radial η_n [%]	Annular η_n [%]	Radial η_n [%]	Annular η_n [%]	Radial η_n [%]
1	(1,0)	0.019	0.003	0.009	0.003	0.007	0.003
2		0.009	0.002	0.008	0.003	0.007	0.003
3	(0,0)	0.038	0.008	0.020	0.008	0.014	0.008
4	(2,0)	0.089	0.024	0.080	0.025	0.061	0.018
5		0.047	0.011	0.064	0.012	0.061	0.018
6	(Torsion)	2.361	0.562	2.268	0.572	2.176	0.559
7	(3,0)	0.652	0.521	2.089	0.334	2.478	0.513
8		0.179	0.145	2.089	0.334	2.478	0.137

Table 8.7: Comparison between the loss factor-added mass weighting parameter of the radial and outer split circumferential configurations for the plane gearwheel

Mode		Two Sections		Four Sections		Six Sections	
	(m,n)	Annular H	Radial H	Annular H	Radial H	Annular H	Radial H
1	(1,0)	0.006	0.003	0.003	0.003	0.002	0.003
2		0.003	0.002	0.002	0.003	0.002	0.003
3	(0,0)	0.011	0.008	0.006	0.008	0.004	0.008
4	(2,0)	0.026	0.024	0.025	0.025	0.020	0.018
5		0.014	0.011	0.020	0.012	0.020	0.018
6	(Torsion)	0.701	0.562	0.703	0.572	0.705	0.559
7	(3,0)	0.194	0.521	0.648	0.334	0.803	0.513
8		0.053	0.145	0.648	0.334	0.764	0.137

8.2.1 Segmented Configurations

Considering now the segmented configurations presented in Figure 8.2, the obtained results and comparison with the correspondent complete setups can be presented in Table 8.8, for the damping capacity, and in Table 8.9, for the loss factor-added mass weighting. Note that $\Delta_{r\,\eta_n}$ and $\Delta_{r\,H}$ represent the relative difference of the sectioned radial configuration loss factor and loss factor-added mass balancing parameter in respect to the correspondent continuous setup, respectively. The natural frequency values are presented in the correspondent mode shapes (Figures 8.7, 8.8 and 8.9), where the total displacement is represented, and the receptance's Bode plot is not presented once the curves overlapped, being nearly impossible to distinguish them.

From Table 8.8 it is possible to conclude that the split radial configurations present less damping capacity than the correspondent complete circular sections for all the studied modes, except for the last one. This phenomenon may be due to the fact that in the considered interruption the boundary effects are not relevant since the boundary is not subjected to significant shear strain variations, except for the (3,0) mode because of the correspondent mode shape.

However, when analyzing the balancing parameter relating the damping capacity and the mass added to the system, H, it is possible to verify that the previous relations remained, except for the torsion mode, where the split configurations' performance increased, surpassing the continuous setups. This variation occurs because the damping capacity decrease on this mode was not significant, which when balanced with the minor added mass lead to a higher value of this parameter.

Comparing the interruption effects on the radial and circumferential configurations, applied in the plane gearwheel, it is possible to conclude that in the first case they are more beneficial.

Table 8.8: Interrupted radial configurations' loss factor results for the plane gearwheel

Mode		Split Two Sections $\Delta m = 10.31\,\mathrm{g}$		Split Four Sections $\Delta m = 20.62\,\mathrm{g}$		Split Six Sections $\Delta m = 30.93\,\mathrm{g}$	
	(m,n)	η_n [%]	$\Delta_{r\,\eta_n}$ [%]	η_n [%]	$\Delta_{r\,\eta_n}$ [%]	η_n [%]	$\Delta_{r\,\eta_n}$ [%]
1	(1,0)	0.002	-35.830	0.003	-37.065	0.004	-37.127
2		0.001	-38.483	0.003	-37.065	0.004	-37.127
3	(0,0)	0.002	-63.834	0.005	-63.819	0.007	-63.879
4	(2,0)	0.012	-40.665	0.025	-40.458	0.029	-37.002
5		0.007	-28.389	0.014	-29.790	0.029	-37.002
6	(Torsion)	0.433	-8.086	0.882	-7.912	1.295	-7.746
7	(3,0)	0.575	31.768	0.771	37.782	1.686	30.832
8		0.170	40.035	0.771	37.815	0.550	59.216

Table 8.9: Interrupted radial configurations' loss factor-added mass weighting parameter results for the plane gearwheel

Mode		Split Two Sections $\Delta_{r\,m} = 0.74\,\%$		Split Four Sections $\Delta_{r\,m} = 1.48\,\%$		Split Six Sections $\Delta_{r\,m} = 2.22\,\%$	
	(m,n)	H	$\Delta_{r\,H}$ [%]	H	$\Delta_{r\,H}$ [%]	H	$\Delta_{r\,H}$ [%]
1	(1,0)	0.002	-27.458	0.002	-28.854	0.002	-28.924
2		0.001	-30.457	0.002	-28.854	0.002	-28.924
3	(0,0)	0.003	-59.116	0.003	-59.098	0.003	-59.166
4	(2,0)	0.016	-32.924	0.017	-32.690	0.013	-28.783
5		0.009	-19.047	0.010	-20.629	0.013	-28.783
6	(Torsion)	0.584	3.906	0.595	4.102	0.583	4.290
7	(3,0)	0.777	48.959	0.520	55.759	0.759	47.902
8		0.230	58.305	0.520	55.795	0.247	79.989

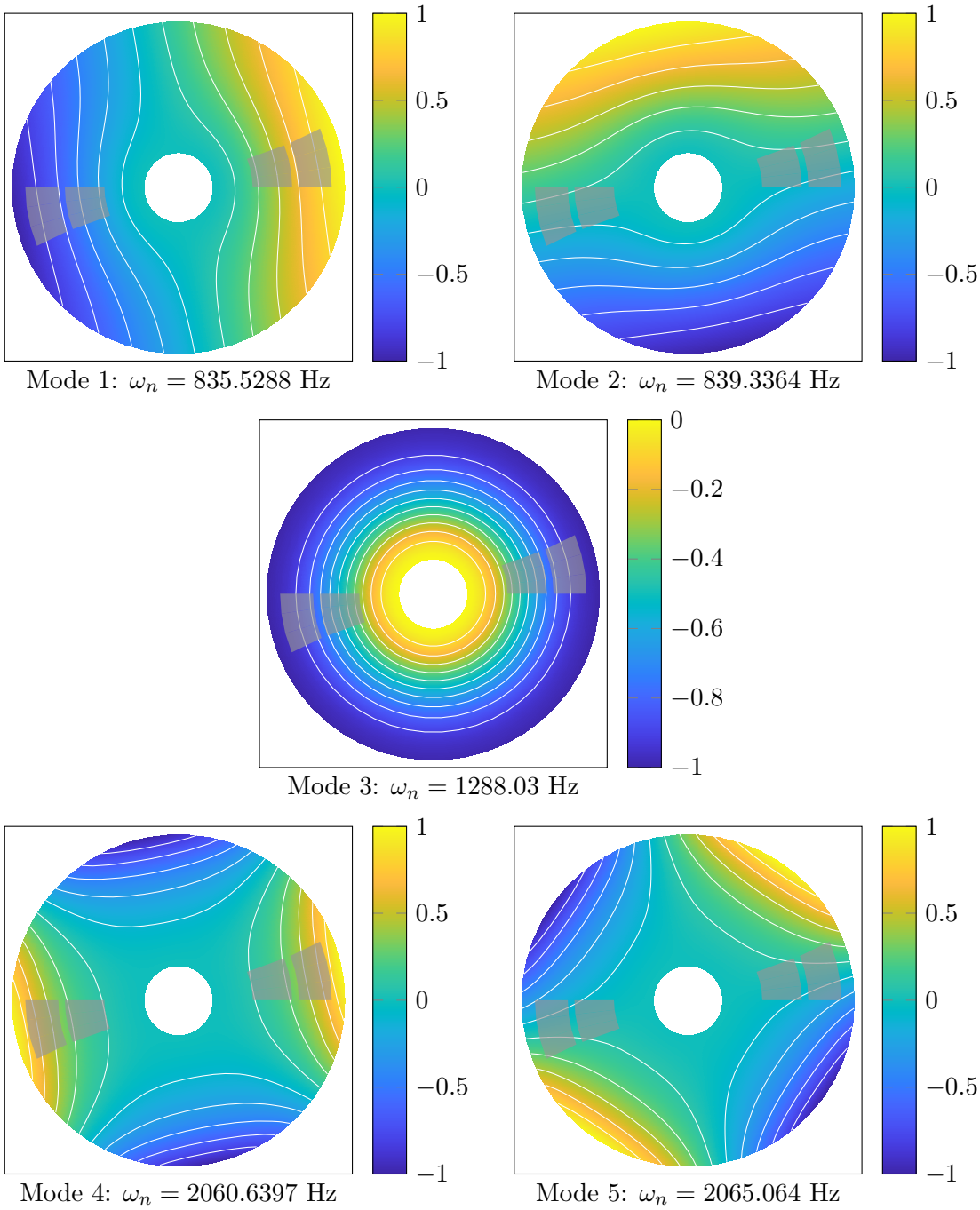

Figure 8.7: Plane gearwheel with split two sections radial damping device mode shapes.

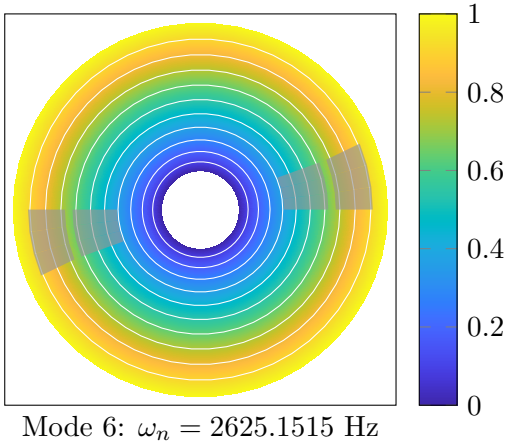

Mode 6: $\omega_n = 2625.1515$ Hz

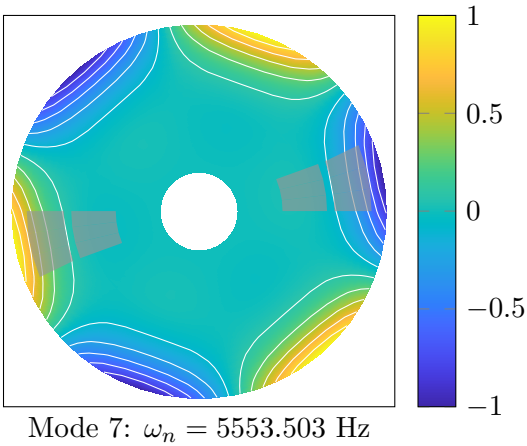

Mode 7: $\omega_n = 5553.503$ Hz

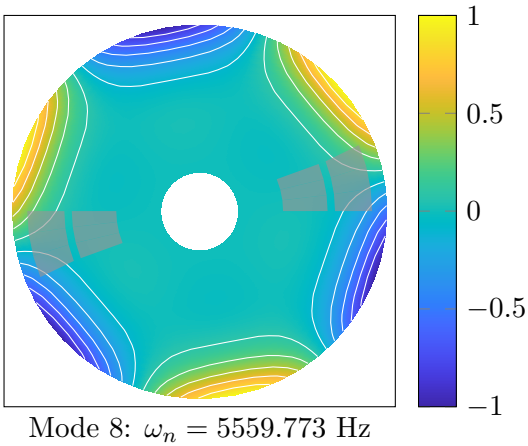

Mode 8: $\omega_n = 5559.773$ Hz

Figure 8.7: Plane gearwheel with split two sections radial damping device mode shapes. *(Continued)*

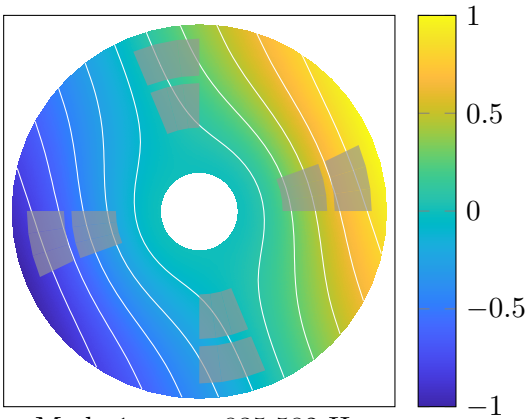

Mode 1: $\omega_n = 835.582$ Hz

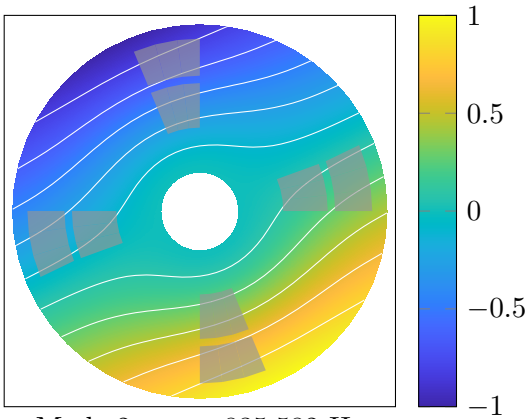

Mode 2: $\omega_n = 835.582$ Hz

Figure 8.8: Plane gearwheel with split four sections radial damping device mode shapes.

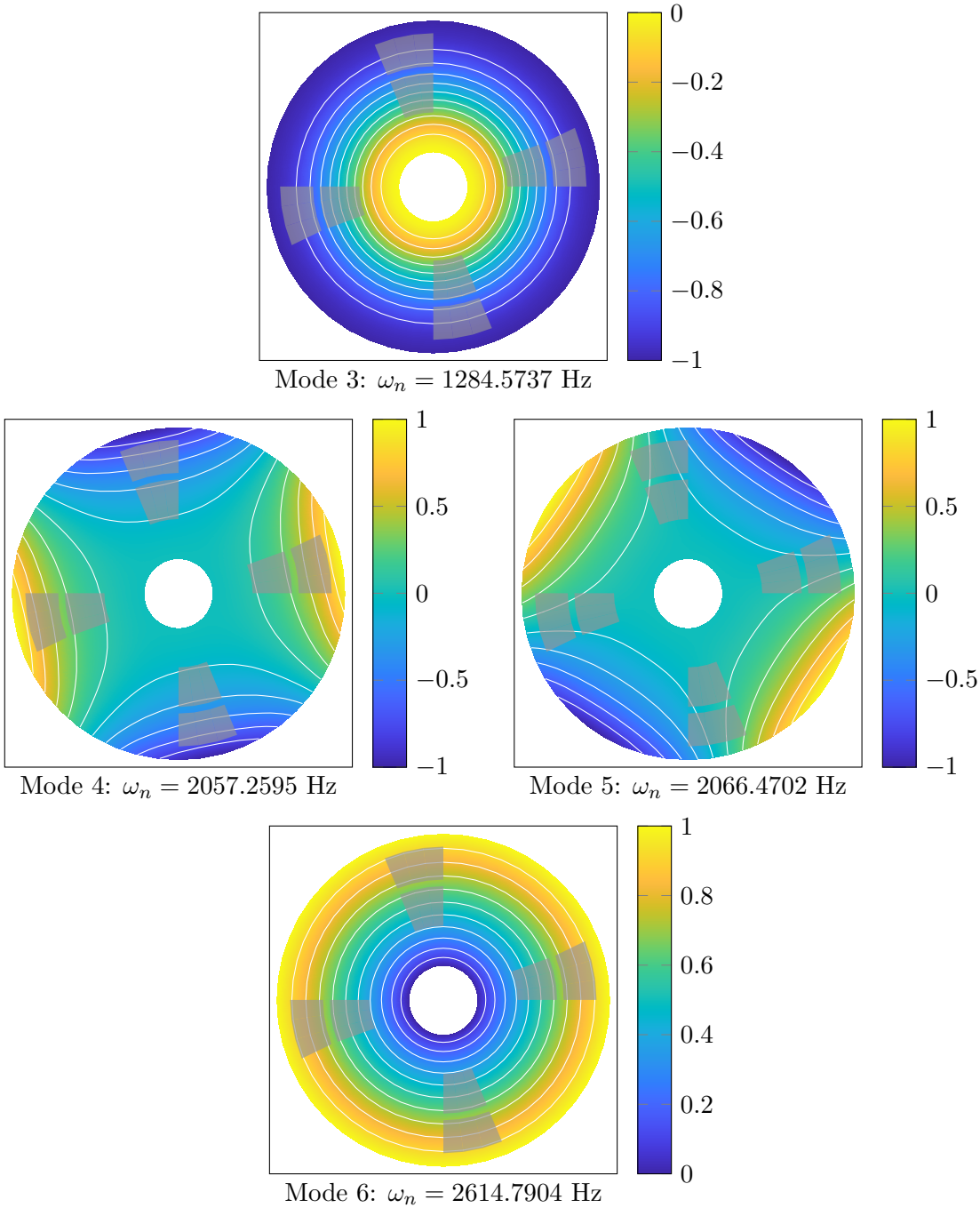

Figure 8.8: Plane gearwheel with split four sections radial damping device mode shapes. *(Continued)*

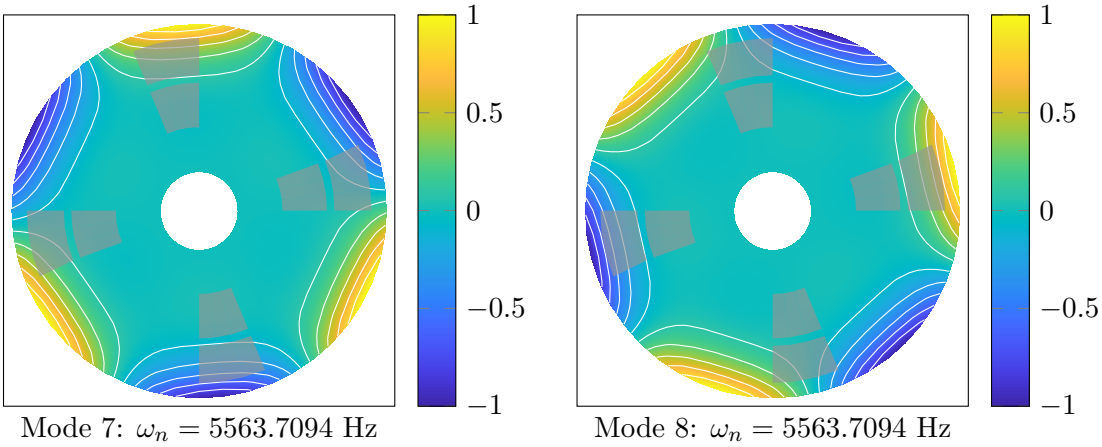

Figure 8.8: Plane gearwheel with split four sections radial damping device mode shapes. *(Continued)*

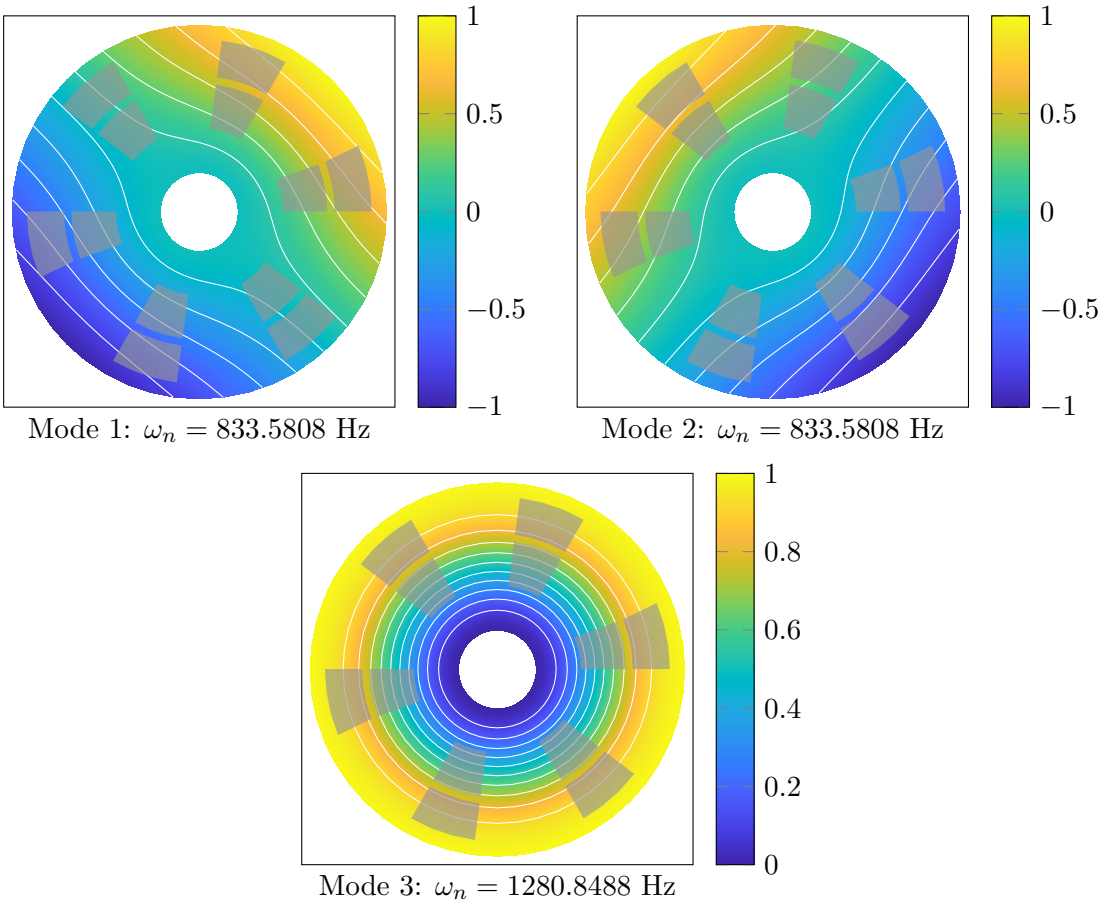

Figure 8.9: Plane gearwheel with split six sections radial damping device mode shapes.

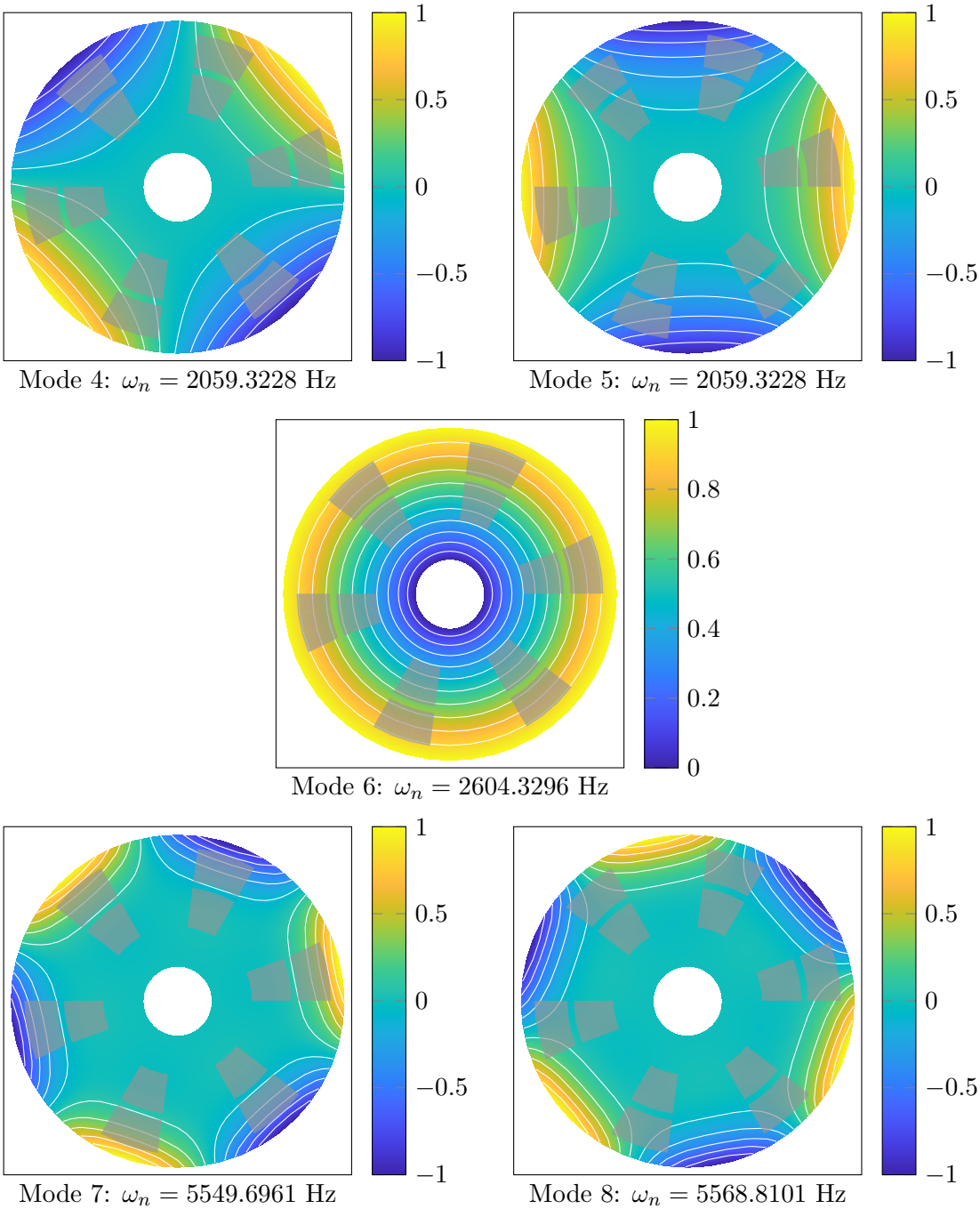

Figure 8.9: Plane gearwheel with split six sections radial damping device mode shapes. *(Continued)*

8.3 Sloped Damped Gearwheel

The study of radially configured damping devices applied in sloped gearwheels also began with the continuous ones. Table 8.10 presents the modal analysis results for these setups, where again $\Delta_{r\,\eta_n}$ represents the relative difference of the four and six sections' loss factor values in respect to the two radii' results. On the other hand, Table 8.11 presents the loss factor-added mass weighting results, H, for the present configurations.

Figures 8.10, 8.11 and 8.12 present the normal modes' total displacement for each configuration.

Finally, the receptance's Bode plot for these cases, as well as for the non-treated sloped gearwheel, can be presented in Figure 8.13, where the considered node and degree of freedom of the excitation and the response record were the same as considered previously.

Table 8.10: Complete radial damping devices configurations' modal analysis results for the sloped gearwheel

Mode		Two Radii $\Delta m = 11.66\,\mathrm{g}$		Four Radii $\Delta m = 23.31\,\mathrm{g}$			Six Radii $\Delta m = 34.96\,\mathrm{g}$		
	(m,n)	ω_n [Hz]	η_n [%]	ω_n [Hz]	η_n [%]	$\Delta_{r\,\eta_n}$ [%]	ω_n [Hz]	η_n [%]	$\Delta_{r\,\eta_n}$ [%]
1	(1,0)	1090.47	0.003	1089.66	0.024	763.201	1086.41	0.035	1183.108
2		1095.17	0.020	1089.66	0.024	17.011	1086.41	0.035	73.932
3	(2,0)	2091.30	0.014	2087.56	0.029	110.140	2089.10	0.071	413.473
4		2096.02	0.032	2097.23	0.067	104.867	2089.10	0.071	118.996
5	(Torsion)	2552.50	0.440	2541.54	0.899	104.422	2530.68	1.318	199.801
6	(0,0)	2849.56	0.015	2840.30	0.031	102.344	2831.05	0.047	201.800
7	(3,0)	5482.21	0.290	5491.13	0.732	152.676	5481.70	0.867	199.396
8		5485.13	0.430	5491.13	0.732	70.188	5491.01	1.262	193.543

Table 8.11: Loss factor and added mass weighting, H, for the complete radial configurations in the sloped gearwheel

Mode	(m,n)	Two Radii $\Delta_{r\,m} = 0.84\,\%$	Four Radii $\Delta_{r\,m} = 1.67\,\%$		Six Radii $\Delta_{r\,m} = 2.51\,\%$	
		H	H	$\Delta_{r\,H}$ [%]	H	$\Delta_{r\,H}$ [%]
1	(1,0)	0.003	0.014	331.600	0.014	327.703
2		0.024	0.014	-41.949	0.014	-42.023
3	(2,0)	0.016	0.017	5.070	0.028	71.158
4		0.039	0.040	2.434	0.028	-27.001
5	(Torsion)	0.522	0.534	2.211	0.522	-0.066
6	(0,0)	0.018	0.019	1.172	0.019	0.600
7	(3,0)	0.344	0.435	26.338	0.343	-0.201
8		0.511	0.435	-14.906	0.500	-2.152

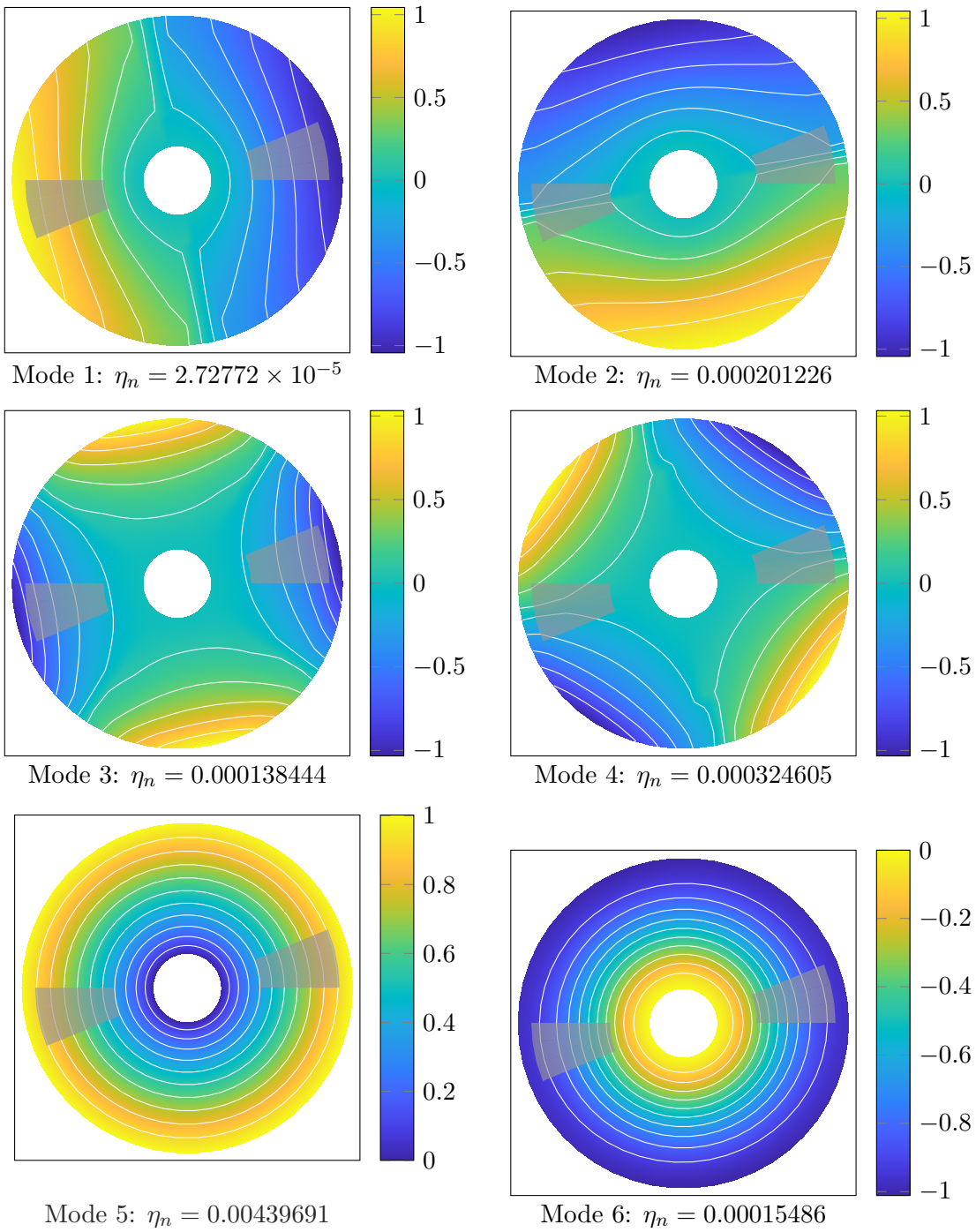

Figure 8.10: Sloped gearwheel with two sections radial damping device mode shapes.

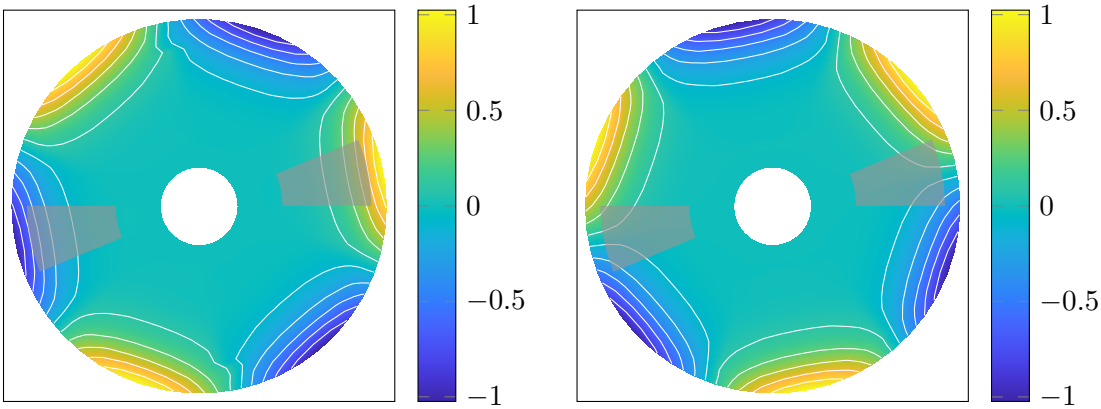

Mode 7: $\eta_n = 0.00289604$ Mode 8: $\eta_n = 0.00429975$

Figure 8.10: Sloped gearwheel with two sections radial damping device mode shapes. *(Continued)*

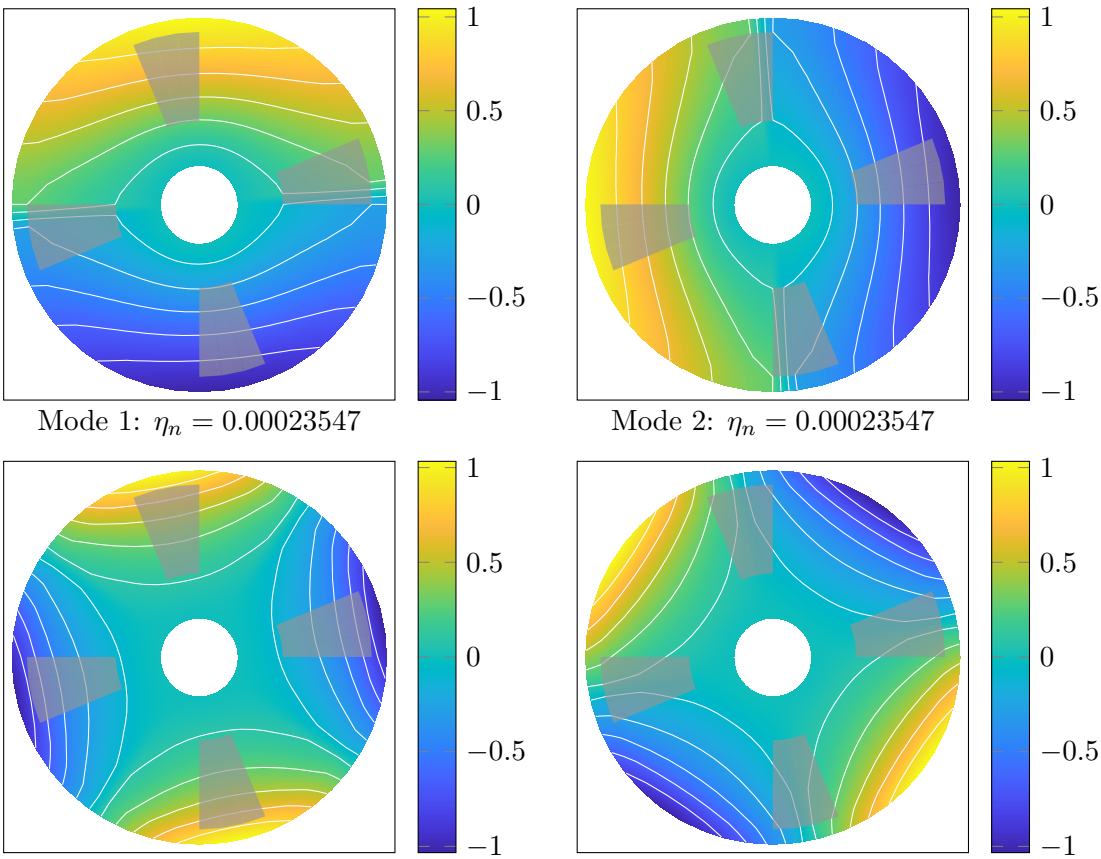

Mode 1: $\eta_n = 0.00023547$ Mode 2: $\eta_n = 0.00023547$

Mode 3: $\eta_n = 0.000290926$ Mode 4: $\eta_n = 0.00066501$

Figure 8.11: Sloped gearwheel with four sections radial damping device mode shapes.

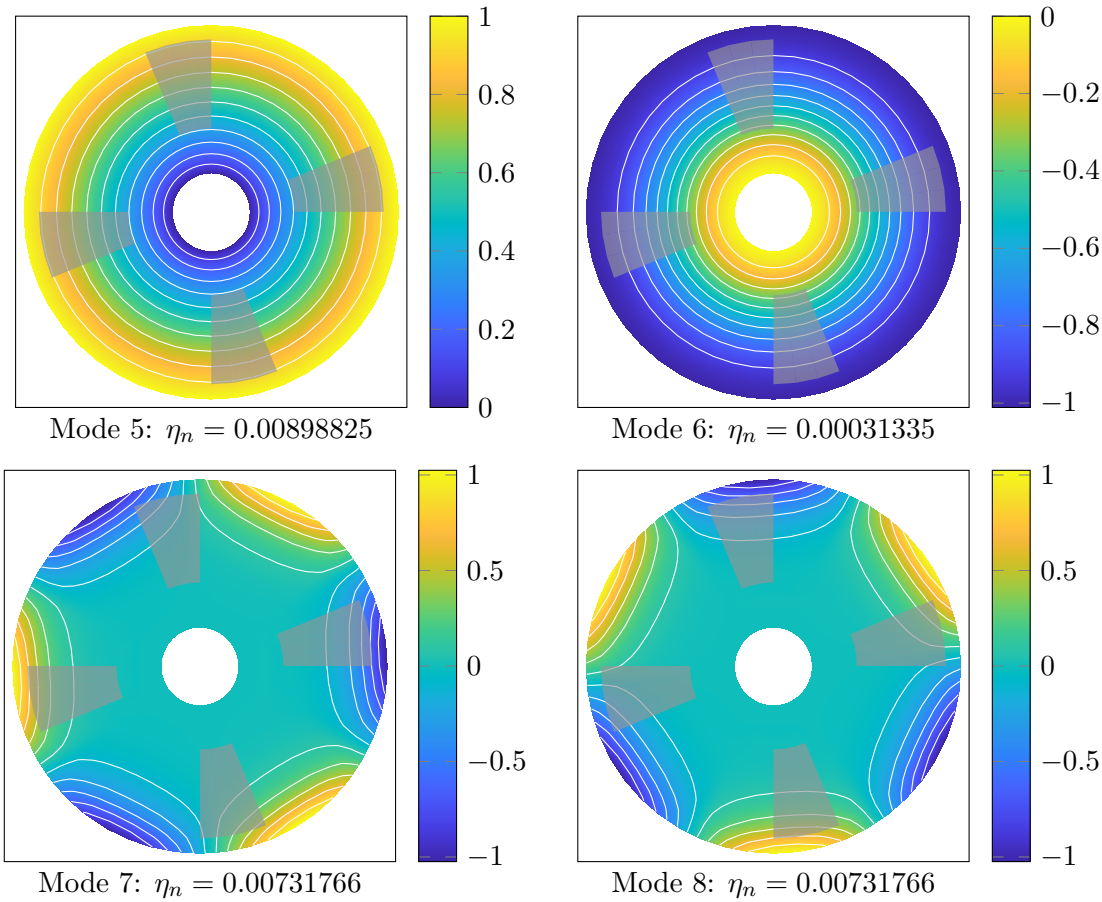

Figure 8.11: Sloped gearwheel with four sections radial damping device mode shapes. *(Continued)*

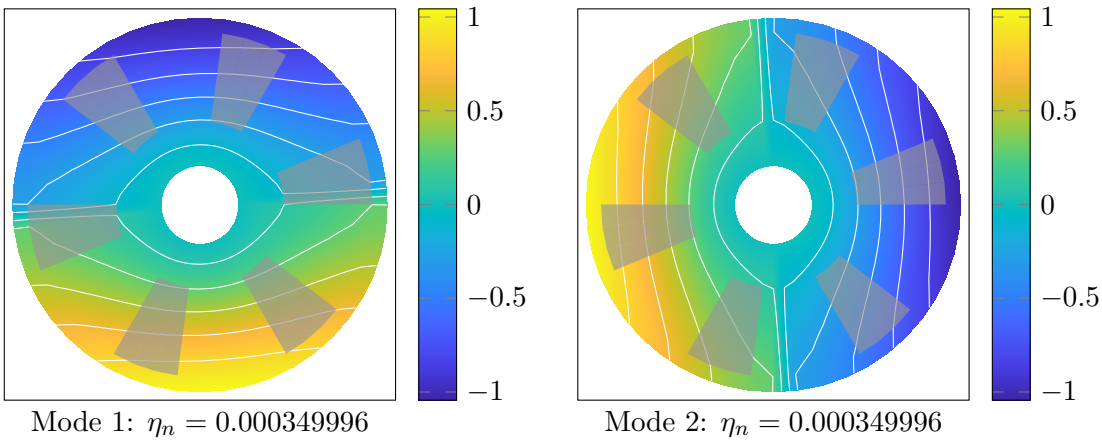

Figure 8.12: Sloped gearwheel with six sections radial damping device mode shapes.

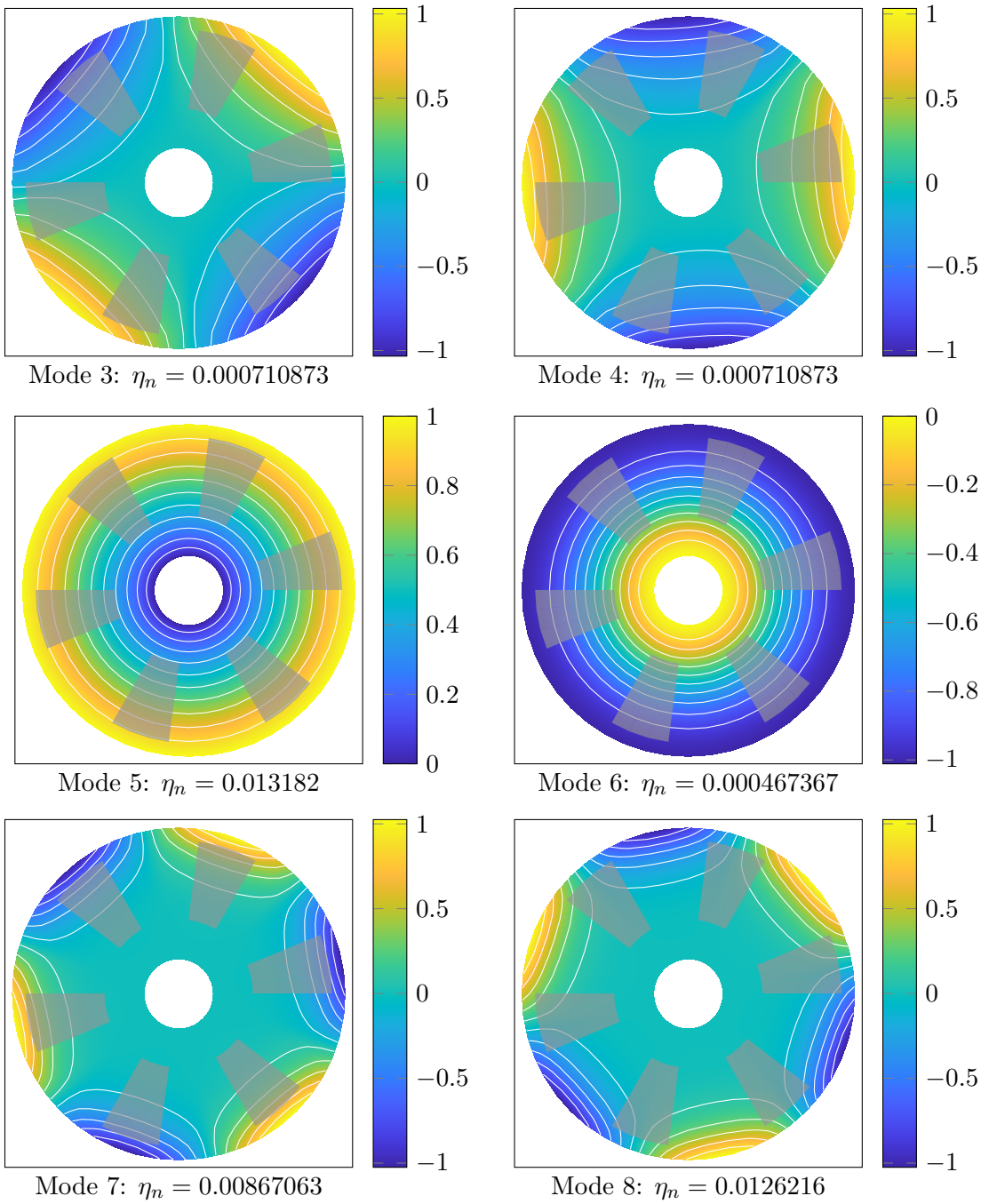

Figure 8.12: Sloped gearwheel with six sections radial damping device mode shapes. *(Continued)*

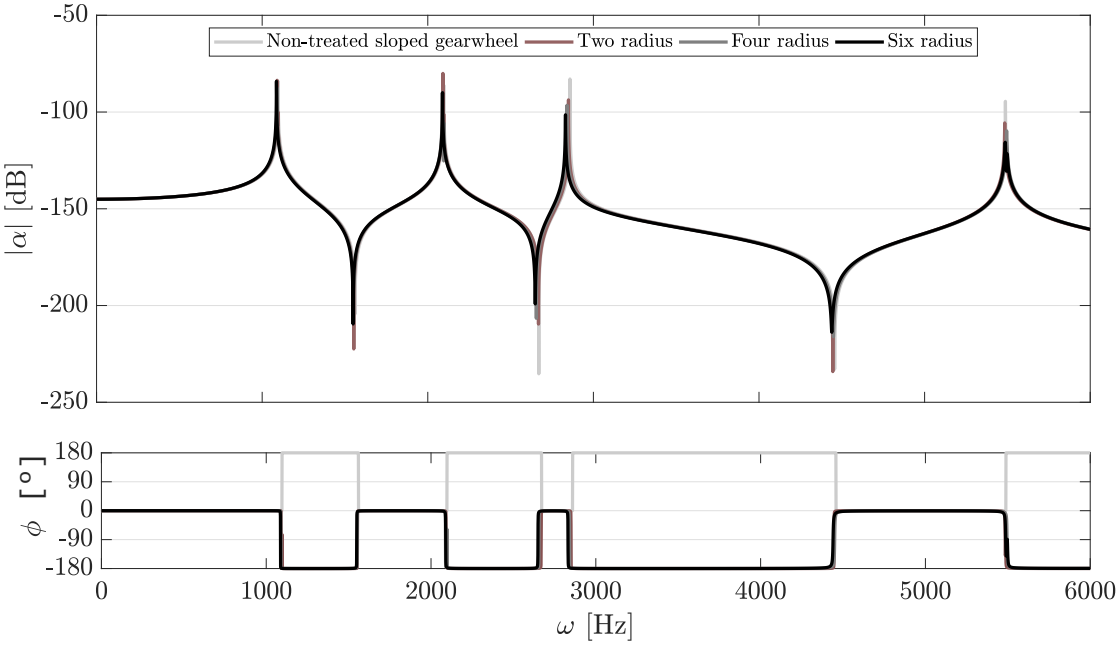

Figure 8.13: Receptance's Bode plot for the complete radial damping device configurations applied on the sloped gearwheel.

Analyzing Table 8.10, it is clear that, as for the plane gearwheel, the number of sections was associated with a better damping capacity, since the loss factors' values were always higher, again because of the higher quantity of dissipative elements involved.

However, when considering the loss factor-added mass balancing parameter, H, in Table 8.11, the previously mentioned high superiority is partially undone. In fact, the results came closer and the two radii configuration's performance even surpassed the others for some modes, namely the ones where the damping device overlapped the nodal nodes.

On the other hand, it is possible to conclude that, for the sloped gearwheel, the positioning of the damping devices in the nodes led to a better damping performance, contrarily to what was verified for the plane case. This phenomenon may be explained, again, by the mode shapes, since for the sloped gearwheel the bending of the web is smaller, thus decreasing the shear strains induced in the viscoelastic material, when compared to the plane case. Despite it was previously concluded that the shear strains in the nodal area are smaller in the sloped gearwheel, it revealed to be more important for damping effects when using radially configured damping devices.

Considering now the split outer ring shaped devices and comparing their damping capacity with the correspondent present configurations (Table 8.12), it is possible to verify that the energy dissipation is higher for all the circumferential configurations. On the other hand, comparing the loss factor-added mass balanced performance (Table 8.13) of these configurations, it revealed that the circumferentially shaped devices also presented a generally better performance, from which it is possible to conclude that the suggested radial setups do not compete with the design proposed by Marsaudon and Cutuli [2014] for the sloped gearwheel case.

Table 8.12: Comparison between the damping capacities of the radial and outer split circumferential configurations for the sloped gearwheel

	Mode	Two Sections		Four Sections		Six Sections	
	(m,n)	Annular η_n [%]	Radial η_n [%]	Annular η_n [%]	Radial η_n [%]	Annular η_n [%]	Radial η_n [%]
1	(1,0)	0.060	0.003	0.052	0.024	0.049	0.035
2		0.057	0.020	0.052	0.024	0.049	0.035
3	(2,0)	0.198	0.014	0.145	0.029	0.113	0.071
4		0.115	0.032	0.129	0.067	0.113	0.071
5	(Torsion)	2.232	0.440	2.144	0.899	2.057	1.318
6	(0,0)	0.200	0.015	0.116	0.031	0.087	0.047
7	(3,0)	0.535	0.290	2.015	0.732	2.143	0.867
8		0.422	0.430	2.015	0.732	2.628	1.262

Table 8.13: Comparison between the loss factor-added mass weighting parameter of the radial and outer split circumferential configurations for the sloped gearwheel

	Mode	Two Sections		Four Sections		Six Sections	
	(m,n)	Annular H	Radial H	Annular H	Radial H	Annular H	Radial H
1	(1,0)	0.018	0.003	0.016	0.014	0.016	0.014
2		0.017	0.024	0.016	0.014	0.016	0.014
3	(2,0)	0.058	0.016	0.044	0.014	0.036	0.014
4		0.034	0.039	0.040	0.040	0.036	0.028
5	(Torsion)	0.657	0.522	0.658	0.534	0.660	0.522
6	(0,0)	0.059	0.018	0.036	0.019	0.028	0.019
7	(3,0)	0.157	0.344	0.619	0.435	0.688	0.343
8		0.124	0.511	0.619	0.435	0.844	0.500

8.3.1 Segmented Configurations

Considering the segmented configurations presented in Figure 8.2, the obtained results and comparison with the correspondent complete setups can be presented in Table 8.14, for the damping capacity, and in Table 8.15 for the loss factor-added mass weighting. Note that $\Delta_{r\,\eta_n}$ and $\Delta_{r\,H}$ represent the relative difference of the sectioned radial configuration loss factor and loss factor-added mass balancing parameter in respect to the correspondent continuous setup, respectively. The natural frequency values are presented in the correspondent mode shapes (Figures 8.14, 8.15 and 8.16), where the total displacement is represented, and the receptance's Bode plot is not presented once the curves overlapped, being nearly impossible to distinguish them.

Table 8.14: Interrupted radial configurations' loss factor results for the sloped gearwheel

Mode		Split Two Sections $\Delta m = 10.31\,\mathrm{g}$		Split Four Sections $\Delta m = 20.62\,\mathrm{g}$		Split Six Sections $\Delta m = 30.93\,\mathrm{g}$	
	(m,n)	η_n [%]	$\Delta_{r\,\eta_n}$ [%]	η_n [%]	$\Delta_{r\,\eta_n}$ [%]	η_n [%]	$\Delta_{r\,\eta_n}$ [%]
1	(1,0)	0.002	-31.749	0.019	-17.363	0.029	-17.374
2		0.018	-11.773	0.019	-17.363	0.029	-17.374
3	(2,0)	0.008	-41.073	0.017	-41.048	0.055	-22.914
4		0.028	-14.251	0.057	-14.860	0.055	-22.914
5	(Torsion)	0.404	-8.020	0.828	-7.878	1.216	-7.716
6	(0,0)	0.012	-24.606	0.023	-27.829	0.035	-24.816
7	(3,0)	0.406	40.020	0.833	13.794	1.206	39.063
8		0.411	-4.511	0.833	13.794	1.219	-3.386

Table 8.15: Interrupted radial configurations' loss factor-added mass weighting parameter results for the sloped gearwheel

Mode		Split Two Sections $\Delta_{r\,m} = 0.74\,\%$		Split Four Sections $\Delta_{r\,m} = 1.48\,\%$		Split Six Sections $\Delta_{r\,m} = 2.22\,\%$	
	(m,n)	H	$\Delta_{r\,H}$ [%]	H	$\Delta_{r\,H}$ [%]	H	$\Delta_{r\,H}$ [%]
1	(1,0)	0.002	-25.309	0.013	-9.566	0.013	-9.577
2		0.023	-3.448	0.013	-9.566	0.013	-9.577
3	(2,0)	0.011	-35.513	0.011	-35.485	0.024	-15.640
4		0.036	-6.160	0.037	-6.827	0.024	-15.640
5	(Torsion)	0.526	0.659	0.538	0.815	0.527	0.992
6	(0,0)	0.015	-17.492	0.015	-21.019	0.015	-17.722
7	(3,0)	0.527	53.232	0.541	24.531	0.523	52.184
8		0.534	4.499	0.541	24.531	0.529	5.730

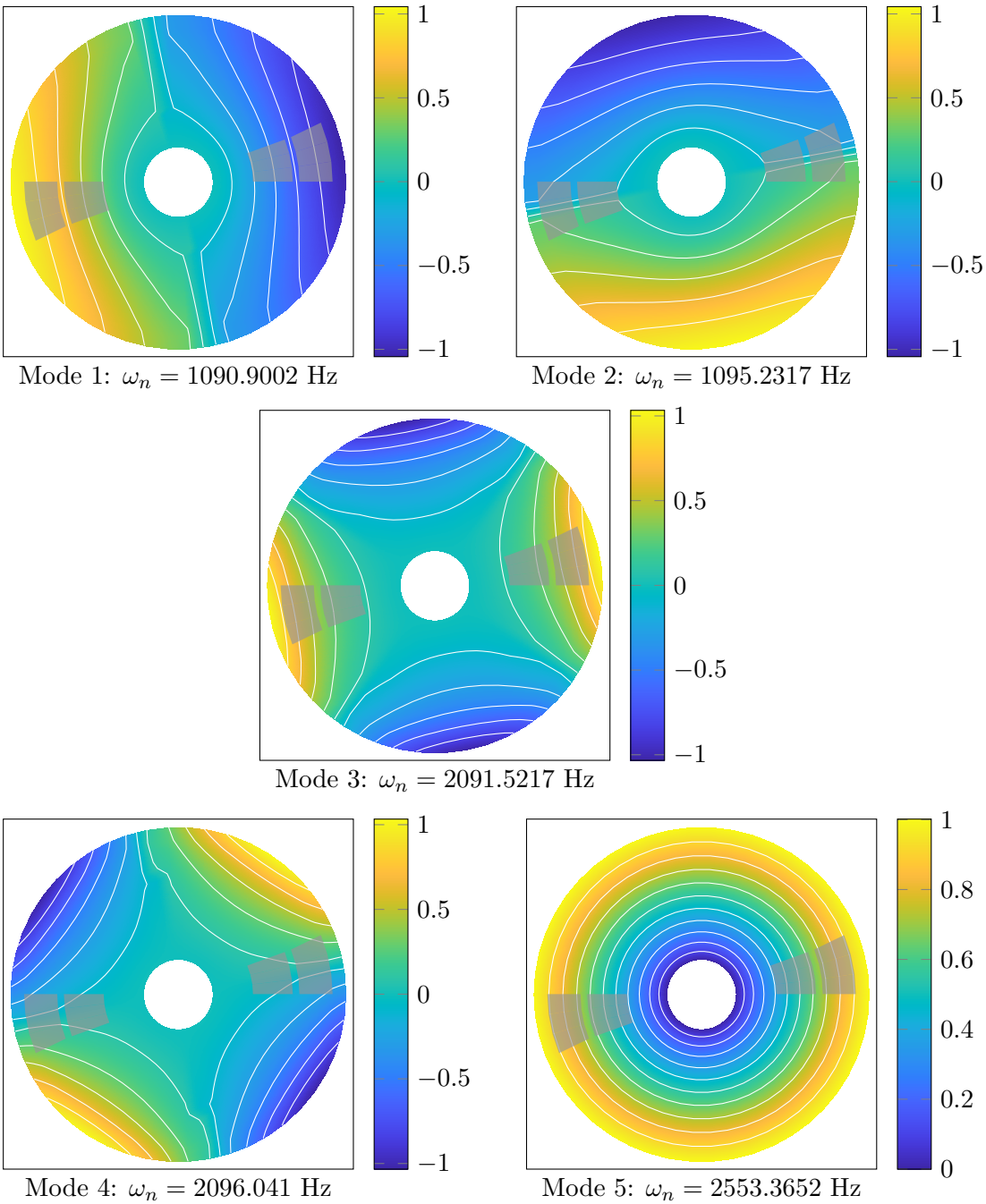

Figure 8.14: Sloped gearwheel with split two sections radial damping device mode shapes.

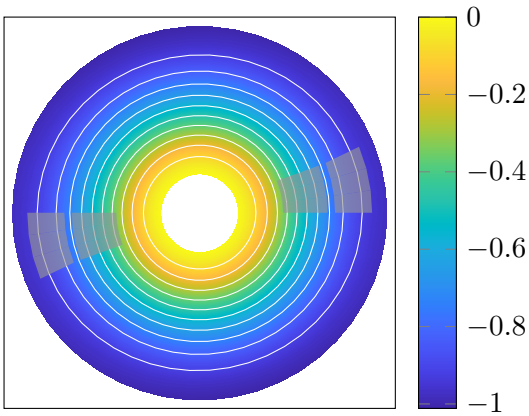

Mode 6: $\omega_n = 2850.2257$ Hz

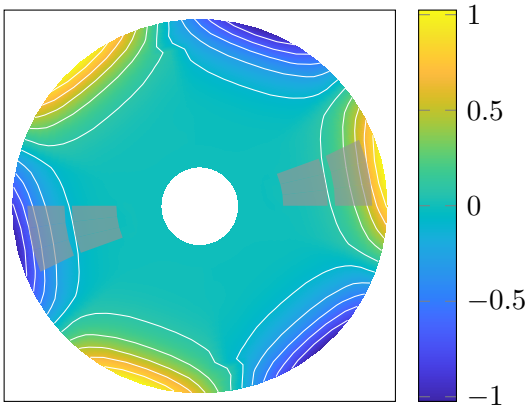

Mode 7: $\omega_n = 5481.0392$Hz

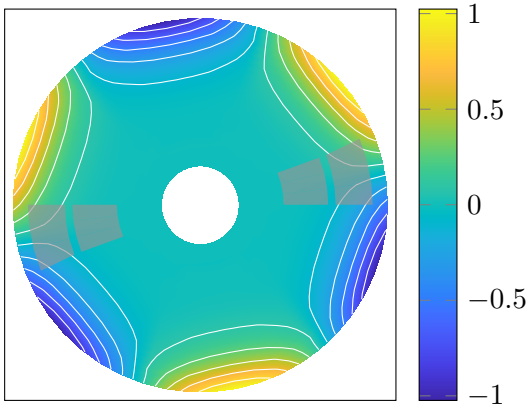

Mode 8: $\omega_n = 5484.9916$ Hz

Figure 8.14: Sloped gearwheel with split two sections radial damping device mode shapes. *(Continued)*

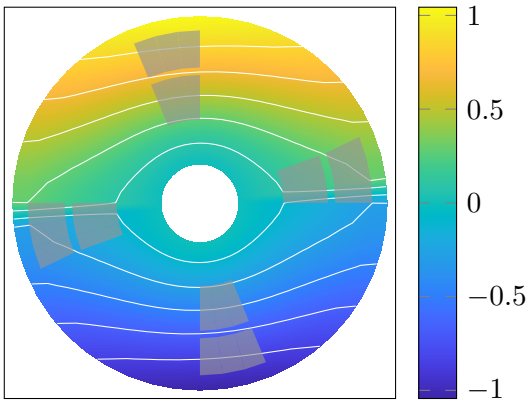

Mode 1: $\omega_n = 1090.1732$ Hz

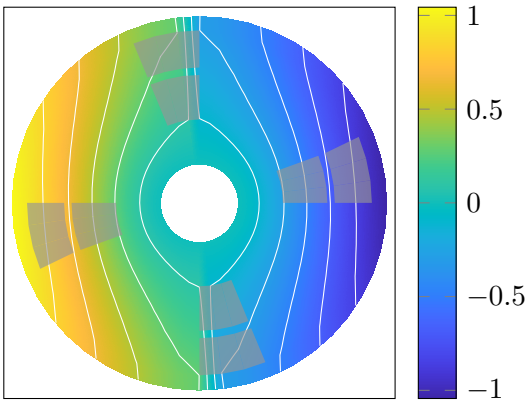

Mode 2: $\omega_n = 1090.1732$ Hz

Figure 8.15: Sloped gearwheel with split four sections radial damping device mode shapes.

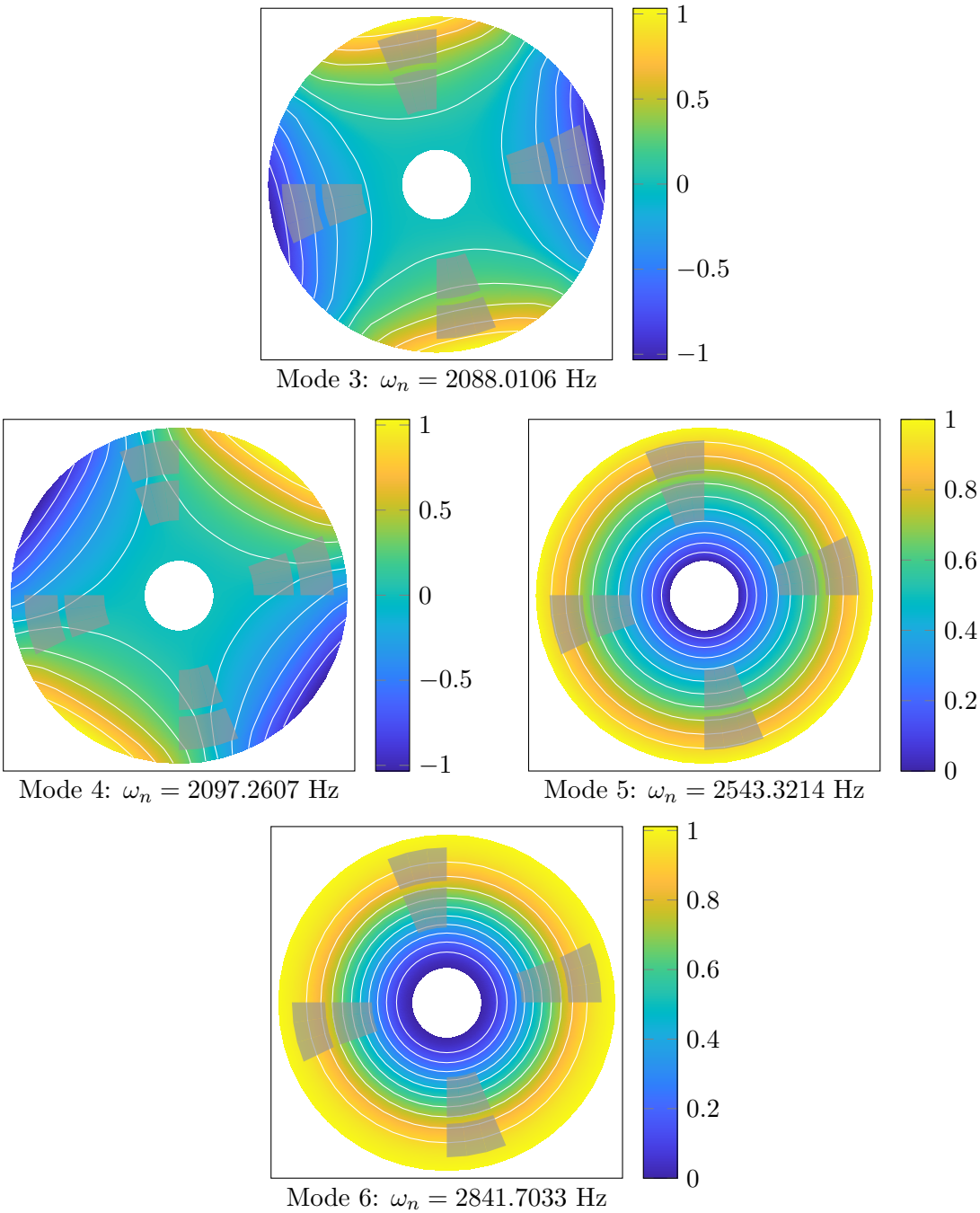

Figure 8.15: Sloped gearwheel with split four sections radial damping device mode shapes. *(Continued)*

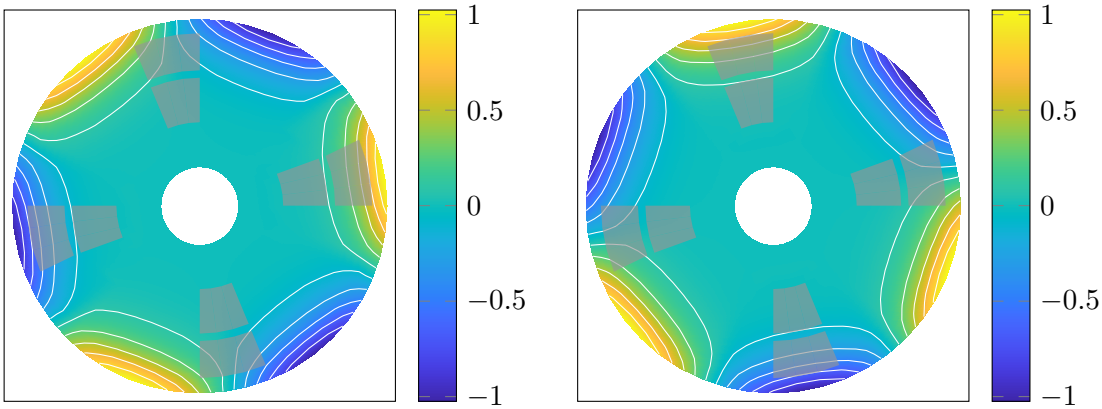

Mode 7: $\omega_n = 5489.7492$ Hz Mode 8: $\omega_n = 5489.7492$ Hz

Figure 8.15: Sloped gearwheel with split four sections radial damping device mode shapes. *(Continued)*

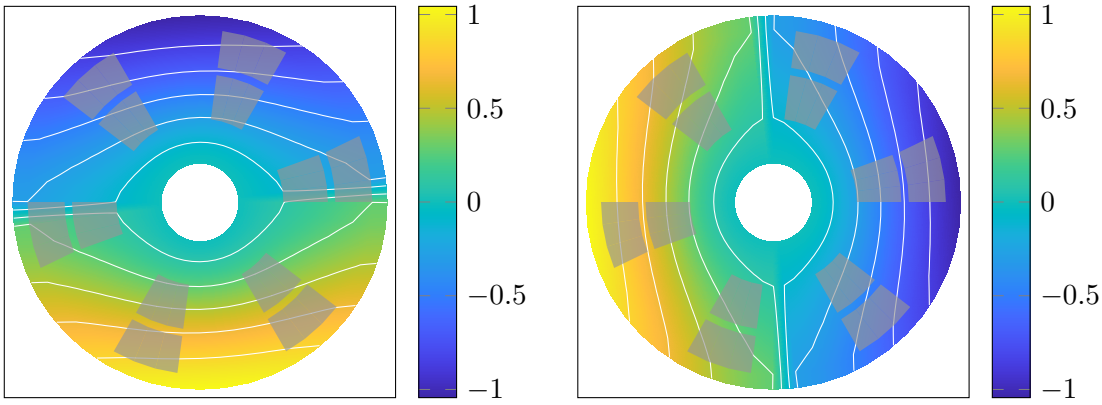

Mode 1: $\omega_n = 1087.1685$ Hz Mode 2: $\omega_n = 1087.1685$ Hz

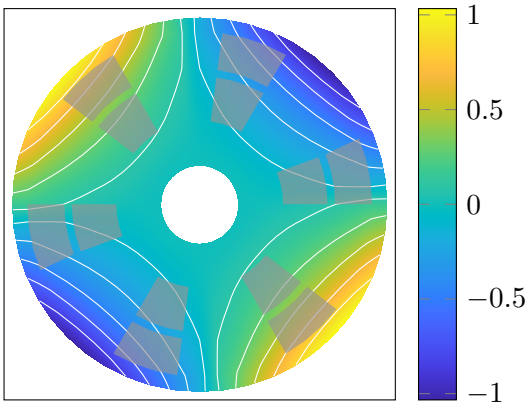

Mode 3: $\omega_n = 2089.4659$ Hz

Figure 8.16: Sloped gearwheel with split six sections radial damping device mode shapes.

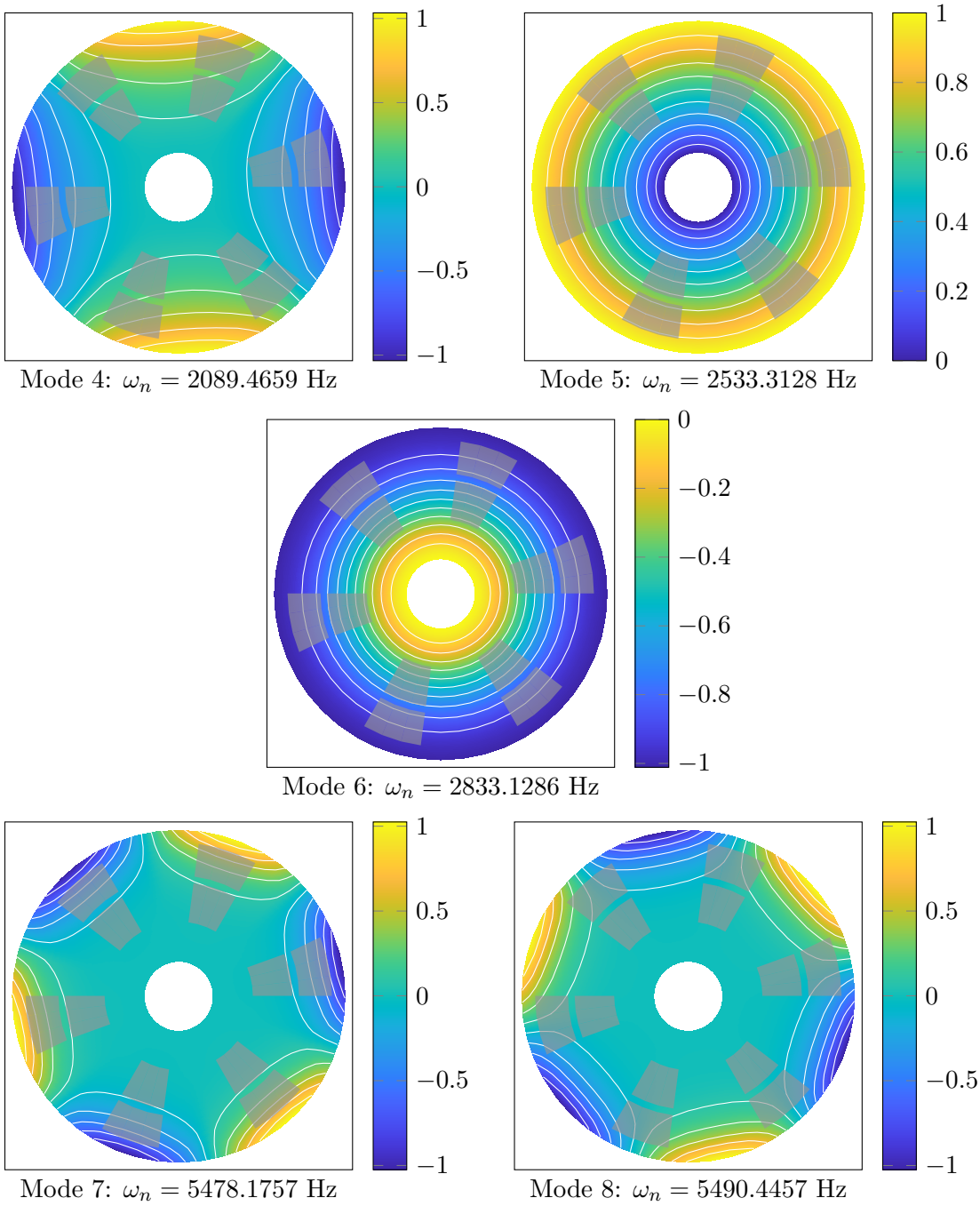

Figure 8.16: Sloped gearwheel with split six sections radial damping device mode shapes. *(Continued)*

From Table 8.14, it is possible to conclude that the split radial configurations present less damping capacities than the correspondent complete circular sections for all cases except for the seventh mode (the mode (3,0) with lower natural frequency value), which may be due to the same reasons as presented for the plane gearwheel. However, when analyzing the balancing parameter relating the damping capacity and the mass added to the system, H, it is possible to verify that the previous relations remained, except for the torsion mode, where the split configurations' performance increased and reached nearly the same level as for the continuous setups.

Again, comparing the interruption effects on the radial and circumferential configurations applied in the sloped gearwheel it is possible to conclude that for the second case they are more beneficial.

8.4 Inclination Effect

In order to better evaluate the inclination effect on the efficiency of the radially configured damping devices, the variation of the setup's loss factors was plotted for α angles between 55° and 125°, which means $\beta \in [-35°, 35°]$. Again, note that the negative values of β can be seen as the application of the viscoelastic damping devices on web's convex face (while the positive values were for the concave side), meaning that the influence of the side where the treatment is applied was also studied.

The results of the configuration with two radial patches are presented in Figure 8.17. Note that only one setup's behavior is presented because the observed evolutions for the other configurations were the same. On the other hand, the natural frequency values were not plotted also because their evolution is nearly the same as the one previously presented for the non-treated gearwheel (Figure 6.10).

From Figure 8.17 it is possible to see that the evolution previously verified for the circumferential configurations is not valid for all the studied modes for the radial setups. In the modes with multiple mode shapes (the ones with diametral nodes) it is possible to verify different evolutions depending if the damping device overlaps the nodal or the antinodal areas. In fact, for the modes with lower natural frequency (damping device exposed to the maximum transverse displacement) the loss factor is bigger for negative than for the correspondent positive angle values, which means that for these cases the higher damping capacity would occur if the treatment was applied over the convex side of the web. On the other hand, for the modes with higher natural frequency value (damping device in the nodal areas) the loss factor is higher for positive than for the correspondent negative angle value, which means that for these cases the higher damping capacity occurs if the treatment is applied over the concave side of the web.

8.5 Conclusion

As a conclusion for the present Chapter addressing the damping efficiency analysis of the suggested radial damping treatments, the bar graphs in Figures 8.5 and 8.19 can be presented, where the values for the balancing parameter H are plotted for the plane and sloped gearwheels, respectively.

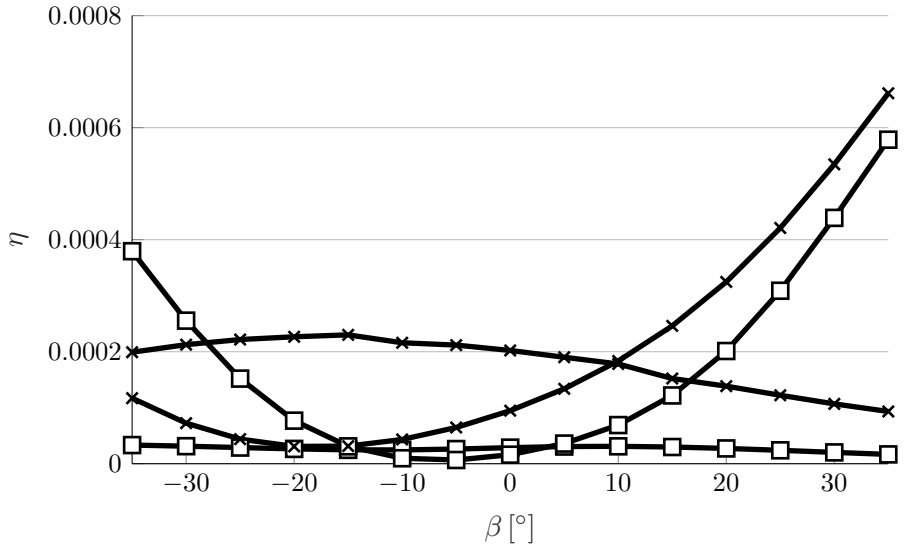

(a) Modes (1,0) and (2,0).

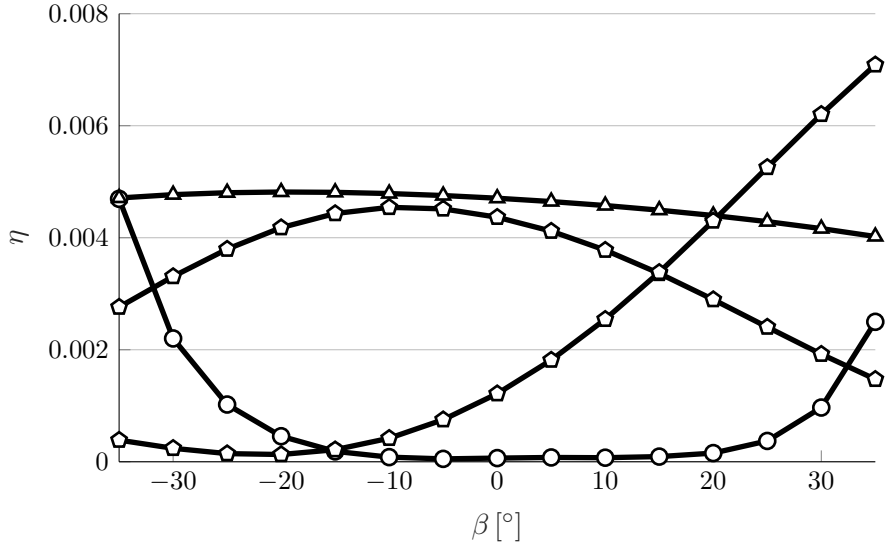

(b) Modes (0,0), (Torsion) and (3,0).

Figure 8.17: Inclination angle effect on the damping behavior of the two sections radial configuration.

Mode (1,0) Mode (0,0) Mode (2,0) Mode (3,0)

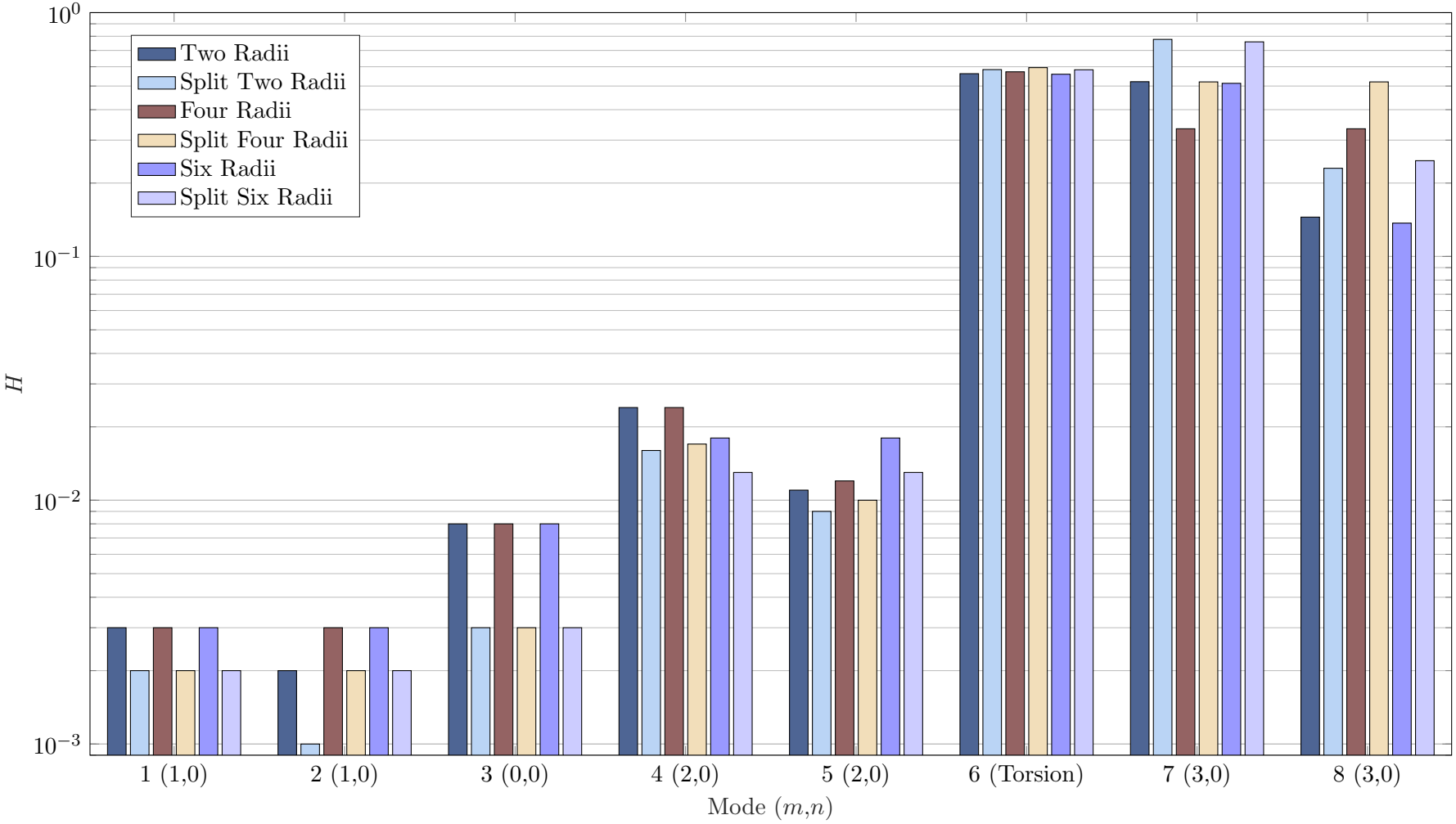

Figure 8.18: Loss factor-added mass weighting parameter, H, values for the radial damping treatments applied on the plane gearwheel.

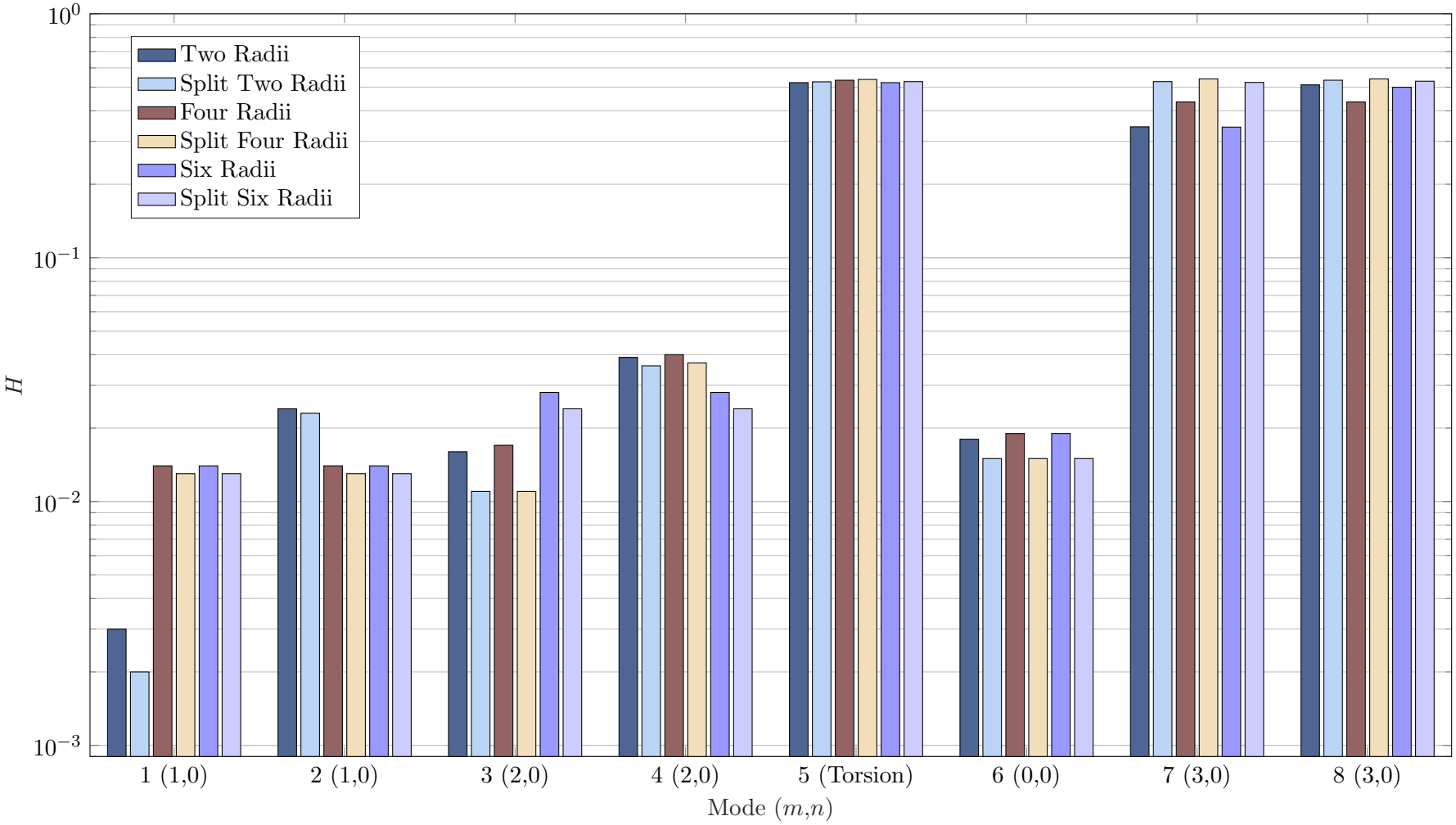

Figure 8.19: Loss factor-added mass weighting parameter, H, values for the radial damping treatments applied on the sloped gearwheel.

Chapter 9

Conclusion

In the present work, a numerical tool to obtain the dynamic analysis of plane and sloped gearwheels with viscoelastic damping treatments, spinning at velocities under 20 000 rpm, was created. Defining a set of parameters for the wheel and the damping device, the algorithm was able to execute the modal and the frequency response analysis from which the energy dissipation and vibrations reduction performance could be determined.

Spinning structures, namely disks, experience changes in their stiffness and dynamic behavior. In fact, it was seen that three different effects arise from such motion: the centrifugal softening, the centrifugal stiffening and the Coriolis effect. The first results from considering that large displacements occur, which represents a geometric non-linearity, and leads to a reduction of stiffness. However, it was also possible to conclude that it is only verified when points of the structure change their distance to the rotation axis and is only significant for very high speeds. The second effect results from the action of the centrifugal force, acting away from the rotation axis and inducing traction stresses for the centrally clamped rotating disk. When performing a modal or frequency response analysis, this force must be accounted for through a matrix, which might be obtained considering the updated Lagrangian approach, using the second Piola-Kirchhoff stress tensor and the Green-Lagrange strain tensor and applying a linearization around the system's stationary state. Finally, the Coriolis effect leads to the split of the bending modes with one or more diametral nodes into a forward and a backward traveling waves, where the first increases it natural frequency and the second one decreases.

Viscoelastic materials reveal themselves as an interesting passive damping mechanism mostly because of their wide range of applications resulting from the relatively high efficiency-cost and efficiency-weight ratios. The vibrations reduction performance can be improved using the suitable treatment configuration and through optimization techniques, such as partial/local application. The damping capacity of these materials comes from the interaction between their long molecular chains and consequent dissipation of energy as heat, and which varies with the working temperature and the frequency of the loading. These dependencies led to the development of suitable constitutive models that contemplate both parameters. On the other hand, they also impose special care on the analysis methods.

The layerwise theory allows the appropriate representation of the shear strains and, consequently, the resulting deformation energy on a multi-layered structure with a simple

geometric model associated. Adding the rotational motion to its classic assumptions, it is possible to conclude that a spinning facet shell element based on a layerwise theory was successfully formulated and implemented. On the other hand, a geometric model of gearwheels which contemplated the possibility of a sloped web and a thicker outer rim for the teeth was also developed and implemented. The previously mentioned simulation tools were successfully validated for the study of plane and sloped disks rotating with velocities between 0 and 20 000 rpm, by comparison with results found in the literature and obtained using a commercial finite element method software. The main reasons that may led to the difference on the results for higher velocities may be based on the usage of bi-dimensional plane elements, that did not allow the correct representation of the web-outer rim connection, and because the compared results might be obtained using slightly different assumptions or finite element formulations.

The dimensions of the gearwheel considered on the patent proposed by Marsaudon and Cutuli [2014] were determined using the information given by its producer and the simulation of the working conditions on KISSsoft®. On the other hand, the viscoelastic material considered for the damping devices was the 3M^{TM} ISD112, mainly because it is a very commonly used material in viscoelastic damping devices with CLD configuration for automotive, aerospace, electrical and mechanical applications. The thicknesses considered for each layer were standard values when using this material.

Having defined and implemented all the necessary tools, an intensive dynamic study of the plane and sloped non-treated gearwheels was successfully conducted. It was possible to conclude that the inclination angle led to the increase of the natural frequencies of some modes and to the decrease of others, which was related to the correspondent mode shapes, that presented higher or lower, respectively, energy needs to promote the structure's deformation. The thicker outer rim's influence was also examined, from where it was possible to conclude that it increased the natural frequency of the modes with significant bending in the outer edge of the structure and decreased the natural frequency of the other modes once the significant addition of mass was not balanced with the required stiffness addition. An individual evaluation of the spinning effects on the non-treated gearwheels was also conducted, from which it was possible to conclude that for the 0-6000 rpm velocity range they were not significant to the modal parameters. However, when considering the 0-100 000 rpm velocity range the changes on the natural frequencies values were clearly verified, and all followed the expected evolution.

The damping efficiency of circumferential and radial devices was studied, both complete and interrupted. In addition to the loss factor and natural frequency analyses, a new dimensionless evaluation parameter that weights the energy dissipation capacity and the added mass to the structure, $H = \frac{\eta}{\Delta_{rm}}$, was proposed and used. For circumferentially configured setups' results, it was possible to conclude that, for the complete cases, the device covering all the treatable area revealed the best damping capacity. However, when considering the balancing variable H, it was possible to conclude that its superiority decreased and was even broken in some cases, such as the first two modes of the plane gearwheel with the inner ring and nearly all modes of the sloped gearwheel with the outer ring. This proved the interest of the proposed parameter, since the higher damping capacity of the treatment covering all the possible area resulted from the fact that a higher quantity of dissipative elements was added to the structure, which would not be completely evident if only the loss factor was used in this performance evaluation.

It was possible to conclude that the complete circumferential damping devices revealed different behaviors for the plane and the sloped gearwheels. In fact, for the plane case, the inner annulus showed a better performance for the three first modes, while for the second

case the outer ring revealed better damping capacity for all the modes. This phenomenon might be due to the effects combination from the correspondent mode shapes' deformation and the action of the centrifugal force. The inclination angle of the web led to the reduction of the bending strains verified near the gearwheels center and, consequently, the decrease of the shear effects in the viscoelastic material, which conducted to the loss of importance of the inner ring for damping purposes. On the other hand, for the sloped gearwheel, the centrifugal force and the significant coupling effects might have led to the increase of the energy dissipation phenomena, since the resultant influence in the membrane displacements and rotations was higher and, consequently, the shear strains in the viscoelastic material increased. The higher the inclination angle, the more significant these effects become. The interruption of the circular damping devices led to the appearance of boundary effects in the treatment, which improved the performance on some modes for the outer ring and for both gearwheels. These results were in accordance with Marsaudon and Cutuli [2014], since the interruption of the circular shaped treatment near the outer teeth rim was suggested as an efficiency improvement method.

The application of the complete circumferential damping devices over the concave side of the gearwheel revealed significantly better damping results than when applied over the convex side, which also agreed with what was proposed by Marsaudon and Cutuli [2014]. However, the authors of the patent justified this effect with the compression induced by the centrifugal force and not with the increased shear strains due to the coupling influence. It can be comprehended that these compressive loads force the molecular chains to be closer and to interact more, which might result in the increase of the energy dissipation. Nevertheless, the implemented finite element did not contemplate the layers' thickness deformation, once the considered value for the viscoelastic layer's thickness ($e_1 = 0.5\,\mathrm{mm}$) was so reduced that it was expected that the compression effects could be neglected. Consequently, the present model was not able to simulate and evaluate the compression effects. For much bigger thicknesses, such as the maximum values proposed by Marsaudon and Cutuli [2014] and higher, these might have some influence and must be considered.

The radial configurations were materialized as two, four and six circular section patches of damping treatment and were suggested as a possible new setup that could lead to a better performance, since they occupy the nodal and antinodal regions. It was concluded that, for the plane gearwheel, the positioning of the radial damping devices in the antinodes led to better damping performances, while for the sloped gearwheel this was verified for the treatment overlapping the nodes. This difference may be due to the decrease of the bending in the maximum displacement zones, which led to lower shear strains generated in the viscoelastic layer, with the increase of the inclination angle. Comparing these configurations with the circumferential shaped devices, it was possible to conclude that the first ones presented significantly lower damping capacity, independently of the web's inclination angle, from which it was possible to affirm that the suggested setups do not compete with the design proposed by Marsaudon and Cutuli [2014]. The interruption of the patches did not reveal the damping capacity improvements, except for the fifth mode, contrarily to what was verified for the split annular shapes. Finally, the inclination angle effect was individually studied, but the results did not agree with the ones for the circumferential configurations, since, for some modes, the positioning of the damping device over the convex side of the web would improve its performance.

Taking into consideration all the objectives initially proposed for this work and what was achieved, it can be concluded that they were completely reached, both in what concerns the development and implementation of a valid and useful numerical analysis tool, and also what deals with the study of the damping efficiency of devices using viscoelastic materials

applied in rotating gearwheels.

9.1 Future Work

The present work can be seen as an introductory study of the dynamic analysis of rotating structures with viscoelastic damping treatments, namely disks and gearwheels, where there is plenty of room for improvement and for new analysis to be done. Some interesting developments and possibilities for future work on this subject can be identified:

- Study the influence of the layers' thickness in the damping efficiency and the dynamic behavior of treated gearwheels. The increase of the loss factors is expected, however this evolution might not be the same in for all configurations, leading to new optimal devices;
- Develop and implement a model that includes the thickness deformation of the layers, so that the centrifugal force's compressive effects can be properly analyzed;
- Study the damping performance dependency of the proposed devices configurations on the spinning velocity of the gearwheels;
- Assay different configurations for the damping devices, such as integrated layer setups, in which the viscoelastic material patches would be inserted in the middle of the gearwheels' webs during the manufacturing process, and multi-layer treatments, which could be materialized by the interleaved deposition of multiple viscoelastic and constraining layers;
- Develop the necessary tools and perform an experimental modal analysis of a rotating damped gearwheel in order to properly validate the obtained results.

References

3M. 3M Viscoelastic Damping Polymer 112 Series. Technical report, 3M, 2017. URL `http://multimedia.3m.com/mws/media/828134O/3m-viscoelastic-damping-polymer-112-series.pdf?fn=1123MDampingPolymerTDS{_}Final`.

T. K. Ahn and C. D. Mote. Mode identification of a rotating disk. *Experimental Mechanics*, 38(4):250–254, dec 1998. ISSN 0014-4851. doi: 10.1007/BF02410386.

S. B. Arab, J. D. Rodrigues, S. Bouaziz, and M. Haddar. Dynamic analysis of laminated rotors using a layerwise theory. *Composite Structures*, 2017. doi: 10.1016/j.compstruct.2017.09.033.

N. Baddour. *A Modelling and Vibration Analysis of Spinning Disks*. Phd, University of Toronto, 2001.

N. Baddour and J. W. Zu. A revisit of spinning disk models - Part II: linear transverse vibrations. *Applied Mathematical Modelling*, 25(7):561–578, jul 2001a. ISSN 0307-904X. doi: 10.1016/S0307-904X(00)00066-4.

N. Baddour and J. W. Zu. A revisit of spinning disk models - Part I: derivation of equations of motion. *Applied Mathematical Modelling*, 25(7):541–559, jul 2001b. ISSN 0307-904X. doi: 10.1016/S0307-904X(00)00065-2.

K.-J. Bathe. *Finite Element Procedures in Engineering Analysis*. Prentice-Hall, Inc., 1982. ISBN 0133173054.

A. Bhimaraddi. Sandwich beam theory and the analysis of constrained layer damping. *Journal of Sound and Vibration*, 179(4):591–602, jan 1995. ISSN 0022-460X. doi: 10.1006/JSVI.1995.0039.

A. Castel, A. Loredo, A. El Hafidi, and B. Martin. Complex power distribution analysis in plates covered with passive constrained layer damping patches. *Journal of Sound and Vibration*, 331(11):2485–2498, may 2012. ISSN 0022-460X. doi: 10.1016/J.JSV.2012.01.020.

C.-Y. Chang, M.-Y. Chang, and J. H. Huang. Vibration analysis of rotating composite shafts containing randomly oriented reinforcements. *Composite Structures*, 63(1):21 – 32, 2004a. doi: 10.1016/S0263-8223(03)00121-1.

M.-Y. Chang, J.-K. Chen, and C.-Y. Chang. A simple spinning laminated composite shaft model. *International Journal of Solids and Structures*, 41(3-4):637 – 662, 2004b. doi: 10.1016/j.ijsolstr.2003.09.043.

J. S. Chen. On the linearization of the equations of motion of a rotating disk. *Applied Mathematical Modelling*, 35(1):392–397, 2011. ISSN 0307904X. doi: 10.1016/j.apm.2010.07.003.

L.-W. Chen and W.-K. Peng. The stability behavior of rotating composite shafts under axial compressive loads. *Composite Structures*, 41(3-4):253 – 263, 1998. doi: 10.1016/S0263-8223(98)00022-1.

H. N. Chu and G. Herrmann. Influence of large amplitudes on free flexural vibrations of rectangular elastic plates. *Journal of Applied Mechanics*, 23:532–540, 1956.

R. D. Cook, D. S. Malkus, M. E. Plesha, and R. J. Witt. *Concepts and Applications of Finite Element Analysis*. John Wiley & Sons, 2007. ISBN 0470088214.

C. D'Angelo and C. Mote. Natural frequencies Of a thin disk, clamped by thick collars with friction at The contacting surfaces, spinning at high rotation speed. *Journal of Sound and Vibration*, 168(1):1–14, nov 1993. doi: 10.1006/jsvi.1993.1358.

J. Dias Rodrigues. *Apontamentos de Vibrações de Sistemas Mecânicos*. Faculdade de Engenharia da U.PORTO, PORTO, 2016 edition, 2016.

B. Didier. A Vibration Damping Device, jan 1992.

R. O. Dodson, Jr. and W. Eversman. Free vibration of a centrally clamped spinning circular disk. *AIAA Journal*, 7(10):2010–2012, oct 1969. ISSN 0001-1452. doi: 10.2514/3.5495.

M. A. Dokainish and S. Rawtani. Vibration analysis of rotating cantilever plates. *International Journal for Numerical Methods in Engineering*, 3(2):233–248, apr 1971. ISSN 0029-5981. doi: 10.1002/nme.1620030208.

J. S. Fang and D. Zhou. Free vibration analysis of rotating mindlin plates with variable thickness. *International Journal of Structural Stability and Dynamics*, 17(04):1750046, may 2016. ISSN 0219-4554. doi: 10.1142/S0219455417500468.

G. Genta and M. Silvagni. On Centrifugal Softening in Finite Element Method Rotordynamics. *Journal of Applied Mechanics*, 81, 2014. doi: 10.1115/1.4024073.

T. Gmuer and J. Rodrigues. Shaft finite elements for rotor dynamics analysis. *ASME, Journal of Vibration and Acoustics*, 113:482–493, 1991.

H. Gubran and K. Gupta. The effect of stacking sequence and coupling mechanisms on the natural frequencies of composite shafts. *Journal of Sound and Vibration*, 282(1-2): 231 – 248, 2005. doi: 10.1016/j.jsv.2004.02.022.

S. H. Hashemi, S. Farhadi, and S. Carra. Free vibration analysis of rotating thick plates. *Journal of Sound and Vibration*, 323:366–384, 2009. doi: 10.1016/j.jsv.2008.12.007.

S.-H. Hsieh and J. Abel. Comparison of two finite element approaches for analysis of rotating bladed-disk assemblies. *Journal of Sound and Vibration*, 182(1):91–107, apr 1995. ISSN 0022-460X. doi: 10.1006/JSVI.1995.0184.

B.-G. Hu, M. A. Dokainish, W. M. Mansour, and W. M. Mansour. A modified MSE method for viscoelastic systems: a weighted stiffness matrix approach. *Journal of Vibration and Acoustics*, 117(2):226–231, apr 1995. doi: 10.1115/1.2873923.

C. D. Johnson and D. A. Kienholz. Finite element prediction of damping in structures with constrained viscoelastic layers. *AIAA Journal*, 20(9):1284–1290, 1982. doi: 10.2514/3.51190.

C. D. Johnson, D. A. Kienholz, E. M. Austin, and M. E. Schneider. Design and analysis of damped structures using finite element techniques. *Proceedings of Conference on Mechanical Vibration and Noise (ASME)*, 131(85):10–13, 1985.

D. I. G. Jones. *Handbook of Viscoelastic Vibration Damping*. John Wiley & Sons, Chichester, England, 1st edn. edition, 2001. ISBN 0 471 49248 5.

E. M. Kerwin. Damping of flexural waves by a constrained viscoelastic layer. *The Journal of the Acoustical Society of America*, 31(7):952–962, jul 1959. ISSN 0001-4966. doi: 10.1121/1.1907821.

J. Killian and Y. Lu. A finite element modeling approximation for damping material used in constrained damped structures. *Journal of Sound and Vibration*, 97(2):352–354, nov 1984. doi: 10.1016/0022-460X(84)90329-8.

N. Kinkaid, O. O'Reilly, and P. Papadopoulos. Automotive disc brake squeal. *Journal of Sound and Vibration*, 267(1):105 – 166, 2003. ISSN 0022-460X. doi: 10.1016/S0022-460X(02)01573-0.

B. Kirchgäßner. Finite elements in rotordynamics. *Procedia Engineering*, 144:736–750, jan 2016. ISSN 1877-7058. doi: 10.1016/J.PROENG.2016.05.079.

H. Lamb and R. V. Southwell. The vibrations of a spinning disk. *Proceedings of the Royal Society A: Mathematical, Physical and Engineering Sciences*, 99(699):272–280, jul 1921. ISSN 1364-5021. doi: 10.1098/rspa.1921.0041.

M. Marsaudon and P. Cutuli. Pinion Vibration Damping Using Viscoelastic Patch, 2014.

M. P. Mignolet, C. D. Eick, and M. V. Harish. Free vibration of flexible rotating disks. *Journal of Sound and Vibration*, 196(5):537–573, 1996. ISSN 0022460X. doi: 10.1006/jsvi.1996.0502.

R. A. S. Moreira. *Modelação e Análise de Tratamentos Viscoelásticos Multi-camada para Controlo Passivo de Vibrações*. Phd, Faculdade de Engenharia da Universidade do Porto, 2004.

R. A. S. Moreira. Structural dynamics and viscoelastic passive damping treatments. In *Modern Mechanical Engineering*, pages 89–107. Springer, Berlin, Heidelberg, 2014. doi: 10.1007/978-3-642-45176-8_5.

R. A. S. Moreira, J. D. Rodrigues, and A. J. M. Ferreira. A generalized layerwise finite element for multi-layer damping treatments. *Computational Mechanics*, 37(5):426–444, apr 2006. doi: 10.1007/s00466-005-0714-1.

A. H. Nayfeh, A. Jilani, and P. Manzione. Transverse vibrations of a centrally clamped rotating circular disk. *Nonlinear Dynamics*, 26:163–178, 2001.

J. L. Nowinski. Nonlinear transverse vibrations of a spinning disk. *Journal of Applied Mechanics*, 31(1):72–78, mar 1964. doi: 10.1115/1.3629573.

H. Oberst and K. Frankenfeld. Über die Dämpfung der Biegeschwingungen dünner Bleche durch fest haftende Beläge. *Acustica*, 2(4):181–194, 1952.

E. Oñate. *Structural Analysis with the Finite Element Method. Linear Statics - Volume 2: Beams, Plates and Shells.* Springer, first edition, 2013. ISBN 978-1-4020-8743-1.

T. B. R. Sino, E. Chatelet, and G. Jacquet. Dynamic analysis of a rotating composite shaft. *Composites Science and Technology*, 68(2):337 – 345, 2008. doi: 10.1016/j.compscitech.2007.06.019.

M. D. Rao. Recent applications of viscoelastic damping for noise control in automobiles and commercial airplanes. *Journal of Sound and Vibration*, 262(3):457–474, may 2003. ISSN 0022-460X. doi: 10.1016/S0022-460X(03)00106-8.

J. Reddy. An evaluation of equivalent-single-layer and layerwise theories of composite laminates. *Composite Structures*, 25(1-4):21–35, jan 1993. ISSN 0263-8223. doi: 10.1016/0263-8223(93)90147-I.

J. N. Reddy. *Mechanics of Laminated Composite Plates : Theory and Analysis.* CRC Press, 1997. ISBN 0849331013.

D. Ross, E. E. Ungar, E. M. Kerwin Jr, and E. M. Kerwin. Damping of plate flexural vibrations by means of viscoelastic laminae. *Structural Damping - Asme Publication*, 1959.

Y. Sadasiva Rao and B. Nakra. Vibrations of unsymmetrical sandwich beams and plates with viscoelastic cores. *Journal of Sound and Vibration*, 34(3):309–326, jun 1974. ISSN 0022-460X. doi: 10.1016/S0022-460X(74)80315-9.

Safran Helicopter Engines. Arriel 1D1 & 1E2 Sale Brochure, 2012. URL `https://www.safran-helicopter-engines.com/sites/turbomeca/files/arriel{_}1d1{_}1e2{_}-{_}sale{_}brochure{_}0.pdf`.

J. G. Simmonds. The Transverse Vibrations of a Flat Spinning Membrane. *Journal of the Aerospace Sciences*, 29(1):16–18, jan 1962. ISSN 1936-9999. doi: 10.2514/8.9297.

S. Singh and K. Gupta. Composite shaft rotordynamic analysis using a layerwise theory. *Journal of Sound and Vibration*, 191(5):739 – 756, 1996. doi: 10.1006/jsvi.1996.0153.

S. K. Sinha. Determination of natural frequencies of a thick spinning annular disk using a numerical RayleighRitz's trial function. *The Journal of the Acoustical Society of America*, 81(2):357–369, feb 1987. ISSN 0001-4966. doi: 10.1121/1.394901.

R. V. Southwell. On the free transverse vibrations of a uniform circular disc clamped at its centre; and on the effects of rotation. *Proceedings of the Royal Society A: Mathematical, Physical and Engineering Sciences*, 101(709):133–153, may 1922. ISSN 1364-5021. doi: 10.1098/rspa.1922.0032.

R. V. Southwell and F. Gough. The free transverse vibration of airscrew blades. *British A. R. C. Reports and Memoranda*, 766, 1921.

C. Vasques, R. Moreira, and J. D. Rodrigues. Viscoelastic damping technologies part II: Experimental identification procedure and validation. *Journal of Advanced Research in Mechanical Engineering*, 1(2):96–110, 2010a.

C. M. A. Vasques, R. A. S. Moreira, and J. D. Rodrigues. Viscoelastic damping technologies part I: Modeling and finite element implementation. *Journal of Advanced Research in Mechanical Engineering*, 1(2):76–95, 2010b.

M.-J. Yan and E. H. Dowell. Governing equations for vibrating constrained-layer damping sandwich plates and beams. *Journal of Applied Mechanics*, 39(4):1041, dec 1972. doi: 10.1115/1.3422825.

H. H. Yoo and S. K. Kim. Flapwise bending vibration of rotating plates. *International Journal For Numerical Methods in Engineering*, 55:785–802, 2002. doi: 10.1002/nme.521.